Volume 97 • Number 1 • September 2026
Established in 1923 • ISSN 1945-0702

The Chemist

Journal of the American Institute of Chemists

In this Issue:

Official journal of
The American Institute of Chemists, Inc.
http://www.theaic.org/pub_thechemist_journals/

The Chemist

Established in 1923, The Chemist is the official publication of The American Institute of Chemists, Inc. (AIC). The Chemist was published quarterly in magazine format up until 2006. The Chemist is currently being set up and formatted as an online journal.

The American Institute of Chemists, Inc. does not necessarily endorse any of the facts or opinions expressed in the articles, book reviews, or advertisements appearing in The Chemist. Subscription: $35 per year to members, $100 per year to non-members. Single copy: $50. The Chemist (ISSN-0009-3025) is published online by The American Institute of Chemists, Inc.

Volume 97 | Issue 1 | 2026

The Chemist

Journal of the American Institute of Chemists

Editorial

Alexander G. Zestos, Ph. D
American University

Nayiri M. Kaissarian, Ph.D
Montgomery College

Dear Readers,

Another year brings us another issue of *The Chemist,* published by the American Institute of Chemists (AIC). Recent developments have brought us new discoveries in the field, such as the development of metal organic frameworks (MOFs) for energy storage, dissipation, sensing, and environmental applications. Moreover, the use of AlphaFold developed by Google DeepMind to predict protein folding and three-dimensional structures of proteins from their amino acid primary structure sequences has also revolutionized protein structure prediction and helped address "the protein folding problem." These were just two developments from the last two Nobel Prizes in Chemistry over the last two years. The development of machine learning (ML) and artificial intelligence (AI) has also revolutionized the chemical sciences as it has revolutionized almost every other field of study as well.

The current issue of *The Chemist* highlights many contributions on natural product synthesis, characterization, and analysis, which has been a recent and recurring theme of this journal. Some of these products include Aerial Part Extracts from *Jaundea pinnata*, Aniline Impacts on Human Skin, Oil Recovered Over Nanocrystalline Cellulose, Stem Bark of *Cordia millenii*, and *Juniperus excelsa* M.Bieb Extracts from Its Leaves and Seeds, Rice Husk, and many others. As many of our contributing authors are from all over the world, we learned about the nutritional and healing properties of exotic plants from various locations.

We also learned about synthetic organic chemistry from Phenyl-2-chloropropionate Synthesis, Crosslinked Alginate–Acrylic Acid–PVA Hydrogel for Efficient Trypan Blue Removal, Brilliant Blue Dye, Schiff Base-Metronidazole Derivatives, and Methyl Anthracenes. Other studies included: Fatty Acids Profiling and Skincare Formulation from *Ricinus communis* (Castor) Seed Oil, Analysis of Novalac, and a study on Aluminum Foil Waste.

The American Chemical Society (ACS) has just recently celebrated its 150th year anniversary, while the American Institute of Chemists is still thriving and still awards the Chemical Pioneer and Gold Medal awards. This is a testament to the enduring nature of chemistry in everyday society.

Best wishes in the upcoming year.

The Chemist
Journal of the American Institute of Chemists

Chemical Composition, Antibacterial, Antifungal, and Antioxidant Activities of Aerial Part Extracts from *Jaundea pinnata*

A.A. Ahmad[1,2], S.B. Issa[3*], Y.T. Yakub[1], A. Jimoh[1], A.O. Issa[4,] A.A. Hamid[1,5*]

[1]Department of Chemistry, Faculty of Physical Sciences, University of Ilorin, Ilorin, Nigeria
[2]Department of Science Laboratory Technology, Institute of Applied Sciences, Kwara State Polytechnic, Ilorin, Kwara State, Nigeria
[3]Department of Materials Science and Engineering, Norwegian University of Science and Technology, Trondheim, Norway
[4]Department of Chemistry, Faculty of Physical Sciences, Ahmadu Bello University, Zaria, Kaduna, Nigeria
[5]Department of Pharmaceutical Chemistry and Analysis, School of Pharmacy, Kampala International University, Western Campus, Uganda

**Corresponding authors (E-mail: issashuaib40@gmail.com; shuaib.b.issa@ntnu.no; hamidmemo@gmail.com; hamid.aa@unilorin.edu.ng)*

Abstract: *Jaundea pinnata* is an underexploited medicinal plant with antibacterial and anti-inflammatory properties. To establish its ethnomedicinal efficacy, this research assessed the chemical composition, antioxidant, and antimicrobial activities of its chloroform, ethyl acetate, and methanol extracts. Preliminary phytochemical screening revealed the presence of cardiac glycosides, tannins, terpenoids, volatile oils, and alkaloids. The extracts exhibited noteworthy inhibition against six bacterial and four fungal strains. Antioxidant tests showed that the chloroform extract exhibited the highest activity, followed by ethyl acetate, while methanol displayed the lowest. Gas Chromatography-Mass Spectrometry (GC-MS) identified 10 compounds in the chloroform extract [predominantly phytol (5.60%)], 17 in ethyl acetate [oleic acid (23.05%) being the most abundant], and 15 in methanol [9-octadecenoic acid (Z)-, methyl ester (35.35%) being the major component]. These results highlight the significant antimicrobial and antioxidant properties of *J. pinnata*, suggesting its potential application in treating infections or oxidative-stress related conditions.

Key Words: *Jaundea pinnata*, antibacterial activity, antifungal activity, antioxidant activity, DPPH radical scavenging, GC-MS, 9-octadecenoic acid (Z)-, methyl ester

1. Introduction

Jaundea pinnata is a member of the family Connaraceae, which is a subgroup of dicotyledons. It is a shrub or small tree that can grow up to 6-7 m in height [1]. Its leaflets, present in 2-4 pairs, assume an elliptic-oblong form, spanning dimensions of 2.5 to 16 cm in length and 1.5 to 7 cm in width. The degree of leaflet reticulation and venation prominence varies depending on the geographical location of the plant. Notably, the flowers of this species exude a fragrant aroma [2]. *J. pinnata* is native to tropical Africa, with a range extending from Guinea to the southern Nigeria and further to the northeastern and eastern regions of Africa [1]. A comprehensive phytochemical screening of the methanolic stem bark extract of the plant revealed the presence of alkaloids, tannins, flavonoids, saponins, and steroids [3]. *Jaundea pinnata*, in its essence, possesses antimicrobial efficacy; reported findings indicate that its hot water extract effectively restrained *Acinetobacter baumannii* and *Salmonella typhimurium* [4]. A subsequent study of the methanolic stem bark extract revealed its possession of anti-arthritic and anti-inflammatory attributes, providing a rational basis for its ethnomedicinal application in addressing Rheumatoid Arthritis (RA), a chronic, inflammatory, and systemic autoimmune ailment [5]. Furthermore, it has been recognized that this plant serves as an animal repellent and is documented to have toxic effects on animals in Kenya [1].

This research focuses on the chemical composition, antimicrobial and antioxidant properties of the plants' aerial part extracts. It is pertinent to note that, to the best of our knowledge, research regarding this plant's biological activities is limited.

2. Materials and Methods

Plant Collection and Identification

Fresh aerial parts of *Jaundea pinnata* were collected from the botanical garden of Forestry Research Institute of Nigeria (FRIN), Ibadan, Oyo State, Nigeria in July 2021, and authenticated by Dr. Odewo of the Institute. A voucher specimen (FHI 109517) was deposited at the herbarium section. The aerial parts of the plant were carefully rinsed with water, air-dried, and subsequently ground into fine powder. The weight of the resulting powder was determined to be 1225 g. This fine powder underwent sequential extraction using chloroform, ethyl acetate, and methanol for 12 days, employing the cold extraction technique. The resulting chloroform (1.082 g), ethyl acetate (2.061 g), and methanol (2.076 g) extracts were obtained through filtration, followed by concentration of each extract to obtain 3 crude extracts by rotary evaporation. These crude extracts were then stored in the refrigerator for future use.

Phytochemical Screening

The preliminary phytochemical studies of the crude extracts were conducted using standard procedures that have been documented in previous studies [6-11].

Antimicrobial Assays

Test microorganisms

Clinical strains of ten (10) test microorganisms from the Department of Medical Microbiology, University College Hospital, Ibadan were screened in the Laboratory of Pharmaceutical Microbiology Department, University of Ibadan, Ibadan, Nigeria. The test strains were comprised of 6 human pathogenic bacteria and 4 fungi. For antibacterial assay, cultures of the bacteria, which made up of 2 gram-positive (*Staphylococcus aureus* and *Bacillus subtilis*) and 4 gram-negative (*Escherichia coli*, *Pseudomona aeruginosa*, *Salmonella typhi*, and *Klebsiellae pneumonae*) were used. Meanwhile, *Candida albicans*, *Aspergillus niger*, *Penicillium notatum*, and *Rhizopus stolonifer* were the fungi utilized for antifungal assay.

Media

In this study, nutrient agar, Sabouraud dextrose agar, nutrient broth and tryptone soya agar (Oxoid Ltd) were used. Chloroform, ethyl acetate, and methanol were also used in solubilizing the extracts and act as negative controls in the assays.

Antimicrobial agents

Gentamycin (10 µg/mL) and Tioconazole (0.7 mg/mL) were utilized as standard reference drugs in the study.

Determination of antimicrobial activity

(a)Agar diffusion – pour plate method (bacteria)

Overnight cultures of each organism were prepared by taking a loop-full of the organisms from the stock and inoculating each into 5 mL of sterile nutrient broth. These were then incubated for 24 hours at 37°C. From the overnight cultures, 0.1 mL of each organism was taken and mixed with 9.9 mL of sterile distilled water to achieve a 1:100 dilution (i.e., 10^{-2} M inoculum concentration) of the test organism. From this diluted solution (10^{-2} M) of the test organism, 0.2 mL was taken and placed into the prepared sterile nutrient agar, which was maintained at 45°C. The mixture was then aseptically poured into sterile petri dishes and allowed to solidify for 60 minutes [12].

Using a sterile cork borer with an 8 mm diameter, seven wells were created corresponding to the number of different graded concentrations of the sample. The graded concentrations (6.25–100 mg/mL) of the sample were placed within the wells, each in duplicate to ensure reliable results and separated from the controls. The plates were left undisturbed for 2 hours to facilitate proper pre-diffusion. Subsequently, the plates were uprightly incubated for 24 hours at 37°C.

(b)Agar diffusion - surface plate method (fungi)

A sterile Sabouraud Dextrose Agar solution (62 g/L) was meticulously prepared and then poured into sterile plates in duplicate, allowing it to properly set. 0.2 mL of the 10^{-2} M diluted organism solution was uniformly spread onto the agar surface using a sterile spreader. Seven wells were made using a sterile cork borer with an 8 mm diameter. Within each well, graded concentrations of the extracts, including controls, were introduced. The plates were left undisturbed for 120 minutes to enable proper diffusion of the extracts into the agar, a phase known as pre-diffusion. Following this, the plates were incubated in an upright position at 28°C for 48 hours [13].

Antioxidant Activity

The free radical scavenging activity of the extracts was assessed by employing the 2,2-diphenyl-1-picrylhydrazyl (DPPH) radical scavenging assay, following the procedures outlined by Blois [14] and Desmarchelier *et al.* [15]. The extract was weighed and subsequently dissolved in 100 mL of methanol. A solution containing 0.1 mM of DPPH in methanol was then prepared. This DPPH solution produced a violet/purple color in methanol solution. To evaluate the scavenging activity, the extract (1.6 mL) in methanol was mixed with 2.4 mL of the aforementioned DPPH solution, at varying concentrations ranging from 10 to 150 µg/mL. The resulting mixture was vigorously agitated and allowed to incubate in darkness at room temperature for a duration of 30 minutes. Following this, the absorbance of the mixtures was measured at a wavelength of 517 nm utilizing a U-V (Ultraviolet-Visible) spectrometer (Perkin-Elmer Model). Vitamin C was used as a reference standard. The experiment was replicated three times for each concentration. The percentage of DPPH radical scavenging activity was determined using the subsequent equation:

$$\%\ \text{DPPH radical scavenging activity} = \left(\frac{\text{A of control} - \text{A of sample}}{\text{A of control}}\right) \times 100$$

where A = Absorbance.

The IC_{50} values, denoting the inhibition concentration at 50%, were estimated from the % inhibition versus concentration plot, using a non-linear regression algorithm. This representation illustrates the extract dose necessary to induce a 50% reduction in absorbance at 517 nm [16].

GC-MS Analysis of the Extract

The GC-MS analysis of chloroform, ethyl acetate and methanol plant extracts were conducted at the Shimadzu Training Centre for Analytical Instruments (STC) in Lagos, using the GCMS-QP2010SE instrument from Shimadzu, Japan. This instrument was equipped with the Optima 5 ms capillary column (30 × 0.25 mm^2) having a 0.25 µm film thickness. The procedure followed the method outlined by Ajiboye *et al*. [17], with slight modifications. The gas chromatographic conditions were as follows: pure helium served as the carrier gas with a flow rate of 1.56 mL/min and a linear velocity of 37 cm/s. The initial column oven temperature was set at 60°C, and it was programmed to increase to 160°C at a rate of 10°C/min, and then finally to 250°C. A hold time of 2 minutes per increment was applied. The injection volume was 0.5 µL in the splitless mode, utilizing a split ratio of 1:1. The injector temperature was maintained at 250°C. Regarding the mass spectrometer parameters, the ion source temperature stood at 230°C, while the interface temperature was set at 250°C. A solvent delay of 4.5 minutes was implemented, and the acquisition occurred within a scan range of 50–700 amu. The electron ionization mode was used, with a multiplier voltage of 70 eV and 185 eV, respectively. For compound identification, the retention time, fragmentation pattern, and mass spectral data of the unknown components in the extracts were compared against entries in the Wiley and National Institute of Standards and Technology (NIST) libraries. This comprehensive approach facilitated accurate compound identification.

3. Results and Discussion

Phytochemical Screening

The preliminary phytochemical screening of *Jaundea pinnata* indicates the presence of cardiac glycosides, tannins, terpenoids, volatile oils and alkaloids in all the three extracts.

Anthraquinones and saponins were both found in the chloroform and ethyl acetate extracts but not in the methanol extract. Flavonoids were found in the chloroform extract only, whereas steroids were found to be present in the methanol extract only (Table 1). The presence of this important class of phytochemicals could be an indicator that *Jaundea pinnata* may have pharmacological importance. For instance, as natural polyphenols, flavonoids are well-recognized for their exceptional antioxidant properties [16,18]. Concurrently, tannins, such as condensed tannins, fall under the category of phenolic compounds, characterized by the presence of oligomers and polymers of flavan-3-ol monomeric units. Numerous studies have reported diverse biological activities associated with condensed tannins, including noteworthy antioxidant effects [16,19-21].

Table 1. Phytochemical Tests Results of Chloroform, Ethyl Acetate, and Methanol Extracts of *J. pinnata* (Aerial Parts)

S/N	Phytochemicals	Whole plant extract		
		Chloroform	Ethyl acetate	Methanol
1	Anthraquinones	+	+	-
2	Cardiac glycosides	+	+	+
3	Flavonoids	+	-	-
4	Saponins	+	+	-
5	Steroids	-	-	+
6	Tannins	+	+	+
7	Terpenoids	+	+	+
8	Volatile oils	+	+	+
9	Alkaloids	+	+	+

+ = presence; - = absence of corresponding phytoconstituents

Antimicrobial Activity

The antimicrobial assay is presented in Table 2. From the antibacterial study, the chloroform, ethyl acetate and methanol extracts inhibited the growth of all the test organisms at all concentrations, although the test organisms were just fairly inhibited at low concentrations (6.25–25 mg/mL). At moderate to high concentrations (50–100 mg/mL), all the three extracts showed significant inhibition of all the test organisms. The methanolic extract showed better inhibition than the ethyl acetate extract, whereas the chloroform extract displayed the least inhibition of the test organisms. However, the results of the antifungal assay indicated effective inhibition of all the test organisms by all the three extracts, at all concentrations, except for the chloroform extract which was resisted by *Rhizopus stolonifer* at a concentration of 6.25 mg/mL. Here, the inhibition also increases with increase in the concentration. The test organisms were only fairly inhibited at lower concentrations, between 6.25 and 25 mg/mL, but at medium to high concentrations (50–100 mg/mL), the extracts showed significant antifungal activity. In addition, the methanol extract displayed higher anti-fungal activity than the chloroform extract although with almost similar activity as the ethyl acetate extract.

Table 2. Antimicrobial Activity of Chloroform, Ethyl Acetate and Methanol Extracts of *J. pinnata* (Aerial Parts)

Extracts	Extracts conc. (mg/mL)	Mean zone of inhibition (mm)									
		S.a	***E.c***	***B.s***	***P.a***	***S.t***	***K.p***	***C.a***	***A.n***	***P.n***	***R.s***
Chloroform	6.25	10	10	10	10	10	10	10	10	10	-
	12.5	13	14	13	13	12	13	12	12	11	10
	25	15	16	17	15	15	16	14	13	13	12
	50	18	18	19	17	17	18	16	16	15	14
	100	20	21	23	19	19	22	18	18	17	16
	-ve	-	-	-	-	-	-	-	-	-	-
	+ve	39	39	39	39	38	39	28	27	27	26
Ethyl acetate	6.25	14	14	11	14	12	14	10	10	10	10
	12.5	18	17	14	17	16	18	14	14	12	12
	25	21	21	18	20	19	22	16	15	14	14
	50	24	24	22	23	22	25	18	17	16	16
	100	27	27	25	26	25	29	20	18	18	18
	-ve	-	-	-	-	-	-	-	-	-	-
	+ve	40	40	38	40	38	38	28	27	27	27
Methanol	6.25	15	14	15	17	14	16	12	12	11	10
	12.5	19	18	19	21	17	20	14	14	14	14
	25	23	21	23	24	21	23	16	16	16	16
	50	27	24	27	27	25	27	18	18	18	18
	100	30	28	30	30	28	30	20	20	19	20
	-ve	-	-	-	-	-	-	-	-	-	-
	+ve	40	40	38	40	38	38	28	27	27	27

S.a = Staphylococcus aureus; E.c. = Escherichia coli; B.s. = Bacillus subtilis; P.a = Pseudomonas aeruginosa; S.t. = Salmonellae typhi; K.p. = Klebsiellae pneumonae; C.a = Candidas albicans; A.n = Aspergillus niger; P.n. = Penicillum notatum; R.s. = Rhizopus stolon; +ve = Gentamicin (10 µg/mL) for bacteria or Tioconazole (0.7 mg/mL) for fungi; -ve = Solvent of dilution

From the foregoing, it can be deduced that the three extracts exhibit antimicrobial activity and their effects on the microbes depend on the concentration of the extract – the higher the concentration, the higher the antimicrobial activity. The activity may be attributed to the presence of bioactive compounds, such as terpenoids, alkaloids and tannins. The better inhibition of methanol extract, compared to the chloroform and ethyl acetate extracts, may be due to the presence of steroids, as shown in Table 1.

Antioxidant Activity

The reduction ability of DPPH radical, indicative of antioxidant activity, was determined by measuring the decrease in absorbance induced by plant antioxidants– a process wherein the free radical accepts an electron or hydrogen radical, transforming into a stable diamagnetic molecule [16]. Hence, the scavenging potential of the plant extracts (chloroform, ethyl acetate, and methanol) against DPPH radicals were analyzed, and the results of the analysis are shown in Table 3 and Figure 1.

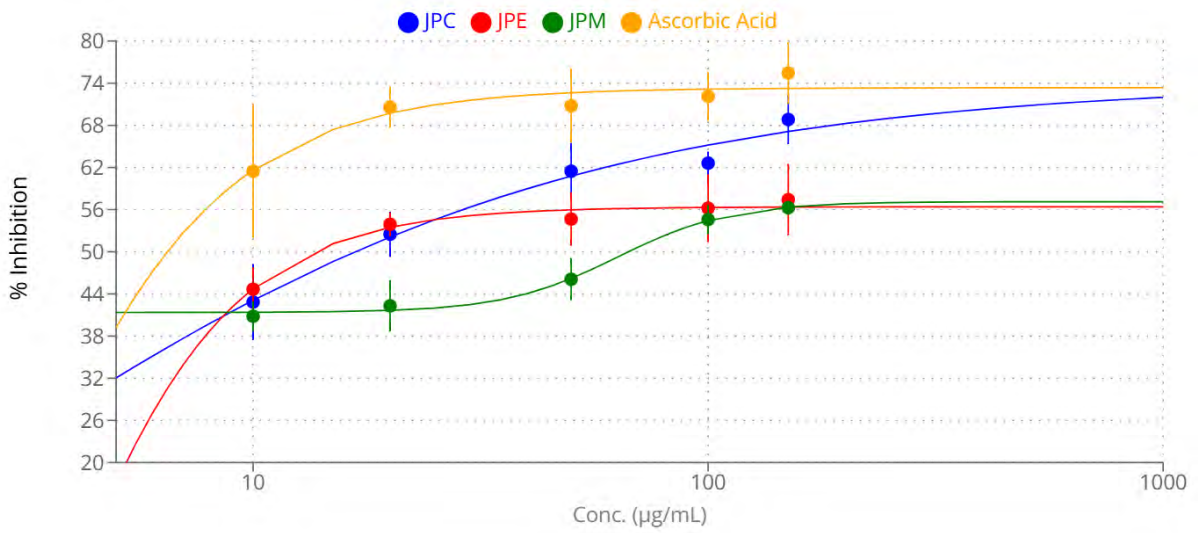

Figure 1. DPPH Scavenging Potential of Crude Extracts of *J. pinnata* (Aerial Parts), Compared with Ascorbic Acid as Standard; JPi = *J. pinnata*'s Chloroform (i = C), Ethyl Acetate (i = E), and Methanol (i = M) Extract

The results indicated that the extracts scavenged DPPH radicals in a dose-dependent manner with the chloroform extract displaying the highest percentage inhibition (68.83%) at 150 µg/mL.

Table 3. Determination of Free-Radical Scavenging Capacity for the Extracts from *J. pinnata* (Aerial Parts)

Concentration (µg/mL)	%IJPC	%IJPE	%IJPM	%IA
10	42.85 ± 3.83	44.67 ± 2.21	40.82 ± 1.49	61.47 ± 6.69
20	52.50 ± 2.27	53.91 ± 1.20	42.31 ± 2.56	70.58 ± 2.05
50	61.47 ± 2.84	54.66 ± 2.68	46.09 ± 2.12	70.78 ± 3.72
100	62.62 ± 1.15	56.21 ± 3.42	54.59 ± 1.45	72.13 ± 2.47
150	68.83 ± 2.46	57.42 ± 3.58	56.28 ± 0.42	75.44 ± 3.11

Values are average ± standard error of the mean (SEM) from three replicates; %IJPi = percentage inhibition of *J. pinnata* (i = C (chloroform); E (ethyl acetate); and M (methanol) extract); %IA = percentage inhibition of ascorbic acid (standard)

Illustrated in Figure 1 are the scavenging effects of the three plant extracts and the standard on DPPH radicals, with their IC_{50} values determined using an IC_{50} calculator [22], based on a dose-dependent, non-linear regression algorithm. The IC_{50} values of chloroform, ethyl acetate, and methanol extracts are 2.11 µg/mL, 3.16 µg/mL, and 63.25 µg/mL, respectively, whereas that of ascorbic acid is 2.42 µg/mL. The observed IC_{50} values indicate pronounced antioxidant properties for both the chloroform and ethyl acetate extracts of the plant, comparable to those of the reference, ascorbic acid. Notably, considering the established inverse relationship between antioxidant activity and IC_{50} values [16], the chloroform extract of *J. pinnata* exhibited the highest antioxidant activity (greater than the reference) among the tested extracts while the methanol extract displayed the weakest antioxidant property. These results can be attributed to the presence of flavonoids in the chloroform extract, which were found lacking in the remaining extracts (Table 1). Despite the absence of flavonoids in both the ethyl acetate and methanol extracts, as revealed by the results from the phytochemical screening (Table 1), the IC_{50} value of the former was very much lower than that of the latter. Possible explanations for this phenomenon may be attributed to the presence of condensed tannins in the ethyl acetate extract, which could be lacking or present in a trace quantity in the methanol extract, or the presence of certain anthraquinones (such as emodin, aloe-emodin, chrysophanol, physcion, rhein, and hypericin) in the ethyl acetate extract, which are known for their reported antioxidant activity [23]. Nevertheless, a more detailed phytochemical profiling, including total phenolic content and anthraquinone profiling, is warranted to substantiate these hypotheses.

4. GC-MS Results

Shown in Tables 4-6 are the GC-MS results from the chloroform, ethyl acetate, and methanol extracts of *J. pinnata* (aerial parts). In the chloroform extract, 10 compounds were identified, the principal one being phytol (5.60%). In contrast, the ethyl acetate extract revealed 17 compounds. Its primary constituents comprised oleic acid (23.05%), n-hexadecanoic acid (12.06%), methyl ester of 9-octadecenoic acid (Z) (11.32%), dibutyl phthalate (10.08%), hexadecanoic acid methyl ester (6.16%), and hexanoic acid (5.80%). Conversely, 15 compounds were identified in the methanol extract, the principal constituents being methyl ester of 9-octadecenoic acid (Z) (35.35%), hexadecanoic acid methyl ester (15.75%), dibutyl phthalate (9.36%), methyl stearate (7.83%), and 15-octadecenoic acid methyl ester (5.89%). These principal components, along with the trace compounds, are likely responsible for the observed free radical scavenging and antimicrobial activities of the plant extracts.

Table 4. GC-MS Analysis of Chloroform Extract of Aerial Part from *J. pinnata*

S/N	Compound Name	Peak Area (%)	Molecular Formular	Molecular Weight (g/mol)	Retention time (min)
1	Oxirane, hexadecyl-	0.66	$C_{18}H_{36}O$	268	15.056
2	Hexadecanoic acid, methyl ester	0.78	$C_{17}H_{34}O_2$	270	15.662
3	n-Hexadecanoic acid	0.11	$C_{16}H_{32}O_2$	298	16.426
4	9-Octadecenoic acid, methyl ester, (E)-	0.54	$C_{19}H_{36}O_2$	296	17.039
5	Phytol	5.60	$C_{20}H_{40}O$	296	17.192
6	Methyl stearate	0.47	$C_{19}H_{38}O_2$	298	17.275
7	4,8,12,16-Tetramethylheptadecan-4-olide	0.22	$C_{21}H_{40}O_2$	324	19.329
8	9-Octadecenamide, (Z)-	0.59	$C_{18}H_{35}NO$	281	19.536
9	Bis(2-ethylhexyl) phthalate	0.20	$C_{24}H_{38}O_4$	390	20.759
10	Vitamin E	0.36	$C_{29}H_{50}O_2$	430	21.300

Table 5. GC-MS Analysis of Ethyl Acetate Extract of Aerial Part from *J. pinnata*

S/N	Compound Name	Peak Area (%)	Molecular Formular	Molecular Weight (g/mol)	Retention time (min)
1	Hexanoic acid	5.80	$C_6H_{12}O_2$	116	6.909
2	Phenol, 2,4-bis(1,1-dimethylethyl)-	0.31	$C_{14}H_{22}O$	206	12.637
3	Tetradecane	0.24	$C_{14}H_{30}$	198	13.674
4	4,4,5,8-Tetramethylchroman-2-ol	2.63	$C_{13}H_{18}O_2$	206	14.020
5	2(3H)-Benzofuranone, hexahydro-3a,7a-dimethyl-3-methylene-, cis-	1.74	$C_{11}H_{16}O_2$	180	14.317
6	2-Pentadecanone, 6,10,14-trimethyl-	0.64	$C_{18}H_{36}O$	268	15.815
7	Hexadecanoic acid, methyl ester	6.16	$C_{17}H_{34}O_2$	270	16.467
8	Dibutyl phthalate	10.08	$C_{16}H_{22}O_4$	278	16.605
9	n-Hexadecanoic acid	12.06	$C_{16}H_{32}O_2$	256	16.839
10	9,12-Octadecadienoic acid, methyl ester	1.19	$C_{19}H_{34}O_2$	294	17.852
11	9-Octadecenoic acid (Z)-, methyl ester	11.32	$C_{19}H_{36}O_2$	296	17.924
12	Phytol	4.44	$C_{20}H_{40}O$	296	18.103
13	Methyl stearate	2.68	$C_{19}H_{38}O_2$	298	18.174
14	Oleic Acid	23.05	$C_{18}H_{34}O_2$	282	18.429
15	9,11-Octadecadienoic acid, methyl ester, (E, E)-	2.21	$C_{19}H_{34}O_2$	294	18.683
16	Methyl 18-methylnonadecanoate	0.60	$C_{21}H_{42}O_2$	326	20.176
17	Docosanoic acid, methyl ester	1.11	$C_{23}H_{46}O_2$	354	21.955

Table 6. GC-MS Analysis of Methanol Extract of Aerial Part from *J. pinnata*

S/N	Compound Name	Peak Area (%)	Molecular Formular	Molecular Weight (g/mol)	Retention time (min)
1	Phenol, 2,4-bis(1,1-dimethylethyl)-	0.32	$C_{14}H_{22}O$	206	12.659
2	Hexadecanoic acid, methyl ester	15.75	$C_{17}H_{34}O_2$	270	16.470
3	Dibutyl phthalate	9.36	$C_{16}H_{22}O_4$	278	16.619
4					
5	9,12-Octadecadienoic acid, methyl ester	2.43	$C_{19}H_{34}O_2$	294	17.857
6	9-Octadecenoic acid (Z)-, methyl ester	35.35	$C_{19}H_{36}O_2$	296	17.933
7	15-Octadecenoic acid, methyl ester	5.89	$C_{19}H_{36}O_2$	296	17.976
8	Phytol	3.38	$C_{20}H_{40}O$	296	18.108
9	Methyl stearate	7.83	$C_{19}H_{38}O_2$	298	18.178
10	Methyl 9-cis,11-trans-octadecadienoate	2.26	$C_{19}H_{34}O_2$	294	18.697
11	cis-11-Eicosenoic acid, methyl ester	1.35	$C_{21}H_{40}O_2$	324	19.916
12	Eicosanoic acid, methyl ester	2.79	$C_{21}H_{42}O_2$	326	20.178
13					
14	Docosanoic acid, methyl ester	4.83	$C_{23}H_{46}O_2$	354	21.957
15	Tetracosanoic acid, methyl ester	0.72	$C_{25}H_{50}O_2$	382	23.528

Phytol, present at 5.60% in the chloroform extract (Table 4) has been reported for its potent *in vitro* antioxidant activity, attributed to its potential to eliminate hydroxyl radicals and nitric oxide and prevent the formation of thiobarbituric acid reactive substances [24]. Its presence, together with the existence of flavonoids (Table 1), may elucidate the chloroform extract's comparatively higher antioxidant property, despite its comparatively lower antibacterial and antifungal activities among the three extracts. Detailed compound information, including compound names, peak areas, molecular formulae, molecular weights and retention times, is provided in Tables 4, 5, and 6 for all the constituents present in each extract. The compounds reported in the table are the ones with the highest matching (> 95%) of spectra and fragmentation patterns with reference to those from the NIST's mass spectral library.

5. Conclusions and Recommendation

The aerial parts of *Jaundea pinnata* have been investigated in this research and the preliminary phytochemical assay revealed the presence of cardiac glycosides, tannins, terpenoids, volatile oils and alkaloids in all the three extracts. Notably, the absence of flavonoids in the ethyl acetate and methanol extracts, steroids in the chloroform and ethyl acetate extracts, and anthraquinones solely in the methanol extract was also observed.

Significant antimicrobial activity was noted across all the three extracts, demonstrating notable inhibition of all the test bacteria and fungi at moderate to high concentrations (50-100 mg/mL). Although relatively lower than those exhibited by the positive control (Table 2: Gentamicin for bacteria or Tioconazole for fungi), the dose-dependent nature of the extracts' activity suggests the possibility to match the antimicrobial activity of the positive control at higher concentrations, say ≥ 200 mg/mL. This supports the ethnomedicinal use of the plant in traditional medicine for conditions associated with bacteria and fungi infections. Furthermore, the plant extracts exhibited substantial efficacy in scavenging DPPH radicals comparable to that of the reference, ascorbic acid, with the chloroform extract displaying slightly higher antioxidant property, thereby affirming their potential therapeutic utility in oxidative stress-related diseases.

Gas Chromatography-Mass Spectrometry (GC-MS) analysis of the extracts identified several peaks corresponding to bioactive compounds, including phytol and oleic acid, which can act as free radical scavengers, helping to neutralize reactive oxygen species (ROS) and reduce oxidative stress in the body.

This comprehensive research, encompassing phytochemical screening, radical scavenging activities, antimicrobial properties, and GC-MS analysis, collectively underscores the rationale for considering the utilization of this plant in alternative and traditional medicine. The study highlights its potential efficacy in treating various ailments, especially those associated with oxidative stress, injury, or microbial infections.

To this end, further investigations are recommended to achieve a comprehensive isolation, identification, characterization, and elucidation of the structures of the bio-active compounds responsible for the ob-served pharmacological effects. The possi-bility of the extracts' antimicrobial activities surpassing those of the positive controls at concentrations ≥ 150 mg/mL could also be verified as an extension of this study.

6. Funding

The research received no external funding.

7. Conflict of Interest

The authors declare no conflict of interest.

8. References

1. Burkill HM in The Useful Plants of West Tropical Africa, Families A-D. Royal Botanic Gardens, Kew UK, 1985, vol 1.
2. Hemsley JH in Flora of Tropical East Africa: Connaraceae, Crown Agents for Overseas Government & Administration, London, 1956, p 27.
3. Gbolade AA, Ogedegbe PO, Amina OA, Aniebe OI. *J. Malar. Res. Phytomed.*, 2021, 5(1), 18–28.
4. Sefunmi A, Kayode OA. *Adv. Biosci. Bioeng.*, 2019, 7(2), 22–26.
5. Gbolade AA, Adedokun OA, Abubakar HY, Sule A. *J. Pharm. Allied Sci.*, 2021, 18(3), 3519–3529.
6. Harborne JB in Phytochemical Methods: A Guide to Modern Technique of Plant Analysis, 3rd ed., Chapman and Hall, London, 1998, pp 1–302.
7. Parekh J, Chanda S. *Turk. J. Biol.,* 2007, 31(1), 457–462.
8. Onwukaeme DN, Ikuegbvweha TB, Asonye CC. *Trop. J. Pharm. Res.*, 2007, 6(2), 725–730.
9. Edeoga HO, Okwu DE, Blessing MO. *Afr. J. Biotechnol.*, 2005, 4(**7**), 685–688.
10. Dahiru D, Onubiyi JA, Umaru HA. *Afr. J. Tradit., Complementary Altern. Med.,* 2006, 3(3), 70–75.
11. Azhagu RR, Gomathi M, Prakasam A, Krishna P, Narayanayyar V, Mahesh P, Siva SS. *Pharm. Innovation J.*, 2017, 6(7), 1032–1038.
12. VandenBerghe AD, Vlietinck AJ in Assay for Bioactivity, Academic Press, London, 1991, vol 6, pp 47–69.
13. Akinpelu DA, Onakoya TM. *Afr. J. Biotechnol.*, 2006, 5(11), 1078–1081.
14. Blois MS. *Nature,* 1958, 181, 1199–1200.
15. Desmarchelier C, Bermudez MJN, Coussio J, Ciccia G, Boveris A. *Int. J. Pharmacogn.*, 1997, 35, 116–120.
16. Chaouche TM, Haddouchi F, Ksouri R, Atik-Bekkara F. *J. Chin. Med. Assoc.*, 2014, 77, 302–307.
17. Ajiboye BO, Ojo OA, Adeyonu O. *J. Acute Dis.*, 2016, 5(5), 423–429.
18. Cakir A, Mavi A, Yıldırım A, Duru ME, Harmandar M, Kazaz C. *J. Ethnopharmacol.*, 2003, 87, 73–83.
19. Ksouri R, Megdiche W, Falleh H, Trabelsi N, Boulaaba M, Smaoui A, Abdelly C. *C. R. Biol.*, 2008, 331(11), 865–873.
20. Maisuthisakul P, Suttajit M, Pongsawatmanit R. *Food Chem.*, 2007, 100, 1409–1418.
21. Vinson JA, Dabbagh YA, Serry MM, Jang J. *J. Agric. Food Chem.*, 1995, 43, 2800–2802.
22. AAT Bioquest, I. Quest Graph™ IC_{50} Calculator, 2025.
23. Locatelli M, Epifano F, Genovese S, Giuseppe C, Končić MZ, Kosalec I, Kremer D. *Nat. Prod. Commun.*, 2011, 6(9), 1275–1280.
24. Santos CC, Salvadori MS, Mota VG, Costa LM, de Almeida AA, de Oliveira GA, Costa JP, de Sousa DP, de Freitas RM, de Almeida, RN. *Neurosci. J.*, 2013, 1–9.

The Chemist
Journal of the American Institute of Chemists

Theoretical Structural Analysis and IR Spectroscopic Differences of Constitutional Isomers of 4-Bromo-Di-tert-Butyl Aniline and Their Impact on Human Skin

***Muhammad Aziz[1,2], Nazima Yousaf Khan[1,2], Asim Nisar[2]**

[1]Institute of Biochemistry University of Balochistan, Quetta, Pakistan
[2]Pakistan Chemical Computational Society
**Corresponding author (E-mail: aziz1sh@hotmail.com)*

Abstract: This pilot study investigates the infrared (IR) spectroscopic differences among constitutional isomers of 4-bromo-di-tert-butyl aniline and evaluates their structural, vibrational, and dermatological properties using computational methods. Three isomers 4-bromo-3,5-di-tert-butyl aniline (Isomer A), 4-bromo-2,6-di-tert-butyl aniline (Isomer B), and 4-bromo-5,6-di-tert-butyl aniline (Isomer C) were analyzed employing density functional theory (DFT) at the B3LYP/6-31G* level. Geometry optimization and vibrational frequency calculations were performed using GAMESS, and theoretical IR spectra were simulated and compared.

The calculated IR spectra reveal complete overlap between Isomers A and B, indicating no significant vibrational differences despite their constitutional variation. In contrast, Isomer C exhibits minor variations in alkane C–H stretching and amine vibrational modes, attributed to the asymmetric positioning of tert-butyl substituents on the aromatic ring. All simulated spectra fall within the 400–3600 cm^{-1} range and show characteristic functional group vibrations consistent with aniline derivatives.

Quantitative structure–activity relationship (QSAR) modeling was employed to assess skin sensitization potential using multiple validated endpoints. The results indicate that all three isomers are predicted skin sensitizers, suggesting that these compounds may pose dermatological risks and are unsuitable for cosmetic applications. Overall, this study demonstrates the utility of combined DFT-based vibrational analysis and QSAR modeling for evaluating structural isomerism and predicting potential health hazards within the aniline family.

Key Words: Infrared spectroscopy, constitutional isomers, QSAR, skin sensitization, density functional theory (DFT)

CC1=CC(=CC(=C1Br)C)N
CC(C)(C)c1cc(Br)cc(c1N)C(C)(C)C

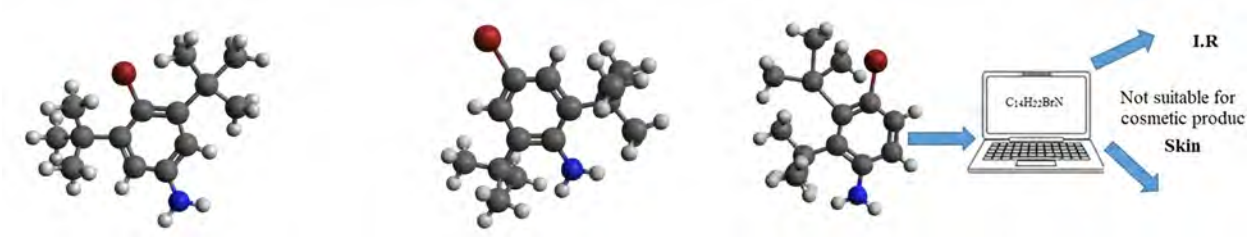

1. Introduction

The molecular formula of the compounds investigated in this study is $C_{14}H_{22}BrN$. Three constitutional isomers were considered: 4-bromo-3,5-di-tert-butyl aniline (Isomer A), 4-bromo-2,6-di-tert-butyl aniline (Isomer B), and 4-bromo-5,6-di-tert-butyl aniline (Isomer C). Infrared spectroscopy is a well-established analytical technique for identifying organic compounds and differentiating constitutional isomers that share the same molecular formula but differ in atomic connectivity [1]. The integration of experimental spectroscopy with computational analysis provides a robust framework for vibrational mode assignment and structural characterization.

Aniline derivatives constitute an important chemical family with extensive applications in environmental assessment, pharmaceuticals [2], polymer industries, agro-chemicals [3], textile dyes, paints, stationery products [4], and hair dyes [5]. The compound $C_{14}H_{22}BrN$ represents a moderately substituted member of this family. Substitution by tert-butyl groups can influence the intrinsic electronic and vibrational properties of aniline derivatives. Notably, aniline-based materials have demonstrated metallic-like behavior in conducting polymers [6,7], making them valuable in industrial applications. Furthermore, aniline derivatives serve as useful test systems for evaluating the accuracy of DFT methods in pharmaceutical and materials research [8]. Previous computational investigations have provided insight into reaction pathways and non-planar geometries of aniline derivatives using ab initio and DFT approaches [9,10]. Advances in computational chemistry and vibrational spectroscopy software have significantly enhanced the ability to predict molecular properties prior to experimental synthesis [11]. In materials science and chemical safety assessment, computational chemistry and toxicity prediction have become indispensable tools.

Skin sensitization remains a major concern for consumers and regulatory authorities, particularly for cosmetic ingredients [12]. Computational prediction of dermatological effects allows early-stage hazard screening while reducing reliance on animal testing. With continued development of computational chemistry platforms, predictive modeling has become an essential compl-ement to experimental investigations [13]. However, selecting an appropriate computational model for substituted aniline derivatives remains challenging. The present study addresses this issue by combining DFT-based vibrational analysis with QSAR-based dermatological assessment. Figure 1 features the

optimized forms of the three different isomers (A, B & C).

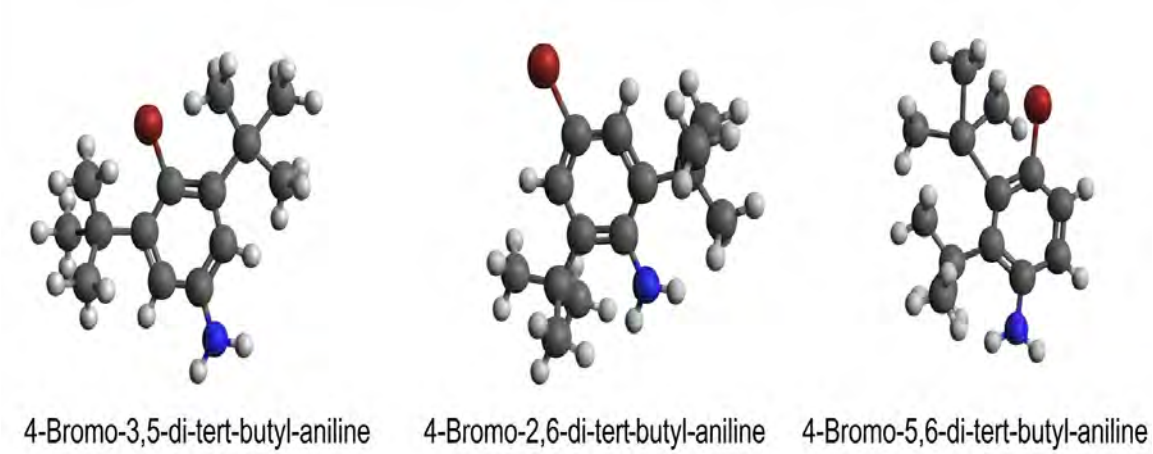

Fig 1. Arrangement of Isomers

Stereochemistry of Isomers

Each molecule contains an amino group attached to a single aromatic ring, with bromine substitution at the meta position. The aromatic ring comprises six carbon atoms, while two tert-butyl groups (4 + 4 carbon atoms) are attached at positions 3/2/5 and 5/6/6, giving a total of 14 carbon atoms. The molecules contain twenty-two hydrogen atoms, three double bonds, and no triple bonds, as illustrated in Figure 1.

2. Computational Method

Molecular structures were constructed using Avogadro 1.2 Molecular Editor [14]. Each isomer was geometrically optimized, and theoretical results were compared using the KnowItAll Informatics System. Vibrational frequency calculations and IR spectra simulations were performed using the GAMESS program [15]. Skin sensitization potential was evaluated using the LabMol Pred-Skin QSAR platform [16].

Parameter Use

IR spectra calculations were conducted using the B3LYP functional with the Pople 6-31G* basis set. It enhances the time of computation, giving better results. Parameters for electrostatic potential map calculations are same as the above parameters.

3. Computational Results

Isomer

Aniline molecular docking simulating base results show that isomers .All three isomers exhibited an identical molecular weight of 284.2 g/mol. Molecular weight provides very useful information such as viscosity. Higher molecular weight monomers require additional energy during formation processes. The molecular docking simulation tool is easily incorporated. Also, it more accurately models near to reality. Total number of atoms is 38.

I.R Theoretical Value

The spectrogram for IR value for 4-bromo-3,5-di-tert-butyl-tert aniline Isomer (A & B) lies in 0-3500 cm^{-1}. It is clearly interpreted from Figure 2. The following attachments are bonded with an aromatic ring:

- Alkanes: To confirm alkanes there are three types of atoms attachments, which are as follows:

$C-(CH_3)_3$, $R-CH_3$ &$CH-(CH_3)_2$.$C-(CH_3)_3$, C-H bending vibration, CH_3 asymmetric bending, 1470-1430 cm/1, CH_2 asymmetric bending, 1485-1445 cm/1, C-C medium stretching 1200cm/1. CH_3 asymmetric stretching, 3158 cm/1, CH_3 symmetric stretching, 3070 cm/1, which is slightly far, as shown in the spectrogram in Figures 2 and 3.

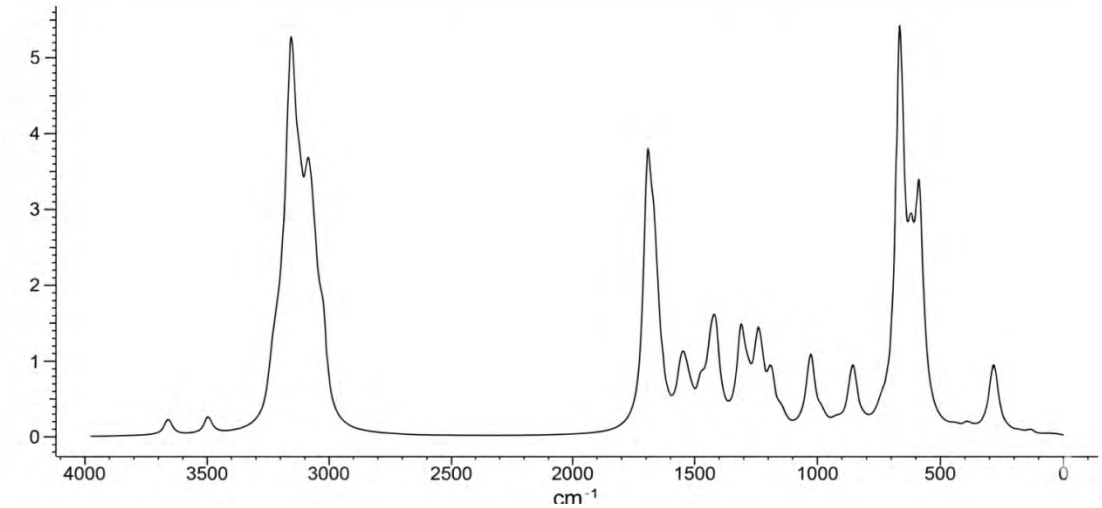

Fig 2. IR Spectrogram of 4-Bromo-3, 5-di-butyl-tert aniline (Isomer A)

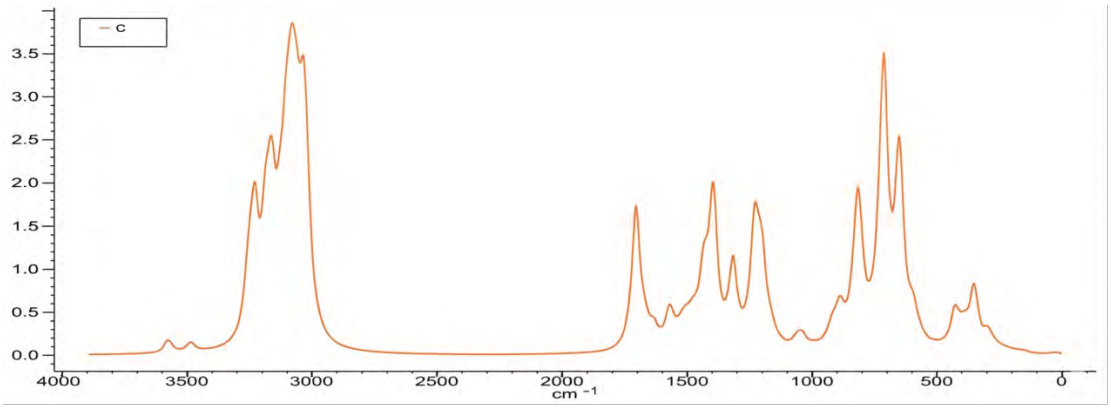

Fig 3. IR Spectrogram of 4-Bromo-5,6-di-tert-butyl aniline (Isomer C)

- Amine group: The presence of primary amine C-N medium stretching at 1304 cm^{-1}.NH_2, de-forming at 1629 cm/1, NH anti-symmetric, very minute peak at 3488 cm/1.
- Aromatic ring: The aromatic ring contains 1, 3, 4 & 5 substitute attachments, i.e., 1, 3, 4 & 5 carbons, as shown in Figure 1. C-H strong starching vibration peak at 3146 cm/1. Overtone of C-H wagging at 1692 cm-1. A minute peak of ring deformation at 851 cm-1. The presence of ring stretching at 17000 -1400cm^{-1}.
- Halogen group: The Isomer contains one halogen member, i.e., bromine, which is attached with carbon 4, and shows strong vibration at 664-528 cm^{-1}.

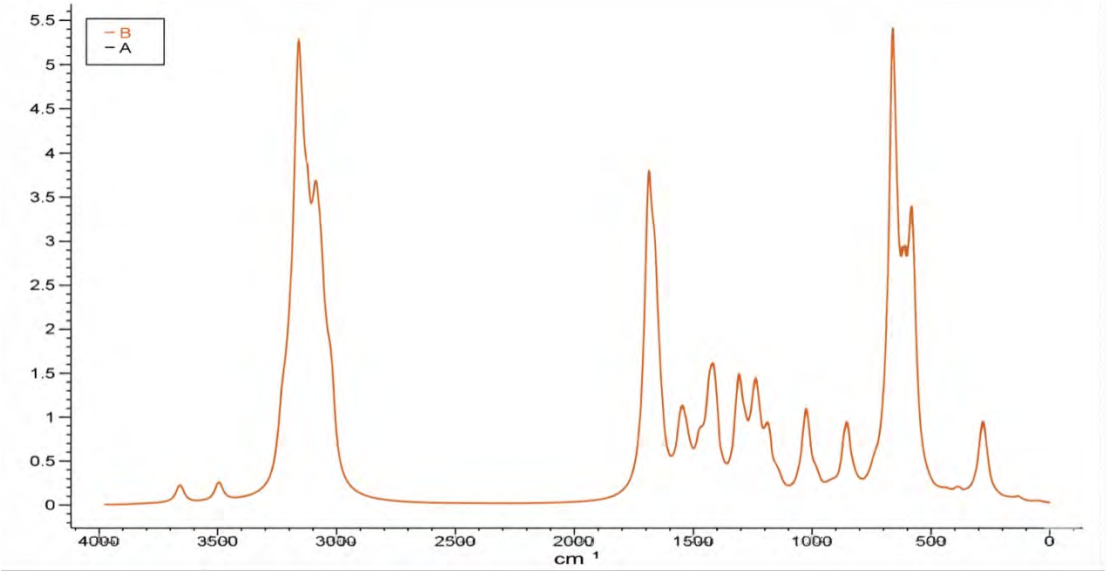

Fig 4. Compression Between Isomer (A) & Isomer (B) IR Spectrogram

From Figure 4, it is clear that both Isomers A & B are showing the same spectrogram (so there is no need to explain Isomer B separately).

From Figure 4, the IR spectra of Isomers A and B exhibit complete overlap, indicating no significant vibrational differences. It is further revealed that there is no difference.

Ergo, for determination of IR frequency, it is hard to differentiate the results.

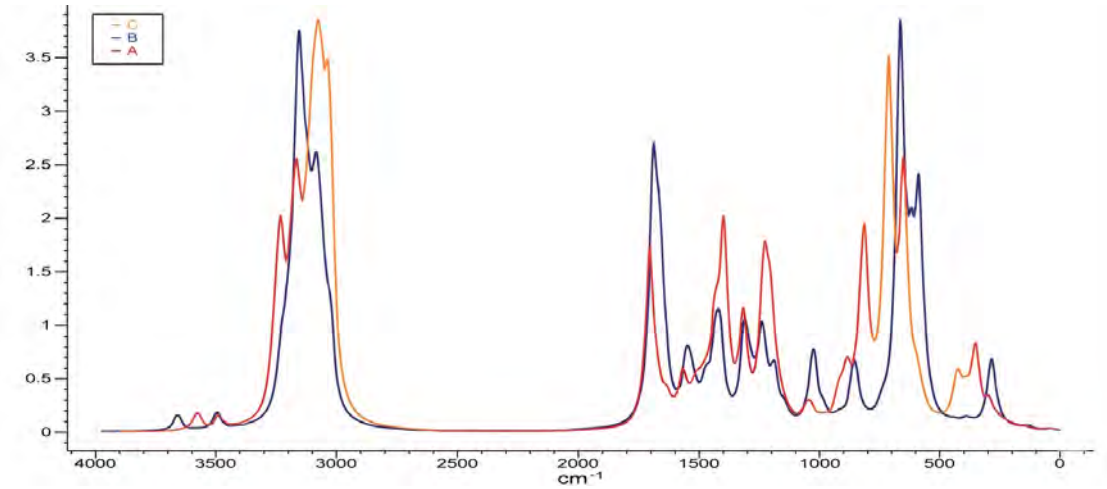

Fig 5. Compression Between Isomer (A), Isomer (B) & Isomer (C) IR Spectrogram

Theoretical NMR Analysis

From Figure 5, it is clear to see that the alkane C-H medium antisymmetric 1400 cm/1 intensity; the other alkane C-H symmetric intensity of Isomer C is also slightly high. The alkane CH symmetric at 3090 cm/1 high peak means strong vibration. These are due to the attachment of butyl atoms at one side. While the vibration of amine groups also slightly fluctuates, as shown in the spectrogram in Figure 5, small antisymmetric vibration of NH 3450 cm/1 are due to antisymmetric movement of hydrogen atoms that are attached with a nitrogen atom.

Theoretical NMR Analysis

Theoretical NMR chemical shift calculations were performed to evaluate the proton and carbon environments of the three constitutional isomers. The predicted ^{1}H NMR chemical shift values are presented in Table 2, while the corresponding ^{13}C NMR values are summarized in Table 3. Variations in the chemical shifts are primarily attributed to differences in substitution positions of tert-butyl groups on the aromatic ring, which influence local electronic environments.

Electrostatic Potential Map

In chemistry, electrostatic potential is a classical and fundamental concept. Many observables of molecules, such as dipole moments, chemical shift, and electromagnetic

spectra, can be correlated to atomic charges in the molecule, and many structure-property theories of molecules are based on the idea of atomic charges. The role of electrostatic potential in chemistry is a well-known [17] well-established concept in chemistry.

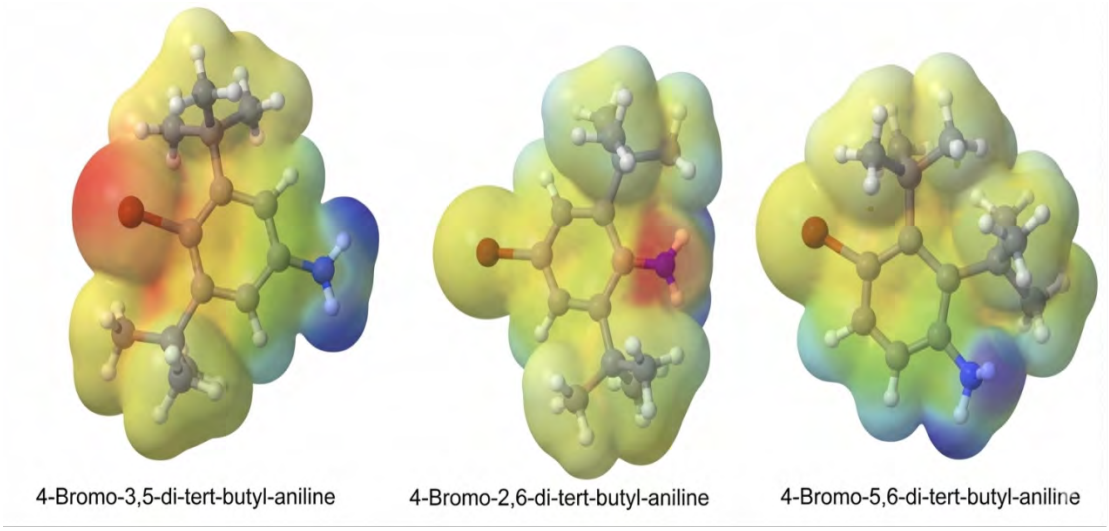

Fig 6. The Electrostatic Potential of Isomers

From Figure 6, it is clear to see that the charges of Isomer C are completely shifted towards one side.

Dermatological evaluation

"Is this organic isomer safe for human use?" is a fundamental question that arises before development and regulation of any cosmetics chemical, and evaluation of its toxicity impact on human skin [18,19]. With advancements in science, the practice of testing chemicals on animals is no longer needed, and the sale of cosmetics products tested on animals is also banned in developing countries.

Tables 1-3 show that the above-mentioned three isomers of aniline are skin sensitizers. This evidence proves that with human skin contact, they can lead to sensitization. These cause problems like damage to the immune system, interference with hormones, and may pose potential long-term health risks, subject to further experimental validation. Patho-mechanisms of the allergic response is a complex mechanism, although all the findings need confirmation in humans. Contact allergy is the result of the activation of both innate and adaptive immunity in response to haptens [20]. Cosmetics products directly used by humans may be released into the environment as an indirect consequence of their use [21].

Table 1. QSAR Models Based Skin Response Results

Test name	Isomer A Probability	Isomer B Probability	Isomer C Probability
1. Human skin	70%	70%	70%
2. Murine local lymph node assay	50%	60%	50%
3. Human cell line activation test	90%	90%	90%
4. Keratino Sens	80%	80%	90%

- Each prediction was performed in triplicate to ensure reliability and reproducibility of the QSAR model outputs.

Table 2. NMR H^1

Isomer A No. of H atoms	PPM	Isomer B No. of H atoms	PPM	Isomer C No. of H atoms	PPM
23,24	6.48	17,18	7.18	17	7.13
17-37	1.41	21-38	1.34	18	6.27
				30-38	1.41
	**********			21-29	1.35

Table 3. NMR 13 C

Isomer A No. of C atoms	PPM	Isomer B No. of C atoms	PPM No. of C atoms	Isomer C No. of C atoms	PPM
3,5	150	1	148	1,3	145
1	140	2,6	137	2	141
2,6	116	3,5	127	5	134
11-16	30.2	4	113	6	118
4	117	9,16	35	4	116
9,10	35.2	10-15	30	13	39
				12	36
	**********			9-15	30

4. Conclusion

The present computational study provides a systematic vibrational and dermatological assessment of three constitutional isomers of 4-bromo-di-tert-butyl aniline using density functional theory and QSAR-based modeling. The IR spectroscopic analysis demonstrates that Isomers A and B exhibit complete spectral overlap, indicating that constitutional variation at these substitution positions does not produce distinguishable vibrational differences. In contrast, Isomer C shows minor variations in alkane C–H stretching and amine vibrational modes, which can be attributed to the asymmetric placement of tert-butyl substituents on the aromatic ring.

Although the applied DFT methodology successfully reproduces key vibrational features of the aniline derivatives, the results also highlight the inherent limitations of purely theoretical approaches in fully resolving subtle isomeric differences in IR spectroscopy. Nevertheless, the combined use of vibrational analysis and electrostatic potential mapping provides valuable insight into substitution-dependent electronic effects within the aniline framework.

QSAR-based dermatological evaluation predicts that all three isomers possess skin-sensitizing potential. These findings suggest that, despite minor structural and vibrational differences, the constitutional isomerism examined here does not significantly alter the predicted dermatological risk profile. Accordingly, the studied compounds appear unsuitable for cosmetic applications, subject to further experimental validation. Overall, this work emphasizes the usefulness of integrated DFT and QSAR methodologies for evaluating structural isomerism, vibrational behavior, and potential health hazards of aniline derivatives. The approach presented here may serve as a supportive framework for preliminary hazard screening and for guiding regulatory considerations related to cosmetic and consumer-use chemicals.

5. Supplementary Data

Meta data associated with the current study also obtain from corresponding author on request.

6. References

1. Van der Meer F. Near-infrared laboratory spectroscopy of mineral chemistry: A review. *Int. J. Appl. Earth Obs. Geoinf*., 2018, 65, 71-78.
2. Holm JB, Chalmey C, Modick H, Jensen LS, Dierkes G, Weiss T, Jensen BAH, Nørregård MM, Borkowski K, Styrishave B, Koch HM, Mazaud-Guittot S, Jegou B, Kristiansen K, Kristensen DM. Aniline is rapidly converted into paracetamol impairing male reproductive development. *Toxicol. Sci*., 2015, 148(1), 288-298.
3. Shchukin AO, Vasilyev AV, Rudenko AP. New method of alkenylation of anilines by acetylene compounds in the superacid HSO_3F. *Tetrahedron*, 2008, 64(27), 6334-6340.
4. Travis AS in The Chemistry of Anilines, ed. Zivi Rappoport, John Wiley and Sons, Chichester, 2007.
5. McCafferty LK. Hair dyes and their toxic effects: Classification and description. *Arch. Dermatol. Syphilol.*, 1926, 14(2), 136-144.
6. Lee K, Cho S, Park SH, Heeger A, Lee C-W, Lee S-H. Metallic transport in polyaniline. *Nature*, 2006, 441(7089), 65.
7. Lee SH, Lee DH, Lee K, Lee CW. High-performance polyaniline prepared via polymerization in a self-stabilized dispersion. *Adv. Funct. Mater*., 2005, 15(9), 1495-1500.
8. Hoi KH, Çalimsiz S, Froese RD, Hopkinson AC, Organ MG. Amination with Pd-NHC complexes: Rate and computational studies involving substituted aniline substrates. *Chem. - Eur. J*., 2012, 18(1), 145-151.
9. Davies IW, Marcoux J-F, Kuethe JT, Lankshear MD, Taylor JD, Tsou N, Dormer PG, Hughes DL, Houk KN, Guner V. Demonstrating the synergy of synthetic, mechanistic, and computational studies in a regioselective aniline synthesis. *J. Org. Chem*., 2004, 69(4), 1298-1308.
10. Dykstra C, Frenking G, Kim K, Scuseria G in Theory and Applications of Computational Chemistry: The First Forty Years, Elsevier, 2011.
11. Siesler HW. Vibrational spectroscopy. In: Reference Module in Materials Science and Materials Engineering, Elsevier, 2016.
12. Dent M, Amaral RT, Da Silva PA, Ansell J, Boisleve F, Hatao M, Hirose A, Kasai Y, Kern P, Kreiling R, Milstein S, Montemayor B, Oliveira J, Richarz A, Taalman R, Vaillancourt E, Verma R, O'Brien Cabral Posada NV, Weiss C, Kojima H. Principles

underpinning the use of new methodologies in the risk assessment of cosmetic ingredients. *Comput. Toxicol*., 2018, 7, 20-26.
13. Barone V. Computational spectroscopy. In: Reference Module in Chemistry, Molecular Sciences and Chemical Engineering, Elsevier, 2013.
14. Hanwell MD, Curtis DE, Lonie DC, Vandermeersch T, Zurek E, Hutchison GR. Avogadro: An advanced semantic chemical editor, visualization, and analysis platform. *J. Cheminf.*, 2012, 4(1), 17.
15. Perri MJ, Weber SH. Web-based job submission interface for the GAMESS computational chemistry program. *J. Chem. Educ*., 2014, 91(12), 2206-2208.
16. Braga RC, Alves VM, Muratov EN, Strickland J, Kleinstreuer N, Trospsha A, Andrade CH. Pred-Skin: A fast and reliable web application to assess skin sensitization effect of chemicals. *J. Chem. Inf. Model*., 2017, 57(5), 1013-1017.
17. Politzer P, Truhlar DG. Introduction: The role of the electrostatic potential in chemistry. In: Chemical Applications of Atomic and Molecular Electrostatic Potentials: Reactivity, Structure, Scattering, and Energetics of Organic, Inorganic, and Biological Systems, eds. Peter Politzer, Donald G. Truhlar, Springer US, Boston, 1981, pp 1-6.
18. Kimber I, Basketter DA, Berthold K, Butler M, Garrigue JL, Lea L, Newsome C, Roggeband R, Steiling W, Stropp G, Waterman S, Wiemann C. Skin sensitization testing in potency and risk assessment. *Toxicol. Sci.*, 2001, 59(2), 198-208.
19. Kimber I, Basketter DA, Berthold K, Butler M, Garrigue J-L, Lea L, Newsome C, Roggeband R, Steiling W, Stropp G, Waterman S, Wiemann C. Skin sensitization testing in potency and risk assessment. *Toxicol. Sci.*., 2001, 59(2), 198-208.
20. Cavani A, De Pità O, Girolomoni G. New aspects of the molecular basis of contact allergy. *Curr. Opin. Allergy Clin. Immunol*., 2007, 7(5), 404-408.
21. Tarazona JV. Environmental Risk Assessment, Cosmetic and Consumer Products. In: Encyclopedia of Toxicology, 3rd ed., ed. Philip Wexler, Academic Press, Oxford, 2014, pp 394-397.

The Chemist
Journal of the American Institute of Chemists

Recycling and Valorization of Spent Lubricating Oil Recovered Over Nanocrystalline Cellulose

[a]Feyisike E. Odofin, [a]Maryam A. Abdurrazaq, [a,b]Emmanuel A. Taiwo, [c]Temitope A. Hamzat, Mariam T. Baker, [b]Olubunmi Atolani

[a]Department of Chemistry, University of Ilorin, P.M.B 1515, Ilorin, Nigeria.
[b]Department of Chemistry, Kogi State University, PMB 222, Kabba, Nigeria
[c]Department of Chemistry, Kwara State University, Malete, Nigeria
Corresponding author (E-mail: eataiwo@ksukabba.edu.ng)

Abstract: The recycling and green valorization of spent lubricating oil are crucial processes for mitigating environmental pollution and conserving resources. In this study, spent oil was recovered using column chromatography over a silica-nanocrystalline cellulose matrix. The spent oil was also further used in grease formulation. *Hura crepitans* seed oil, an underutilized non-edible seed oil was extracted saponified with wood ash-derived potash and used to prepare bio-based soap. The soap was then combined with recovered lubricating oil to formulate grease. Physicochemical analysis, including specific gravity, viscosity, pour point, and GC-MS analysis, revealed significant recovery of quality oil for further use. The quality of the bio-based grease also revealed potential industrial applications. This study demonstrates an eco-friendly and efficient method for recycling and valorization of spent oil while introducing a novel use of non-edible plant oils in lubricant production.

Key Words: *Hura crepitans*, nanocrystalline cellulose, spent oil, valorization, grease, green chemistry

1. Introduction

Lubricating oils play a critical role in reducing friction and wear in machinery, enhanceing performance, and prolonging equipment lifespan. However, during service, these oils degrade due to thermal stress, oxidation, and contamination with metal particles, soot, and water [1]. The result is spent lubricating oil (SLO), a hazardous waste that poses serious environmental and public health risks if improperly managed. Proper recycling for reuse through processes like re-refining is essential to mitigate these risks and recover valuable resources [2]. Conventional dispos-

al methods, such as landfilling, open dumping, or incineration, led to soil and groundwater contamination which contribute to greenhouse gas emissions. Oil discharge to the environment is source of pollution [3].

Figure 1.

Figure 2.

Spent lubricating oil (Figure 1) are complex mixtures resulting from the breakdown of virgin oil (Figure 2) during service. The chemical composition of spent lubricating oil includes hydrocarbons base oil, additives, environmental contaminants, and degradation products. Each component of the oil plays important role in the oil's function and its degradation over time. Important chemical components of spent lubricating oil include base oil and degraded products. Base oil forms the foundation of lubricating oil and generally accounts for 70–90% of the oil's composition. They are derived from either petroleum (mineral oil) or synthesized through chemical processes (synthetic oil) [4]. Degraded products: The degradation of lubricating oil results in the formation of various chemical byproducts that compromise the oil's performance. The degradation is mainly due to thermal breakdown, oxidation, and chemical reactions with contaminants. The degraded product occurs in the form of oxidized hydrocarbons and polymerized species.

The growing emphasis on environmental sustainability and resource conservation has prompted the exploration of greener strategies for SLO treatment. Among these, re-refining and valorization are increasingly recognized as viable options for recovering useful components from waste oils. These approaches not only reduce the demand for virgin base oils but also support circular economy principles by transforming waste into value-added products. Valorization refers to the process of transforming this waste into valuable products through various recovery or reprocessing methods. Therefore, valorization not only reduces environmental burden but also supports resource recovery and circular economy principles. Valorization which is guided by the 3R concept: Reduce, Reuse, and Recycle, often goes beyond to include energy recovery and upcycling of waste into higher-value products. The objectives of valorization are to: prevent waste from entering landfills, enhance sustainability in production and consumption and stimulate innovation in green technologies or waste management [6].

One of the promising yet underexplored techniques for SLO recovery is the use of bio-based materials in oil purification processes. Nanocrystalline cellulose (NCC), derived from plant biomass, has gained attention as a renewable and efficient separation medium due to its high surface area, biodegradability, and adsorption properties. When integrated into chromatographic systems, NCC can enhance the selective recovery of lighter oil fractions from degraded lubricants.

In parallel, the use of non-edible seed oils in industrial formulations such as greases offers an environmentally friendly alternative to petroleum-based ingredients. *Hura crepitans* (sandbox tree) seed oil (Figure 3), abundant in tropical regions, is a non-edible and renewable resource with suitable physicochemical properties for saponification and grease production.

Figure 3.

Figure 4.

This study aims to recover clean lubricating oil (Figure 4) from spent lubricating oil over a nanocrystalline cellulose bed and to valorize the spent oil with bio-oil from the seeds of the sandbox tree (*Hura crepitans*). The seed oil was utilized as a raw material for saponification with KOH from soda ash to make soap used for grease production.

2. Materials and Method

Spent lubricating oil was collected from used automobile engines within Ilorin, Nigeria. *Hura crepitans* seeds were harvested from mature fruits in Ilorin and authenticated at the herbarium of the University of Ilorin. Analytical-grade

reagents and solvents including n-hexane, methanol, and sulfuric acid were used. Potash used for saponification was derived from dried wood ash, and nanocrystalline cellulose used as part of the stationary phase for chromatographic separation was obtained as a gift from the department of Chemistry, University of Ilorin, Nigeria.

Extraction of *Hura crepitans* Seed Oil

Harvested *Hura crepitans* seeds were dehulled, air-dried, and milled into fine powder. Oil extraction was carried out using a reflux system with a solvent mixture of n-hexane, methanol, and sulfuric acid in a ratio of 42:33:1 mL [7]. A total of 110 g of seed powder was refluxed for 1 hour under controlled heat. The resulting mixture was cooled, filtered, and the oil was extracted with hexane. Then, the solvent was recovered by distillation. The oil yield was determined based on the initial seed mass**.**

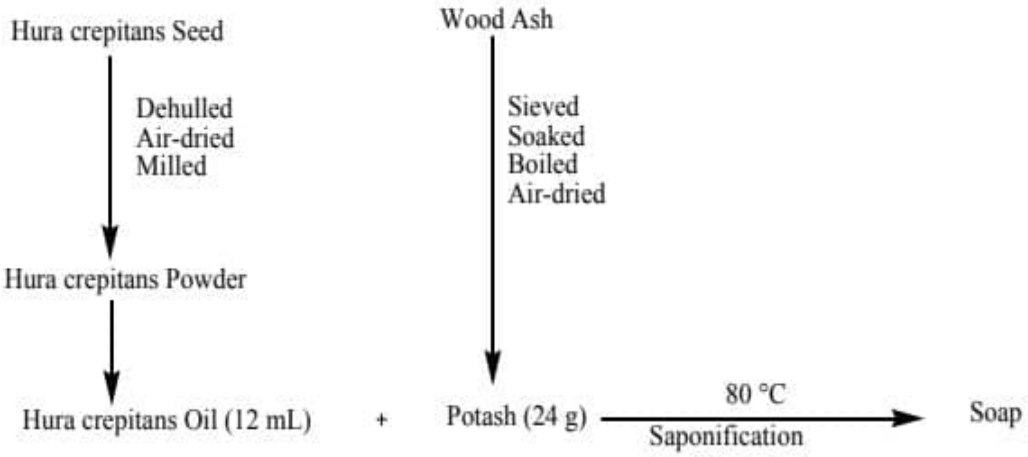

Scheme 1: Scheme of Extraction of Hura Crepitans Oil and Valorization with Potash

Preparation of Soap from *Hura crepitans* Oil

Following standard protocols [8], saponification of the extracted oil was carried out using a potash prepared from wood ash. A mixture of 12 mL of seed oil and 24 g of aqueous potash was heated at 80°C with continuous stirring until the formation of a uniform soap mass was observed. The resulting soap was air-dried and stored for use in grease formulation.

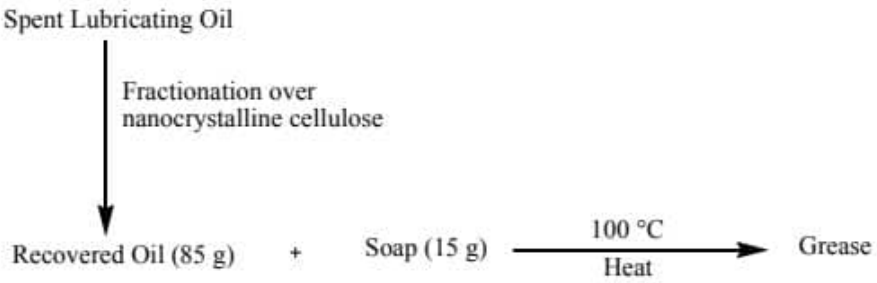

Scheme 2: Scheme for Recycling and Valorization of Spent oil with Soap

Fractionation of Spent Lubricating Oil on Column Chromatography

Spent oil samples were subjected to column chromatography to isolate cleaner oil fractions. A glass column (50 cm × 0.5 cm) was packed with a homogeneous blend of silica gel and nanocrystalline cellulose in a 1:1 ratio as the stationary phase. Approximately 15.84 g of spent oil was loaded onto the column and eluted using n-hexane as the mobile phase. Fractions were collected primarily based on color, and elution profile. The recovered oil was classified as dark, medium, and light fractions.

The recovered oil fraction was analyzed using gas chromatography–mass spectrometry (GC-MS) to determine its chemical composition and to assess the efficiency of the recovery process. For comparative purposes, a sample of virgin lubricating oil was also subjected to GC-MS analysis under identical conditions. The resulting chromatographic profiles were evaluated to identify changes in hydrocarbon structure, the presence or removal of degradation products, and the restoration of base oil quality.

Grease Formulation

Grease was formulated by blending 15 g of Hura crepitans-based soap with 85 g of the recovered oil fraction. The mixture was heated to approximately 100°C and stirred continuously until a smooth, homogenous grease was obtained. The prepared grease was allowed to cool and stored for physicochemical analysis.

Physicochemical Analysis

Following standard procedure [9,10], the following analyses were conducted on the virgin oil, spent oil, recovered oil, and seed oil:

Specific Gravity: The specific gravity of virgin, spent, and *Hura crepitans* oil was measured using a pycnometer. It was weighed empty, with water, and with each oil sample, ensuring no air bubbles and a clean exterior before weighing.

Kinematic Viscosity: Viscosity of virgin, spent, and *Hura crepitans* oil was measured using an Ostwald viscometer, calibrated with distilled water. About 10 ml of each sample was drawn above the upper mark and allowed to flow under gravity. Flow time between two points was recorded with a stopwatch at room temperature. The viscometer was cleaned before each test to ensure accuracy.

Pour Point: The pour point (the lowest temperature at which oil still flows) was determined for three oil samples (virgin lubricating oil, spent lubricating oil, and *Hura crepitans* oil). Each sample was placed in a clean test jar with a thermometer and cooled in a controlled bath. At every 3°C drop, the jar was removed and tilted to check for flow, with each check done within 3–5 seconds to prevent temperature rise. The process continued until no flow was observed, and the pour point was recorded as 3°C above that temperature. All apparatus were cleaned and dried after each test.

Saponification Value: Evaluated via standard titration using potassium hydroxide and hydrochloric acid.

Yield Determination: Percentage yields of extracted and recovered oils were computed based on initial mass. All tests were conducted in triplicate to ensure reproducibility and average recorded.

3. Results and Discussion

Hura crepitans seed oil typically appears as a yellowish liquid with moderate viscosity and a density, 0.9-1.0 g/cm³ (Table 1). Its Saponification value indicates its potential for soap production.

The recovered oil fraction exhibited improved properties compared to untreated spent oil, as shown in Table 1.

Table 1. Physicochemical Properties of Oils

Parameter	Virgin Oil	Spent Oil	*Hura crepitans*
Specific Gravity (g/cm^3)	0.872	0.869	0.900
Viscosity (sec)	639.6	913.8	497.8
Pour point (°C)	-30	-15	-6
Saponification Value (mg KOH/g)	-	-	171.1

Discussion

The specific gravity values (Table 1) obtained suggest that all three oils are less dense than water, as expected for hydrocarbon-based oils. The spent lubricating oil had a specific gravity of 0.869 g/cm³, slightly lower than the virgin lubricating oil at 0.872 g/cm³, likely due to degradation and accumulation of lighter decomposition by-products over time. This minor decrease is consistent with previously reported changes in density due to oxidative breakdown and contamination in used engine oils [11].

The *Hura crepitans* seed oil exhibited a high specific gravity at 0.919 g/cm³, indicating a denser molecular composition, possibly due to the presence of higher molecular weight triglycerides and fatty acids. This aligns with findings in plant-based oils known for their higher saturation or functional group content [12]. These differences in specific gravity can influence the applications of each oil, especially in formulations such as grease production, where oil density and viscosity play a role in determining the final product's performance and texture.

The viscosity of spent lubricating oils is often high compared to fresh oil due to oxidation and the presence of contaminants such as soot and metal particles. The high viscosity affects the flow characteristics of the oil and can lead to reduced efficiency in lubrication systems [13]. Virgin oil, being unused and clean, had moderate viscosity. *Hura crepitans* oil had the lowest viscosity, likely due to its plant-based composition, lighter molecular weight, and minimal impurities. The viscosity trend (Spent > Virgin > Hura) aligns with the impact of degradation and supports *Hura* oil's potential use in low-viscosity, eco-friendly lubricants.

Gas Chromatography – Mass Spectrometry Analysis

GC-MS is widely employed for analyzing the volatile and semi-volatile components in spent lubricating oil. It provides a detailed profile of hydrocarbons, degradation products, and contaminants like fuel residues [14]. The chemical composition of the Recovered Spent Oil and the virgin oil was obtained by subjecting them to Gas Chromatography-Mass Spectrometry (GC-MS) analysis.

Approximately 0.2 g of each sample was diluted in 2.0 mL using hexane and further to a microgram unit before injection into the Shimadzu GC-2010 gas chromatograph. The parameters for the analysis is as indicated: The detector, FID at 220°C, nitrogen gas flowing at 1.0 mL/min on an Optima 35 capillary column (30 m × 0.53 mm ID; 0.32 mm) with a split ratio 1:30 and injector temperature, 250°C.The column temperature was maintained at 40°C for five minutes before increasing to 280°C (5°C/min) with a delay at that temperature for an additional five minutes. For the GC-MS, a Jeol JMS-HX 110 mass spectrometer with a source at 270°C and 70 eV coupled with a Hewlett-Packard 6890 gas chromatograph was used. The injector was configured to split at 1:30 and temperature at 270°C. Compound identification was established by comparing the MS fragmentation with authentic samples and data obtained on the NIST Library Version 3.0 mass spectral software database. The chemical composition of the hexane extracts as obtained from the GC-MS is as shown in Table 2.

Gas Chromatography–Mass Spectrometry (GC-MS) was employed to characterize the hydrocarbon composition of virgin (of same origin with the spent) and column recovered oil from spent lubricating oil samples extracted using hexane and purified via column chromatography. Sixteen compounds (Table 2) were identified in both the virgin oil and the recovered spent oil. With four overlaps observed between the two samples, most components were significantly different, indicating major chemical changes to the oil during operation. Although the coinciding compounds had slightly different retention time, this is apparently due to the degree of complexity in both samples.

Table 2. Comparison of Percentage Chemical Composition of Both Oils

S/N	All Compounds	Molecular Formula	Virgin Oil Composition		Recovered Spent Oil Composition	
			% Composition	Retention Time (Minutes)	% Composition	Retention Time (Minutes)
1	Tetratetracontane	$C_{44}H_{90}$	4.89	17.59	4.45	17.56
2	2-Cyclohexylnonadecane	$C_{25}H_{50}$	_	_	3.69	18.29
3	17-Pentatriacontene	$C_{35}H_{70}$	_	_	3.71	18.41
4	n-Pentacosane	$C_{25}H_{52}$	_	_	11.09	18.69
5	n-Hentriacontane	$C_{31}H_{64}$	_	_	4.91	18.76
6	Pentatriacontane	$C_{35}H_{72}$	8.84	20.82	3.33	18.88
7	Tritetracontane	$C_{43}H_{88}$	2.61	23.83	7.80	19.12
8	2-Methylhexacosane	$C_{27}H_{56}$	_	_	10.14	19.14
9	2-Methyltetracosane	$C_{25}H_{52}$	_	_	5.71	19.39
10	2-Hexyl-1-decanol	$C_{16}H_{34}O$	_	_	5.62	19.64
11	30-Triacontanediol	$C_{30}H_{62}O_2$	_	_	3.41	20.12
12	n-Tetracontane	$C_{40}H_{82}$	18.30	52.44	17.80	43.41
13	1-(Methylnonyl) cyclohexane	$C_{16}H_{32}$	_	_	2.70	22.07
14	3-Methyltridecane	$C_{14}H_{30}$	_	_	2.85	22.08
15	2-Methylhexacosane	$C_{27}H_{56}$	_	_	4.92	22.62
16	2-Methyltetracosane	$C_{25}H_{52}$	_	_	7.78	22.94
17	2-Octyldecan-1-ol	$C_{18}H_{38}O$	2.63	17.74	_	_
18	Phytane	$C_{20}H_{42}$	2.48	19.65	_	_

19	n-Nonadecane	$C_{19}H_{40}$	2.66	20.71	_	_
20	n-Heneicosane	$C_{21}H_{44}$	2.73	21.79	_	_
21	Heptadecane	$C_{21}H_{44}$	2.53	22.93	_	_
22	n-Hexacosane	$C_{26}H_{54}$	4.44	24.18	_	_
23	n-Pentatriacontane	$C_{35}H_{72}$	18.14	50.08	_	_
24	n-Octadecane	$C_{18}H_{38}$	2.98	25.03	_	_
25	1-Pentacontanol	$C_{50}H_{102}O$	4.24	25.60	_	_
26	Eicosane	$C_{20}H_{42}$	5.83	25.69	_	_
27	Heptadecylcyclohexane	$C_{23}H_{46}$	2.29	25.83	_	_
28	Heptacosanol	$C_{27}H_{57}O$	6.47	28.02	_	_
29	n-tetratetracontane	$C_{44}H_{90}$	5.22	28.97	_	_

In both samples, n-tetracontane ($C_{40}H_{82}$) was the most prevalent of these. It showed up at a retention time of (52.44 mins) with (18.30%) area in virgin oil and at 43.41 minutes with (17.80%) area in recovered spent oil. Its persistence shows that it is thermally resilient, but its decreased abundance in spent oil points to partial breakdown, most likely caused by high-temperature oxidative processes. According to Okonkwo *et al*., in 2023 [15], n-tetracontane is a long-chain linear alkane that greatly enhances the viscosity, lubricity, and film strength of base oils. Its potential application as a molecular fingerprint or marker for oil integrity is supported by its steady presence. Another high-molecular-weight alkane, tetratetracontane ($C_{44}H_{90}$), was also present in both oils, with 4.45% in spent oil and 4.89% in virgin oil, and decreases, presumably, as a result of redistribution or degradation during service. These saturated hydrocarbons are typically non-reactive and resistant to cracking, hence their survival in the spent fraction. Several straight-chain and branched alkanes which were exclusive to the virgin oil, include: n-pentatriacontane (18.14%), n-octadecane (2.98%), eicosane (5.83%), 1-pentacontanol (4.24%) and phytane (2.48%). The absence of these in the recovered spent oil suggests that they were either oxidized, volatilized, thermally cracked, or transformed into other hydrocarbons during use. For example, the total absence of n-pentatriacontane, despite its high original abundance, may result from oxidative cleavage and conversion into alkenes or branched alkanes.

The GC-MS data of the spent oil revealed newly formed compounds not present in the virgin oil, which includes 17-pentatriacontene (2.71%), 2-cyclohexyl-nonadecane (3.69%), 2-hexyl-1-decanol (5.62%), 30-triacontanediol (3.41%). These are probably intermediates of heat degradation or oxidation products. While the emergence of alcohols and diols suggests oxidation at terminal methyl groups, the creation of alkenes (such as 17-pentatriacontene) indicates dehydrogenation events. Finally, the results re-affirm the potential utilization of GC-MS analysis in tracking degradation markers in lubricating oils. Kim *et al*. in 2014 [16] demonstrated the capability of GC-MS combined with statistical modeling to distinguish between fresh and used oils, a method that parallels the approach in this study.

4. Conclusion

The recycling and valorization of spent lubricating oil presents a sustainable and economically viable approach to mitigating environmental pollution and conserving natural resources. By transforming waste oil into reusable products through processes such as re-refining, distillation, and chemical treatment, this practice not only reduces dependence on virgin crude oil but also supports circular economy principles, by reducing the risks of environmental pollution. Effective recycling strategies help minimize the ecological risks posed by indiscriminate disposal, while valorization enhances the value chain by converting waste into useful secondary products such as fuels, base oils, and additives. As global energy demands continue to rise, the adoption of efficient, eco-friendly recycling technologies for spent lubricants is essential for promoting environmental stewardship and industrial sustainability.

5. References

1. Thinprukgam K, Tungasmit D, Tungasmita S. Degradation factors of semi-synthetic lubricant oil for gasoline-CNG engine. *J. Appl. Sci. Emerging Technol.*, 2023.
2. Osman DI, Attia SK, Taman AR. Recycling of used engine oil by different solvent. *Egypt. J. Pet.*, 2018, 27(2), 221-225.
3. Adetitun DO, Akinmayowa V, Atolani O, Olayemi A. Biodegradation of jet fuel by three Gram negative Bacilli isolated from kerosene contaminated soil. *Pollution*, 2018.
4. Mang,T, Lingg G. Base oils. *Lubr. Lubr.*, 2017, 51-82.
5. Udonne JD. A comparative study of recycling of used lubrication oils using distillation, acid and activated charcoal with clay methods. *J. Pet. Gas Eng.,* 2011, 2(2), 12–19.
6. Kothari R, Singh A, Pandey A, Tyagi V, Egamberdieva D, Bellingrath-Kimura S, Arora N. Valorization of bio-waste material: Future dimensions for path. *Environ. Sustainability*, 2021, 4(2).
7. Atolani O, Oladapo FC, Olupade OC, Ekejiuba GC, Taiwo EA. Preparation, characterization and anti-inflammatory evaluation of fortified cosmeceutical emollient from the seed oil of *Azadirachta indica* A. Juss. *Chemist*, 2025, 96(1).
8. Atolani O, Adamu N, Oguntoye OS, Zubair MF, Fabiyi OA, Oyegoke RA, Adeyemi OS, Areh ET, Tarigha DE, Kambizi L, Olatunji GA. Chemical characterization, antioxidant, cytotoxicity, anti-*Toxoplasma gondii* and antimicrobial potentials of the *Citrus sinensis* seed oil for sustainable cosmeceutical production. *Heliyon*, 2020, 6.
9. Akaninwor GC, Wali SA. Assessment and analysis of performance characteristics of selected locally manufactured lubricants (engine oils). *J. Fluid Mech. Mech. Des.*, 2025, 1-12.
10. Wolak A, Zając G, Słowik T. Measuring kinematic viscosity of engine oils: A comparison of data obtained from four different devices. *Sensors*, 2021, 21(7), 2530.

11. Dickson UJ. Development of analytical, phyto- and myco-remediation techniques to manage petroleum-contaminated soils. Ph.D. Thesis, Nottingham Trent University, UK, 2020.
12. Adewuyi A, Oderinde RA, Ojo DF. Biodiesel from the seed oil of *Treculia africana* with high free fatty acid content. *Biomass Convers. Biorefin.*, 2012, 2(4), 305-308.
13. Zhang Y, Ma Z, Feng Y, Diao Z, Liu Z. The effects of ultra-low viscosity engine oil on mechanical efficiency and fuel economy. *Energies*, 2021, 14(8), 2320.
14. Chua CC, Brunswick P, Kwok H, Yan, J, Cuthbertson D, van Aggelen G, Shang D. Tiered approach to long-term weathered lubricating oil analysis: GC/FID, GC/MS diagnostic ratios, and multivariate statistics. *Anal. Methods*, 2020, 12(43), 5236.
15. Okonkwo CP, Ajiwe VIE, Obiadi MC, Okwu MO, Ayogu, JI. Production of biodiesel from the novel non-edible seed of *Chrysobalanus icaco* using natural heterogeneous catalyst: Modeling and prediction using Artificial Neural Network. *J. Cleaner Prod.*, 2023, 385, 135631.
16. Kim NY, Nam GM, Kim Y, Lee D-K, Park SY, Lee K, Lee J. Identification and classification of fresh lubricants and used engine oils by GC/MS and Bayesian model. *Anal. Sci. Technol.*, 2014, 27(1), 41–59.

The Chemist
Journal of the American Institute of Chemists

Chemical Characterization and Acetylcholinesterase Inhibitory Activity of Non-Polar Component of the Stem Bark of *Cordia millenii*

Emmanuel A. Taiwo[1,2]*, Oluwadasolami E. Elugoke[1], Olubunmi Atolani[1]

[1]Medicinal Chemistry Unit, Department of Chemistry, University of Ilorin PMB 1515, Ilorin, Nigeria
[2]Department of Chemistry, Kogi State UniversityPMB 222, Kabba, Nigeria
**Corresponding author (E-mail: eataiwo@ksukabba.edu.ng)*

Abstract: *Cordia millenii* (family Boraginaceae) is an important medicinal plant widely used in African traditional medicine, particularly in southwestern Nigeria, for the management of pain and related inflammatory conditions. This study aimed to characterize the chemical composition and evaluate the acetylcholinesterase inhibitory activity of the *n*-hexane extract of the stem bark of *C. millenii*. The extract was analyzed using gas chromatography (GC) and gas chromatography–mass spectrometry (GC–MS) on an HP-5 column. The major constituents identified in the extract were 2-butoxyethyl laurate (11.96%), methyl (7E)-7-hexadecenoate (10.87%) and methyl-11,16-octadecadienoate (12.45%). The extract exhibited moderate *in vitro* acetylcholinesterase inhibitory activity of 38.32% at 150 µg/mL compared with the reference drug Donepezil, which showed 49.10% inhibition at the same concentration. The presence of these bioactive constituents may contribute to the observed biological activity and supports the potential pharmacological relevance of *C. millenii* in the management of inflammation-related and neurological disorders. Overall, the chemical profile of the *n*-hexane stem bark extract highlights the potential of this plant as a source of bioactive compounds for pharmaceutical applications.

Key Words: *Cordia millenii*, ethnomedicine, pharmacophore, anti-inflammatory, acetylcholinesterase

1. Introduction

Alzheimer's disease (AD) is a complex, progressive, and irreversible neurodegenerative disorder characterized by cognitive decline and memory impairment. The

disease arises from dysregulation in multiple biochemical pathways and interacting neuronal systems, ultimately leading to neuronal dysfunction and degeneration [1-4]. It is estimated to affect approximately 36 million individuals worldwide and accounts for about 60–80% of all dementia cases [5]. One of the key therapeutic strategies for the management of AD involves the inhibition of acetylcholinesterase, an enzyme responsible for the breakdown of acetylcholine in the synaptic cleft. Drugs such as Donepezil, Rivastigmine, and Galantamine are commonly used as acetylcholinesterase inhibitors in the treatment of AD.

Over the past century, herbal medicine has become an increasingly important component of healthcare systems worldwide [6]. Despite significant advances in modern pharmacotherapy, medicinal plants continue to play a vital role in disease management due to their accessibility, affordability, and diverse pharmacological properties [7]. Historically, plants have served as valuable sources of bioactive compounds with therapeutic potential, particularly as anti-infective agents and pharmacologically active secondary metabolites [8]. Extracts, tinctures, and other preparations derived from plants and animals have long been used in traditional medicine to manage various human ailments. Consequently, natural products remain an important reservoir for drug discovery, and numerous plant-derived compounds have contributed significantly to modern therapeutics [9-13]. Given the continuing global burden of diseases such as cancer and HIV, the exploration of natural resources for bioactive compounds remains a critical area of research [14].

Cordia millenii (family Boraginaceae) is a tropical African forest tree widely distributed across several regions of the continent. The species can grow up to approximately 20 m in height, and in some regions such as Uganda, it may reach heights of about 40 m with a bole diameter of over 1 m [15,16]. In Nigeria, the plant is locally known as “omo” in the Yoruba language and “omah” in Benin, reflecting its cultural importance, particularly in the construction of traditional talking drums [17,18]. Beyond its economic importance in the timber industry, *C. millenii* has also gained attention for its extensive use in traditional herbal medicine [19-21].

Ethnomedicinally, different parts of *C. millenii* are used in [19] the treatment of a variety of ailments, including fever, cough, diarrhea, dysentery, toothache, stomachache, inflammation-related disorders, and parasitic infections [19,20,22-24]. In southeastern Nigeria, the seed powder mixed with palm oil is traditionally applied for the treatment of ringworm and itching [25]. In Cameroon and other West African countries, leaf decoctions are commonly administered to expel intestinal worms and to treat asthma, cough, and cold. Additionally, the flowers of *C. millenii* provide an important source of nectar and pollen for honeybees [26]. Previous studies have reported several biological activities of *C. millenii* extracts, including antimicrobial, antioxidant, and anti-infertility effects, as well as protective activity against lipopolysaccharide-induced neuroinflammation [16, 27-28].

Phytochemical investigations have revealed the presence of several classes of secondary metabolites in *C. millenii*, including sterols, triterpenes, and fatty acid derivatives. However, most studies have focused primarily on polar or moderately polar extracts such as methanol, ethanol, and ethyl acetate fractions. In contrast, non-polar extracts (e.g., *n*-hexane fractions) are known to contain a wide range of bioactive constituents such as fatty acid esters, terpenoids, sterols, and

hydrocarbons. Despite this, the chemical composition of the non-polar constituents from the stem bark of *C. millenii* remains poorly characterized, representing a notable phytochemical knowledge gap.

Furthermore, although *C. millenii* is widely used in traditional medicine for the management of pain, inflammation, and wound healing, its potential neuropharmacological activity has not been extensively investigated. In particular, little information is available regarding the acetylcholinesterase inhibitory potential of its non-polar constituents. This is important because acetylcholinesterase inhibition remains a key therapeutic approach in the management of neurodegenerative disorders such as AD. Moreover, currently available synthetic acetylcholinesterase inhibitors, including Tacrine, Donepezil, Rivastigmine, and Galantamine, used for the treatment of cognitive dysfunction and memory impairment associated with Alzheimer's disease, are often associated with adverse effects such as gastrointestinal disturbances, hepatotoxicity, and limited long-term efficacy.

Consequently, there is increasing interest in identifying plant-derived acetylcholinesterase inhibitors as safer and more accessible and effective therapeutic alternatives [29], particularly in regions where medicinal plants constitute an essential component of primary healthcare. Although *C. millenii* is widely recognized in African ethnomedicine, comprehensive scientific validation of its bioactive constituents and mechanisms of action remains limited. Therefore, the present study investigated the chemical composition and *in vitro* acetylcholinesterase inhibitory activity of the *n*-hexane extract of the stem bark of *C. millenii* in order to substantiate its traditional medicinal applications and identify potential bioactive compounds of pharmacological interest.

2. Experimental

Plant Materials Preparation

The stem bark of *Cordia millenii* tree was collected from Ekiti State, Nigeria and authenticated in the herbarium at the Department of Plant Biology, University of Ilorin, Ilorin, Nigeria. The stem bark was chopped into bits and dried at room temperature to remove moisture, weighed, and extracted with *n*-hexane for 5 days with intermittent changing of the solvent. The crude extract obtained was filtered, concentrated, and stored in sample vials in a cool dry place for further work.

Gas Chromatography–Mass Spectroscopy (GC-MS) Analysis

The chemical composition of the hexane extract of *Cordia millenii* stem bark was obtained by subjecting it to Gas Chromatography–Mass Spectrometry (GC-MS) analysis. Approximately, 0.2 g sample was diluted in 2.0 mL using hexane for stock solution and further to a microgram unit before injection into the Shimadzu GC-2010 gas chromatograph. The parameters for the analysis is as indicated: The detector, FID at

220°C, nitrogen gas flowing at 1.0 mL/min on a Optima 35 capillary column (30 m × 0.53 mm ID; 0.32 mm) with split ratio 1:30 and injector temperature, 250°C.The column temperature was maintained at 40°C for five minutes before increasing to 280°C (5°C/min) with a delay at that temperature for an additional five minutes. For the GC-MS, a Jeol JMS-HX 110 mass spectrometer with a source at 270°C and 70 eV coupled with a Hewlett-Packard 6890 gas chromatograph was used. The injector was configured to split at 1:30 and temperature at 270°C. Compound identification was established by comparing the MS fragmentation with authentic samples and data obtained on the NIST Library Version 3.0 mass spectral software database. The chemical composition of the hexane extracts, as obtained from the GC-MS, is as shown in Table 1.

Table 1. Chemical Composition of *n*-Hexane Extract of *Cordia millenii* Stem Bark

S/N	RT (min)	Compound Name	Molecular Formula	% Composition
1	9.86	Methyl 2-octylcyclopropane-1-octanoate	$C_{20}H_{38}O_2$	0.94
2	10.90	17-Octadecynoic acid	$C_{18}H_{32}O_2$	1.51
3	11.74	Ambrettolide	$C_{16}H_{28}O_2$	4.12
4	12.48	cis-10-Nonadecenoic acid	$C_{19}H_{36}O_2$	0.79
5	13.30	Methyl cis-10-nonadecenoate	$C_{20}H_{38}O_2$	3.71
6	13.88	Methyl 18-methylnonadecanoate	$C_{21}H_{42}O_2$	5.01
7	14.26	4-Methyl-E-4-hexadecen-1-ol	$C_{17}H_{34}O$	3.09
8	14.92	Methyl 13,16-octadecadienoate	$C_{19}H_{34}O_2$	1.53
9	15.31	Palmitoleic acid	$C_{16}H_{30}O_2$	1.09
10	15.46	Methyl 7-hexadecenoate	$C_{17}H_{32}O_2$	1.08
11	15.67	Methyl palmitate	$C_{17}H_{34}O_2$	2.65
12	15.70	Methyl henicosanoate	$C_{22}H_{44}O_2$	1.60
13	16.00	2-Butoxyethyl laurate	$C_{18}H_{36}O_3$	**11.96**
14	16.80	Arachidyl alcohol (Arachic alcohol)	$C_{20}H_{42}O$	0.73
15	16.86	Methyl 9,12-octadecadienoate	$C_{19}H_{34}O_2$	1.41
16	16.89	Methyl 11-octadecenoate	$C_{19}H_{36}O_2$	1.60
17	17.09	Methyl behenate	$C_{23}H_{46}O_2$	4.41
18	17.63	Methyl 10-nonadecenoate	$C_{20}H_{38}O_2$	1.80
19	18.24	1-Monolinolein	$C_{21}H_{38}O_4$	5.30
20	18.31	2-Butoxyethyl oleate	$C_{24}H_{46}O_3$	4.97
21	18.42	Methyl tricosanoate	$C_{24}H_{48}O_2$	4.17
22	18.52	4E-1,4-Icosadiene	$C_{20}H_{38}$	0.68
23	18.62	2-Butoxyethyl nonanoate	$C_{15}H_{30}O_3$	2.60
24	18.74	Linoleic acid	$C_{18}H_{32}O_2$	1.05
25	19.27	Methyl-11,16-octadecadienoate	$C_{19}H_{34}O_2$	**12.45**
26	19.38	4-Methyl-E-4-hexadecen-1-ol	$C_{17}H_{34}O$	1.55
27	19.73	17-Octadecynoic acid	$C_{18}H_{32}O_2$	0.76
28	20.16	Methyl (7E)-7-hexadecenoate	$C_{17}H_{32}O_2$	**10.87**
29	20.74	(4Z,15Z)-4,15-Octadecadienyl acetate	$C_{20}H_{36}O_2$	0.73
30	21.40	Trans-Squalene	$C_{30}H_{50}$	4.10
31	21.70	Methyl pentacosanoate	$C_{26}H_{52}O_2$	1.75

Acetylcholinesterase Inhibitory Assay (Ellman Method)

Acetylcholine (ACh) is an important neurotransmitter that plays a critical role in memory and cognitive function. Acetylcholinesterase (AChE) is the enzyme responsible for the termination of nerve impulse transmission at cholinergic synapses through the rapid hydrolysis of acetylcholine. Consequently, inhibition of AChE has become an important therapeutic strategy for the management of several neurological disorders, including Alzheimer's disease, senile dementia, ataxia, Myasthenia gravis, and Parkinson's disease. The anti-cholinesterase activity of *Cordia millenii* extract is as shown in Figure 1.

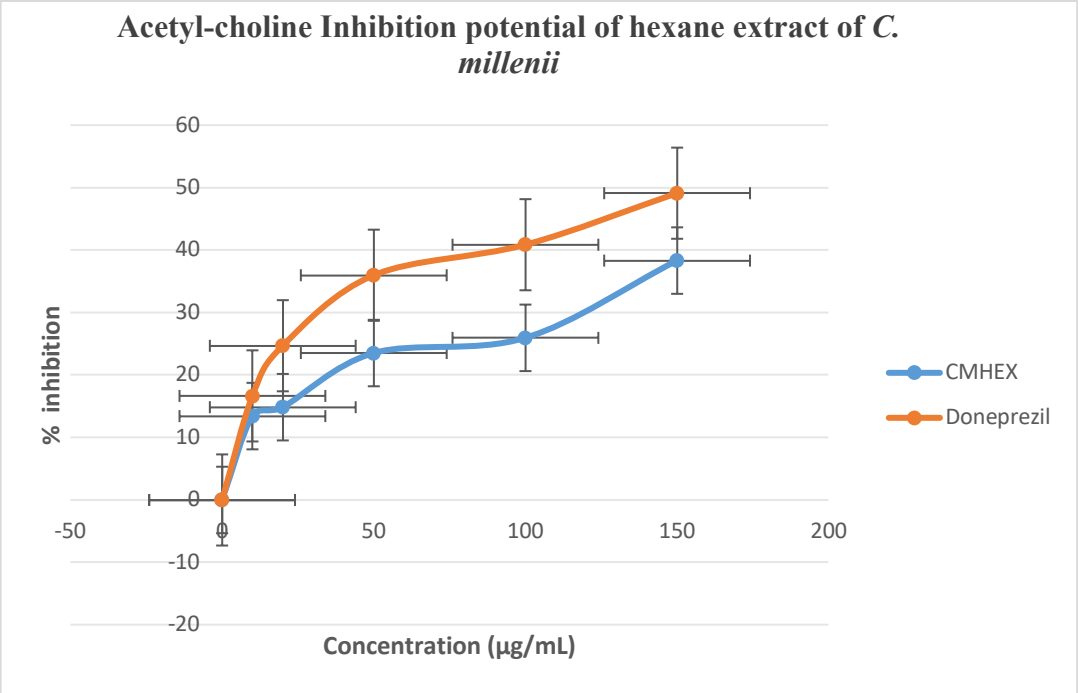

Fig 1. Acetyl-Choline Inhibition Potential of Hexane Extract of *C. millenii*

The acetylcholinesterase (AChE) inhibitory activity of the extract was determined using the colorimetric method developed by George L. Ellman with minor modifications. This assay is based on the enzymatic hydrolysis of acetylthiocholine iodide by acetylcholinesterase to produce thiocholine, which subsequently reacts with 5,5′-dithiobis-(2-nitrobenzoic acid) (DTNB) to yield the yellow-colored 5-thio-2-nitrobenzoate anion. The intensity of the yellow color formed is directly proportional to enzyme activity and is measured spectrophotometrically at 412 nm.

The enzyme used in the assay was acetylcholinesterase obtained from electric eel (*Electrophorus electricus*). The reaction mixture consisted of 200 µL of 0.1 M phosphate buffer (pH 8.0), 20 µL of the test extract, and 20 µL of the enzyme solution (0.5 U/mL). The mixture was pre-incubated at 25 °C for 15 min. Thereafter, 10 µL of DTNB (3 mM) and 10 µL of the substrate Acetylthiocholine iodide (15 mM) were

added to initiate the reaction. The change in absorbance was monitored at 412 nm using a UV–visible spectrophotometer.

The percentage inhibition of AChE activity was calculated using the equation:

$$\text{Inhibition (\%)} = \left(\frac{(\text{Acontrol} - \text{Asample})}{\text{Acontrol}}\right) \times 100$$

where Acontrol represents the absorbance of the control reaction (without extract) and Asample represents the absorbance in the presence of the extract.

The standard inhibitor Donepezil was used as the positive control. All experiments were performed in triplicate (n = 3), and results were expressed as mean ± standard deviation (SD). The IC_{50} value (Table 2) represents the concentration required to inhibit 50% of acetylcholinesterase activity, where a lower IC_{50} indicates greater inhibitory potency. The reference drug Donepezil, a well-est-ablished acetylcholinesterase inhibitor used in the management of Alzheimer's disease, exhibited significantly higher inhibitory potency compared with the hexane extract of *Cordia millenii* (CMHEX). Although CMHEX showed lower activity than the standard drug, it demonstrated measurable inhibition of acetylcholinesterase, indicating the presence of bioactive constituents capable of interacting with the enzyme.

Table 2. IC_{50} Value of CMHEX and Donepezil

SAMPLE	IC_{50} VALUE ± SEM (MG/ML)
CMHEX	220±4.481
Donepezil	127.7±5.767

The observed activity may be attributed to the combined effects of multiple phytochemicals present in the extract, which may act synergistically to produce enzyme inhibition. Such synergistic interactions are commonly reported in plant extracts, where complex mixtures of compounds contribute collectively to the observed biological activity. Although the inhibitory effect of CMHEX was weaker than that of Donepezil, the findings suggest that the non-polar constituents of *C. millenii* may possess potential neuropharmacological relevance. Further studies involving isolation of the active compounds, mechanistic evaluation, and comprehensive pharmacological and toxicological investigations are required to fully establish their therapeutic potential in the management of neurodegenerative disorders.

3. Discussion

The medicinal properties of plants depend on the chemical substances (phytochemicals) that have a particular physiological action on the human body. These phytochemicals possess the potential to prevent and cure the harmful effects of germs and free radicals in the human body. Results from the GC-MS analysis carried out showed the presence of 31 compounds in the *n*-hexane extract of *Cordia millenii* (Table 1). The analysis revealed a complex mixture of fatty acids, fatty acid esters, alcohols, terpenoids, and hydrocarbons, which accounts for 100% of the total extract composition**.** The predominance of lipophilic compounds suggests that the extract is chemically aligned with other bioactive plant oils known for pharmacological properties.

Among the identified compounds, methyl-11,16-octadecadienoate (12.45%), 2-butoxyethyl laurate (11.96%) and methyl (7E)-7-hexadecenoate (10.87%) were the most abundant. These unsaturated fatty acid esters are reported to possess antioxidant, antimicrobial, and anti-inflammatory activities, which may contribute to the ethnomedicinal uses of *Cordia millenii*. Other notable esters such as methyl-18-methylnonadecanoate (5.01%), 2-butoxylehyl oleate (4.97 %), and methyl tricosanoate (4.17%) further reinforce the antioxidant potential of the extract, as unsaturated fatty acid derivatives have been associated with radical scavenging and cytoprotective effects [30]. Lipid-derived compounds and fatty acid derivatives have also been shown to exhibit acetylcholinesterase inhibitory activity and potential neuroprotective properties in recent studies [31].

In addition, the presence of ambrettolide (4.12%) and 1-monolinolein, (5.30%) highlights the extract as a reservoir of macrocyclic lactones and monoacylglycerols, which are compounds with known antimicrobial and anti-inflammatory relevance. Similarly, long-chain alcohols such as 4-methyl-E-4-hexadecen-1-ol and arachic alcohol were detected. Fatty alcohols often exhibit emollient and protective roles in plants, suggesting possible applications in dermatological formulations.

Most importantly, the extract contained trans-squalene (4.10%), a triterpene hydrocarbon recognized for its wide biological roles including antioxidant, anticancer, and cholesterol-lowering activities [32]. The detection of squalene in the extract strengthens the potential therapeutic value of *Cordia millenii*, particularly in oxidative stress-related conditions. Although some constituents such as methyl palmitate (2.65%)**,** methyl behenate (4.41%)**,** and linoleic acid (1.05%) were present in lower proportions, their combined activities could synergistically contribute to the pharmacological efficacy of the extract. The overall chemical profile, dominated by unsaturated fatty acid esters, aligns with the reported activities of *Cordia* species as traditional remedies against microbial infections and inflammatory disorders. Furthermore, plant-derived metabolites such as alkaloids, flavonoids, terpenoids, and fatty acid derivatives have been widely investigated as potential cholinesterase inhibitors due to their ability to modulate cholinergic neurotransmission. Recent reviews [33] have highlighted the increasing interest in natural products as sources of acetylcholinesterase inhibitors for the management of neurodegenerative disorders such as Alzheimer's disease, particularly because synthetic inhibitors may produce undesirable side effects [34].

The identified compounds possess many biological properties and moderate acethylcholinesterase activity when compared with the standard, Donepezil. The *n*-hexane extract of *Cordia millenii* stem has been found to exhibit reasonable cholinesterase inhibitory ability which makes it useful in the treatment of inflammations, dementia (memory loss and mental changes) associated with mild, moderate, or severe Alzheimer's disease and other disorders. *Cordia millenii* exhibits significant AChE inhibitory activity.

4. Conclusion

The results of this study provided an insight into the properties of the extracts of *Cordia millenii* used traditionally for the treatment of various inflammatory diseases. The GC-MS revealed that the *n*-hexane extract of *Cordia millenii* stem bark demonstrates a rich chemical composition dominated by unsaturated fatty acid esters and terpenoids, which are compounds well recognized for their antioxidant, antimicrobial, and cytoprotective properties. These findings provide a chemical basis for the traditional use of the plant in ethnomedicine and justify further pharmacological evaluation to confirm its bioactivities. The presence of all the secondary metabolites showed that *Cordia millenii* stem bark extract could be used in the management of various inflammatory diseases. Therefore, further investigation is highly recommended. The chemical composition of the *Cordia millenii* hexane extract highlights its versatility and potential for various applications, which not only supports its traditional uses, but also opens up new possibilities in modern industries, especially in pharmaceuticals.

5. Conflict of Interest:

Authors declare no conflict of interest.

6. References

1. Kaushik A, Singh J. A study on Alzheimer's disease. *Int. J. Comput. Appl.*, 2019, 975, 8887.
2. Anwal L. A comprehensive review on Alzheimer's disease. *World J. Pharm. Pharm. Sci.*, 2021, 10(7), 1170.
3. Fymat AL. Alzheimer's disease: A path to a cure. *J. Neurol. Psychol. Res.*, 2022, 3(1), 1-15.
4. Perluigi M, Di Domenico F, Butterfield DA. Oxidative damage in neurodegeneration: roles in the pathogenesis and progression of Alzheimer disease. *Physiol. Rev.*, 2024, 104(1), 103-197.
5. Prince M, Wimo A, Guerchet M. Ali GC, Wu YT, Prina M, "World Alzheimer Report 2015 - The Global Impact of Dementia: An analysis of prevalence, incidence, cost and trends", commissioned report from Alzheimer's Disease International, University of Cambridge, London, 2015.

6. Sen S, Chakraborty R. Revival, modernization and integration of Indian traditional herbal medicine in clinical practice: Importance, challenges and future. *J. Tradit. Complementary Med.*, 2017, 7(2), 234-244.
7. Manisha DRB, Begam AM, Chahal KS, Ashok MA. Medicinal plants and traditional uses and modern applications. *J. Neonat. Surg.*, 2025, 14(3).
8. Marchese A, Arciola CR, Coppo E, Barbieri R, Barreca D, Chebaibi S, Sobarzo-Sánchez E, Nabavi SF, Nabavi SM, Daglia M. The natural plant compound carvacrol as an antimicrobial and anti-biofilm agent: Mechanisms, synergies and bio-inspired anti-infective materials. *Biofouling*, 2018, 34(6), 630-656.
9. Kingston DGI. Modern natural products drug discovery and its relevance to biodiversity conservation, *J. Nat. Prod.*, 2011, 74, 496-511.
10. Atolani O, Oguntoye H, Areh ET, Adeyemi OS, Kambizi L. Chemical composition, anti-toxoplasma, cytotoxicity, antioxidant, and anti-inflammatory potentials of *Cola gigantea* seed oil. *Pharm Biol.*, 2019, 57(1), 154-160.
11. Atolani O, Ayeni AE, Usman MA, Adejumo JO, Ibukun OJ, Kola-Mustapha AT, Njinga NS, Quadri LA, Ajani EO, Amusa TO, Bakare-Odunola MT, Oladiji AT, Kambizi L. Isolation, characterization and *in vitro* alpha-amylase inhibition potential of novel bioactives from *Vernonia amygdalina*. *Chemist*, 2023, 94(2).
12. Erukainure OL, Atolani O, Muhammad A, Katsayal SB, Ebhuoma OO, Ibeji CU, Mesaik MA. Targeting the initiation and termination codons of SARS-CoV-2 spike protein as possible therapy against COVID-19: The role of novel harpagide 5-O-β-D-glucopyranoside from *Clerodendrum volubile* P Beauv. (Labiatae). *J. Biomol. Struct. Dyn.*, 2022, 40(6), 2475-2488.
13. Rahaman MM, Hossain R, Herrera-Bravo J, Islam MT, Atolani O, Adeyemi OS, Owolodun OA, Kambizi L, Daştan SD, Calina D, Sharifi-Rad J. Natural antioxidants from some fruits, seeds, foods, natural products, and associated health benefits: An update. *Food Sci. Nutr.*, 2023, 11(4), 1657-1670.
14. Okaiyeto K, Oguntibeju OO. African herbal medicines: Adverse effects and cytotoxic potentials with different therapeutic applications. *Int. J. Environ. Res. Public Health*, 2021, 18(11), 5988.
15. Babweteera F. *Cordia millenii*: On the risk of local extinction? *Afr. J. Ecol.*, 2009, 47(3), 367-373.
16. Nnanga NGA, Vandi D, Flora MA, Ngalle V, Sidjui LS, Sikadeu S, Toghueo RMK, LN Famen, Soh D, Mpondo EM. Preliminary screening of *Cordia mellenii* and their antimicrobial and antioxidant activities. *Int. J. Res. Stud. Biosci.*, 2015, 3(12), 39-46.
17. Tekena MG, Ochuba P. Fashion and music trends in the 21st century Nigeria. *J. Creat. Arts, Commun. Media Stud.*, 2022, 1(1), 58-90.
18. Kipo SL, Ofori K, Kwakye NK, Johnson R, El Boakye M, Gyasi YAO, Owusu FA. Physicochemical and microbiological characteristics of stem bark exudate gum of *Cordia millenii* tree in conventional release tablets. *Sci. World J.*, 2023.
19. Ehiagbonare JE, Onyibe HI, Ehiagbonare PO. Conservation studies on four medicinal taxa of southern Nigeria. *Sci. Res. Essays*. 2008, 3(2),

40-45.
20. Namukobe J, Kasenene JM, Kiremire BT, Byamukama R, Kamatenesi-Mugisha M, Krief S, Dumontet V, Kabasa JD. Traditional plants used for medicinal purposes by local communities around the northern sector of Kibale National Park, Uganda. *J. Ethnopharmacol.*, 2011, 136(1), 236-245.
21. Mark J, Newton AC, Oldfield S, Rivers M in The International Timber Trade: A working list of commercial timber tree species, Botanic Gardens Conservation International Descanso House, Richmond, UK, 2014.
22. Babawale OP, Taiye FR, Adetunji OS. Ethnobotanical survey of plants used as memory enhancer in three states of southwestern Nigeria. *J. Appl. Pharm. Sci.*, 2016, 6(9), 209-214.
23. Avoseh ON, Ogunwande IA, Afolabi PO, Lawal OA, Thang TD, Ascrizzi R, Guido F. Essential oil of *Cordia millenii* from Nigeria. *Am. J. Essent. Oils Nat. Prod.*, 2018, 6(4), 13-17.
24. Zeukang RD, Siwe-Noundou X, Fotsing MT, Kuiate TT, Mbafor JT, Krause RWM, Choudhary MI, Atchadé AT. Cordidepsine is a potential new anti-HIV depsidone from *Cordia millenii*, Baker. *Molecules*, 2019, 18(3), 14.
25. Udeozo IP, Eboatu AN, Arinze RU, Okoye HN. Some fire characteristics of fifty-two Nigerian timbers. *Anachem J.*, 2011, 5(1), 920-927.
26. Hicks CC, Levine A, Agrawal A, Basurto X, Breslow SJ, Carothers C, Charnley S, Coulthard S, Dolsak N, Donatuto J, Garcia-Quijano C, Mascia MB, Norman K, Poe MR, Satterfield T, St Martin K, Levin PS. Engage key social concepts for sustainability. *Science*, 2016, 352(6281), 38-40.
27. Nnadozie IJ, Olajide OC, Agbabiaje OO, Okpuzor J. Effect of *Cordia millenii* extract on reproductive hormone in cisplatin induced infertility in female albino rats. *J. Adv. Biomed. Stud.*, 2017, 2(1), 27-35.
28. Olatunji BP, Fasola TR, Onasanwo SA, Akinyemi AJ, Adeniyi PA, Ishola AO. Neuronal alterations and antioxidant status of lipopolysaccharide induced neuronal damage in mice: Efficacy of three medicinal plants. *J. Appl. Pharm. Sci.*, 2017, 7(2), 156-162.
29. Mukherjee PK, Kumar V, Mal M, Houghton PJ. Acetylcholinesterase inhibitors from plants. *Phytomedicine*, 2007, 14(4), 289-300.
30. Khan M, Yi F, Rasul A, Li T, Wang N, Gao H, Ma T. Alantolactone induces apoptosis in glioblastoma cells via GSH depletion, ROS generation, and mitochondrial dysfunction. *IUBMB Life*, 2012, 64, 783-794.
31. Garcia-Quinto E, Sollecito-Rovella S, Amador-Luna VM, Montero L, Fernandez-Lorente G. Acetylcholinesterase inhibition and antioxidant activity of DHA-disubstituted phosphorlipids. *Mol. Nutr. Food Res.*, 2025, 69(14).
32. Spanova M, Daum G. Squalene – biochemistry, molecular biology, process biotechnology, and applications. *Eur. J. Lipid Sci. Technol.*, 2011, 113(11), 1299-1320.
33. Murray AP, Biscussi B, Cavallaro V, Donozo M, Rodriguez S. Naturally occurring cholinesterase inhibitors from plants, fungi, algae, and animals: A review of the most effective inhibitors reported in 2012–2022. *Curr. Neuropharmacol.*, 2024, 22(10), 1621-1649.
34. AlNasser MN, Alboraiy GM,

Alsowig EM, Alqattan FM. Cholinesterase inhibitors from plants and their potential in Alzheimer's treatment: A systematic review. *Brain Sci.*, 2025, 15(2), 215.

The Chemist
Journal of the American Institute of Chemists

Biosynthesized Silver Nanoparticles Using Two *Juniperus excelsa* M.Bieb Extracts from Its Leaves and Seeds

Manar Abdullah Abou Hassan[1*], Mariam Abdul Razak Drakli[2]

[1 2]*Department of Chemistry, Faculty of Medicine, Syrian Private University, Syria*
[2]*(E-mail: mariamdarakli44@gmail.com)*
**Corresponding author (E-mail: manarhassan330@gmail.com)*

Abstract: The biosynthesis of nanomaterials is an important aspect of nanotechnology due to its cost-effective and eco-friendly procedure where plant extract-based green synthesis of metal nanoparticles (NPs) has become a popular approach in the field of nanotechnology. In this work, silver nanoparticles (AgNPs) were synthesized quickly and in an eco-friendly manner using both the leaves and seeds extracts of *Juniperus excelsa* M.Bieb and an aqueous solution of silver nitrate without any toxic chemicals. The study was conducted using two concentrations of silver nitrate (0.08 and 0.16 mol/L). Two extracts were also prepared, one aqueous and the other alcoholic from each of the seeds and leaves of the juniper plant. Silver nanoparticles that resulted were examined using Scanning Electron Microscopy (SEM) and Energy Dispersive X-ray Spectroscopy (EDX). The synthesis of silver nanoparticles was determined by the color change of the silver nitrate from colorless to brownish by the addition of the studied extracts. High resolution scanning electron microscope confirmed the multiform nature and the high crystallinity of silver nanoparticles on an average size of 8-45 nm. The spectrum (EDX) analysis showed that the elemental composition contained mostly silver. Silver nanoparticles produced by aqueous extraction showed smaller sizes than nanoparticles produced by alcoholic extract. The sizes of silver nanoparticles produced were smaller at 0.08 M of $AgNO_3$.

Key Words: *Juniperus excelsa,* green synthesis, silver nanoparticles, plant extracts, EDX, SEM

1. Introduction

The term “nano” comes from the Latin *nanus*, meaning “dwarf”. This kind of technology is supported in physics, chemistry, materials science, biotechnology, and biosciences, among others, to achieve a multidisciplinary understanding of the phenomena that occur in the materials [1]. Nanotechnology, a relatively new area of

study and research, is the "design, characterization, production and application of structures, devices and systems, by controlling shape and size at the nanometer scale". The particle matter usually ranges from 1 to 100 nm in size. A nanometer (nm) is a billionth of a meter, 10^{-9}. Within this range, materials may have properties considerably different from those expected when they have larger dimensions. Nanoscience depends on the fundamental properties of nano size objects [2]. Nanoparticles are an important class of nanomaterials studied as nanotechnology [1].

Biosynthesis of nanoparticles is becoming a hot topic across the world; this field encompasses a wide spectrum of applications. It plays a critical role with its vast application in nanomedicines, chemical sensing, drug delivery, data storage, cell biology, textiles, food industries, antioxidants, photocatalytic organic dye-degradation, cosmetics, agriculture, and antimicrobial agents [3]. The metallic nanoparticles are considered the most promising as they possess remarkable antibacterial properties due to their large surface area to volume ratio, which can counteract growing microbial resistance against metal ions, antibiotics, and the development of resistant strains. Of these metallic nanoparticles, silver nanoparticles stand out, because of their unique properties, such as chemical stability, good conductivity, catalytic, antibacterial, anti-viral, antifungal, and anti-inflammatory activities. They are usually found as components of composite fibers, cryogenic superconducting materials, cosmetic products, food industry, and in electronic components. Ag nanoparticles have found applications in the biomedical field such as in wound dressings, topical creams, antiseptic sprays, and fabrics. Ag nanoparticles display a broad biocidal effect against pathogenic microorganisms via a disruption of their unicellular membrane, hence, disturbing enzymatic activities. Ag nanoparticles have also been successful in cancer diagnosis and treatment as well [2]. The biological synthesis of nanomaterials has been put into practice since it uses temperature, pH, and pressures that are considered mild conditions. In addition, it has advantages over other synthesis methods, including higher productivity and lower costs. Biological synthesis uses microorganisms and plants (or their extracts). There is a particular interest in using plants because they have many phytochemicals, including ketones, aldehydes, flavonoids, amides, terpenoids, carboxylic acids, phenols, and ascorbic acids. These components are known to reduce metal salts and create metal nanoparticles. However, although there are several studies on nanoparticles, the exact mechanism involved in this process remains uncertain [1].

The plant extracts consist of different bioactive compounds. Phytochemicals sourced from plants assist in the process of conversion of silver ions to AgNPs; the same phytochemicals play dual roles of reducer and stabilizers agents. Concentration of these phytochemicals determines the size, shape, and surface properties of the AgNPs, which defines their functional properties and potential uses [4]. Commonly known as coniferous plants, junipers belong to the genus Juniperus of the family Cupressaceae The genus Juniperus is a monophyletic that consists of almost seventy species [5]. Juniperus is the third largest genus among the conifers found in the world. Plants belonging to this genus grow slowly and can live up to 2000 years. These coniferous plants can be found in all sizes ranging from small flat shrubs to giant forest trees. One thing that makes junipers stand out among other plants is that they can survive in

different sites enduring extreme and rapid fluctuations in temperature. They can grow in arid places where other plants cannot survive [5]. *J. excelsa* subsp. excelsa is a medicinal plant that has been used to treat dysmenorrheal, cough, bronchitis and colds, jaundice and tuberculosis, and to induce menses and expel fetuses [6]. Juniper species are especially used in traditional medicine due to their analgesic, diuretic, antibacterial, anti-microbial, anti-inflammatory, and liver-protective effects [7].

In view of the above, the main purpose of this experimental study was to synthesize Ag-NPs from *Juniperus excelsa* M.Bieb leaves and seeds extracts in an inexpensive and simple way, and to characterize these nanoparticles at two different concentrations of Ag^+ ion.

2. Materials and Method

The study was conducted in the laboratories of Syrian Private University, Atomic Energy Commission of Syria, the National Commission for Biotechnology in Damascus.

Preparation of Plant sample

The plant of *Juniperus excelsa* M.Bieb that used in the study was collected in July 2023 from the al-Khusha in mountains of al-Qalamoun, Ras al-Ma'arra village, Yabroud area, Damascus countryside, Syria. The fresh leaves and seeds were separated from the bark and cleared with tap water. Then, they were washed with distilled water thoroughly and dried for 15 days at room temperature in shadow. The leaves and seeds were stored at -20°C until use.

Finally, they were crushed into small pieces immediately before use with an electric grinder, where the particle dimensions were less or equal to 0.2 mm.

Preparation of Plant Leavs and Seeds Extracts

Extraction was done using the method described by Corciova *et al.* in 2022 with some modification. 25 g of each dried and powder *Juniperus excelsa* M.Bieb leaves and seeds were extracted with 100 ml of distilled water, with continuous stirring by a magnetic stirrer at 6 rpm for one hour (at room temperature). Then, it was heated to 60°C for another hour with the same conditions. The alcoholic extract was prepared in the same way, replacing ethanol with distilled water. Each mixture was soaked and left to stand for 24 hours at 4°C and then filtered using Whitman No. 1 filter paper. After that, each supernatant was evaporated using a vacuum rotary evaporator to concentrate the extracts [8].

Preparation Silver Nitrate ($AgNO_3$) Solution

The mother solution was prepared from silver nitrate 1M, by dissolving 33.974 g of it in 200 ml of deionized water. Then two dilute solutions were prepared to obtain con-

centrations of 0.08 and 0.16 M from the mother solution. The containers were kept away from light to prevent oxidation of the silver ions.

Synthesis and Characterization of Silver Nanoparticles

The synthesis of nanoparticles (Ag-NPs) was carried out by adding 10 mL from the stock solution of each extract to 90 mL for each concentration of $AgNO_3$ aqueous solutions, separately, in a 250 mL flask. The addition was conducted slowly at 25°C for 4 hours with continuous stirring by a magnetic stirrer. While stirring, the color change was monitored where the reaction color transformed from light yellow to dark brown, which indicates the time-dependent formation of Ag-NPs. Afterward, no further color transformation was perceived until the end of the reaction. After that, the pH of the solution adjusted to a value of 7. The solutions were left to stand for 24 h, then were filtered with Whitman No. 1 filter paper. The obtained product was dried at 60°C for 8 h in an oven. Finally, a black powder (nanoparticles) is achieved. They were removed after weighing and transferred to a closed container and kept for further analysis [9].

Characterization of AgNPs

The characterization of synthesized nanoparticles was carried out as follows, according to the methods described earlier in Baran (2018). The surface structure was visualized by SEM (TESCAN, Czech Republic) at an accelerating voltage of 30 kV, and elemental analysis measurement was done using EDX (EDAX, USA) at an accelerating voltage of 20 kV [10].

3. Statistical Analyses

The data was subjected to one way-ANOVA IBM SPSS software package for Windows (Version 20, SPSS, Inc., Chicago, IL); the statistical significance was evaluated at $P \leq 0.05$. The results were presented as mean ± standard deviation based on three replications.

4. Results and Discussion

Researchers discovered nanoparticles made from microorganisms and plant extracts are more cost-effective compared to physical and chemical methods and act as reducing and stabilizing agents. The advantages of synthesis from plant extracts include a sanitary working environment, health and environmental protection, less waste, and the most stable products. Nanoparticle properties are determined by the plant extract sources; individual phytochemical combinations in extracts differ substantially depending on the plant source. As a result, changing the extract composition can

change the characteristics of AgNPs [3]. For the synthesis of plant-based nanoparticles, the following are necessary:

a. metal salt,
b. reducing agent, and
c. stabilizing or capping agent for controlling the size of nanoparticles and preventing their aggregation [2].

In general, nanoparticle synthesis involves mixing plant extracts with metal precursor salts. They can interact under different reaction conditions (pH, temperature, concentrations, etc.). Here, the formation of nanoparticles takes place in stages. It begins with the set of species equilibrium; once dissolved, the extracts and the precursor salt coordination complexes are formed between the metal ion and the phytochemicals of the extract. The sites where the nanoparticles will grow are created at the second nucleation stage. At the third stage of growth and adsorption, small adjacent nanoparticles come together to form particles of a larger size. Finally, during termination, the final shape of the nanoparticles occurs [1]. The extracts used for nanoparticle synthesis have a wide variety of secondary metabolites involved in nanoparticle reduction, formation, and stabilization. Phytochemicals in the extracts include phenols, flavonoids, alkaloids, terpenoids, proteins, carbohydrates, and amino acids [1].

For biosynthesis, an aqueous $AgNO_3$ solution was mixed with an aqueous and alcoholic *Juniperus excelsa* M.Bieb extract from leaves and seeds (Figure 1).

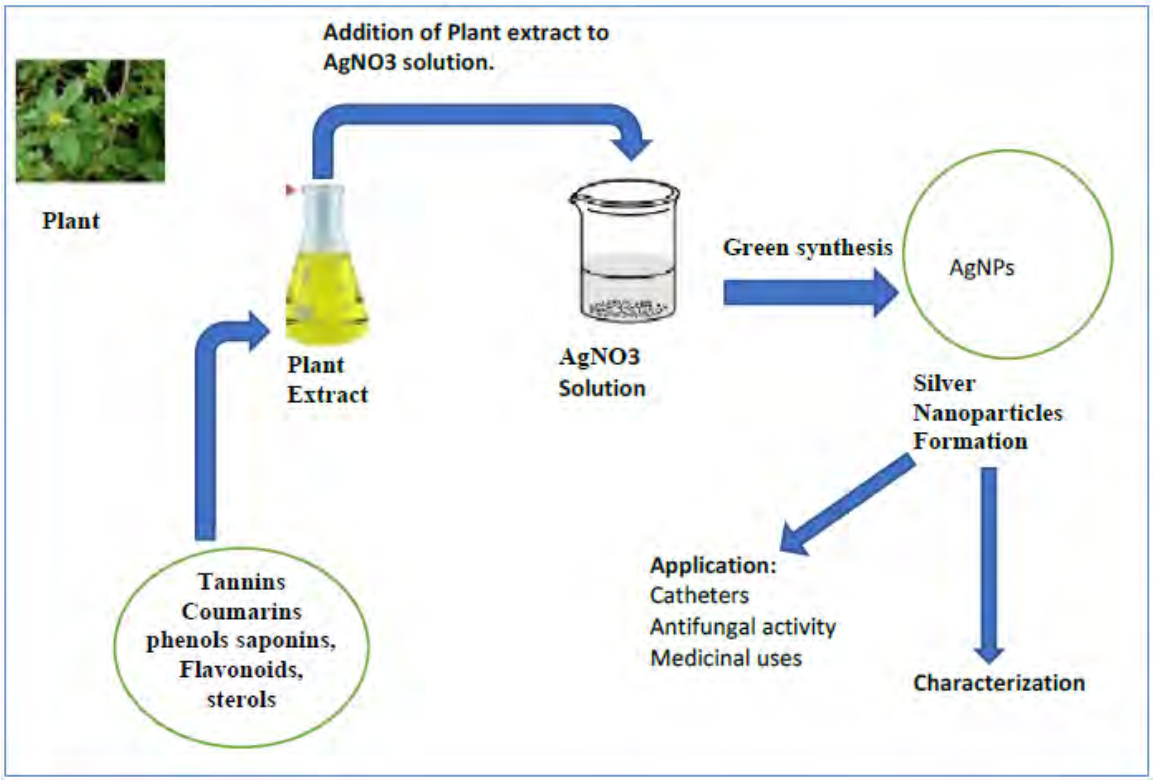

Figure 1. Schematic Diagram of Green Synthesis of Silver Nanoparticles

Visual observation showed that the color of the leaves and seeds extracts of *Juniperus excelsa* M.Bieb, after treatment with Ag precursors, change in color of the reaction mixture from light yellow to dark brown, indicating the formation of AgNPs. This color change is due to quantum confinement and the nanoparticles' dependence on their optical properties [11].

Nanoparticles (NPs) have been the subject of significant analysis due to their ease of preparation, high surface-to-volume ratio, diverse optical properties, unique surface chemistry, and relative simplicity in functionalization compared to their bulk counterparts. The methods frequently used to characterize NPs are UV Visible absorption spectroscopy, SEM (Scanning Electron Microscopy), TEM (Transmission Electron Microscopy), XRD (X-ray Diffraction), DLS (Dynamic Light Scattering), FTIR (Fourier Transmission Infrared Spectroscopy), and EDX (Energy Dispersive X-ray) [12].

In this study, both SEM and EDX were used: Scanning Electron Microscopy (SEM) for providing information about nanoparticle morphology, size, and homogeneity, and Energy Dispersive X-ray spectroscopy (EDX) for estimates of the abundance of elements present over nanoparticles surface.

SEM has an ability to contribute morphology and microstructure of bulk as well as nanostructures [13]. Based on the obtained SEM images, the synthesized nanoparticles had various shapes, most of which are irregular and get agglomerated and are multiform. Building blocks of various bioactive reducing agents, lower capping ability of extracts, and H-bonding present in bioactive molecules could be the reason for the agglomeration of the nanoparticles [14].

The average particle size, as calculated using the ImageJ software, from the SEM image was found to be between 13-40 nm, 16-32 nm for aqueous extract of leaves, 13-24 nm, 28-40 nm for alcoholic extract of leaves at 0.08 and 0.16 M, respectively. While was between 8-30 nm, 13-28 nm for aqueous extract of seeds, 16-36 nm, 20-45 nm for alcoholic extract of seeds at 0.08 and 0.16 M, respectively (Figure 2-9).

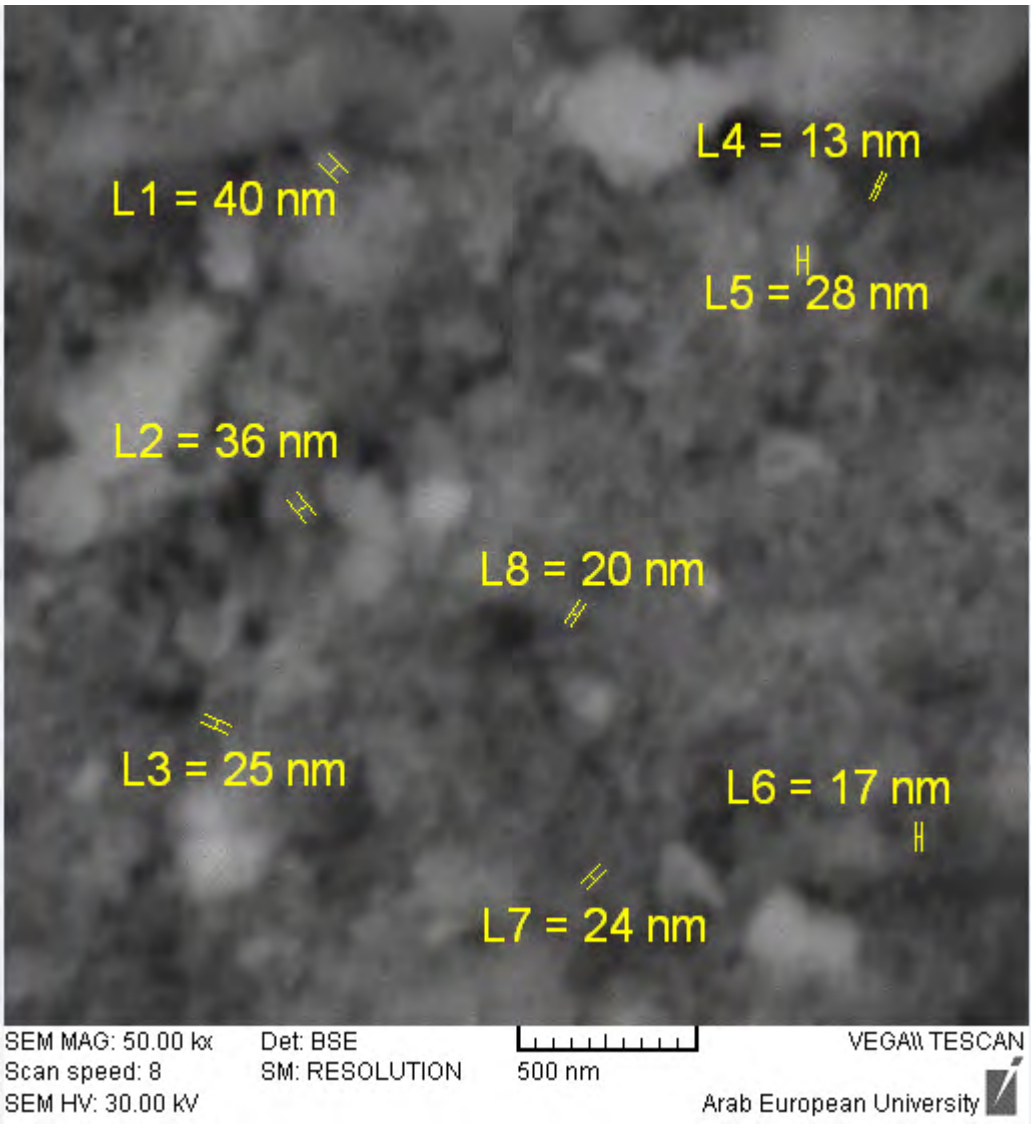

Figure 2. SEM Micrograph of the Ag-NPs at 0.08 M $AgNO_3$ Using Aqueous Extract of *Juniperus excelsa* M.Bieb Leaves

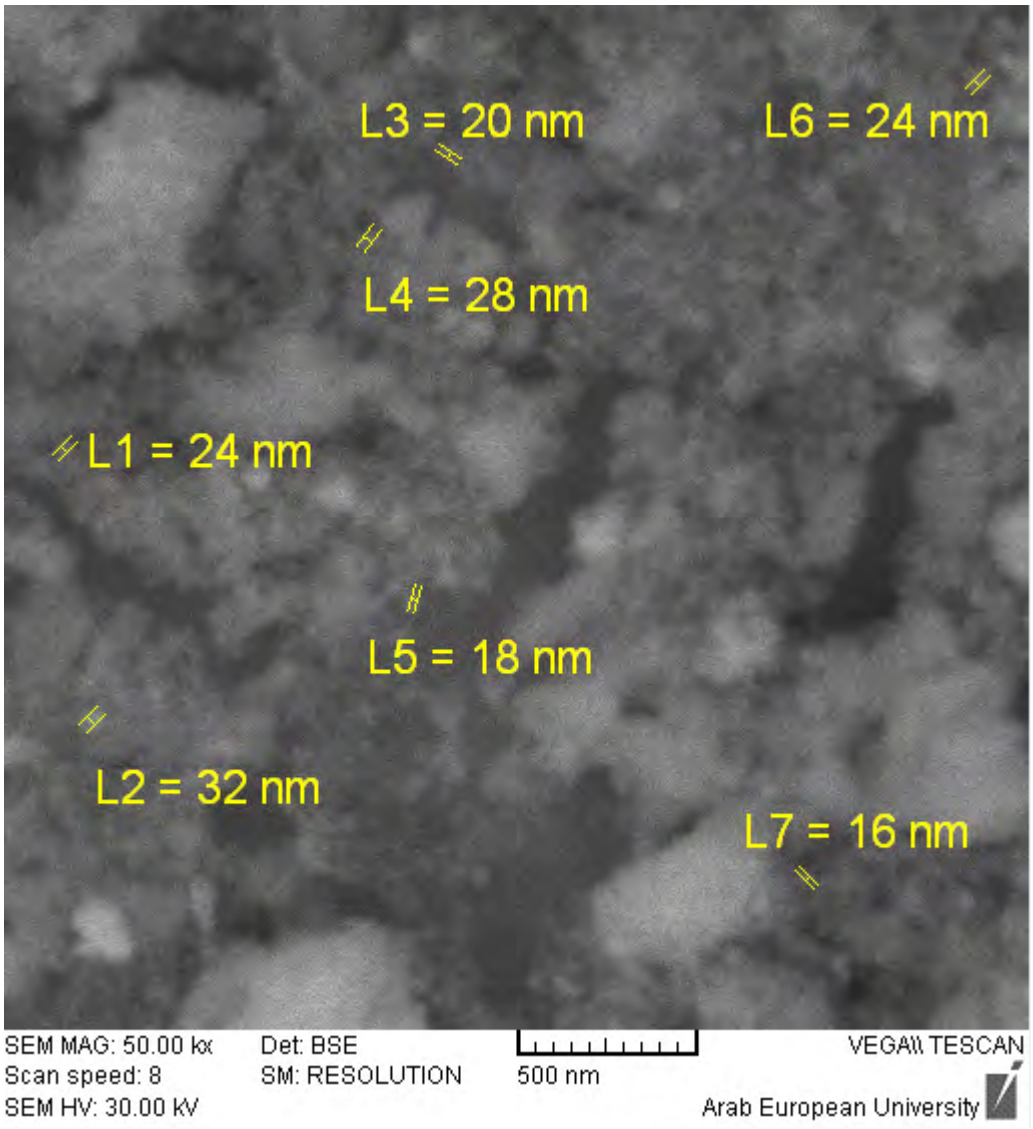

Figure 3. SEM Micrograph of the Ag-NPs at 0.16 M $AgNO_3$ Using Aqueous Extract of *Juniperus excelsa* M.Bieb leaves

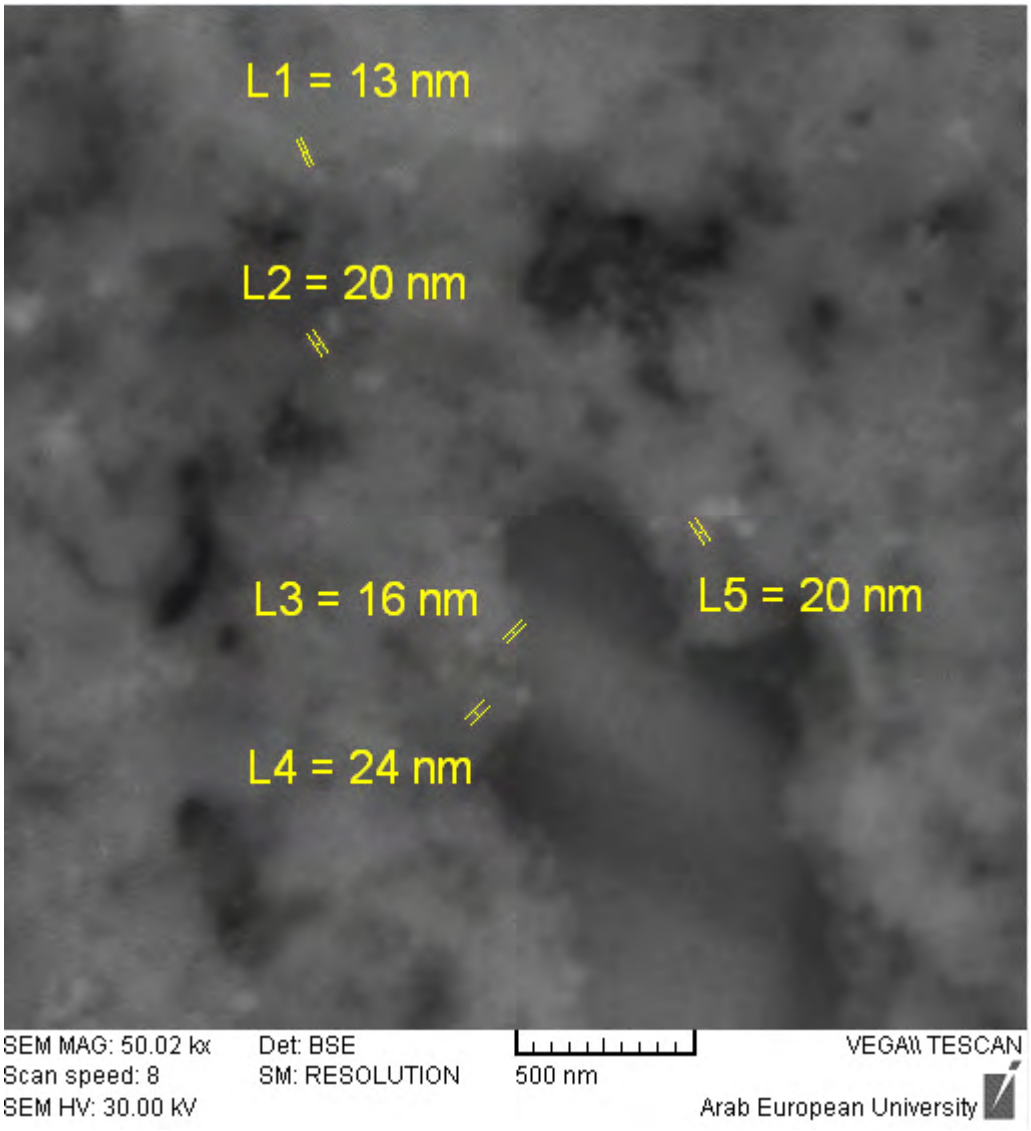

Figure 4. SEM Micrograph of the Ag-NPs at 0.08 M $AgNO_3$ Using Alcoholic Extract of *Juniperus excelsa* M.Bieb Leaves

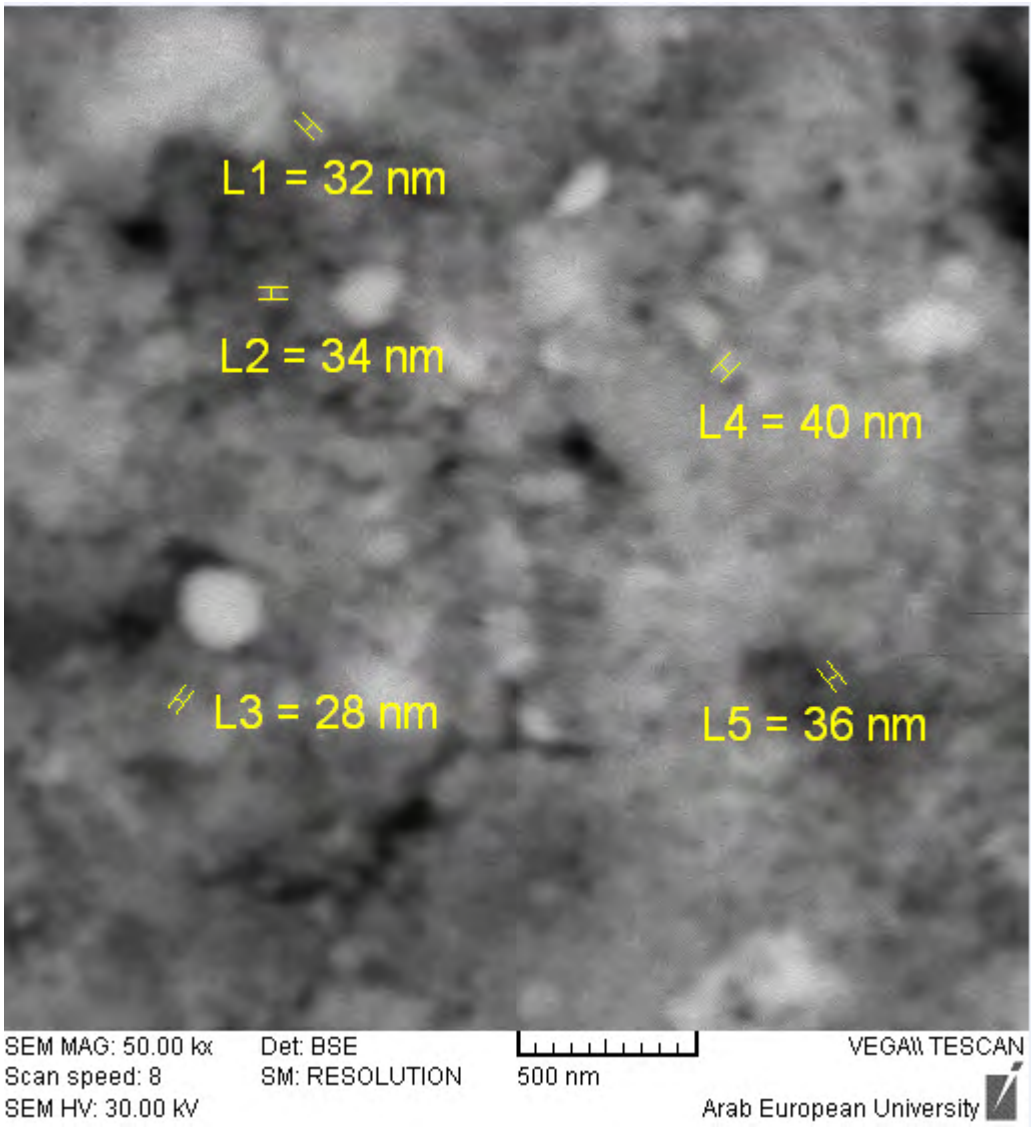

Figure 5. SEM Micrograph of the Ag-NPs at 0.16 M $AgNO_3$ Using Alcoholic Extract of *Juniperus excelsa* M.Bieb Leaves

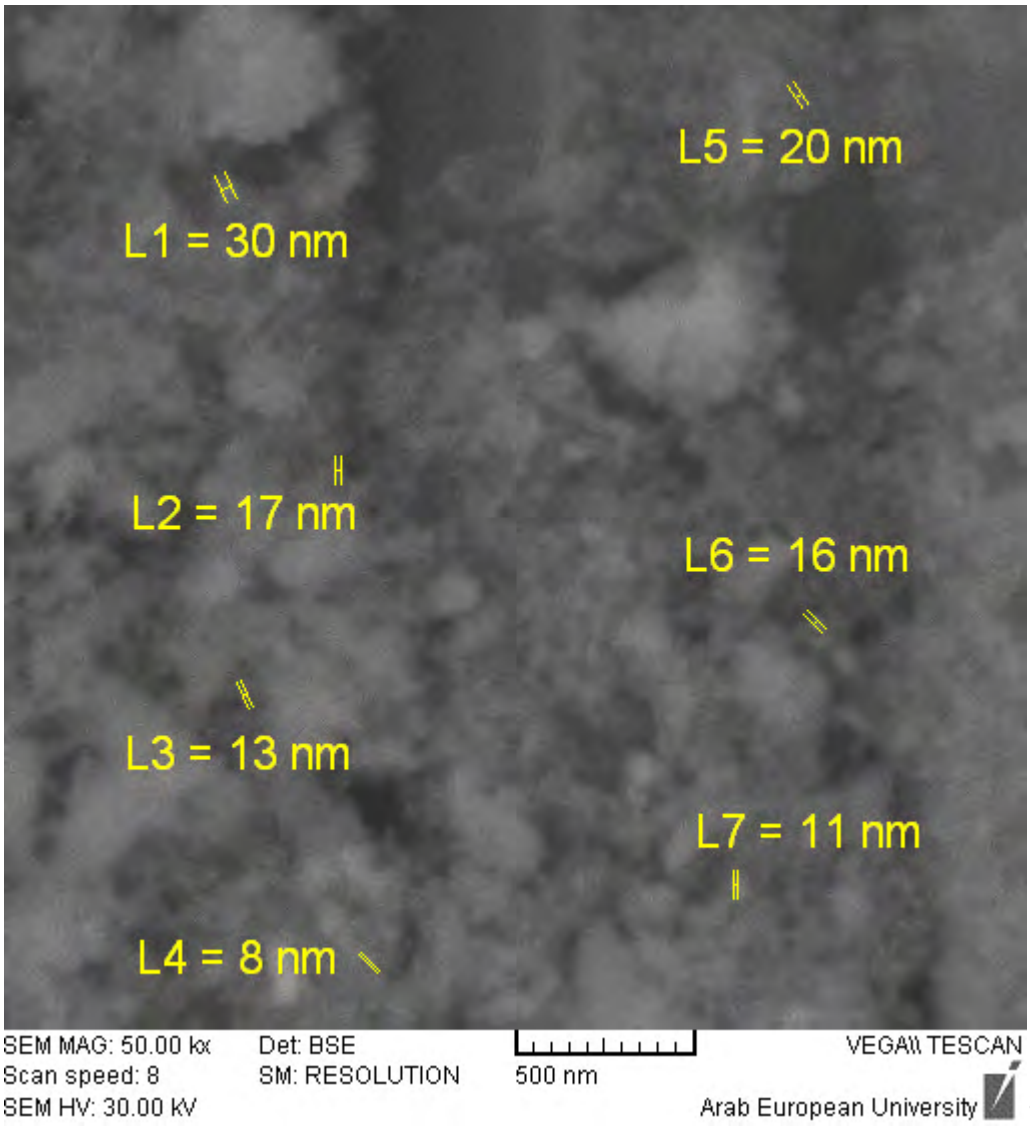

Figure 6. SEM Micrograph of the Ag-NPs at 0.08 M $AgNO_3$ Using Aqueous Extract of *Juniperus excelsa* M.Bieb Seeds

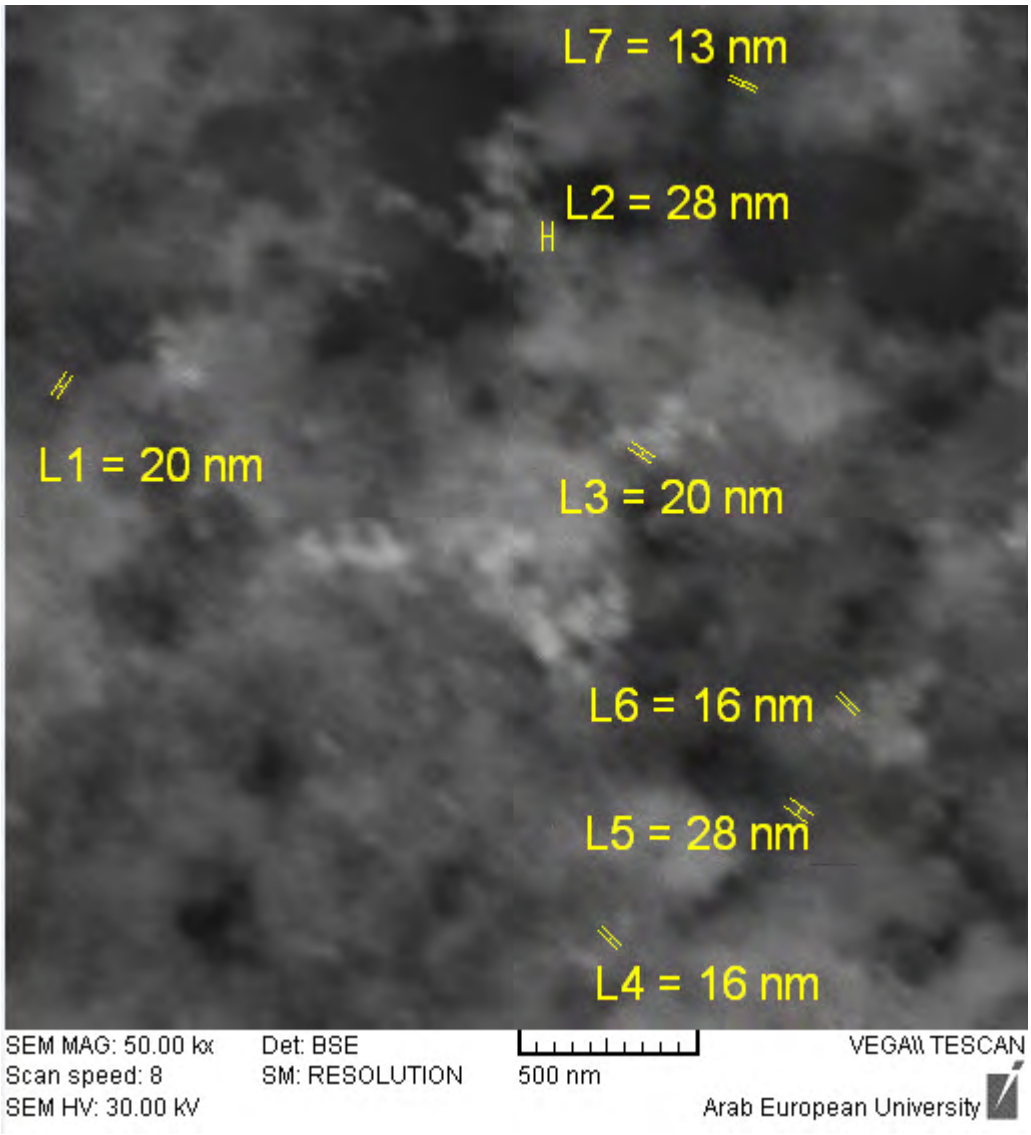

Figure 7. SEM Micrograph of the Ag-NPs at 0.16 M $AgNO_3$ Using Aqueous Extract of *Juniperus excelsa* M.Bieb Seeds

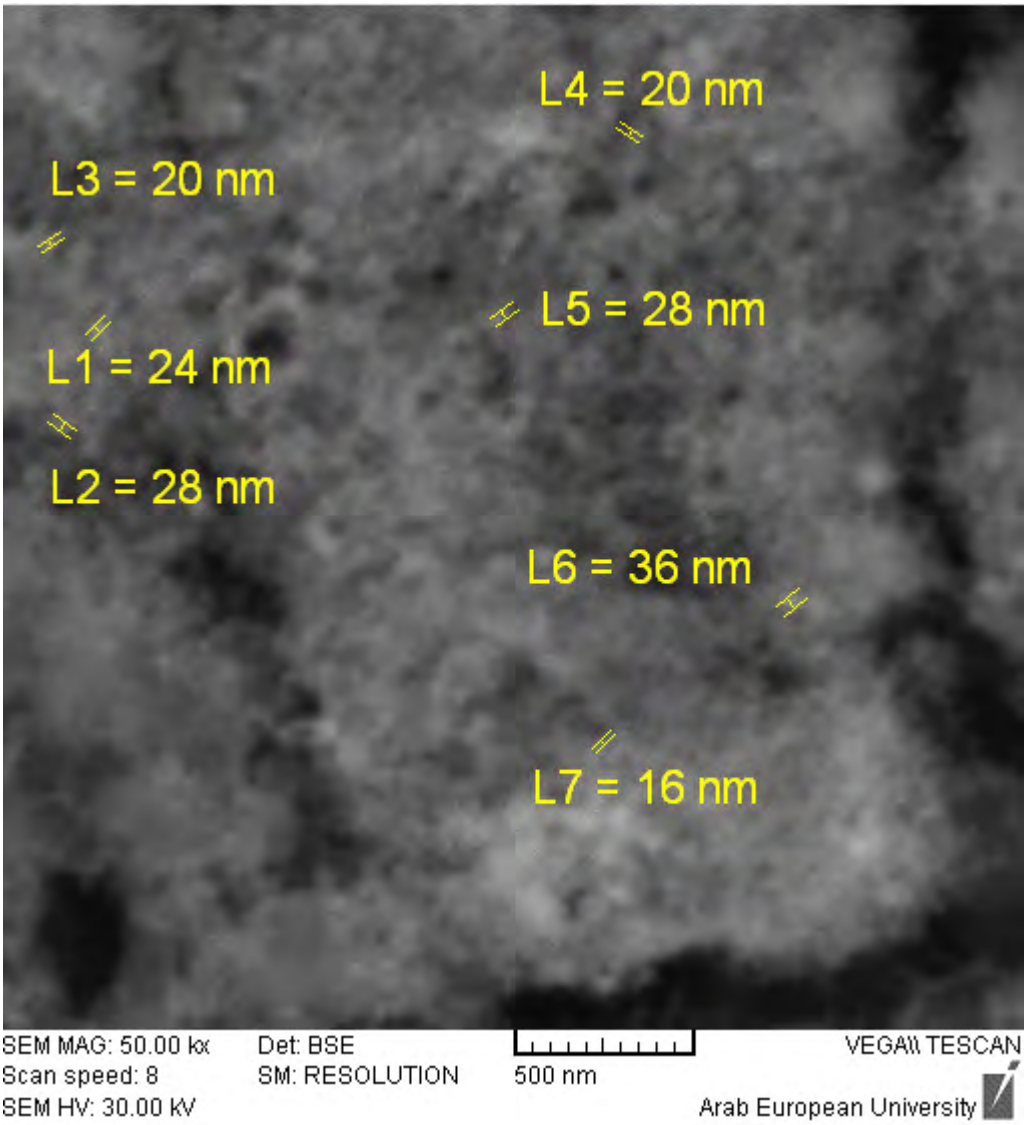

Figure 8. SEM Micrograph of the Ag-NPs at 0.08 M $AgNO_3$ Using Alcoholic Extract of *Juniperus excelsa* M.Bieb Seeds

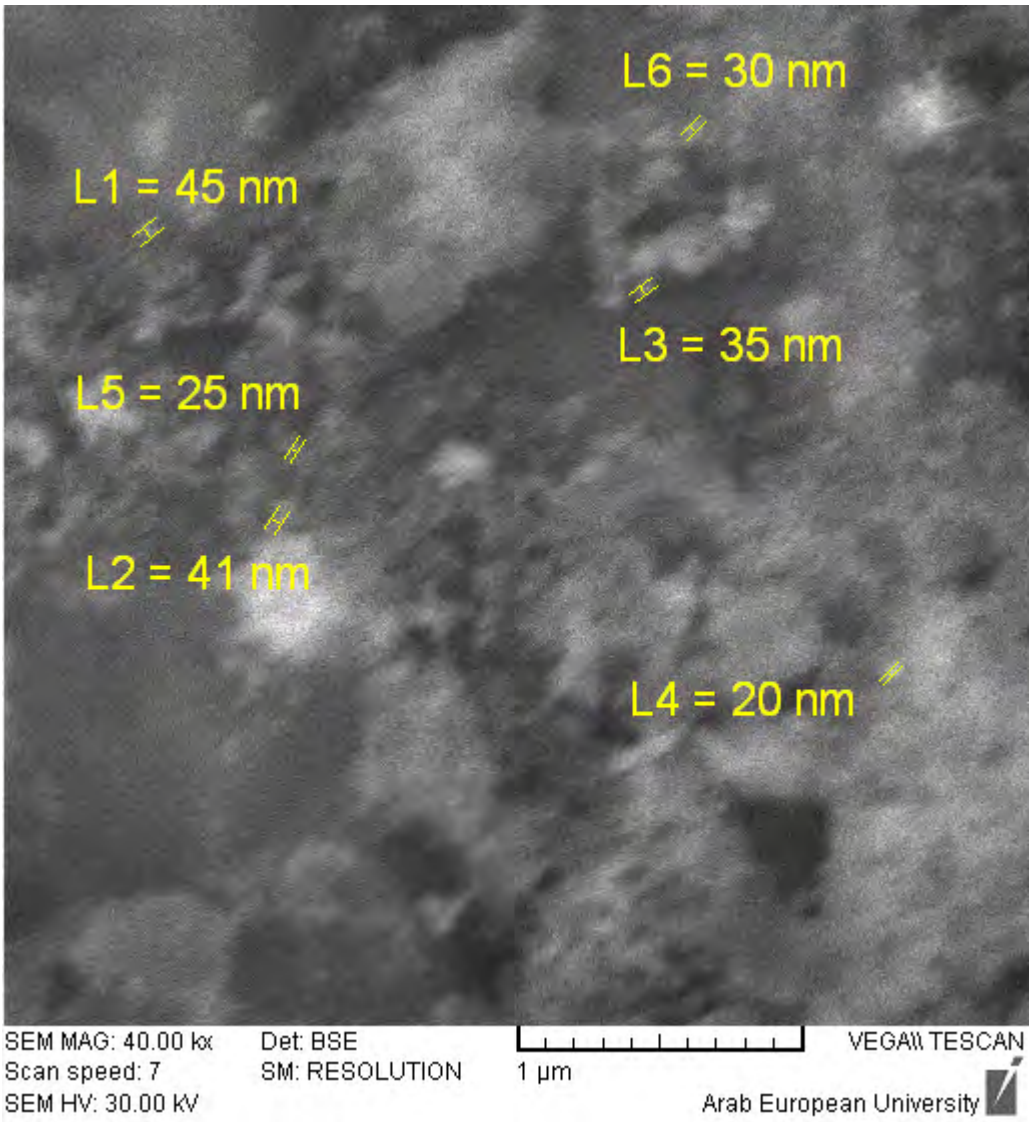

Figure 9. SEM Micrograph of the Ag-NPs at 0.16 M $AgNO_3$ Using Alcoholic Extract of *Juniperus excelsa* M.Bieb Seeds

The research studies on the silver nanoparticle synthesis performed showed that the nanoparticles formed ranged in size from 80.11 to 157.01 nm [15], 72.656 nm [16], and 17.3 nm [17]. To use nanoparticles as drug delivery systems, they should be in the range of 10–100 nm. Even though NPs smaller than 10 nm can pass through the nuclear pore and interact with chromosomes and DNA, which is advantageous for gene therapy and diagnostics, they are probably not suitable for drug delivery. For nanomedical applications, the preferred size of nanoparticles is less than 200 nm [18]. In this study, the NPs had a size of less than 100 nm, suggesting the proper size for drug delivery.

The previous results show that the lower concentration of silver nitrate (0.08 M) produced smaller nanoparticles than the higher concentration (0.16 M) for all samples studied on leaves and seeds with their aqueous and alcoholic extracts.

EDX is an analytical method used to find the chemical compositions of various elements and to determine the relative abundance of particular chemical elements on a solid surface. EDX works on the principle of an interaction of some source of X-ray excitation and a sample. Due to a variance in their atomic structures, every single element proffers the individual assortment of peaks on its electromagnetic emission spectrum. Bombardment of high energy particles on an atom which contains ground state electrons results in the formation of electron-hole by releasing an excited electron from the inner shell. An electron from the outer shell and higher energy shell try to fill the empty shell and this energy disparity between the high-energy shell and the lower energy shell may be dispensed under the form of an X-ray. This could be covered by an energy-dispersive spectrometer. Emitting X-rays helps to identify specific elements and its proportion [10].

Two samples of silver nanoparticles produced from the aqueous extract of the seeds and from the alcoholic extract of juniper leaves were tested for Energy Dispersive X-ray (EDX).

In the EDX analysis, it was observed that the content of the element belonged largely to silver. Data analysis revealed that EDX spectra of Ag-NPs mainly contained a specific and intense peak at ~3 keV for Ag (88.2% and 88.14%) and for O (11.8% and 11.86%) for the alcoholic extract of the leaves and the aqueous extract of the seeds, respectively, at the concentration 0.08M of silver nitrate. Consequently, the results confirmed the synthesis of Ag-NPs (Figure 10-11).

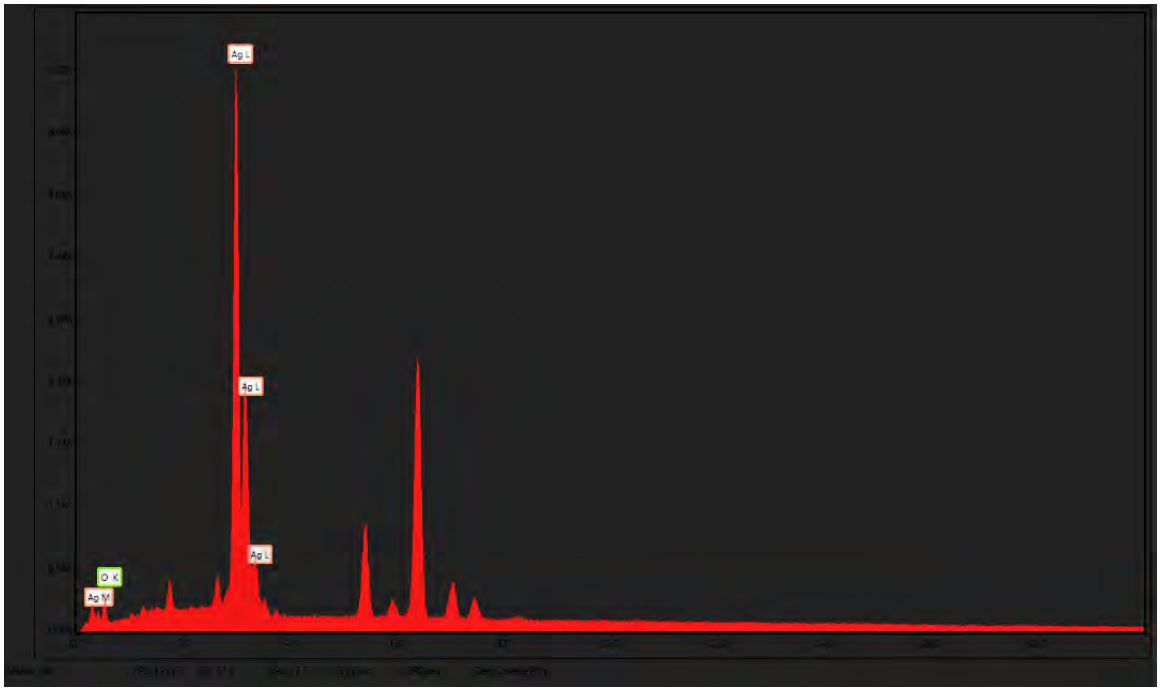

Figure 10. Analysis of the Elemental Composition by the EDX Analysis of AgNPs Using Alcoholic Extract of *Juniperus excelsa* M.Bieb Leaves at 0.08 M $AgNO_3$

Figure 11. Analysis of the Elemental Composition by the EDX Analysis of AgNPs Using Aqueous Extract of *Juniperus excelsa* M.Bieb Seeds at 0.08 M $AgNO_3$

The studied particles were not observed to have impurities from the hetero-elements of silver and oxygen in the Ag-NPs, so these results indicated that the reaction product was composed of high purity nanoparticles.

5. Conclusion

There are three ways to make nanoparticles: physical, chemical and green synthesis. Green synthesis is the best since it's very simple, easy to perform, inexpensive, highly efficient, and environmentally friendly. It is the chemical constituents of plants, proteins, carbohydrates, alkaloids, tannins, phenolics, oils and saponins, which can act as reducing and capping agents for NP synthesis. The shape and size distribution of plant-based NP can be controlled by an optimization of reaction conditions, such as temperature, pH, and the amount of plant material. Moreover, the reaction can be scaled up. Silver nanoparticles have proven helpful as nanomedicine, chemical reactions in solar cells, biochemical sensors, and batteries. Ag nanoparticles have found applications in the biomedical field, such as in wound dressings, topical creams, antiseptic sprays, and fabrics. Also, they display a broad biocidal effect against pathogenic microorganisms via a disruption of their unicellular membranes, therefore, disrupting their enzymatic activities. Ag nanoparticles have also been successful in cancer diagnosis and treatment.

6. Acknowledgment

The authors are thankful to the Syrian Private University and Atomic Energy Commission of Syria for providing the facility to conduct the experiments in laboratories.

7. Funding

This research received no external funding.

8. Conflict of Interest

The manuscript was written through contributions of the two authors, and these two authors contributed equally. The authors have given approval to the final version of the manuscript.

The authors declare no conflict of interest.

9. References

1. Bouttier-Figueroa DC, Cortez-Valadez M, Flores-Acosta M, Robles-Zepeda RE. Synthesis of metallic nanoparticles using plant's natural extracts: Synthesis mechanisms and applications. *Biotecnia*, 2023, 25(3), 125-139. DOI: 10.18633/biotecnia.v25i3.1916
2. Jagessar RC. Plant extracts based nanoparticles, a good perspective in the development of drugs in nanomedicine. *Mod. Approaches Drug Des.*, 2020, 3(2), 10-31031. DOI: 10.31031/MADD.2020.03.000556
3. Pradhan AK, Sahoo SR, Satapathy S, Pradhan S, Sankar J. Green synthesis of silver nanoparticles from various plant extracts and its applications: A mini review. *World J. Biol. Pharm. Health Sci.*, 2022, 11(1), 050-061. https://doi.org/10.30574/wjbphs.2022.11.1.0100
4. Kaur S, Mishra M, Sharma A, Mittal V, Duklan N, Sashank SS, Soni H, Hussain M. Eco-friendly synthesis of silver nanoparticles: A sustainable route for multifunctional applications with advanced characterization. In: E3S Web of Conferences, EDP Sciences, 2024, vol 588, p 01010. https://doi.org/10.1051/e3sconf/202458801010
5. Kashani SA, Ali I, Hasni MS, Asrar M, Ahmad J, Shahzad MZ. Nutritional and anti-nutritional study of *Juniperus excelsa* (M.Bieb) of Ziarat, Balochistan, Pakistan. *Environ. Sci. Ecol.: Curr. Res.*, 2020, 1(0008).
6. Emami SA, Abedindo BF, Hassanzadeh-Khayyat M. Antioxidant activity of the essential oils of different parts of *Juniperus excelsa* M.Bieb. subsp. excelsa and *J. excelsa* M.Bieb. subsp. polycarpos (K. Koch) Takhtajan (Cupressaceae). *Iran. J. Pharm. Res.*, 2011, 10(4), 799.
7. Eryigit T, Yildirim B, Ekici K. Chemical composition, antioxidant and antibacterial properties of *Juniperus*

excelsa M.Bieb. leaves from Türkiye. *Acta Sci. Pol., Hort. Cult.*, 2023, 22(1), 11-17. https://doi.org/10.24326/asphc.2023.4577

8. Corciovă A, Mircea C, Burlec AF, Fifere A, Moleavin IT, Sarghi A, Tuchiluş C, Ivănescu B, Macovei I. Green synthesis and characterization of silver nanoparticles using a *Lythrum salicaria* extract and *in vitro* exploration of their biological activities. *Life*, 2022, 12(10), 1643. https://doi.org/10.3390/life12101643
9. Razak Darakli MA, Abou Hassan MA. Green synthesis of silver nanoparticles using figs (*Ficus carica* L.) leaves extract Syrian. *Nanosist., Nanomater., Nanotehnol.*, 2024, 22(2). https://doi.org/10.15407/nnn.22.02.469
10. Razak Darakli MA, Abou Hassan MA. Synthesis and characterization of nanoparticles by using mulberry (*Morus alba* L.), figs (*Ficus carica* L.) and eucalyptus (Camaldulensis L.) leaves extracts in aqueous medium. *Nanosist., Nanomater., Nanotehnol.*, 2026, 24(4). (accepted and in press)
11. Dogra S, Sharma MD, Tabassum S, Mishra P, Bhatt AK, Bhuyar P. Green biosynthesis of silver nanoparticles (AgNPs) from *Vitex negundo* plant extract and its phytochemical screening and antimicrobial assessment next to pathogenic microbes. *J. Microbiol., Biotechnol. Food Sci.*, 2023, (4). https://doi.org/10.55251/jmbfs.5993
12. Mawthoh ABT, Seram D, Watt HJ. Green synthesized plant-based nanotechnology: Cutting edge innovation fostering sustainability and revolutionizing agriculture. In: E3S Web of Conferences, EDP Sciences, 2023, vol 453, p 01018.
13. Powar NS, Patel VJ, Pagare PK, Pandav RS. Cu nanoparticle: Synthesis, characterization and application. *Chem. Methodol.*, 2019, 3, 457-480. DOI:10.22034/chemm.2019.154075.1112
14. Üstün E, Önbaş SC, Çelik SK, Ayvaz MÇ, Şahin N. Green synthesis of iron oxide nanoparticles by using *Ficus carica* leaf extract and its antioxidant activity. *Biointerface Res. Appl. Chem.*, 2022, 12(2), 2108-2116. https://doi.org/10.33263/BRIAC122.21082116
15. Al-Shammari HI, Al-Zubaidi HK. Effectiveness of entomopathgenic fungi *Beauveria bassiana* in synthesis of silver nanoparticles and their impact on some instars of citrus mealybug *Planococcus citri* (Risso), Pseudococcidae: Hemiptera. *Iraqi J. Agric. Res*., 2017, 22(8), 78-89.
16. Das G, Shin HS, Patra JK. Key health benefits of Korean ueong dry root extract combined silver nanoparticles. *Int. J. Nanomed.*, 2022, 4261-4275.
17. Acay H. Biosynthesis and characterization of silver nanoparticles using fig (*Ficus carica*) leaves: A potential antimicrobial activity. *Appl. Ecol. Environ. Res.*, 2019, 17, 13793-802.
18. Kumkoon T, Srisaisap M, Boonserm, P. Biosynthesized silver nanoparticles using *Morus alba*(white mulberry) leaf extract as potential antibacterial and anticancer agents. *Molecules*, 2023, 28(3),1213. https://doi.org/10.3390/molecules28031213

The Chemist
Journal of the American Institute of Chemists

Synthesis of Phenyl-2-chloropropionate via the Reaction of Phenol with 2-Chloropropionyl Chloride

Abdushukurov Anvar Kabirovich[1], Mamatkulov Nematillo Narzullaevich[2], Ochilov Mansur[3], Akhmedova Kumush Shakhobiddin kizi[4*]

[1]Doctor of Chemistry, Professor, Faculty of Chemistry (abdushukurov-ximik@mail.ru)
[2]Doctor of Chemistry (DSc) Associate Professor, Faculty of Chemistry (nematillomamatqulov767@gmail.com)
[1,2]National University of Uzbekistan named after Mirzo Ulugbek Tashkent, Republic of Uzbekistan
[3]Assistant Lecturer, Almalyk State Technical Institute, Almalyk, Republic of Uzbekistan (mansurochilov2003@gmail.com)
[4]PhD, Almalyk State Technical Institute, Almalyk, Republic of Uzbekistan
**Corresponding author (E-mail: kumushpardaeva98@gmail.com)*
https://orcid.org/0000-0003-1955-4559

Abstract: In this study, it was established for the first time that the reaction of phenol and sodium phenolate with 2-chloropropionyl chloride, conducted at the boiling temperature of benzene, leads to the formation of phenyl-2-chloropropionate as an individual compound. As a result of the reaction of phenol with 2-chloropropionyl chloride in an acetone solution, it was determined that both O-acylation occurs, yielding phenyl-2-chloropropionate, and C-acylation proceeds, resulting in the formation of 4-hydroxyphenyl-2-chloropropionate. The formation of 4-hydroxyphenyl-2-chloropropionate in the reaction was substantiated by theoretical data. During the reaction of phenol with 2-chloropropionyl chloride in the presence of benzene and acetone as solvents, the reaction was carried out at the boiling point of the solvents, and the optimal reaction time was selected, which ensured a high yield of phenyl-2-chloropropionate. The structure of the synthesized phenyl-2-chloropropionate was confirmed by IR spectroscopy, ^{1}H NMR, ^{13}C NMR, and gas chromatography–mass spectrometry (GC-MS). The IR, ^{1}H NMR, ^{13}C NMR, and GC-MS spectra of phenyl-2-chloropropionate were analyzed in detail.

Key Words: Phenol, phenyl-2-chloropropionate, 2-chloropropionyl chloride, ^{1}H NMR, ^{13}C NMR, GC-MS spectra

1. Introduction

At present, the preparation of derivatives of 2-chloropropionyl chloride is one of the new important directions in organic chemistry. 2-Chloropropionyl chloride is an acylating agent, and the compounds it forms with phenol open the way for the synthesis of highly active organic compounds.

It is known that in Friedel–Crafts acylation reactions of aromatic hydrocarbons using chloroacetyl chloride as the acylating agent, solvents such as carbon disulfide, nitromethane, and others are usually employed in the presence of aluminum chloride as a catalyst. Under these reaction conditions, benzene, toluene, naphthalene, c-hydrindacene, fluorene, and fluorenones readily undergo condensation reactions with chloroacetyl chloride [1].

Heterocyclic arenes, phenols, and derivatives of phenols have also been acylated in a similar way [2].

In the chloroacetylation reaction of phenol with aluminum chloride as a catalyst, the hydroxyl group directs substitution to the para-position (equation 1) [3-4].

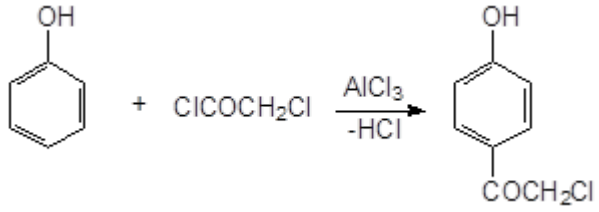

(1)

The acylation reaction of anisole with acetic anhydride has been carried out in the presence of $CoCl_2 \cdot 6H_2O$, $FeCl_3 \cdot 6H_2O$, and $FeCl_3$ catalysts. In the reaction, 1 mol of anisole was reacted with 1.3 mol of acetic anhydride, and 10% catalyst relative to the reagents was used. In addition, 0.5 g of a catalyst prepared from arylalkyl ionic liquids containing various palladate counterions and iron(III) chloride hexahydrate (TAAIL) was employed. The reaction was conducted at 60°C for 24 hours (equation 2) [5].

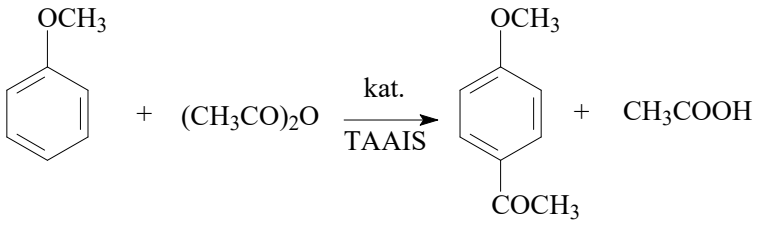

Kat=$CoCl_2 \cdot 6H_2O$, $FeCl_3 \cdot 6H_2O$, $FeCl_3$

(2)

Previously, when anhydrous Lewis acids were used in this reaction, the yield was low. When aqueous catalysts such as $CoCl_2 \cdot 6H_2O$, $FeCl_3 \cdot 6H_2O$, and $FeCl_3$ were used as catalysts, the acylation reaction showed regioselective influence, yielding

pre-dominantly the *para*-isomer. In particular, compared to $FeCl_3$, the use of $FeCl_3 \cdot 6H_2O$ resulted in a higher proportion of the *para*-isomer. In the Friedel–Crafts acylation reaction carried out with 1 mmol of benzene derivatives, 2 equivalents of acetic anhydride, 0.5 g of TAAIL, and 10 mol% $FeCl_3 \cdot 6H_2O$ catalyst at 60°C, 5% of the *ortho*-isomer was obtained (equation 3).

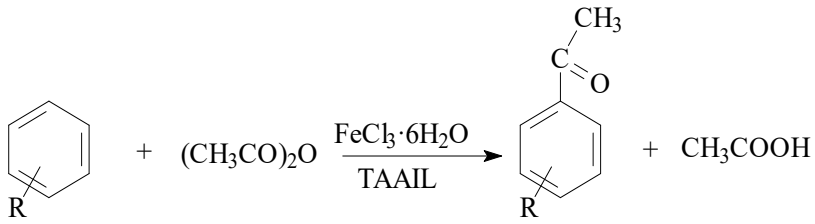

(3)

where R = H, 4 hours, 65%; R = 4-Me, 4 hours, 72%; R = 2,4,6-Me, 4 hours, 83%; R = 2,4,6-OMe, 4 hours, 84%; R = 2,3,5,6-Me, 72 hours, 94%; R = 2,3,5,6-Me, 4 hours, 85% yields were obtained.

The authors reported that when phenol and naphthol were acylated with acetic anhydride in the presence of $ZnCl_2$ and Al_2O_3, the reaction proceeded regio-selectively to yield the ortho-isomer relative to the hydroxyl group (equation 4) [6].

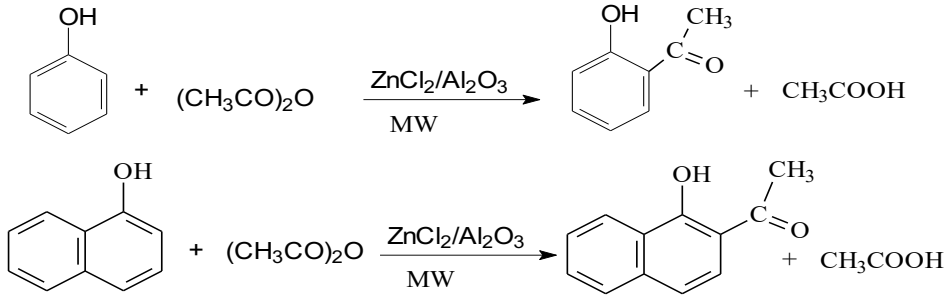

(4)

When compounds containing various substituents on the phenolic ring were subjected to reaction with acetic acid under similar conditions, it was also established that the *ortho*-isomer relative to the hydroxyl group was formed (equation 5).

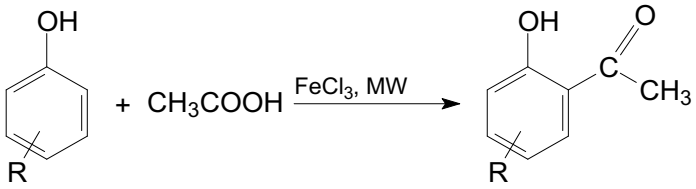

(5)

where R = 2,3-benzo; 3,4-benzo; m-CH_3, p-CH_3, m-OH, p-OH, m-NO_2, o,p-$(CH_3)_2$. All reactions were conducted under solvent-free conditions.

Researchers carried out the reaction of phenol with trifluoromethanesulfonic acid

(TfOH) catalyst in a methyl cyanide solution at room temperature. The reaction proceeded as follows (equation 6) [7]:

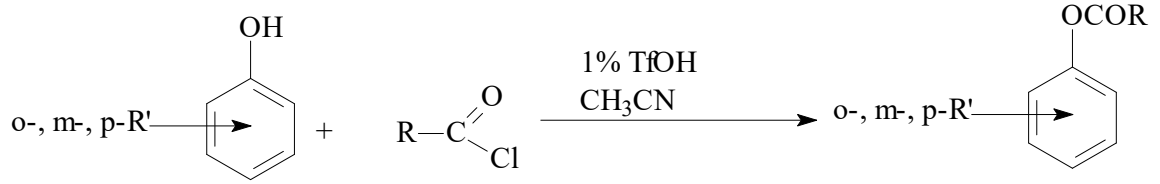

R'=H, o-, m-, p=CH_3; R=CH_3, C_2H_5, n-C_3H_7, n-C_4H_9, n-C_5H_{11}, n-C_6H_{13}, n-C_9H_{19}, C_6H_5 (6)

The authors conducted the reaction of phenol and o-, m-, and p-cresols with 1% TfOH–CH_3CN at room temperature for one hour, successfully obtaining O-acylated products.

The researchers also carried out reactions of phenol, o-cresol, m-cresol, and p-cresol in the presence of concentrated TfOH catalyst, with equimolar amounts of reagents at room temperature, achieving the formation of C-acylated products. The reaction proceeded as follows (equation 7):

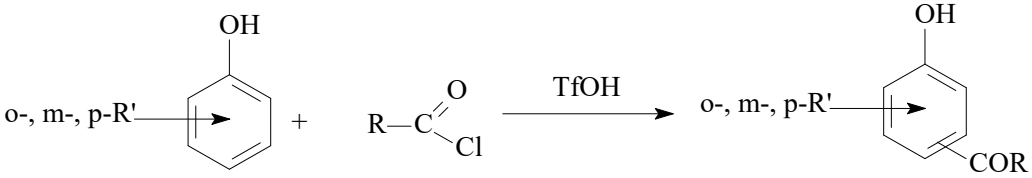

R'=H, o-, m-, p=CH_3; R=CH_3, C_2H_5, n-C_3H_7, n-C_4H_9, n-C_5H_{11}, n-C_6H_{13}, n-C_9H_{19}, C_6H_5 (7)

In this reaction, the acyl group in phenol and o-cresol predominantly attached at the para-position relative to the hydroxyl group, in p-cresol at the ortho-position, and in m-cresol both ortho and para to the hydroxyl group. The relative reactivity of phenol and cresols in the C-acylation reaction was found to be as follows:

Phenol > o-cresol > p-cresol > m-cresol

The chloracetylation reactions of the monomethyl ether of hydroquinone with Lewis acids were found to produce both O- and C-chloracetylated products (equation 8). Favorable reaction conditions were determined.

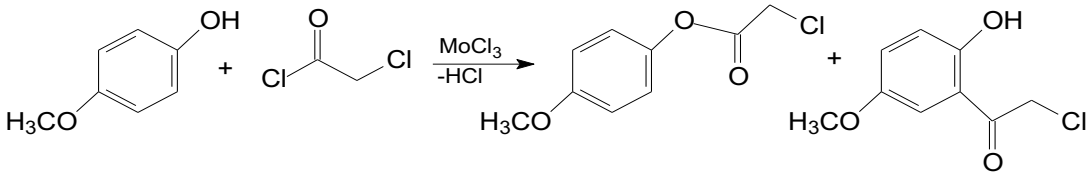

(8)

Experiments showed that when these reactions were conducted without catalysts, but in the presence of solvents, the O-chloracetylated products were obtained in high yields. From the experiments, it was established that these reactions proceed very slowly, over periods of up to 24 hours [8-9].

When thymol was chloracetylated in an organic solvent medium without a catalyst, the reaction proceeded regioselectively to form the corresponding esters (equation 9).

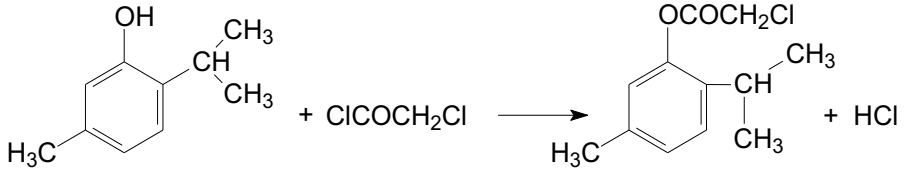

(9)

In particular, when the chloracetylation of thymol was carried out in chloroform, only O-chloracetylation occurred, yielding chloracetylthymol in 95% yield [10].

During the reaction of thymol with chloroacetyl chloride, the electron density in the chloroacetyl chloride molecule shifts toward the electronegative oxygen atom, resulting in the oxygen acquiring a partial negative charge. Due to the influence of the electronegative chlorine and oxygen atoms, the carbon atom acquires a partial positive charge, which interacts with the lone electron pairs of the hydroxyl group in the thymol molecule, allowing the process to proceed further.

One of the most important and widespread types of reactions in organic chemistry is nucleophilic substitution reactions occurring at a saturated carbon atom. It should be noted that the nucleophilic substitution reaction is frequently used in the synthesis of substances. In the science of organic chemistry, nucleophilic substitution reactions at saturated carbon atoms have played a crucial role in the emergence and development of fundamental concepts regarding reaction mechanisms. It is well known that dipolar aprotic solvents (such as DMSO, DMF, TGF, acetone, dioxane) facilitate bimolecular nucleophilic substitution reactions of alkyl halides by solvating the cation in the salt of the carboxylic acid. The reaction of O-chloroacetyl thymol with the disodium salt of oxalic acid in dimethylformamide was proposed to proceed according to the following scheme (equation 10):

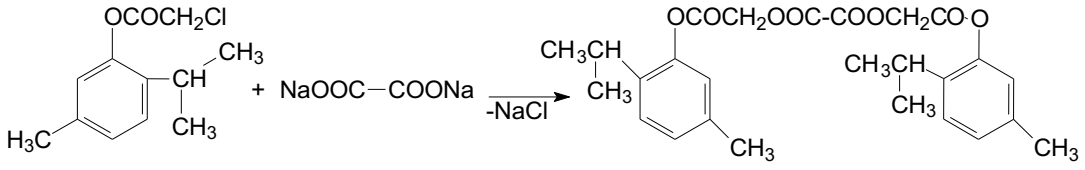

(10)

In order to study the acylation reactions of phenols and their derivatives in greater depth, chloracetylation reactions of dihydric phenols were performed. Since the isomers of dihydroxybenzene possess multiple reactive centers, the reactions were carried out under various conditions [11-12]. When chloroform was used as the solvent, it was established that only the O-chloracetylation product was formed. When hydroquinone

was heated with chloroacetyl chloride in chloroform for 16 hours, bis-1,4-O-chloracetylhydroquinone was obtained. The reaction proceeds according to the following equation (11) [13]:

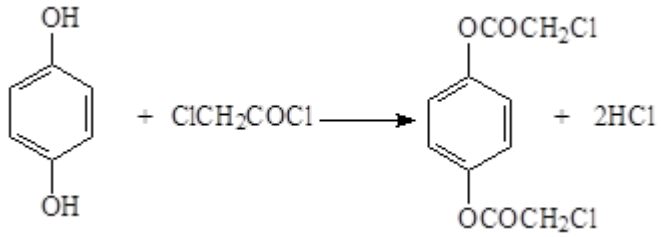

(11)

When the reaction of sodium glycolate with bis-1,4-O-chloracetylhydroquinone was conducted in DMF under 1:1:3 molar ratios, the process lasted 5 hours and yielded the product in 76% yield. It was found that further prolongation of the reaction time and variation in the molar ratio of the reagents did not affect the yield of the product. Therefore, these reaction conditions can be considered optimal. The reaction equation (12) is as follows:

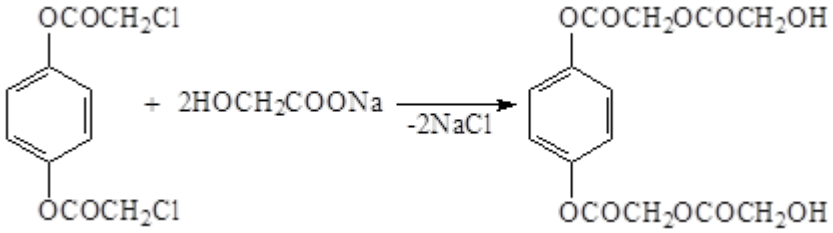

(12)

In this context, the reaction equation and mechanism of para-methoxyphenyl chloroacetate with sodium glycolate in dimethylformamide were also studied. The solvation of sodium cations in DMF facilitates the entry of the $HOCH_2COO^-$ ion into the organic phase and promotes the reaction. The researchers developed a mechanism for the formation of the products of these reactions. From this mechanism, it was determined that dimethylformamide solvates the sodium cation of glycolate, thereby enhancing the reactivity of the glycolate anion [12].

Hydroquinone possesses properties that regulate plant growth. When the chlorine atom attached to the carbon atom adjacent to the ketone group is substituted by another nucleophilic group, its negative effect on plant organisms may be reduced. For this purpose, reactions of dichloroacetylhydroquinone with the sodium salts of phenol, p-methoxyphenol, p-chlorophenol, and β-naphthol were carried out. Based on these studies, the following reactivity series of the nucleophilic reagents was established [14]: p-methoxyphenol < phenol < β-naphthol < p-chlorophenol.

Literature sources have studied the reactions of phenols and isomeric cresols with chloroacetyl chloride [15-16]. However, the chloracetylation reaction of phenol with 2-chloropropionyl chloride has not been investigated. The novelty of this study lies in conducting the chloracetylation reaction of phenol with 2-chloropropionyl chloride to synthesize phenyl-2-chloropropionate. This study aims to synthesize phenyl-2-chloropropionate through the reaction of phenol

with 2-chloropropionyl chloride, and to utilize it as a basis for obtaining novel organic compounds.

2. Methods and Materials

All chemicals and reagents used in this study were of analytical grade purity. Phenol (94.11 g/mol, 99.1%), 2-chloropropionyl chloride (126.97 g/mol, 97%), absolute benzene (78.11 g/mol, 99%), sodium (22.98 g/mol, 97%), calcium chloride (319.85 g/mol, 95%), acetone (58.079 g/mol, 98%), and deionized water (DW) were used for solution preparation and washing procedures.

Synthesis of Phenyl-2-chloropropionate in Benzene Solution

In all experiments, equimolar quantities of reagents were used. The reaction time was determined by the cessation of hydrogen chloride evolution.

Experiment No. 1. Into a round-bottom flask equipped with a reflux condenser, 4.7 g (0.05 mol) of phenol, 6.35 g (0.05 mol) of 2-chloropropionyl chloride, and 30 mL of absolute benzene were added and heated for 10 hours. A hydrogen chloride outlet tube was attached to the upper part of the reaction flask, and the evolved HCl gas was absorbed in water to form hydrochloric acid. The evolution of hydrogen chloride was periodically monitored using litmus paper. To separate unreacted phenol, the reaction product was washed with 10% aqueous alkali and extracted into the benzene layer. The organic layer was then dried over $CaCl_2$. Benzene was removed from the reaction mixture under ambient conditions, and the remaining product was distilled under reduced pressure using a simple distillation apparatus (110–112°C / 10 mm Hg). The yield of phenyl-2-chloropropionate was 3.8 g (42%).

Experiment No. 2. The reaction of 4.7 g (0.05 mol) of phenol with 6.35 g (0.05 mol) of 2-chloropropionyl chloride in 30 ml of absolute benzene was carried out over 12 hours. The yield of phenyl-2-chloropropionate was 5 g (54%).

Experiment No. 3. The reaction of 4.7 g (0.05 mol) of phenol with 6.35 g (0.05 mol) of 2-chloropropionyl chloride in 30 ml of absolute benzene was carried out over 15 hours. The yield of phenyl-2-chloropropionate was 5.9 g (64%).

Preparation of Phenyl-2-chloropropionate from Sodium Phenolate and 2-Chloropropionyl Chloride in Benzene Solution

Experiment No. 1. In a round-bottom flask equipped with a reflux condenser, 4.7 g (0.05 mol) of phenol was placed and dissolved in absolute benzene. Cleaned

sodium metal (free from oxide film) was gradually added to the solution. To form sodium phenolate, the reaction mixture was further heated for 2 hours. Next, 6.35 g (0.05 mol) of 2-chloropropionyl chloride was added, and the mixture was heated for 4 hours. As a result of the reaction, a white precipitate of sodium chloride formed, and its quantity began to increase. The reaction product was washed with 10% aqueous alkali and extracted into benzene solution. It was then dried over $CaCl_2$. Benzene was removed from the reaction mixture under ambient conditions, and the remaining product was distilled under vacuum (110–112°C / 10 mm Hg) using a simple distillation apparatus. The yield of phenyl-2-chloropropionate was 4.7 g (51%).

Experiment No. 2. In absolute benzene solution, 4.7 g (0.05 mol) of phenol was reacted with 1.15 g (0.05 mol) of sodium to synthesize sodium phenolate. To this, 6.35 g (0.05 mol) of 2-chloropropionyl chloride was added, and the reaction was conducted over 5 hours. The yield of phenyl-2-chloropropionate was 5.3 g (58%).

Experiment No. 3. In absolute benzene solution, 4.7 g (0.05 mol) of phenol was reacted with 1.15 g (0.05 mol) of sodium to synthesize sodium phenolate. To this, 6.35 g (0.05 mol) of 2-chloropropionyl chloride was added, and the reaction was conducted over 6 hours. The yield of phenyl-2-chloropropionate was 6.6 g (72%).

Synthesis of Phenyl-2-chloropropionate in Acetone Solution

Experiment No. 1. In a round-bottom flask fitted with a reflux condenser, 4.7 g (0.05 mol) of phenol, 6.35 g (0.05 mol) of 2-chloropropionyl chloride, and 25 ml of acetone were added and heated for 7 hours. A hydrogen chloride outlet tube was attached to the upper part of the reaction flask. The evolution of hydrogen chloride was periodically monitored using litmus paper. After the reaction, acetone was first removed under ambient conditions. The reaction product was then washed with 10% aqueous alkali, extracted into benzene, and dried over $CaCl_2$. Benzene was removed under ambient conditions, and the remaining product was distilled under vacuum (110–112°C / 10 mm Hg) using a simple distillation apparatus. The yield of phenyl-2-chloropropionate was 4.1 g (45%).

Experiment No. 2. In an appropriately equipped reaction apparatus, 4.7 g (0.05 mol) of phenol, 6.35 g (0.05 mol) of 2-chloropropionyl chloride, and 25 ml of acetone were added and heated for 9 hours. When the evolution of hydrogen chloride ceased, the process was stopped. After the acetone was removed, the reaction product was washed with water and extracted into benzene. The yield of phenyl-2-chloropropionate was 4.8 g (53%).

Experiment No. 3. In an appropriately equipped reaction apparatus, 4.7 g (0.05 mol) of phenol, 6.35 g (0.05 mol) of 2-chloropropionyl chloride, and 25 ml of acetone were added and heated for 12 hours. When the evolution of hydrogen chloride ceased, the process was stopped. After the acetone was removed, the reaction product was washed with water and extracted into benzene. The yield of phenyl-2-chloropropionate was 5.7 g (62%).

Since this study was specifically focused on the synthesis of phenyl-2-chloropropionate,

the reactions were not carried out at a single fixed temperature and time. Instead, the processes were conducted at the boiling temperatures of the respective solvents. The reaction time was determined and monitored using the Beilstein test. For this reason, the influence of variations in these parameters on product yield was not discussed in the manuscript.

To separate the main product, phenyl-2-chloropropionate, from possible impurities, washing with alkaline water followed by vacuum distillation was applied.

Characterization of Phenyl-2-chloropropionate Obtained Under Various Conditions by IR, ^{1}H NMR, and ^{13}C NMR Spectroscopy

IR spectra were recorded on a Bruker INVENIO X spectrometer in accordance with ASTM E573. ^{1}H NMR spectra were recorded in $CDCl_3$ on a Unity+400 (Varian) instrument operating at 400 MHz. HMDS was used as an internal standard in the ^{1}H NMR spectra. In the ^{13}C NMR spectra, the chemical shift of the solvent was used as the internal standard.

Gas chromatography–mass spectrometry (GC-MS) was carried out using a GC 8890 GC module coupled with a 5977 MSD detector (Agilent, USA). A 5HP-MS capillary column with polar stationary phase (30 m × 0.25 mm × 0.3 µm) was used under the following conditions: Injector temperature: 280°C, Carrier gas: H_2, 1 ml/min, Thermostat program: Initial 60°C (hold 1 min), ramp 10°C/min to 180°C, then 6°C/min to 230°C (hold 5 min), Detector temperature: 250°C, Ionization by electron impact at 70 eV; MS recording started after 4 minutes (time corresponding to the solvent peak), m/z range: 10–500.

To identify the composition of the product formed by the reaction of phenol with 2-chloropropionyl chloride, thin-layer chromatography (TLC) was performed. In a hexane–ethyl acetate system at a 6:2 volume ratio on Silufol UV-254 plates, a single spot with Rf = 0.42 was observed. This compound was identified as phenyl-2-chloropropionate.

3. Results and Discussion

The synthesized phenyl-2-chloropropionate is a colorless liquid with a pleasant odor. Its boiling point is 110–112°C at 10 mm Hg. In a hexane–ethyl acetate system at a 6:2 volume ratio on Silifol UV-254, it shows an Rf value of 0.42. The refractive index nD20 was determined to be 1.5012. The electrical conductivity was measured at 1.383 (unit).

The reaction of phenol with 2-chloropropionyl chloride was conducted under various conditions. Initially, sodium metal was gradually added to phenol dissolved in absolute benzene. After sodium phenolate had formed, 2-chloropropionyl chloride was added gradually. During the reaction, the sodium phenolate salt dissolved, and the reaction was completed. The reaction scheme (equation 13) can be depicted as follows:

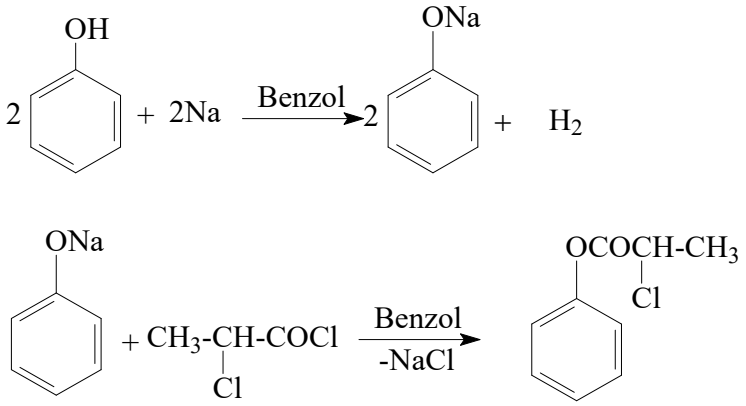

(13)

To investigate how the reaction between phenol and 2-chloropropionyl chloride proceeds in aprotic solvents and what products are formed, reactions were carried out in acetone solution. The product obtained from the reaction was analyzed. When an aqueous solution of $FeCl_3$ was added to the product, a violet coloration characteristic of the hydroxyl group was observed. Analysis of the product by thin-layer chromatography (TLC) revealed the presence of two spots.

The reaction thus proceeds via O-acylation to form phenyl-2-chloropropionate, and theoretically via C-acylation to form 4-hydroxyphenyl-2-chloropropionate (equation 14).

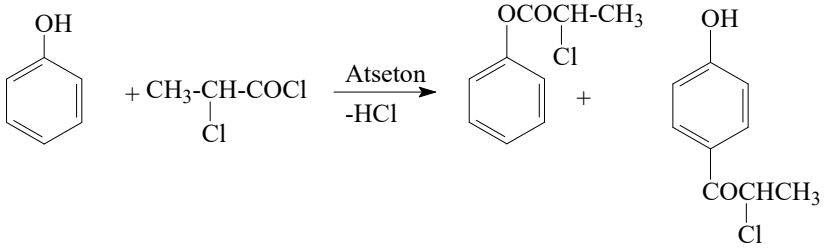

(14)

When acetone was used as the solvent, the C-acylated compound 4-hydroxyphenyl-2-chloropropionate was formed, and the reaction product yield was also higher. This can be explained by the formation of a relatively bulky and stable (I) complex under the reaction conditions, which promotes the formation of 4-hydroxyphenyl-2-chloropropionate (Figure 1):

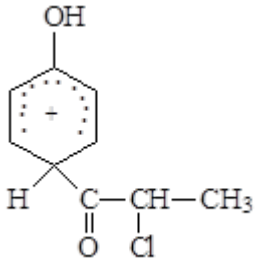

Figure 1. σ-Complex of 4-(2-chloropropionyl)phenol.

The absence of acyl group substitution at the ortho position in the phenol chloracetylation reaction can be explained as follows:

1) Because 2-chloropropionyl chloride is bulky, steric hindrance prevents the reaction at the ortho position.

2) The chloropropionyl cation (electrophile) formed in the complex with 2-chloropropionyl chloride is unstable due to mesomeric effects, resulting in high selectivity (equation 15):

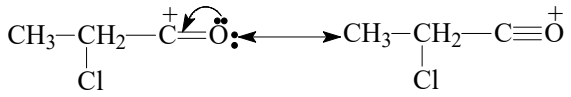

(15)

Therefore, the most favorable and stable para-isomer is formed in the reaction.

3) Considering the charge distribution in the π-complex formed during electrophilic substitution on the aromatic ring, the –OH group in the phenol nucleus directs the acyl group to the para position, where it exerts a greater influence on the complex, resulting in the formation of p-hydroxyphenacyl chloride (Figure 2) [17].

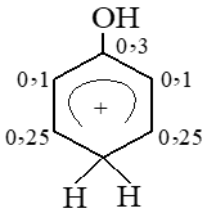

Figure 2. σ-Complex of phenol.

The selectivity of the acyl group and the directing influence of I-type substituents in the aromatic ring toward the para position are known from the literature [18-19].

The reaction of phenol with 2-chloro-propionyl chloride was carried out under various conditions in benzene and acetone solutions. When phenol was reacted with 2-chloropropionyl chloride in benzene solution, the reaction proceeded as follows (equation 16):

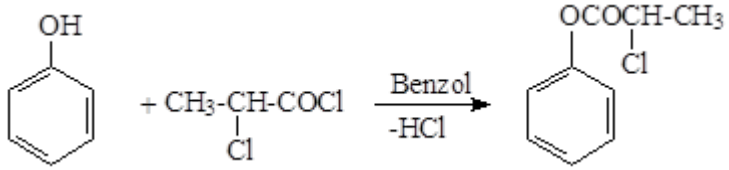

(16)

To determine the composition of the chloropropionylation product of phenol with 2-chloropropionyl chloride, thin-layer chromatography (TLC) was conducted. In a hexane–ethyl acetate system (6:2 by volume) on Silifol UV-254, the product displayed a single spot with an Rf value of 0.42.

The reaction product was subjected to physicochemical analysis. From IR, ^{1}H NMR, ^{13}C NMR, and gas chromatography–mass spectrometry, the structure of phenyl-2-chloropropionate was confirmed. In the analysis of the IR, ^{1}H NMR, ^{13}C NMR, and chromatographic mass spectra of phenyl-2-chloropropionate, literature sources were consulted [20–23].

The infrared (IR) spectrum of phenyl-2-chloropropionate was recorded in the range of 4000–400 cm^{-1} using the ATR (Attenuated Total Reflectance) method. The main absorption bands identified in the spectrum confirm the presence of functional groups in the compound.

A strong absorption band observed at 1756 cm^{-1} corresponds to the stretching vibration of the carbonyl (C=O) group in the ester moiety, indicating that the substance is in the ester form. The band at 1596 cm^{-1} corresponds to the stretching vibration of C=C bonds in the aromatic ring. The bands at 1068, 1143, 1191, and 1239 cm^{-1} are attributable to C–O–C stretching vibrations, further confirming the presence of ester functional groups. The absorptions at 2985 cm^{-1} and 3062 cm^{-1} are interpreted as stretching vibrations of =C–H bonds in the aromatic ring. The signal at 688 cm^{-1} corresponds to the deformation vibration of C–H bonds in a mono-substituted benzene ring. The absorption at 1488 cm^{-1} is related to the asymmetric deformation vibration of a methyl ($–CH_3$) group. The absorption observed at 750 cm^{-1} corresponds to the C–Cl stretching vibration, confirming the presence of chlorine atoms in the compound.

Furthermore, the absence of a broad absorption band in the 3200–3600 cm^{-1} region, which is characteristic of hydroxyl (O–H) groups, indicates that the compound has transitioned from an acidic to an ester form (Figure 3). Overall, the obtained IR spectrum fully corresponds to the proposed structure of phenyl-2-chloropropionate.

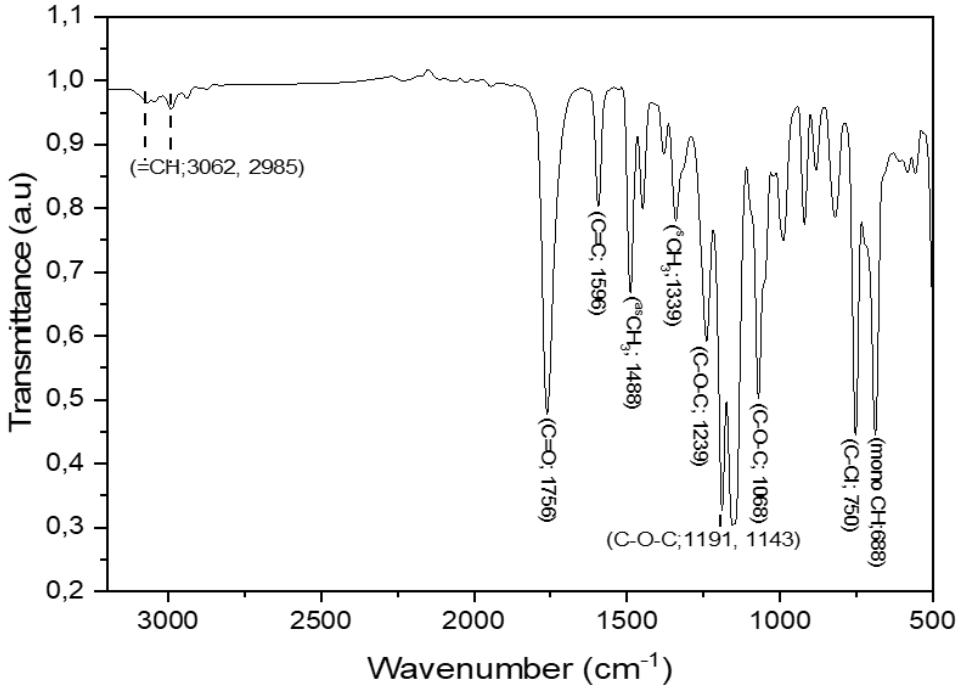

Figure 3. IR Spectrum of Phenyl-2-chloropropionate

The ^{1}H NMR spectrum of phenyl-2-chloropropionate was recorded in $CDCl_3$ solution at 600 MHz using a Unity+600 (Varian) spectrometer (Figure 4).

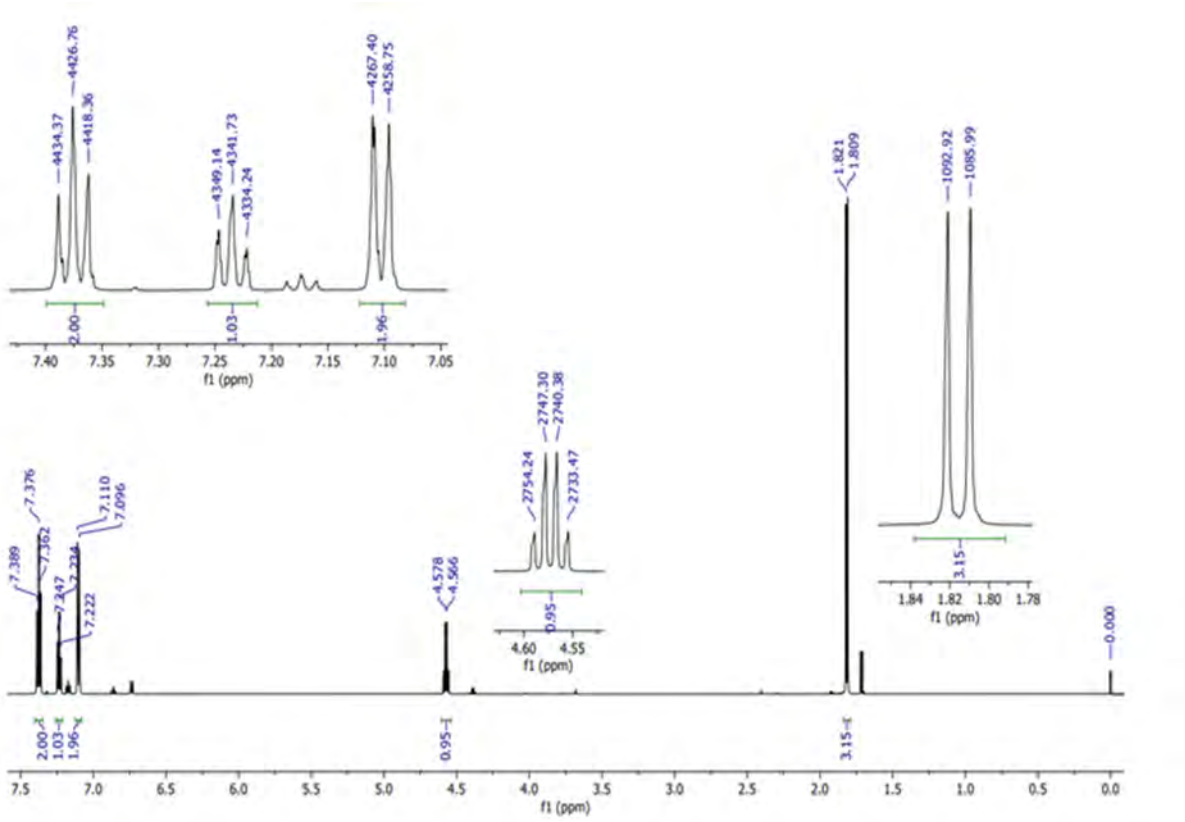

Figure 4. ^{1}H NMR Spectrum of Phenyl-2-chloropropionate

The following proton signals were identified in the obtained spectrum: A singlet at 1.75 ppm corresponding to the protons of the $-CH_3$ (methyl) group. Another singlet at 4.50 ppm corresponding to the protons of the CH_2 group adjacent to the carbonyl (C=O) group and chlorine atom. The relatively high chemical shift value of this signal is due to the influence of the electronegative atoms (Cl and C=O). A set of multiplet signals in the range of 7.05–7.40 ppm, characteristic of aromatic ring protons, confirming the presence of the phenyl ring.

All observed signals and chemical shift values in the ^{1}H NMR spectrum fully match the proposed structure of phenyl-2-chloropropionate. In particular, the presence and order of individual signals for CH_3, CH_2, and aromatic protons serve as reliable confirmation of the compound's structure.

The ^{13}C NMR spectrum of phenyl-2-chloropropionate is shown in Figure 5.

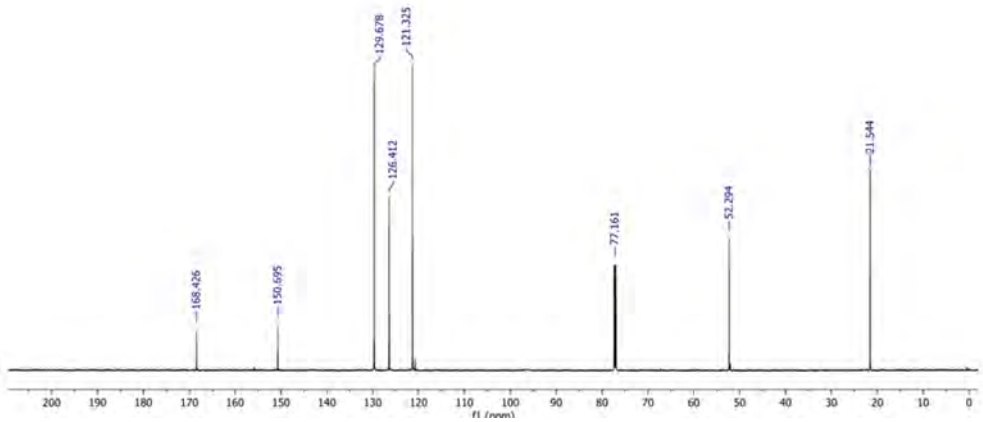

Figure 5. ^{13}C NMR Spectrum of Phenyl-2-chloropropionate

The ^{13}C NMR spectrum of phenyl-2-chloropropionate showed ten characteristic peaks corresponding to the carbon atoms.

The singlet peaks at 21.54, 52.29, 121.32, 126.41, 129.67, 150.69, and 168.42 ppm are attributed to carbons of the phenyl-2-chloropropionate molecule, confirming its structure. The singlet at 77.16 ppm corresponds to the chloroform solvent.

Upon injection of phenyl-2-chloropropionate into the GC–MS instrument under the specified conditions, a molecular ion with m/z = 184 was detected at a retention time of 5.396 minutes.

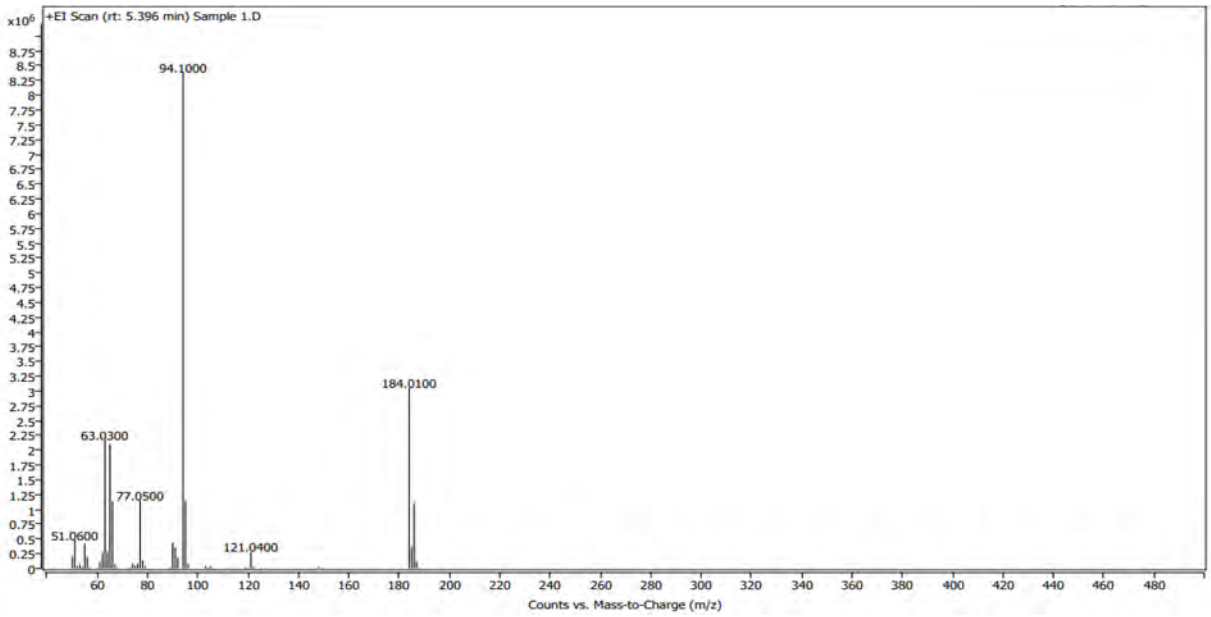

Figure 6. Fragmentation Scheme of the Molecular Ion of Phenyl-2-chloropropionate in GC–MS

As shown in Figure 6, the fragmentation pattern of the molecular ion of phenyl-2-chloropropionate is presented. Additionally, fragment ions were identified at m/z = 184.0, m/z = 121, m/z = 94.1, m/z = 77.0, m/z = 63.0, and m/z = 51.0.

From the molecular ion of phenyl-2-chloropropionate, an ethyl chloride cation with m/z = 63 is released in the first fragmentation pathway. In the second pathway, a phenoxycarbonyl cation with m/z = 121 is produced.

From this fragment cation, carbon monoxide elimination results in the formation of a phenoxy cation with m/z = 93. In the next stage, elimination of an oxygen radical from the m/z = 93 ion produces an m/z = 77 fragment. Finally, elimination of an acetylene molecule yields the fragment cation with m/z = 51, completing the fragmentation process. The formation of fragment ions from phenyl-2-chloro-propionate was observed as shown in equation 17.

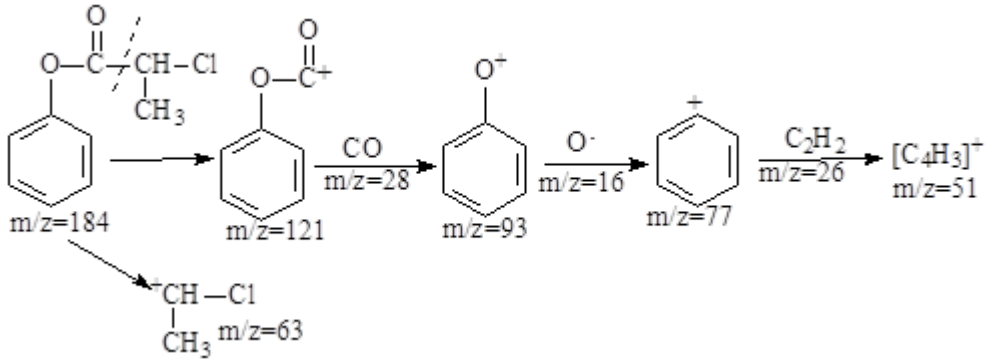

(17)

4. Conclusion

For the first time, we conducted the reaction of phenol with 2-chloropropionyl chloride and synthesized phenyl-2-chloropropionate, which opened a new direction in the chlor-acetylation reactions of aromatic hydro-carbons. During the experiments, equimolar amounts of phenol and 2-chloropropionyl chloride were used. The reactions were carried out both by directly reacting phenol with 2-chloropropionyl chloride in benzene solution and by first preparing sodium phenolate. In the direct reaction conducted in benzene solution by heating for 10–15 hours, the product yields ranged from 42% to 64%. When sodium phenolate was pre-pared in benzene and then reacted, the yield significantly increased, reaching up to 72%. Reactions conducted in acetone as solvent under heating for 7–12 hours resulted in yields of about 45–62%. The experimental results showed that when benzene and acetone were used as solvents, benzene facilitated the reaction more efficiently.

Infrared (IR) spectral analyses confirmed the presence of the ester group in the phenyl-2-chloropropionate molecule (strong C=O absorption at 1756 cm^{-1}), as well as signals characteristic of the aromatic ring and C–Cl bond.

In the ^{1}H Nuclear Magnetic Resonance (NMR) spectrum, the following were identified: a singlet corresponding to the methyl group (1.75 ppm), a singlet corresponding to the CH_2 protons located near the chlorine and carbonyl groups (4.50 ppm), and multiplets corresponding to the aromatic ring protons (7.05–7.40 ppm).

In the ^{13}C NMR spectrum, ten signals corresponding to the carbon atoms were detected, confirming the compound's structure.

GC–MS analysis revealed a molecular ion (m/z=184) and sequential fragmentation pathways, resulting in fragment ions at m/z=121, 94, 77, 63, and 51.

The studies determined that reactions conducted in acetone also produced the C-acylated compound, 4-hydroxyphenyl-2-chloropropionate. This C-acylation reaction was explained by the formation of a moderately bulky and stable complex. Additionally, the absence of acylation at the ortho position was attributed to the large size of the 2-chloropropionyl chloride and steric hindrance. The –OH group in the phenol nucleus directing acylation to the para position corresponds to the selectivity reported in the literature.

5. Acknowledgments

We express our gratitude to the Faculty of Chemistry, Mirzo Ulugbek National University of Uzbekistan and Almalyk State Technical Institute for their support in conducting this work.

6. Funding Sources

This research did not receive any specific grant from funding agencies in the public, commercial, or not-for-profit sectors.

7. References

1. Shivakumara KN. Review on Friedel-Crafts acylation of benzene derivatives using various catalytic systems. *Int. J. Adv. Chem. Res.*, 2021, 3(1), 25-31. DOI: 10.33545/26646781.2021.v3.i1a.32
2. Vekariya RL. A review of ionic liquids: Applications towards catalytic organic transformations. *J. Mol. Liq.*, 2016, 36-38. https://doi.org/10.1016/j.molliq.2016.11.123
3. de Souza ROMA, Miranda LSM, Bornscheuer UT. A retrosynthesis approach for biocatalysis in organic synthesis. *Chem. – Eur. J.*, 2017, 23, 12040-12063. https://doi.org/10.1002/chem.201702235
4. Tamilselvan P, Basavaraju B, Murugesan R, Sampathkumar E. Cobalt(II) acetylacetonate catalyzed Friedel-Crafts acylation of anisole, thioanisole, and toluene. *Catal.*

Commun., 2008, 10(3), 300-303. https://www.researchgate.net/publication/229232684/ DOI: 10.1016/j.catcom.2008.09.025
5. Lerch S, Fritsch S, Strassner T. Friedel–Crafts acylation of benzene derivatives in tunable aryl alkyl ionic liquids (TAAILs). *Beilstein J. Org. Chem.*, 2023, 19, 212-216. https://doi.org/10.3762/bjoc.19.20
6. Naeimi. H, Amini A, Moradian M**.** Regioselective direct *ortho* C-acylation of phenol and naphthol derivatives catalyzed by modified $ZnCl_2$ on Al_2O_3 as catalyst under solvent-free and microwave conditions. *Org. Chem. Front.*, 2014, 1, 415-421. https://pubs.rsc.org/en/content/articlelanding/2014/qo/c4qo00031e
7. Murashige R, Hayashi Y, Ohmori S, Torii A, Aizu Y, Muto Y, Murai Y, Oda Y, Hashimoto M. Comparisons of O-acylation and Friedel-Crafts acylation of phenols and acyl chlorides and Fries rearrangement of phenyl esters in trifluoromethanesulfonic acid: Effective synthesis of optically active homotyrosines. *Tetrahedron*, 2011, 67(3), 641-649. DOI: 10.1016/j.tet.2010.11.047
8. Khurmamatov AM, Akhmedova KS, Sidikov GO, Xudoyberganov AA. Waste tire-based pyrolysis for synthetic fuel and study of its properties. *Nafta-Gaz*, 2025, 6, 389-396. DOI: 10.18668/NG.2025.06.03
9. Sadikova SB, Abdushukurov AK, Choriev AU. Chloroacetylation of hydroquinone and its esters with Lewis acids. *Univers.: Chem. Biol.*, 2019, 5(59), 52-55.
10. Choriev A, Abdushukurov A, Jurayev R, Juraeva M. Synthesis of the di(2-iz di(2-izopropyl-5-methylphenylkarbok-simethylen) oxalate. *Chem. Chem. Eng.*, 2024, 2023(1), 33-38. https://doi.org/10.70189/1992-9498.1579
11. Roswanda R, Sirampun AD, Mukti R. A straightforward selective acylation of phenols over ZSM-5 towards making paracetamol precursors. *Bull. Chem. React. Eng. Catal.*, 2018, 13(3), 472-487. DOI: 10.9767/bcrec.13.3.2856.573-587
12. Liao W-J, Lin S-Y, Kuo Y-S. Site-selective acylation of phenols mediated by a thioacid surrogate through sodium thiosulfate catalysis. *Org. Lett.*, 2022, 24(23), 4207-4211. DOI: 10.1021/acs.orglett.2c01467
13. Choriev AU, Berdimurodov ET, Toshpulatov TI, Sadikova SB. Synthesis of 1,4-phenylene dicarb-oxymethylene glycolate. *Univers: Chem. Biol.*, 2020, 5(71), 54-58. https://7universum.com/ru/nature/archive/item/9303
14. Savinova AA, Falynskova NP. Phenols in the structure of biologically active substances. *Symb. Sci.*, 2020, 11, 20-25. https://cyberleninka.ru/article/n/fenoly-v-strukture-biologicheski-aktivnyh-veschestv/viewer
15. Mamatkulov NN, Abdushukurov AK, Ochilov M. Synthesis of phenyl-2-methylphenoxyacetate via nucleophilic substitution reaction of phenyl-chloro-acetate with 2-Methylphenol. *NamSU Sci. Bull., Namangan*, 2024, 11, 227–231.
16. Mamatkulov NN, Xatamova DM. Method for synthesizing m-tolyl-4-methylphenoxyacetate based on m-tolylchloroacetate. *FarSU Sci. Bull., Fergana*, 2024, 6, 8-13.
17. Chaudhury R in Gateway to Condensed Matter Physics and Molecular Bio-physics: Concepts and Theoretical Perspectives, Apple Academic Press, 2021, p 196.
18. Nasreen A. Efficient and regioselective

acetylation of benzene derivatives with Ac_2O in the presence of mercury tetrathiocyanatocobaltate (II). *Org. Commun.*, 2023, 16(2), 108-116.
19. Rasulov CK, Heydarli GZ, Gasanova GD, Gurbanova SS. Acylation of phenols with acetic acid and its anhydride (mini-review). Bulletin of Tula State University. *Nat. Sci.*, 2023, 4, 18-27.
20. Smirnova NN in Infrared Spectroscopy in the Chemistry of High-molecular Compounds, eds. NN Smirnova, VY Chukhlanov, Vladimir State University named after AG and NG Stoletovs, Vladimir: Publishing House of VlSU, 2021, p 84.
21. Khurmamatov AM, Akhmedova KS. Waste tires based pyrolysis for synthetic fuel and studying its properties. *Chem. Pap.*, 2025, 79, 3883-3893. https://doi.org/10.1007/s11696-025-04041-4
22. Grinenko EV, Fedulina TG, Vasiliev AV in Physicochemical Methods for Analyzing Organic Compounds (Ultraviolet Spectroscopy, Infrared Spectroscopy, Mass Spectrometry, Nuclear Magnetic Resonance Spectroscopy), St. Petersburg, 2018, p 102.
23. Lebedev AT in Mass Spectrometry for Analyzing Environmental Objects, Tekhnosfera, Moscow, 2013, p 632.

The Chemist
Journal of the American Institute of Chemists

Crosslinked Alginate–Acrylic Acid–PVA Hydrogel for Efficient Trypan Blue Removal: Swelling Behavior, Adsorption Isotherms, and Regeneration Performance

Haider Ali Dhaher[1], Aseel M Aljeboree*[2], Khawla K. Jasim[3]

[1,3]Department of Chemistry, College of Sciences, University of Al-Muthanna, Al-Samawah, Iraq
[2]Department of Chemistry, College of Sciences for Girls, University of Babylon, Hilla, Iraq
**Corresponding author (E-mail: annenayad@gmail.com)*

Abstract: In this study, a cross-linked sodium alginate-graft-poly(acrylic acid-co-polyvinyl alcohol) (SA-g-poly(AAC-co-PVA)) hydrogel was successfully prepared through free-radical polymerization and evaluated for its ability to remove Trypan Blue (TB) dye from aqueous media. The samples were characterized using Fourier Transform Infrared Spectroscopy (FTIR), Thermogravimetric Analysis (TGA), X-ray Diffraction (XRD), Transmission Electron Microscopy (TEM), and Field Emission Scanning Electron Microscopy (FESEM). They confirmed the formation of a porous hydrogel network with a predominantly amorphous structure and adequate thermal stability. The adsorption performance was systematically examined under different operational conditions, including the effect of a 200 mg L^{-1} dye concentration on the adsorption of 0.07g of hydrogel at pH 7 and 30°C. The results showed a clear dependence on solution pH, where acidic environments favored dye uptake due to reduced electrostatic repulsion between the anionic dye molecules and the protonated hydrogel surface. A pronounced decline in both removal efficiency (E%) and adsorption capacity (Qe) was observed with increasing pH solution. At pH 3, the hydrogel exhibited excellent adsorption performance, achieving an E of 96% and a Qe of 480 mg g^{-1}. However, when the pH was increased to 11, these values dropped significantly to 41% and 210 mg g^{-1}, respectively, indicating that acidic conditions strongly favor the adsorption process. Increasing the adsorbent dosage increased overall removal efficiency, although a decrease in adsorption capacity per unit mass was observed. Increasing the hydrogel mass from 0.01 g to 0.10 g increased E% from ~50% to ~97%, whereas Qe decreased from ~1500 mg g^{-1} to ~300 mg g^{-1}. The adsorption process proceeded rapidly, achieving an equilibrium capacity of approximately 350 mg g^{-1} within 25 min and reaching about 410 mg g^{-1} at longer contact times. Analysis of equilibrium data revealed that the Freundlich isotherm model provided a better fit (R^2 = 0.9883), indicating multilayer adsorption on heterogeneous sites within the grafted polymer network. Regeneration experiments demonstrated that the hydrogel retained nearly 60% of its initial removal efficiency after five consecutive adsorption–desorption cycles, highlighting its potential for

repeated use. Overall, the prepared hydrogel shows promise as an effective, reusable adsorbent for removing Trypan Blue from wastewater.

Key Words: Polymer composite**,** trypan blue dye**,** adsorption**,** wastewater treatment**,** regeneration

1. Introduction

Water contaminated with dyes requires treatment to remove them using various adsorbents or techniques prior to discharge into local drainage systems or natural water bodies. Dyes are employed across numerous industries, including textiles, cosmetics, ink, plastics, paper, food, pharmaceuticals, pulp, leather, printing, paints, and rubber, owing to their high solubility in water and capacity to impart intense color [1-3]. Trypan blue (TB) is a water-soluble azo dye, classified as an anionic acidic dye, with a molar mass of 960.81 g/mol and a chemical formula of ($C_{34}H_{24}N_6Na_4O_{14}S_4$). It is used in biological staining, vitreoretinal surgery, cell viability assessment, and food coloring processes. However, Trypan Blue (TB) is cytotoxic to cells. Empirical studies have demonstrated that exposure of human retinal pigment epithelial cells (ARPE-19) to TB *in vitro* induces cellular toxicity and reduced viability, with the severity of these effects contingent on the dye concentration and exposure duration. Furthermore, elevated TB concentrations pose a threat to aquatic organisms and the environment. The discharge of untreated water contaminated with this dye can adversely affect natural water bodies, disrupt aquatic ecosystems, and pose significant risks to human and environmental health [4-6].

The release of untreated water contaminated with this dye can adversely affect natural water resources, disrupt aquatic ecosystems, and pose significant health risks to humans, including toxicity and carcinogenicity. To protect the environment from contamination, it is imperative to eliminate TB discharges from various industries in water sources. The issue of dye pollution in water has led to the development of numerous water treatment methods, including advanced oxidation processes, ion exchange, deep eutectic solvents, coagulation-flocculation, adsorption, electrocoagulation, wet oxidation, sedimentation, arc discharge, membrane bioreactors, phytoremediation, reverse osmosis, sequencing batch reactors, and membrane filtration. Among these, adsorption is recognized as one of the most commonly employed treatment techniques because of its cost-effectiveness, simplicity, high efficiency, and environmental compatibility. Various adsorbents, such as clay, hydrogels, activated carbon, and graphene oxide, have been utilized [7,8].

Hydrogels, also known as superabsorbent polymers, are considered innovative materials due to their versatility and Biocompatibility. They consist of three-dimensional cross-linked polymer networks that are water-soluble but swell upon contact with water, enabling them to absorb water and biological fluids without compromising their structural integrity. This absorption capability is attributed to the presence of hydrophilic groups, such as (–OH, – CONH, $–CONH_2$, –COOH, and $-SO_3H$) in the polymer chain [9,10]. These hydrogels can absorb additional biological fluids, and their expanded state allows them to retain substantial amounts of fluid. They have garnered significant attention for their

applications in biomedical, environmental, energy, and engineering fields due to their enhanced water absorption and Biocompatibility. Despite the development of various types of hydrogels, there remains a need for non-toxic, eco-friendly hydrogels that can be easily prepared with the desired properties [11-13].

Many inorganic clay minerals, such as kaolin, bentonite, and attapulgite, along with natural polymeric materials, including polysaccharides (sodium alginate, starch, cellulose, and chitosan), have been employed to develop eco-friendly organic–inorganic superabsorbent composites to reduce production costs and enhance performance. Sodium alginate (SA), an anionic polysaccharide derived from brown seaweed, has been extensively investigated because of its non-toxic nature, biodegradability, and ability to form gels in the presence of divalent cations such as Ca^{2+}. SA is renowned for its exceptional film-forming and gelation properties, rendering it widely utilized in biomedicine, food packaging, and environmental remediation [14,15].

Acrylic acid (AA), a synthetic monomer bearing a carboxylic acid group, is commonly used in hydrogel production due to its ability to impart significant hydrophilicity to the gel. When copolymerized with natural polymers, such as sodium alginate, it enhances mechanical strength and water-absorption capacity while improving the hydrogel's surface characteristics [16,17]. The resulting hybrid or composite hydrogels integrate the advantages of both natural and synthetic materials, making them popular for applications such as drug delivery, wound dressing, biosensing, agriculture, and wastewater treatment. Recently, SA/AA hydrogels have demonstrated considerable potential as effective adsorbents for removing organic dyes and heavy metals from contaminated water, particularly when modified with nanoparticles or other functional fillers to enhance their adsorption capacity and durability [18]. This study aims to develop and evaluate a SA/AA hydrogel for the efficient adsorption and regeneration-based removal of trypan blue dye from aqueous solutions. The research focuses on the hydrogel's structural properties and its performance across multiple cycles.

2. Experimental Part

Materials

Sodium alginate (SA, purity 99%) was used as the main biopolymer backbone, and acrylic acid (AA, purity 98%) was employed as the grafting monomer. Poly(vinyl alcohol) (PVA, ≥99% purity) was used as a hydrophilic polymer to enhance the mechanical stability of the hydrogel network. Potassium per sulfate (KPS, purity 97%) was used as a free-radical initiator, and N, N′-methylene bisacrylamide (MBA, purity 99%) was used as a cross-linking agent. Trypan Blue (TB) dye was selected as the model anionic dye for the adsorption experiments. Hydrochloric acid (HCl) and sodium hydroxide (NaOH) solutions were used to adjust the pH of the samples. All chemicals were of analytical grade, purchased from Sigma-Aldrich, and used as received without further purification. Deionized water was used in all experiments.

Preparation of SA-g-poly(AAC-co-PVA) Hydrogel

The hydrogel was synthesized via free-radical polymerization using sodium alginate (SA), acrylic acid (AA), and poly(vinyl alcohol) (PVA) as monomeric components. Initially, a 2 wt% SA solution was prepared by dissolving 0.50 g of sodium alginate in 20 mL of deionized water under magnetic stirring at 60°C until complete homogenization. In parallel, 0.50 g of PVA was dissolved in 30 mL of deionized water at 80°C to obtain a clear polymer solution, which was subsequently cooled to room temperature. The PVA solution was then combined with the SA solution to form a blended biopolymeric matrix. Separately, the monomer mixture was prepared by diluting 10 mL of acrylic acid (AA; 0.14 mol) with 3 mL of deionized water, followed by the addition of potassium persulfate (KPS; 0.05 g, 0.18 mmol) as the radical initiator and N,N′-methylene bisacrylamide (MBA; 0.05 g, 0.32 mmol) as the covalent cross-linker. This mixture was stirred for 30 min to ensure uniformity. The SA/PVA blend was gradually added to the AA/KPS/MBA solution under continuous stirring to ensure complete dispersion of all components. The final precursor mixture was cast into Petri dishes and thermally polymerized at 60°C for 1–2 h, forming a cross-linked three-dimenional hydrogel network. After gelation, the hydrogels were removed, repeatedly washed with deionized water to remove unreacted species, and dried at 50–60°C to constant mass. This preparation method yielded a mechanically stable hydrogel with enhanced structural integrity and high-water absorption capacity, owing to the combined roles of SA, PVA, and the covalently cross-linked AA network.

Swelling Ratio

Water adsorption studies are critical for evaluating the performance of hydrogel-based adsorbents, as their swelling behavior directly reflects their porosity, hydrophilicity, and accessibility of active sites. These studies quantify the material's ability to uptake and retain water under controlled environmental conditions, such as fixed temperature, humidity, and immersion time.

The swelling behavior is commonly expressed as the swelling ratio (SR), which represents the percentage increase in mass of the hydrogel due to water uptake. This parameter provides a reliable measure of the hydrogel's water-holding capacity and structural flexibility and is calculated using the following equation (1) [19]:

$$(\mathrm{SR}\,\%) = \frac{w_s - w_d}{w_d} \times 100 \quad (1)$$

where w_s is the weight of the swollen hydrogel (g), and Wd is the weight of the dry hydrogel (g).

Study Gel Content

The gel content (Gc%) of the (SA-g-poly(AAC-co-PVA)) hydrogel was determined to quantify the fraction of the hydrogel network that remains insoluble in water. Initially, the hydrogel samples were dried and weighed, then immersed in distilled water for 24 h at 25°C to extract the soluble components. After extraction, the samples were dried again and reweighed. The gel content (Gc%) was calculated using equation 2:

$$(\text{Gc}\%) = \frac{\text{Md}}{\text{Mo}} \times 100 \quad (2)$$

where Md represents the weight of the dried sample after extraction, and Mo corresponds to the initial weight of the dried sample before extraction.

Preparation of Trypan Blue Dye Solution

Figure 1 shows the chemical structure of Trypan Blue dye is an anionic azo dye with the molecular formula ($C_{34}H_{24}N_6Na_4O_{14}S_4$) and a molecular weight of 960.81 g.mol^{-1} illustrates the chemical structure of the TB dye.

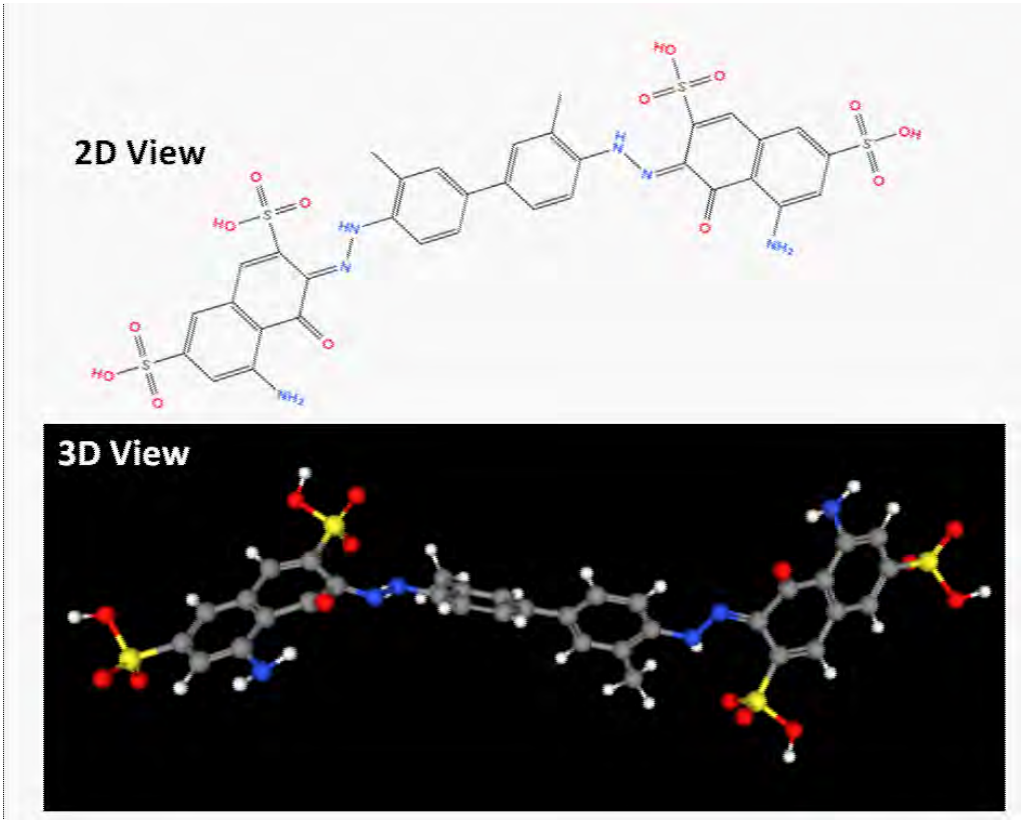

Fig 1. Chemical Structure of Trypan Blue (TB)

A stock solution at 1000 mg L^{-1} was prepared by dissolving 0.1 g of dye powder in 100 mL of distilled water. The maximum absorption wavelength (λ_{max}) was determined using a

UV-Vis spectrophotometer, and the maximum absorbance peak was observed at 588 nm.

Adsorption Studies

Batch adsorption experiments were performed to evaluate the removal efficiency of Trypan Blue (TB) dye using the synthesized SA-g-poly(AAC-co-PVA) hydrogel. All experiments were conducted in 100 mL of dye solution using a water bath shaker at 120 rpm and 30°C. To investigate the effect of initial dye concentration, solutions at 50-500 mg L^{-1} were used with a fixed hydrogel dosage of 0.07 g. The effect of adsorbent dosage was studied by varying the hydrogel amount (0.01–0.10 g) in a dye solution with a constant concentration of 200 mg L^{-1}. The influence of solution pH was examined at values of 3, 7, 8, and 10 by adjusting the pH with 0.1 M HCl and 0.1 M NaOH solution. After reaching equilibrium, the residual dye concentration was determined using a UV-Vis spectrophotometer at (λ_{max}) of 588 nm. The equilibrium adsorption capacity (Q_e $mg.g^{-1)}$ and removal percentage (R%) were calculated using the following equations (3) and (4):

$$Q_e = \frac{(C_o - C_e)V}{W} \quad (3)$$

$$R_{\%} = \frac{C_0 - C_e}{C_0} 100 \quad (4)$$

where Q_e (mg. g^{-1}) denotes the equilibrium adsorption capacity; C_0 and C_e (mg. L^{-1}) represent the initial and equilibrium concentrations of Trypan Blue dye, respectively; V (L) refers to the solution volume of TB dye, and W (g) indicates the mass of the dry hydrogel.

Characterization Techniques

The surface functional groups of the synthesized SA-g-poly(AAC-co-PVA) hydrogel were identified using Fourier Transform Infrared Spectroscopy (FTIR) in the spectral range of 400–4000 cm^{-1}. The surface morphology and porous structure were examined using Field Emission Scanning Electron microscopy (FESEM). To investigate the internal structure and nanoscale particle-size distribution, Transmission Electron Microscopy (TEM) was used. The crystalline nature of the prepared hydrogel was analyzed by X-ray Diffraction (XRD) using Cu-Kα radiation. Furthermore, the thermal stability and degradation behavior of the hydrogel were evaluated using thermogravimetric analysis (TGA) over a temperature range of 25–600°C under a nitrogen atmosphere.

Adsorption Isotherm Models

Nonlinear isotherm adsorption models effectively characterize the interaction between the adsorbent and adsorbate. In this study, the Freundlich and Langmuir isotherm models are employed to examine adsorption. The Freundlich isotherm model is calculated using equation 5:

$$Q_e = K_f C_e^{1/n} \quad (5)$$

The Langmuir isotherm is primarily used to describe the adsorption of dyes from aqueous solutions. The Langmuir isotherm nonlinear model is calculated from equation 6:

$$Q_e = \frac{q_m K_L C_e}{1+K_L C_e} \quad (6)$$

where Qe: amount adsorbed per unit mass of adsorbent at equilibrium ($mg.g^{-1}$), ($mol.g^{-1}$), C_e: equilibrium concentration ($mg.L^{-1}$), ($mol.L^{-1}$), and K_f: capacity factor or Freundlich constant empirical ($L.mg^{-1}$).

1/n: Freundlich exponent, if the (n) value reaches unity, the adsorption is linear; if the n value is above unity, then the adsorption process is physical; if the "n" value is below unity, the adsorption process is chemical.

Langmuir constant empirical, which represents maximum adsorption efficiency ($mg.g^{-1}$), K_L: Langmuir constant (L/mg) or the equilibrium constant of the adsorption process [20].

3. Results and Discussion

Characterization of SA-g-poly (AAC-co-PVA) Hydrogel

FTIR analysis before and after adsorption

The Fourier transform infrared (FTIR) spectra of the SA-g-poly(AAC-co-PVA) hydrogel before and after Trypan Blue adsorption are illustrated in Figure 2. The spectrum of the pristine hydrogel displays a broad absorption band in the region of 3200–3500 cm^{-1}, which is attributed to the stretching vibrations of hydroxyl (–OH) groups associated with sodium alginate and poly(vinyl alcohol), indicating strong hydrogen bonding interactions within the polymeric network [21].

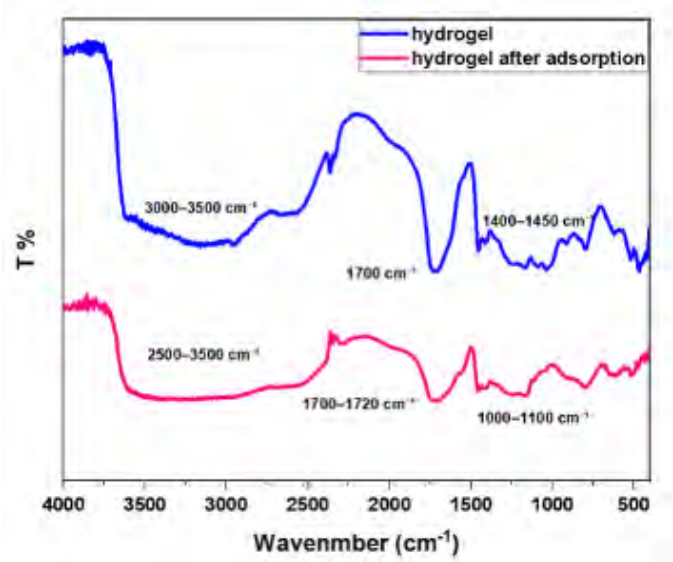

Fig 2. FTIR Spectra of the Synthesized Hydrogel Before and After Trypan Blue Adsorption

The absorption band observed around 1700–1720 cm^{-1} corresponds to the carbonyl (C=O) stretching vibration of acrylic-based units, confirming successful grafting and cross-linking of the polymer chains. In addition, the bands located near 1400–1450 cm^{-1} are assigned to the symmetric stretching vibrations of carboxylate ($–COO^-$) groups, while the peaks appearing in the range of 1000–1100 cm^{-1} are related to C–O and C–O–C stretching vibrations of the polysaccharide backbone [22,23].

After adsorption of Trypan Blue, noticeable changes in the FTIR spectrum were observed, including slight shifts and decreases in the intensity of the –OH and $–COO^-$ related bands. These variations indicate the involvement of hydroxyl and carboxyl functional groups in the adsorption process via electrostatic interactions and hydrogen bonding. The preservation of the prominent characteristic absorption bands after adsorption suggests that the hydrogel framework remains structurally stable during dye uptake [24,25].

Surface morphology analysis (FESEM)

The surface morphology of the prepared hydrogel before and after Trypan Blue adsorption was examined using field-emission scanning electron microscopy (FESEM), as shown in Figure 3a. The FESEM image of the pristine hydrogel reveals a highly porous, interconnected three-dimensional network with irregular cavities distributed throughout the surface. This porous structure is typical of alginate-based hydrogels prepared via free-radical graft polymerization and provides numerous accessible pathways that facilitate dye diffusion and adsorption processes [26,27].

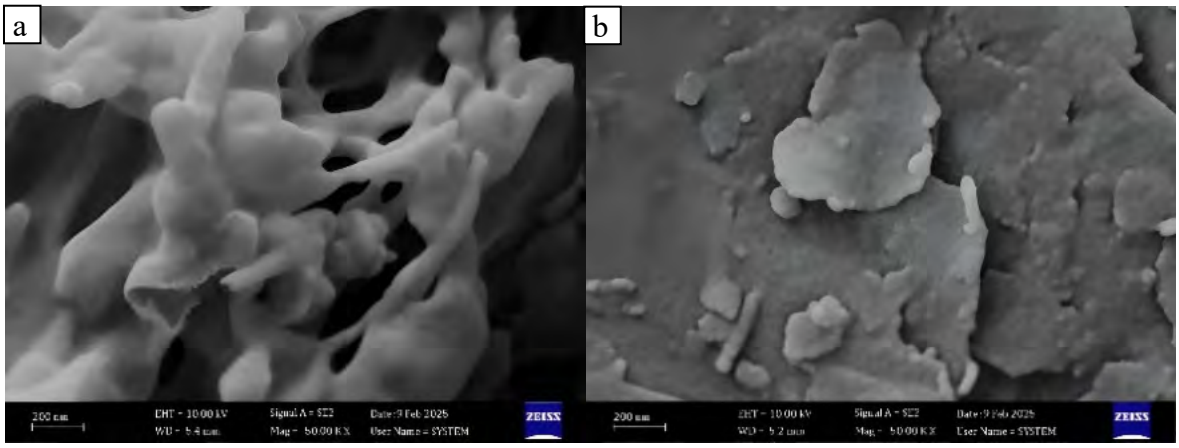

Fig 3. FESEM Images of SA-g-poly (AAC-co-PVA) Hydrogel (a) Before and (b) After the Adsorption Process

After adsorption (Figure 3b), the hydrogel surface becomes denser and partially covered by aggregated layers, indicating effective attachment of Trypan Blue molecules to the hydrogel matrix. The observed reduction in visible pore openings indicates that dye molecules occupy both internal pores and active surface sites via a combination of surface interactions and pore-filling mechanisms. Despite these morphological changes, the three-dimensional network framework remains largely preserved, demonstrating sufficient mechanical stability of the hydrogel during adsorption. This structural integrity is a key factor in maintaining regenerative capability and enabling repeated adsorption cycles [28,29].

Internal structure analysis (TEM)

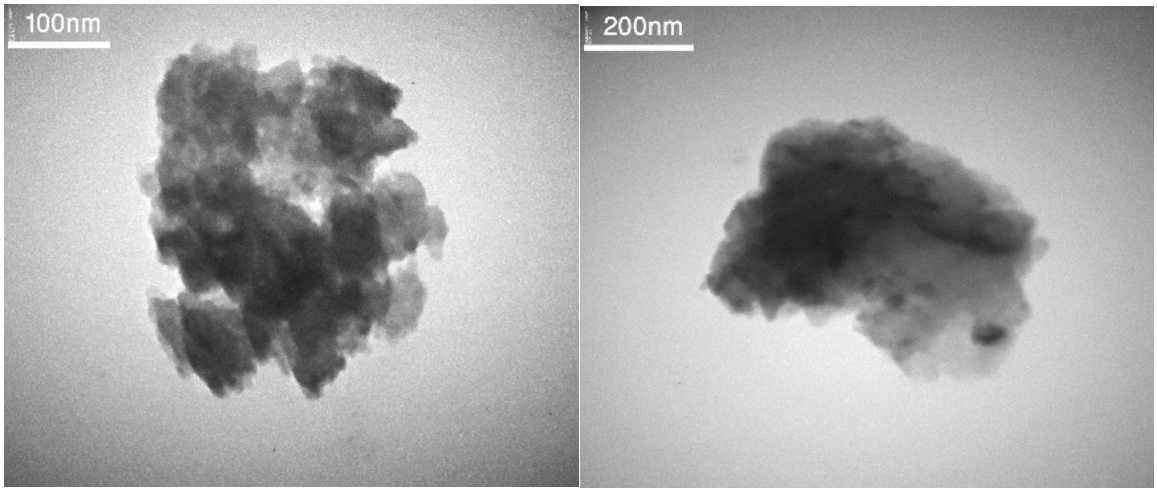

Fig 4. TEM Images of the Hydrogel's Internal Morphology at Different Magnifications

The internal morphology of the prepared hydrogel was investigated using transmission electron microscopy (TEM), as shown in Figure 4. The TEM images reveal irregular agglomerated regions containing nanoscale features dispersed throughout the polymeric matrix. These darker contrast areas correspond to polymer-rich domains formed during grafting and cross-linking and are commonly observed in biopolymer-based superabsorbent hydrogels [30].

At higher magnification, the hydrogel displays clustered internal domains with nonuniform boundaries and a relatively compact network. This structural appearance suggests that acrylic-based grafting onto the alginate backbone leads to the formation of dense nanoscale regions embedded within the swollen hydrogel network. Such features are beneficial for adsorption, as they facilitate dye diffusion and increase the number of accessible interaction sites. In addition, the absence of distinct crystalline lattice fringes confirms the predominantly amorphous nature of the hydrogel, which is advantageous for adsorption applications and is consistent with the XRD observations [31].

X-ray Diffraction (XRD) analysis

The X-ray Diffraction (XRD) pattern of the prepared SA-g-poly (AAC-co-PVA) hydrogel is presented in Figure 5. The diffractogram is characterized by a broad amorphous halo extending over the 2θ range of approximately 15–25°, while distinct crystalline peaks are absent.

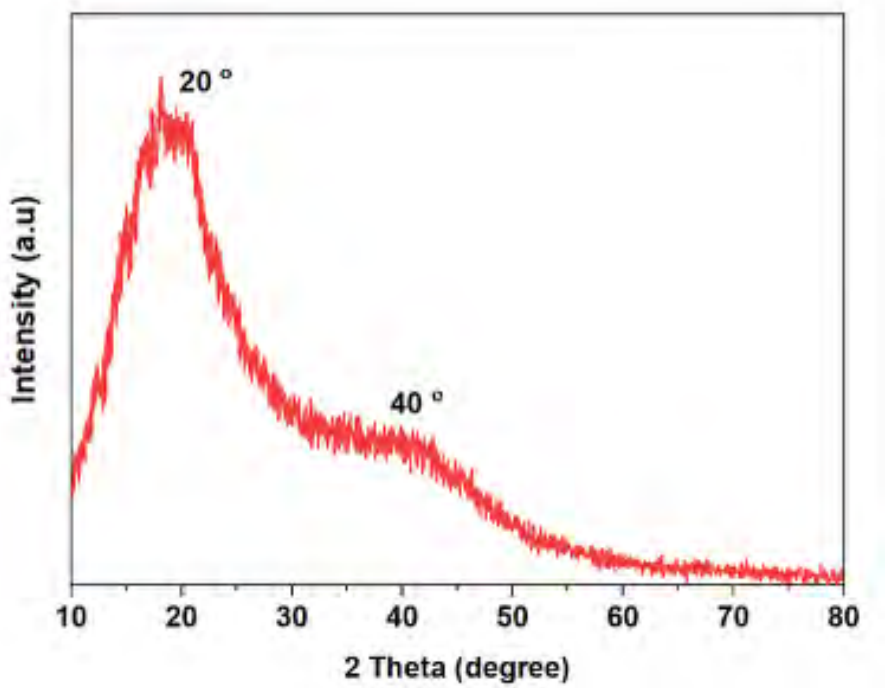

Fig 5. X-ray Diffraction (XRD) Pattern of the Prepared Hydrogel

This feature indicates that the synthesized hydrogel predominantly possesses an amorphous structure. Such diffraction characteristics are frequently reported for

polysaccharide-based hydrogels obtained via graft polymerization and cross-linking processes, in which the introduction of synthetic polymer chains interferes with the regular packing of the biopolymer backbone [32,33].

The suppression of crystalline features can be attributed to the grafting of acrylic segments onto alginate chains and to the physical entanglement of PVA within the three-dimensional cross-linked network. Such structural rearrangements hinder long-range crystalline order and result in a homogeneous amorphous matrix, as reported for alginate- and acrylic-based hydrogel nanocomposites.

The predominance of the amorphous structure is favorable for adsorption processes because it provides greater flexibility of the polymer chains and improves the exposure of functional groups, including hydroxyl (–OH) and carboxyl ($–COO^-$) moieties. Such structural characteristics facilitate more effective interactions between Trypan Blue molecules and the available active sites within the hydrogel network, thereby enhancing adsorption performance [34].

Thermal stability analysis (TGA)

The thermal stability of the prepared alginate–acrylic–PVA hydrogel was evaluated using thermogravimetric analysis (TGA), as illustrated in Figure 6. The resulting TGA profile shows a stepwise weight-loss pattern, which is commonly observed for cross-linked polysaccharide-based grafted hydrogels.

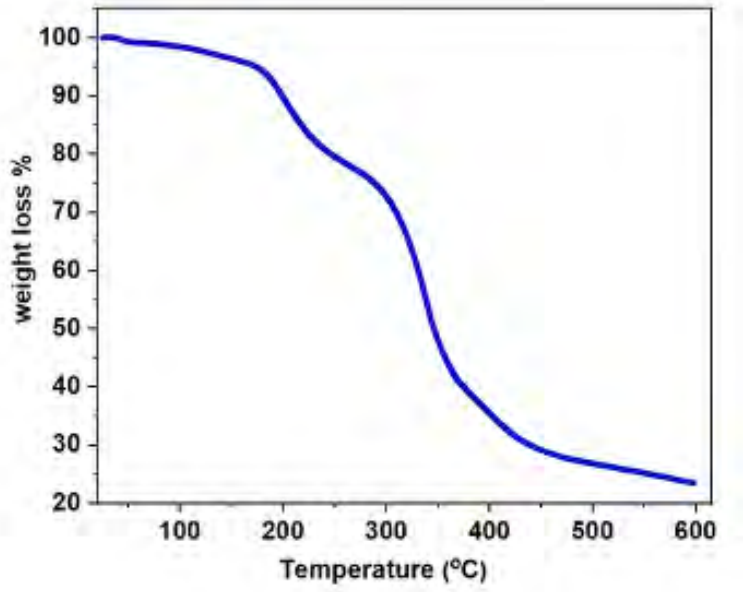

Fig 6. TGA Thermogram of the Alginate–Acrylic–PVA Hydrogel

An initial minor mass loss occurs below approximately 120°C and is mainly related to the release of physically adsorbed and weakly bound water molecules within the hydrogel structure. A second degradation stage is evident in the temperature range of 200–300°C and is attributed primarily to the thermal decomposition of grafted acrylic

components, as well as to the breakdown of pendant functional groups formed during grafting process [35,36]. At temperatures exceeding 300°C, a more substantial weight loss is observed, corresponding to the degradation of the alginate and PVA backbone chains and the progressive collapse of the three-dimensional cross-linked network. The overall degradation behavior, together with the presence of a measurable residual mass at higher temperatures, suggests that the incorporation of acrylic units and PVA chains contributes to improving the thermal stability of native alginate. This observation confirms the formation of a structurally stable, cross-linked hydrogel suitable for adsorption under a range of thermal conditions [37].

Optimization of Reaction Parameters

The synthesis conditions of the SA-g-poly(AAC-co-PVA) hydrogel were systematically optimized to maximize its swelling performance. The effects of reaction time and temperature were evaluated while keeping the concentrations of KPS (0.05 g), MBA (0.05 g), and acrylic acid (0.14 mol L^{-1}) constant.

Effect of reaction time

The reaction time was varied from 2 to 4 h at 60°C. As shown in Figure 7a, the hydrogel exhibited a maximum swelling ratio of 488% at 2 h. Shorter reaction times limit polymer chain growth and network formation, whereas longer reaction times increase crosslinking density by prolonging radical activity. This excessive crosslinking reduces network flexibility and pore size, restricting water penetration and leading to decreased swelling beyond the optimal time [38-40].

Effect of reaction temperature

The reaction temperature was varied from 55 to 75°C in 5°C increments (Figure 7b). Swelling increased with temperature, reaching a maximum of 530% at 75°C. The initial increase is attributed to enhanced thermal decomposition of the initiator (KPS), which generates more free radicals and promotes efficient grafting and network formation. This results in a more open and porous hydrogel structure that favors water uptake. However, at temperatures above the optimum, excessive radical activity increases crosslink density and can lead to chain termination, resulting in a more compact network and reduced swelling [41,42].

Effect of solvent volume

As shown in Figure 7c, the swelling percentage initially increases with increasing solvent volume, reaches a maximum at 100 mL, and then declines.

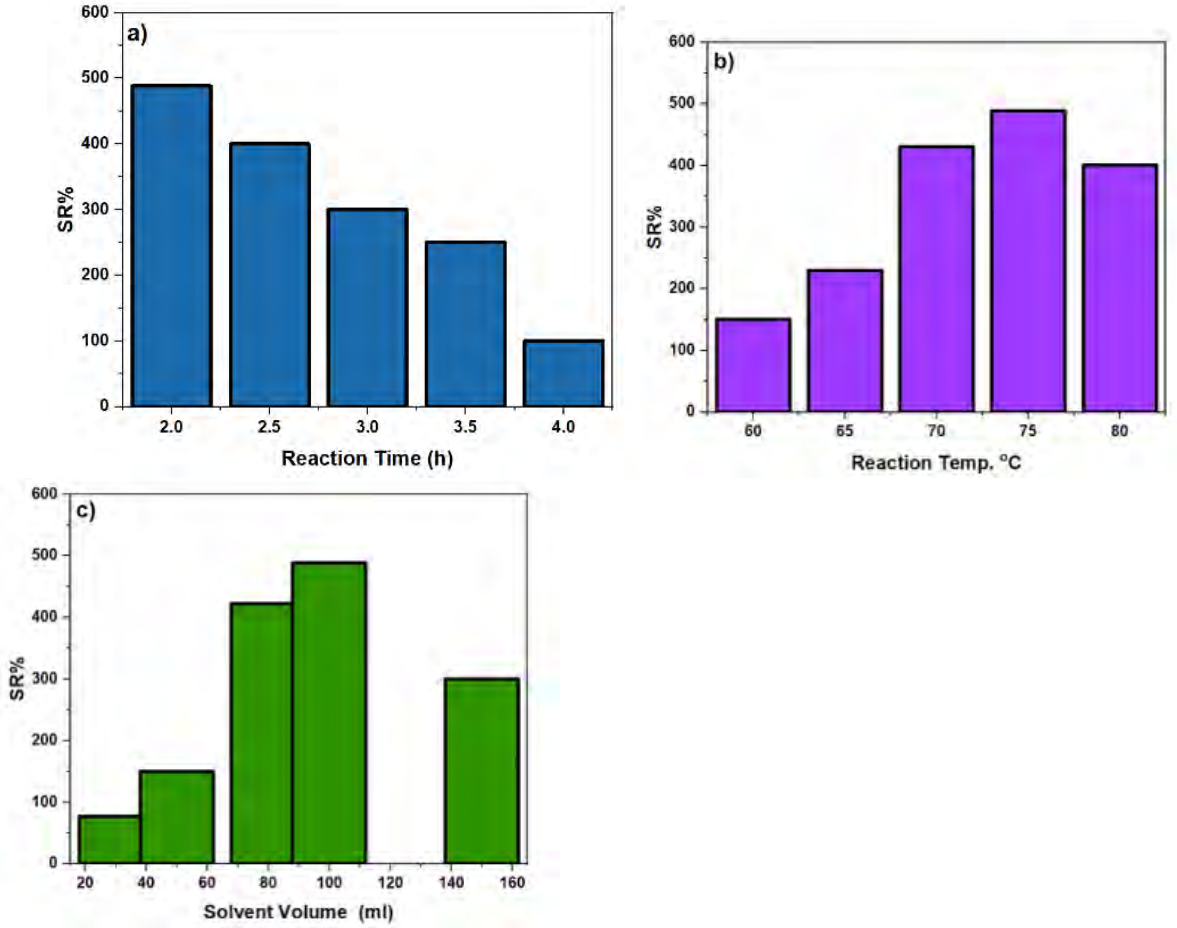

Fig 7. Effect of Several Parameters on the Highest Swelling Percentage of Hydrogel (a) Reaction Time, (b) Reaction Temperature, (c) Solvent Amount

The initial enhancement in swelling is attributed to improved dispersion of monomers and initiator in a larger solvent volume, which facilitates efficient free-radical generation and promotes uniform polymerization and network formation. This results in a more open and porous hydrogel structure that favors water uptake. However, beyond the optimal solvent volume, excessive dilution reduces the frequency of effective radical–monomer collisions, thereby lowering crosslinking efficiency and weakening network formation, thereby decreasing swelling capacity [43,44]. Overall, both reaction time and temperature strongly influence the balance between network formation and crosslinking density. Optimal swelling is achieved when the hydrogel network is sufficiently crosslinked to maintain structural integrity while remaining sufficiently flexible and porous to maximize water absorption [45,46].

Effect of Operational Parameters on Trypan Blue Adsorption

Effect of solution pH

The role of solution pH in controlling Trypan Blue adsorption onto the alginate–acrylic–PVA hydrogel was examined across a pH range of 3–11, as presented in Figure 8. A clear decrease in both removal efficiency (E%) and adsorption capacity (Q_e) was observed with increasing pH, At pH 3, the hydrogel showed high adsorption performance, with E = 96% and Q_e = 480 mg g^{-1} [47,48]. In contrast, at pH 11, both values decreased markedly to E = 41% and Q_e = 210 mg g^{-1}, demonstrating the pronounced decline in adsorption with increasing pH. indicating that acidic conditions favor dye uptake.

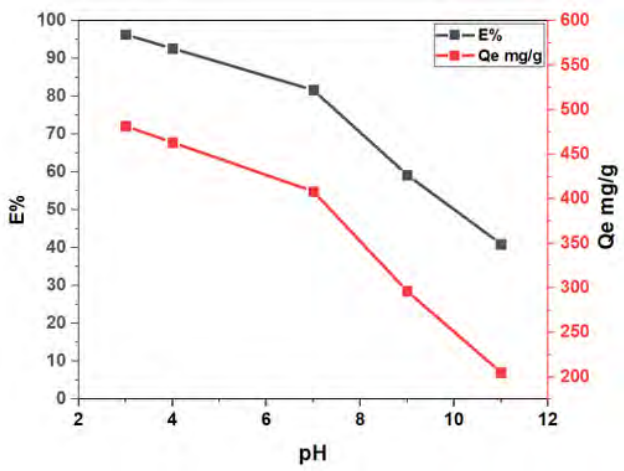

Fig 8. Effect of Solution pH on TB Dye Adsorption, Adsorption Conditions: 30°C, 200 mg L^{-1} Dye, 0.07g Hydrogel

This behavior is associated with changes in the surface charge of the hydrogel arising from the ionization state of functional groups within the alginate/PVA network, particularly carboxylic (–COOH/–COO^-) and hydroxyl (–OH) moieties. Under acidic conditions, protonation converts –COO^- groups into their neutral –COOH form, which lowers electrostatic repulsion between the hydrogel surface and the anionic sulfonate groups (–SO_3^-) of the dye. As a result, adsorption is enhanced through a combination of electrostatic attraction and hydrogen-bonding interactions. Similar pH-controlled adsorption behavior has been reported for polysaccharide- and acrylic-based hydrogel adsorbents. In contrast, under alkaline conditions, deprotonation increases the density of –COO^- sites, thereby strengthening electrostatic repulsion against anionic dye species and weakening adsorption, consistent with charge-governed adsorption observed for related hydrogel systems [49,50].

Point of zero charge (PZC)

Because the adsorption behavior of materials is strongly governed by their surface characteristics, determining the point of zero charge (PZC) provides essential insight into surface charge properties. In this study, the PZC of the (SA-g-poly(AAC-co-PVA)) hydrogel was determined using the pH drift method, a reliable technique for surface characterization. The PZC is the pH at which the net surface charge, including both internal and external sites, is zero. Below pHpzc, the hydrogel surface acquires a positive charge, whereas above pHpzc it becomes negatively charged.

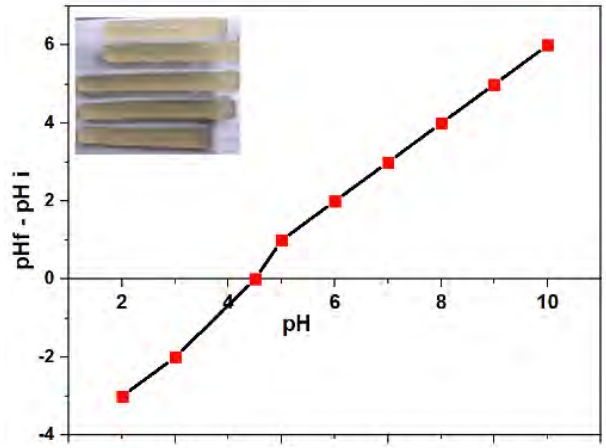

Fig 9. Effect of PZC of the (SA-g-poly(AAC-co-PVA)) Hydrogel

As illustrated in Figure 9, the initial pH (pHi) was plotted against the difference between the initial and final pH (ΔpH) after introducing a fixed amount of hydrogel into a 0.1 N NaCl solution. The pHpzc value was determined to be 4.5, indicating that under typical experimental conditions, the hydrogel surface predominantly carries a negative charge. This behavior suggests that the functional groups along the polymer chains play a key role in governing the surface charge and, consequently, the adsorption performance of the hydrogel [51,52].

Effect of adsorbent dosage

The effect of adsorbent dosage on Trypan Blue adsorption was examined by increasing the hydrogel mass from 0.01 to 0.10 g (Figure 10). As the dosage increased, the removal efficiency (E%) rose markedly, which is mainly attributed to the higher availability of adsorption sites and the larger effective surface area provided by increasing amounts of hydrogel in the solution. For example, increasing the hydrogel mass from 0.01 g to 0.10 g increased E% from ~50% to ~97% (Figure 10).

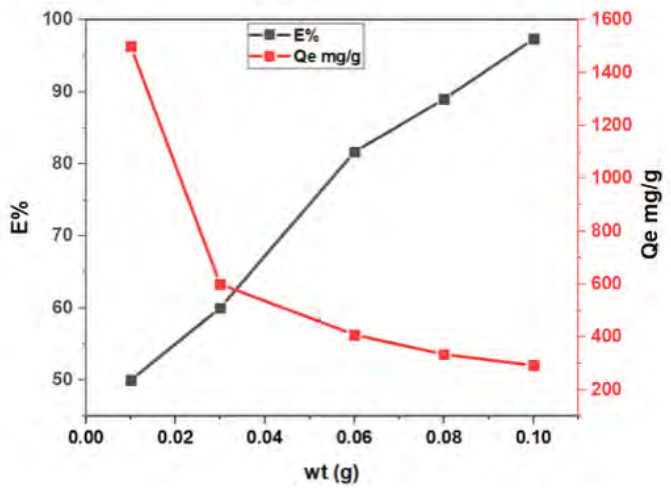

Fig 10. Effect of SA-g-poly(AAC-co-PVA) Hydrogel Dosage on Trypan Blue Adsorption, Adsorption Conditions: 30°C, 200 mg L^{-1} Dye , pH 7

In contrast, the adsorption capacity per unit mass (Qe, mg g^{-1}) decreased with increasing dosage. This behavior is commonly observed for hydrogel-based adsorbents when a fixed initial dye concentration is used, where many adsorption sites remain unsaturated at higher adsorbent dosages. Additionally, increasing hydrogel mass may lead to partial aggregation of swollen polymer domains, thereby reducing the accessibility of internal adsorption sites and decreasing Qe despite improved overall dye removal. Consistent with this, Q_e decreased from ~1500 mg g^{-1} at 0.01 g to ~300 mg g^{-1} at 0.10 g, confirming the opposite trends of E% and Qe with increasing hydrogel dosage [53,54].

Effect of initial Trypan Blue concentration

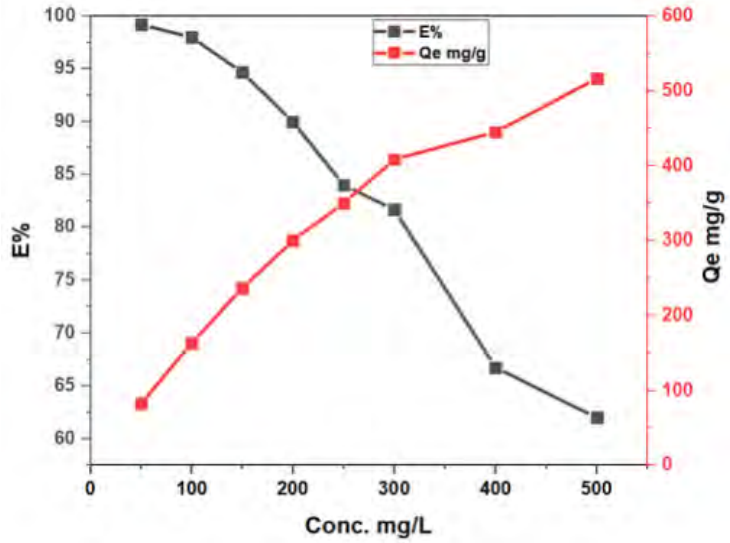

Fig 11. Effect of Initial Trypan Blue Concentration on Adsorption Behavior of the SA-g-poly(AAC-co-PVA) Hydrogel, Adsorption Conditions: 30°C, pH 7, 0.07g Hydrogel

The effect of the initial Trypan Blue concentration on the adsorption performance of the SA-g-poly(AAC-co-PVA) hydrogel was examined over a concentration range of 50–500 mg L^{-1}, as illustrated in Figure 11. An increase in dye concentration was accompanied by a gradual reduction in removal efficiency (E%), whereas the adsorption capacity (Q_e) showed a continuous increase. As shown in Figure 11, increasing the initial Trypan Blue concentration from 50 mg L^{-1} to 500 mg L^{-1} resulted in a noticeable decrease in E, from about 98% at 50 mg L^{-1} to nearly 62% at 500 mg L^{-1}, while Q_e increased significantly from approximately 90 mg g^{-1} to around 520 mg g^{-1} over the same concentration range. At lower concentrations, the abundance of available adsorption sites relative to the number of dye molecules promotes more efficient uptake, thereby increasing removal efficiency. With further increases in the initial concentration, these sites become progressively saturated, intensifying competition among dye molecules and resulting in a noticeable decline in E% [55].

In contrast, the continuous increase in Q_e at higher initial concentrations is attributed to the steeper concentration gradient between the bulk solution and the hydrogel surface, which enhances the mass-transfer driving force and allows greater dye accumulation per unit mass of adsorbent. The opposite trend between E% and Qe with increasing initial dye concentration is characteristic of hydrogel-based adsorbents and has been reported for polysaccharide–acrylic hydrogel systems used in dye adsorption studies [56,57].

Effect of contact time

The effect of contact time on Trypan Blue uptake by the SA-g-poly (AAC-co-PVA) hydrogel is presented in Figure 12. The adsorption capacity (Q_e) increases rapidly during the initial stage, reaching approximately 350 mg/g after about 25 min, which is attributed to the abundance of available active sites and the high concentration gradient between the solution and the hydrogel surface.

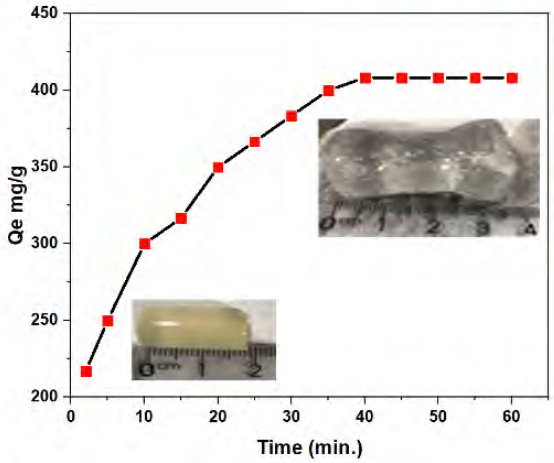

Fig 12. Effect of Contact Time on Trypan Blue Adsorption by the Prepared Hydrogel, Adsorption Conditions: 30°C, 200 mg L^{-1} Dye, 0.07g Hydrogel, pH 7

Beyond this period, the adsorption rate gradually decreases, and equilibrium is attained after approximately 40 min, with a maximum Qe of approximately 410 mg/g. This behavior is related to the progressive occupation of adsorption sites and the development of diffusion resistance within the cross-linked hydrogel network. Similar time-dependent adsorption profiles have been widely reported for polysaccharide-based hydrogels and bio-adsorbents used for dye removal [58].

Adsorption Isotherm

The equilibrium adsorption data of Trypan Blue onto the prepared hydrogel was evaluated using the Langmuir (monolayer) and Freundlich (multilayer) isotherm models, as shown in Figure 13.

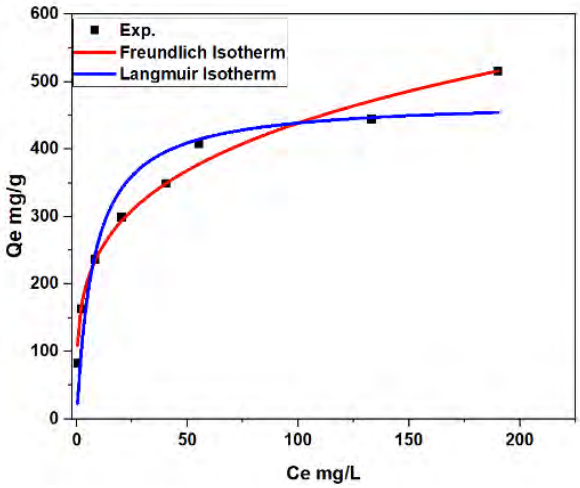

Fig 13. Equilibrium Adsorption Isotherms of TB Dye onto the Prepared Hydrogel, Showing Experimental Data and Fitting with Langmuir and Freundlich Models Under the Studied Conditions

At the same time, the corresponding fitting parameters are summarized in Table 1.

Table 1. Different Parameters of Isotherm Models for TB Dye Adsorption onto the Prepared Hydrogel

Isotherm model	Parameter	Value
Freundlich $Q_e = K_f C_e^{1/n}$	K_f	437.76 ± 10.05
	1/n	0.251 ± 0.017
	R^2	0.9838
Langmuir $Q_e = \frac{Q_m K_L C_e}{1 + K_L C_e}$	Q_m	493.09 ± 36.87 mg g^{-1}
	K_L	0.128 ± 0.050 L mg^{-1}
	R^2	0.8961

The fitting results indicated that the Freundlich model provides a superior description of the experimental data, as evidenced by its higher correlation coefficient (R^2 = 0.983) than the Langmuir model (R^2 = 0.896). This indicates that the adsorption process predominantly follows a multilayer mechanism on a heterogeneous hydrogel surface rather than uniform monolayer coverage [59].

The predominance of the Freundlich model suggests that Trypan Blue molecules interact with adsorption sites of different energies distributed within the grafted polymeric network of the hydrogel. Such adsorption behavior is commonly reported for alginate- and polysaccharide-based hydrogels and reflects the structural complexity and non-uniform surface characteristics inherent to these materials [60,61].

Regeneration Efficiency

The regeneration and reusability performance of the prepared hydrogels was evaluated over five consecutive adsorption–desorption cycles, as illustrated in Figure 14. The hydrogel exhibited an initial removal efficiency of approximately 82%, which gradually decreased with increasing regeneration cycles.

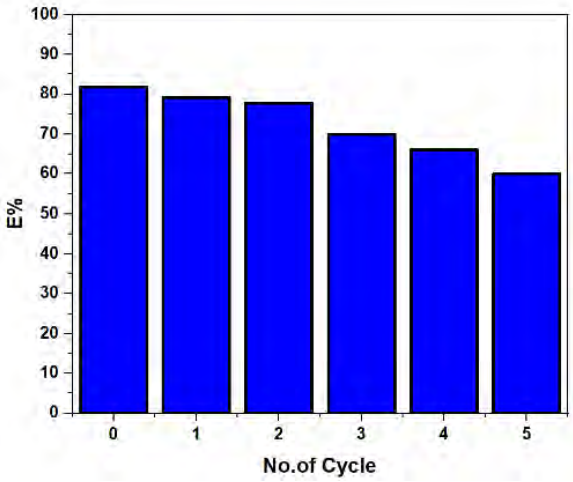

Fig 14. Effect of Regeneration Cycles on Adsorption Efficiency ($E_{\%}$)

After the second cycle, the removal efficiency changed little, remaining around 78%, indicating acceptable preservation of the hydrogel framework and accessibility of a considerable fraction of adsorption sites [62,63]. From the third cycle onward, a more pronounced decrease became evident, and the efficiency dropped to approximately 60% by the fifth cycle. This decline is likely attributable to cumulative effects arising from repeated use, including partial obstruction of active sites, incomplete release of adsorbed dye molecules during desorption, and minor structural fatigue within the crosslinked polymer network. Comparable regeneration trends have been reported for polysaccharide-based and grafted hydrogel systems, supporting the feasibility of employing such materials for multiple adsorption–desorption cycles [64,65].

Comparative Analysis with Existing Adsorbents

To evaluate the adsorption efficiency of the synthesized (SA-g-poly(AAC-co-PVA)) hydrogel for the removal of the anionic Trypan Blue (TB) dye from aqueous solutions, a comparative analysis was performed against previously reported adsorbents. Although direct comparisons are constrained by differences in experimental parameters, including operating conditions and adsorption environments, the results summarized in Table 2 indicate that the prepared hydrogel exhibits a notably high maximum adsorption capacity. These findings highlight the competitive performance and potential applicability of the synthesized hydrogel as an effective adsorbent for removing anionic and cationic dyes.

Table 2. Adsorption Capacity of (SA-g-poly(AAC-co-PVA)) Hydrogel for the Removal of Dyes

Sorbent/Hydrogel	Dye	Qe mg/g	Ref
St-g-AA(H)-AAM	MG	23.59	[66]
Hydrogel/Fe_3O_4	MB	9.76	[67]
BMEP-PVPA hydrogel	MB	284.4	[68]
Chitosan/Fe3O4	MB	9.65	[69]
Alginate/PP beads	ST	30.66	[70]
GG/bacterial cellulose	ST	17.57	[71]
XG-cl-poly (MEMA)/TiO_2	CV	160.33	[26]
Fly ash/TiO_2 - chitosan	MB	55.85	[72]
CMC-g-poly (AA-co-IA) /MMT	ST	19.024	[73]
SA-g-poly(AAC-co-PVA) hydrogel	TB	493.33	In this study

4. Conclusion

The present study demonstrates that a cross-linked SA-g-poly(AAC-co-PVA) hydrogel can effectively remove Trypan Blue (TB) from aqueous solutions. Spectroscopic and microscopic characterizations (FTIR, FESEM, TEM, and XRD) verified the successful formation of a porous and mainly amorphous hydrogel structure, which is advantageous for adsorption processes. The adsorption behavior was found to be highly dependent on the experimental conditions. Acidic media promoted dye uptake, and the highest performance was observed at pH 3, where the removal efficiency exceeded 93%, owing to protonation of surface functional groups and reduced electrostatic repulsion with anionic dye species. The adsorption process proceeded rapidly, reaching equilibrium after approximately 40 min, at which point a high Qe of 410mg/g was achieved, reflecting the fast occupation of readily accessible adsorption sites. Initial dye concentration also played a key role in controlling adsorption performance. The highest removal efficiency was observed at an initial concentration of 50 mg L^{-1} (E% ≈ 98%), whereas increasing the concentration resulted in a gradual decrease in efficiency due to saturation of active sites. Regarding adsorbent dosage, increasing the hydrogel mass improved dye removal, and an optimal dosage of 0.10 g was identified, corresponding to ~95% removal efficiency. Beyond this dosage, the improvement in efficiency became less pronounced due to partial site underutilization.

Isotherm analysis revealed that the adsorption data were better described by the Freundlich model (R^2 = 0.983), indicating a heterogeneous adsorption surface. Furthermore, the hydrogel retained nearly 60% of its initial removal efficiency after multiple regeneration cycles, confirming its reasonable stability and potential for repeated use.

5. References

1. Singh V, Pandit C, Roy A, Pandit S, Rai AK, Rani A, Ranjan N, Rustagi S, Malik S. Degradation of food dyes via biological methods: A state-of-the-art review. *Bioresour. Technol. Rep.*, 2024, 25, 101780.
2. Sherugar P, Padaki M, Naik NS, George SD, Murthy DHK. Biomass-derived versatile activated carbon removes both heavy metals and dye molecules from wastewater with near-unity efficiency: Mechanism and kinetics. *Chemosphere*, 2022, 287, 132085.
3. Sharma S, Sharma G, Kumar A, AlGarni TS, Naushad M, Alothman ZA, Stadler FJ. Adsorption of cationic dyes onto carrageenan and itaconic acid-based superabsorbent hydrogel: Synthesis, characterization and isotherm analysis. *J. Hazard. Mater.*, 2021, 421, 126729. https://doi.org/126710.121016/j.jhazmat.122021.126729
4. Subhan H, Alam S, Shah LA, Ali MW, Farooq M. Sodium alginate grafted poly(N-vinyl formamide-co-acrylic acid)-bentonite clay hybrid hydrogel for sorptive removal of methylene green from wastewater. *Colloids Surf., A*, 2021, 611, 125853. https://doi.org/125810.121016/j.colsurfa.122020.125853
5. Stanciu MC, Nichifor M. Adsorption of anionic dyes on a cationic amphiphilic dextran hydrogel: Equilibrium, kinetic, and thermodynamic studies. *Colloid Polym. Sci.*, 2019, 297(1), 45-57.
6. Shen Y, Li B, Zhang Z. Super-efficient removal and adsorption mechanism of anionic dyes from water by magnetic amino acid-functionalized diatomite/yttrium alginate hybrid beads as an eco-friendly composite. *Chemosphere*, 2023, 336, 139233. https://doi.org/139210.131016/j.chemosphere.132023.139233
7. Sringeri Ganesh P, Kadri Jagadish D, Badalamoole V. Development of gum tragacanth-based graft copolymer hydrogel for the adsorptive removal of dyes from wastewater. *Macromol. Chem. Phys.*, 2025, 226(22), e00225.
8. Sourbh T. Synthesis, characterization and adsorption studies of an acrylic acid-grafted sodium alginate-based TiO_2 hydrogel nanocomposite. *Adsorpt. Sci. Technol.*, 2018, 36(1-2), 458–477.
9. Singh J, Weber ME. Kinetics of one-dimensional gel swelling and collapse for large volume change. *Chem. Eng. Sci.*, 1996, 51(19), 4499-4508. https://doi.org/4410.1016/0009-2509(4496)00254-00250
10. Silva EC, Soares VR, Nörnberg AB, Fajardo AR. Recyclable 3D-printed composite hydrogel containing rice husk biochar for organic contaminants adsorption in tap water. *ACS Appl. Polym. Mater.*, 2023, 5(10), 8415-8429.
11. Sorze A, Valentini F, Dorigato A, Pegoretti A. Development of a xanthan gum based superabsorbent and water retaining composites for agricultural and forestry applications. *Molecules*, 2023, 28(4), 1952. https://doi.org/1910.3390/molecules28041952
12. Sizovs A, McLendon PM, Srinivasachari S, Reineke TM.

Carbohydrate polymers for nonviral nucleic acid delivery. *Top. Curr. Chem.*, 2010, 296, 131-190.
13. Aljeboree AM, Jasim KK, Sabah NA. High-capacity dye adsorption by low-cost combo hydrogel: Kinetic, thermodynamic, and regeneration study. *J. Inorg. Organomet. Polym. Mater.*, 2025, 35(10), 8350-8373.
14. Shirsath SR, Patil AP, Bhanvase BA, Sonawane SH. Ultrasonically prepared poly(acrylamide)-kaolin composite hydrogel for removal of crystal violet dye from wastewater. *J. Env. Chem. Eng.*, 2015, 3(2), 1152-1162: https://doi.org/1110.1016/j.jece.2015.1104.1016
15. Shi W-Y, Ding C, Yan J-L, Han X-Y, Lv Z-M, Lei W, Xia M-Z, Wang F-Y. Molecular dynamics simulation for interaction of PESA and acrylic copolymers with calcite crystal surfaces. *Desalination*, 2012, 291, 8-14.
16. Choudhary S, Sharma K, Kumar V, Sharma V. RSM-CCD directed modeling and optimization of a low-cost adsorbent based on sodium dodecyl sulfate for the selective removal of malachite green and methylene blue dyes: Kinetics, isotherm, and thermodynamics analysis. *Microchem. J.*, 2024, 205, 111158.
17. Chen X, Zhang G, Hou F, Zhu J. Highly effective removal of basic fuchsin dye using carboxymethyl konjac glucomannan grafted acrylic acid-acrylamide/montmorillonite composite hydrogel. *Int. J. Biol. Macromol.*, 2024, 277, 134163. https://doi.org/134110.131016/j.ijbiomac.132024.134163
18. Zheng M, Cai K, Chen M, Zhu Y, Zhang L, Zheng B. pH-responsive poly(gellan gum-co-acrylamide-co-acrylic acid) hydrogel: Synthesis, and its application for organic dye removal. *Int. J. Biol. Macromol.*, 2020, 153, 573-582.
19. Rizwan M, Naseem S, Gilani SR, Durrani AI. Optimization of swelling and mechanical behavior of *Acer platanoides* cellulose combo hydro-gel. *Kuwait J. Sci.*, 2024, 51(2), 100177. https://doi.org/100110.101016/j.kjs.102024.100177
20. Abu-Zurayk RA, Al Bakain RZ, Hamadneh I, Al-Dujaili AH. Adsorption of Pb (II), Cr (III) and Cr (VI) from aqueous solution by surfactant-modified diatomaceous earth: Equilibrium, kinetic and thermodynamic modeling studies. *Int. J. Miner. Process.*, 2015, 140, 79-87.
21. Thakur S, Chaudhary J, Thakur A, Gunduz O, Alsanie WF, Makatsoris C, Thakur VK. Highly efficient poly(acrylic acid-co-aniline) grafted itaconic acid hydrogel: Application in water retention and adsorption of rhodamine B dye for a sustainable environment. *Chemosphere*, 2022, 303, 134917.
22. Thamer, B.M., A. Aldalbahi, Hameed MMA, El-Newehy MH. *In situ* preparation of novel porous nano-composite hydrogel as effective adsorbent for the removal of cationic dyes from polluted water. *Polymers*, 2020, 12(12), 3002. https://doi.org/3010.3390/polym12123002
23. Aljeboree AM, Hussein UA-R, Alkaim AF, Abd S, Alsultany FH, Altimari US. pH-Responsive biopolymer/nano-clay hydrogel beads for dual dye removal: Adsorption kinetics, isotherms, and reusability.

Polym. Bull., 2025, 82(16), 11357-11393.
24. Tshikovhi A, Motaung TE. Chitosan and guar-gum-based polymeric nano-composites for the adsorption of contaminants in water: Insights into adsorption capacities, mechanisms, and applications. *Desalin. Water Treat.*, 2024, 320, 100708. https://doi.org/100710.101016/j.dwt.102024.100708
25. Thombare N, Mishra S, Siddiqui MZ, Jha U, Singh D, Mahajan GR. Design and development of guar gum based novel, superabsorbent and moisture retaining hydrogels for agricultural applications. *Carbohydr. Polym.*, 2018, 185, 169-178. https://doi.org/110.1016/j.carbpol.2018.1001.1018
26. Taktak FF, Özyaranlar E. Semi-interpenetrating network based on xanthan gum-cl-2-(N-morpholin-oethyl methacrylate)/titanium oxide for the single and binary removal of cationic dyes from water. *Int. J. Biol. Macromol.*, 2022, 221, 238-255. https://doi.org/210.1016/j.ijbiomac.2022.1008.1139
27. Taktak F, Gökçe S. Ultrasound-assisted synthesis of biodegradable graphene oxide-based hydrogel nanocomposites for highly efficient and cost-effective removal of methyl orange from aqueous media. *J. Water Process Eng.*, 2024, 58, 104837.
28. Thakur S, Arotiba OA. Synthesis, swelling and adsorption studies of a pH-responsive sodium alginate–poly(acrylic acid) superabsorbent hydrogel. *Polym. Bull.*, 2018, 75(10), 4587-4606.
29. Teweldebrihan MD, Dinka MO. Methyl red adsorption from aqueous solution using *Rumex abyssinicus*-derived biochar: Studies of kinetics and isotherm. *Water*, 2024, 16. DOI: 10.3390/w16162237
30. Tang Y, Li M, Mu C, Zhou J, Shi B. Ultrafast and efficient removal of anionic dyes from wastewater by polyethyleneimine-modified silica nanoparticles. *Chemosphere*, 2019, 229, 570-579.
31. Vahid B, Hossein P, Mohammad SA, Dariush S, Siamak J. Synthesis and characterization of bio-nano-composite hydrogel beads based on magnetic hydroxyapatite and chito-san: A pH-sensitive drug delivery system for potential implantable anticancer platform. *Polym. Bull.*, 2023, 23, 1223. https://doi.org/1210.1007/s00289-00023-05072-00281
32. Vasiraja N, Prabhahar RSS, Joshua A. Preparation and physio–chemical characterisation of activated carbon derived from *Prosopis juliflora* stem for the removal of methylene blue dye and heavy metal containing textile industry effluent. *J. Cleaner Prod.*, 2023, 397, 136579.
33. Varaprasad K, Jayaramudu T, Sadiku ER. Removal of dye by carboxymethyl cellulose, acrylamide and graphene oxide via a free radical polymerization process. *Carbohydr. Polym.*, 2017, 164, 186-194. https://doi.org/110.1016/j.carbpol.2017.1001.1094
34. Wahyu ME, Damayanti D, Wu HS. Production, characterization, and application of KOH-activated biochar from rice straw for azo dye adsorption. *Biomass*, 2025, 5, 40. DOI: 10.3390/biomass5030040
35. Wan S, Zhao W, Xiong D, Li S, Ye Y, Du L. Novel alginate immobilized TiO_2 reusable functional hydrogel beads with high photocatalytic

removal of dye pollutions. *J. Polym. Eng.*, 2022, 42(10), 978-985.
36. Wallenwein CM, Weigel V, Hofhaus G, Dhakal N, Schatton W, Gelperina S, Groeber-Becker FK, Dressman J, Wacker MG. Pharmaceutical development of nanostructured vesicular hydrogel formulations of rifampicin for wound healing. *Int. J. Mol. Sci*., 2022, 23(24).
37. Wan Z, Xiong Z, Ren H, Huang Y, Liu H, Xiong H, Wu Y, Han J. Graft copolymerization of methyl methacrylate onto bamboo cellulose under microwave irradiation. *Carbohydr. Polym.*, 2011, 83(1), 264-269.
38. Wei J, Yan L, Zhang Z, Hu B, Gui W, Cui Y. Carbon nanotube/chitosan hydrogel for adsorption of acid red 73 in aqueous and soil environments. *BMC Chem.*, 2023, 17(1), 104.
39. Wang Y, Shen Z, Wang H, Song Z, Yu D, Li G, Liu X, Liu W. Progress in research on metal ion crosslinking alginate-based gels. *Gels*, 2025, 11, 16. DOI: 10.3390/gels11010016
40. Aljeboree AM, Hussein SA, Altimari US, Mohealdeen SM, Alsultany FH, Alkaim AF. Optimization of swelling and mechanical behavior of novel pH-sensitive terpolymer biocomposite hydrogel based on activated carbon for removal brilliant blue dye from aqueous solution. *Polym. Bull.*, 2025, 82(5), 1447-1478. https://doi.org/1410.1007/s00289-00024-05588-00280
41. Winning D, Wychowaniec JK, Wu B, Heise A, Rodriguez BJ, Brougham DF. Thermoresponsiveness across the physiologically accessible range: Effect of surfactant, cross-linker, and initiator content on size, structure, and transition temperature of poly(N-isopropylmethacrylamide) microgels. *ACS Omega*, 2024, 9(34), 36185-36197.
42. Wang Z, Ning A, Xie P, Gao G, Xie L, Li X, Song A. Synthesis and swelling behaviors of carboxymethyl cellulose-based superabsorbent resin hybridized with graphene oxide. *Carbohydr. Polym.*, 2017, 157, 48-56.
43. Wang J, Sawut A, Wumaer M, Simayi R, Aikebaier M. Preparation of chitosan quaternary ammonium salt-sodium alginate/poly acrylic acid hydrogel and its application in flexible sensing. *J. Mech. Behav. Biomed. Mater.*, 2026, 173, 107231. https://doi.org/107210.101016/j.jmbbm.102025.107231
44. Wang G, Li G, Huan Y, Hao C, Chen W. Acrylic acid functionalized graphene oxide: High-efficient removal of cationic dyes from waste-water and exploration on adsorption mechanism. *Chemosphere*, 2020, 261, 127736.
45. Xinyou M, Lan W, Shiqing G, Yanyan D, Yunqing Z, Chuanyi W, Eric L. Synthesis of a three-dimensional network sodium alginate–poly(acrylic acid)/attapulgite hydrogel with good mechanic property and reusability for efficient adsorption of Cu^{2+} and Pb^{2+}. *Env. Chem. Lett.*, 2018, 16, 653–658.
46. Xiao C, Yang M. Controlled preparation of physical cross-linked starch-g-PVA hydrogel. *Carbohydr. Polym.*, 2006, 64(1), 37-40. https://doi.org/10.1016/j.carbpol.2005.1010.1020
47. Yaarub NA, Alshrefi SM, Rafea FAM, Ahmed T, Al-Mamoori MHK, Al-Nafiey AK, Al-Kaim AF. Optical and morphological characterizations of element oxides compound (Y_2O_3/SeO_2) nano-composite structures synthesized *via* chemistry of

laser ablation. *J. Global Pharma Technol.*, 2018, 10(3), 536-544.
48. Xisto MR, Damacena DHL, de Araújo FP, Alves D, Honorio LMC, Peña-Garcia R, Almeida L, de Oliveira JA, Furtini MB, Osajima JA. Biopolymer gellan-gum-based TiO_2: A green alternative photocatalyst approach for removal of pollutants. *Water*, 2024, 16(2), 315.
49. Yang J, Shojaei S, Shojaei S. Removal of drug and dye from aqueous solutions by graphene oxide: Adsorption studies and chemometrics methods. *npj Clean Water*, 2022, 5(1), 5.
50. Yamakawa T, Tatami J, Komeya K, Meguro T. Synthesis of AlN powder from $Al(OH)_3$ by reduction–nitridation in a mixture of NH_3–C_3H_8 gas. *J. Eur. Ceram. Soc.*, 2006, 26, 2413-2418.
51. Aljeboree AM, Alkaim AF, Alsultany FH, Issa SK. Highly reusable nano adsorbent based on clay-incorporated hydrogel nanocomposite for cationic dye adsorption. *J. Inorg. Organomet. Polym. Mater.*, 2024, 35(2), 1165-1186. https://doi.org/10.1007/s10904-10024-03344-10905
52. Parveen R, Tarannum Z, Ali S, Fatima S. Nanoclay based study on protein stability and aggregation and its implication in human health. *Int. J. Biol. Macromol.*, 2021, 166, 385-400. 310.1016/j.ijbiomac.2020.1010.1197
53. Yang Y, Song S, Zhao Z. Graphene oxide (GO)/polyacrylamide (PAM) composite hydrogels as efficient cationic dye adsorbents. *Colloids Surf., A*, 2017, 513, 315-324.
54. Yang X, Zhang X, Feng X, Xu B, Du C, Zhang E, Shan M, Zhang Y. Novel porous hydrogel beads based on amidoxime modified polymer of intrinsic microporosity for efficient cationic dye removal. *Microporous Mesoporous Mater.*, 2024, 377, 113218. https://doi.org/113210.111016/j.micromeso.112024.113218
55. Yang Z, Ni R, Yang Y, Qi J, Lin X, Zhang Y, Wang L, Wu Y, Li X, Lu H. Carboxymethyl cellulose-based supramolecular hydrogel with thermo-responsive gel-sol transition for temporary plugging of oil pipeline in hot work. *Carbohydr. Polym.*, 2024, 324, 121556. https://doi.org/121510.121016/j.carbpol.122023.121556
56. Alzayd AAM, Radia ND. Novel pH-sensitive of organic composite (kc-g-poly(AAc-co-AAm)/bentonite), synthesis and characterization candidate as a carrier for controlled release system *in vitro* to some drugs. *Carbon Lett.*, 2024, 34(1), 505-517. https://doi.org/510.1007/s42823-42023-00674-42821
57. An J-K, Wang W-B, Wang A-Q. Preparation and swelling properties of a pH-sensitive superabsorbent hydrogel based on psyllium gum. *Starch/Stärke*, 2010, 62(10), 501-507.
58. Aljeboree AM, Ghazi HH, Hussein SA, Jawad MA, Khuder SA, Alkaim AF. Facile fabrication of a low-cost carboxymethyl cellulose–polyacrylamide composite for the highly efficient removal of cationic dye: Optimization, kinetic and reusability. *J. Iran. Chem. Soc.*, 2025, 22(1), 91-111. https://doi.org/110.1007/s13738-13024-03132-13735
59. Vadivelan V, Kumar KV. Equilibrium, kinetics, mechanism, and process design for the sorption of methylene blue onto rice husk. *J. Colloid Interface Sci.*, 2005, 286(1), 90-100.

60. Weber WJJ, Morris JC. Kinetics of adsorption on carbon from solution. *J. Sanit. Eng. Div., Am. Soc. Civ. Eng.*, 1963, 89, 31-59.
61. Wang ZK, Li T-T, Peng HK, Ren H, Lin JH, Lou C-W. Natural-clay-reinforced hydrogel adsorbent: Rapid adsorption of heavy-metal ions and dyes from textile wastewater. *Water Env. Res.*, 2022, 94.
62. Thamer BM, Shaker AA, Abdul Hameed MM, Al-Enizi AM. Highly selective and reusable nanoadsorbent based on expansive clay-incorporated polymeric nanofibers for cationic dye adsorption in single and binary systems. *J. Water Process Eng.*, 2023, 54, 103918. https://doi.org/103910.101016/j.jwpe.102023.103918
63. Aljeboree AM, Alkaim AF, Hussein SA, Alsultany FH, Jawad MA. Ecofriendly k-carrageenan-based hydrogel with strong adsorption and higher abilities to remove crystal violet from aqueous solution: Thermodynamic, isotherm and kinetic investigation. *J. Inorg. Organomet. Polym. Mater.*, 2025, 35(4), 2921-2942.
64. Usmanova GS, Latypova LR, Yusupova AR, Mustafin AG. Preparation of copolymers based on aniline and 2[2-chloro-1-methylbut-2-en-1-yl]aniline and their application for the removal of methyl orange from aqueous solutions. *J. Polym. Env.*, 2025, 33(3), 1585-1600. https://doi.org/1510.1007/s10924-10024-03419-x
65. Ullah N, Ali Z, Khan AS, Adalat B, Nasrullah A, Khan SB. Preparation and dye adsorption properties of activated carbon/clay/sodium alginate composite hydrogel membranes. *RSC Adv.*, 2024, 14(1), 211-221.
66. Al-Aidy H, Amdeha E. Green adsorbents based on polyacrylic acid-acrylamide grafted starch hydrogels: The new approach for enhanced adsorption of malachite green dye from aqueous solution. *Int. J. Env. Anal. Chem.*, 2021, 101(15), 2796-2816. https://doi.org/2710.1080/03067319.03062020.01711896
67. Rana VS, Sharma N. Adsorption profile of anionic and cationic dyes through Fe_3O_4 embedded oxidized Sterculia gum/gelatin hybrid gel matrix. *Int. J. Biol. Macromol.*, 2023, 232, 123098. https://doi.org/123010.121016/j.ijbiomac.122022.123012.123317
68. Anil I, Gunday ST, Bozkurt A, Alagha O. Design of crosslinked hydrogels comprising poly(vinylphosphonic acid) and bis[2-(methacryloy-loxy)ethyl] phosphate as an efficient adsorbent for wastewater dye removal. *Nanomaterials*, 2024, 10(1), 131. https://doi.org/110.3390/nano10010131
69. Zeng L, Xie M, Zhang Q, Kang Y, Guo X, Xiao H, Peng Y, Luo J. Chitosan/organic rectorite composite for the magnetic uptake of methylene blue and methyl orange. *Carbohydr. Polym.*, 2015, 123, 89-98. https://doi.org/10.1016/j.carbpol.2015.1001.1021
70. Abbaz A, Arris S, Viscusi G, Ayat A, Aissaoui H, Boumezough Y. Adsorption of safranin-O dye by alginate/pomegranate peels beads: Kinetic, isotherm and thermodynamic studies. *Gels*, 2023, 9(11), 961. https://doi.org/910.3390/gels9110916
71. Nguyen HT, Ngwabebhoh FA, Saha N, Saha T, Saha P. Gellan gum/bacterial cellulose hydrogel

crosslinked with citric acid as an eco-friendly green adsorbent for safranin and crystal violet dye removal. *Int. J. Biol. Macromol.*, 2022, 222, 77-89. https://doi.org/10.1016/j.ijbiomac.2022.1009.1040

72. Gajera R, Patel RV, Yadav A, Labhasetwar PK. Adsorption of cationic and anionic dyes on photocatalytic fly ash/TiO_2 modified chitosan biopolymer composite. *J. Water Process Eng.*, 2022, 49, 102993. https://doi.org/102910.101016/j.jwpe.102022.102993

73. Mohammadzadeh Pakdel P, Peighambardoust SJ, Arsalani N, Aghdasinia H. Safranin-O cationic dye removal from wastewater using carboxymethyl cellulose-grafted-poly(acrylic acid-co-itaconic acid) nanocomposite hydrogel. *Env. Res.*, 2022, 212, 113201. https://doi.org/113210.111016/j.envres.112022.113201

The Chemist
Journal of the American Institute of Chemists

Highly Adsorbent Derived from Bioresources Residue: Rice Husk-Treated Surface for the Adsorption of Methyl Violet Dye from Aqueous Solution

Njah Kadhim Nimr[1], Bushra Esmail Alkhalili[2], Alaa Mohammed Mahmood[3], Hasan Kadhim Nimr[4], Mohammed Abed Jawad[5], Aseel M. Aljeboree[6*]

[1,2,3,4]Scientific Research Commission, Ministry of Higher Education and Scientific Research, Iraq
[5]Department of Medical Laboratories Technology, Al-Nisour University
Nisour Seq. Karkh, Baghdad, Iraq
[6]Department of Chemistry, College of Science for Women, University of Babylon, Iraq
[*]Corresponding author (E-mail: annenayad@gmail.com)

Abstract: The purpose of this study is to develop an eco-friendly adsorbent from rice husk for the effective removal of alkaline dyes (RH) and its acid-activated carbon (AC-RH). This activated carbon was obtained from rice husks by chemical activation with phosphoric acid as the activating agent. Characterisation of the activated carbon was performed using FESEM, TEM, and BET. Adsorption equilibrium of methylene violet 2B (MV) by Rice Husk activated carbon (AC-RH) was experimentally studied, and the effects of operating parameters, including initial dye concentration (10-100 mg/L), activated carbon dosage (0.01-0.09 g/100 mL), and solution pH (3-11) on the adsorption were investigated systematically. Their adsorption efficiency also increased with pH in alkaline medium, and maximum removal efficiency was observed at pH 11 at ambient temperature (25°C). The adsorption efficiency increased over time, reaching a removal rate of 87% for rice husk-enhanced activated carbon (AC-RH) and 68% for raw rice husk (RH). After this point, all sites reached complete saturation, resulting in a stable removal rate. An adsorption isotherm model, the Freundlich model, described the equilibrium data with the greatest fit (by R^2), meaning it is a heterogeneous surface. Based on the high correlation coefficient (R^2 = 0.9985), the model is reliable, as the adsorption capacities for various adsorbents (AC-RH: 96.11 mg/g and (RH-AC): 76.22 mg/g) were determined at pH 6 and 25°C. These findings emphasised the potential of rice husk-based activated carbon as a promising, eco-friendly, sustainable, inexpensive and efficient adsorbent to remove cationic dyes as an alternative to commercial adsorbents.

Key Words: Adsorption, rice husk, dye, isotherm

1. Introduction

The disposal of huge volumes of synthetic colours in industrial drainage, which is generally untreated effluent, has emerged as a global leading problem threatening environmental systems and making the preservation of human health very hard. Of these dyes, methyl violet 2B (MV-2B) is a cationic dye containing one or two methyl groups bonded to a nitrogen atom and three substituted aryl groups. Due to its stable chromophoric group, MV-2B is used in a number of sectors, including textile, paper, leather, silk, bamboo, and ink, mainly as a dyeing agent [1-4].

As the dye is very water-soluble, its ecological stability and mobility in the aquatic environment is very high. However, this same characteristic also makes it difficult to remove from wastewater once it is in the environment, thus increasing the compound's ecological footprint. Similarly, MV-2B has been associated with marked toxicological significance. Disclosure USA; 2015/10/05: One report found the dye to be a human health hazard and exposure potentially leads to "upper respiratory tract mucosal irritation and dryness, general gastrointestinal disturbance, drowsiness and inflammation of the oral and pharyngeal mucosa", and, moreover, prolonged or high-level exposure may be associated with respiratory dysfunction and circulatory disorders. Due to its water solubility, bioaccumulation in organisms and toxicity, MV-2B-contaminated effluent must be treated before being released into the environment [5,6]. Among the available treatment methods, adsorption has emerged as one of the most efficient approaches for dye removal due to its high selectivity toward organic contaminants. Various adsorbent materials, such as activated carbon, chitosan, metal oxide nanoparticles, and binary metal oxides, have demonstrated promising performance in removing such dyes, emphasising the importance of selecting suitable adsorbents to achieve efficient wastewater remediation. Among these treatment methods, adsorption has been recognized as one of the most effective means for the elimination of dyes due to its high preferential selectivity toward organic pollution. Multiple adsorbent materials, including but not limited to activated carbon, chitosan, metal oxide nanoparticles, and binary metal oxides, have been shown to effectively remove these dyes, underscoring the need to select appropriate adsorbents for efficient wastewater remediation [7-10].

Activated carbon (AC) is generally regarded as a premium adsorbent for wastewater treatment and features a plentiful specific surface area, pronounced porosity, various surface functional groups, high adsorption performance, good chemical stability, and easy regeneration. However, the high production cost of activated carbon hinders its large-scale application [11,12]. On the other hand, adsorbents derived from lignocellulosic sources have obtained increasing interest due to their environment-friendly, renewable, cheap, and abundant nature. A plethora of literature has highlighted the efficiency of converting agricultural residues and biomass wastes into adsorbent materials. These include sugarcane bagasse, soybean husks, residues from *Moringa oleifera* cultivation, sorghum stalks, oil palm fronds and poultry litter, which are highly promising biosorbents for sequestering dyes and other contaminants from wastewater systems [8,13].

Lignocellulosic biomass wastes have traditionally been used to produce activated carbon via thermochemical processes such as conventional pyrolysis or microwave-assisted pyrolysis. Pyrolysis is the most commonly employed method, as it can yield high-quality, porous activated carbon with a

high specific surface area. The choice of a suitable chemical activating agent is the most important step in this process, because is the one that dramatically affects the characteristics of the pore structure, pore size distribution and surface area of the carbon products obtained [14,15]. Zinc chloride ($ZnCl_2$), sulfuric acid (H_2SO_4), phosphoric acid (H_3PO_4), potassium hydroxide (KOH), and sodium carbonate (Na_2CO_3) are all widely used activating agents. In particular, zinc chloride ($ZnCl_2$) has been reported to be the most dominant, as it is known for inducing a well-defined porous structure with high surface area and carbon yield. Phosphoric acid (H_3PO_4)–activated carbon also demonstrated high adsorption performance for various water pollutants. Organic pollutants include malachite green, methylene blue, methyl violet, tetracycline hydrochloride, phenol, etc., as well as toxic metal ions such as Cr(VI) and Cd^{2+}. Rice husk-based activated carbon, for example, showed better adsorption capability towards methyl violet compared to raw rice husk due to improved surface characteristics and an excess of functional groups. The fit of the adsorption process to the Freundlich isotherm indicated heterogeneous multilayer adsorption behaviour. Additionally, this activated carbon demonstrated strong regeneration and reusability, making it a viable and eco-efficient bio-based adsorbent for wastewater treatment applications [16,17]. This research focuses on the using of friendly bioresources for removal of pollutants from aqueous solutions.

2. Materials

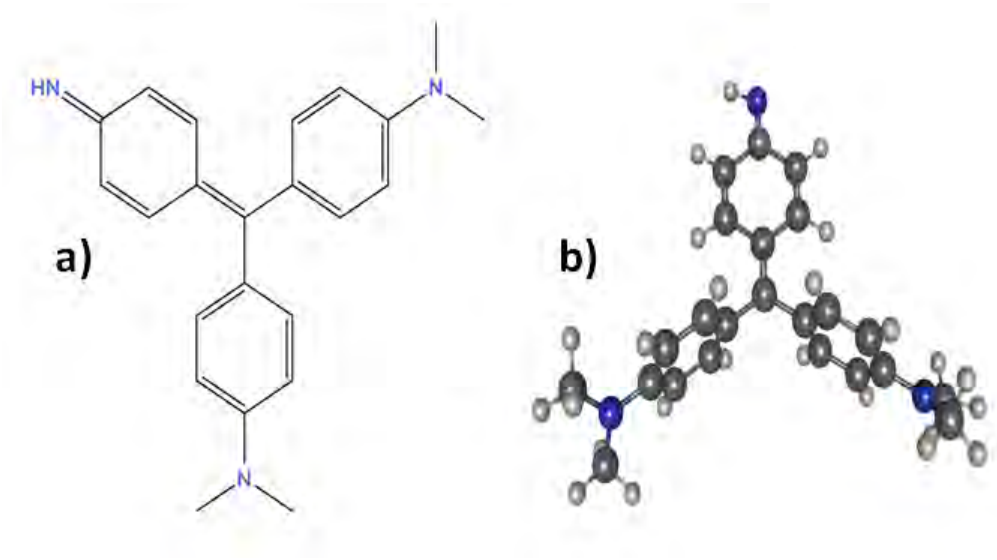

Figure 1. a) 2D Structure b) 3D Structure of MV 2B Dye

Rice Husk (RH) was collected from a local farm in Hillah, Iraq. Methyl violet dye (as shown in Figure 1) (MV 2B; $C_{24}H_{28}ClN_3$; molecular weight 393.94 g/mol, purity 99.87%, maximum wavelength 575 nm) was obtained from Tianjin Kemou Chemical Co., Ltd. Sodium chloride (NaCl, molecular weight 58.44 g/mol), hydrochloric acid (HCl), sodium hydroxide (NaOH, molecular weight 40

g/mol), zinc chloride ($ZnCl_2$, molecular weight 136.315 g/mol) and phosphoric acid (H_3PO_4, molecular weight 97.994 g/mol) were sourced from Sigma-Aldrich.

Activated Carbon Preparation from Rice Husk

The RH was sourced from farms, left undisturbed, and cleaned with water to remove dirt and issues. They were then left to dry in the sun for three days. After this, the specimens were placed in an oven and heated at 100°C for 24 hours to completely eliminate the surface moisture. These dried husks were then ground in a mortar to a very fine powder and sieved to give 2 mm-sized particles. Subsequently, chemical activation was performed on 1 g of rice husks using 2 g of phosphoric acid (H_3PO_4). The pulp was then transferred to a deoxygenated furnace and was calcined at 500°C for 90 min in a nitrogen atmosphere. The activated carbon obtained was called RH-AC and was washed several times with hot distilled water to remove any unreacted acid. The RH-AC powder was dried in an oven at 100°C for 24h after the washing, then sieved to achieve a similar particle size of m, and the final RH-AC powder was retained in a sealed container were carried out the adsorption experiments (Figure 2).

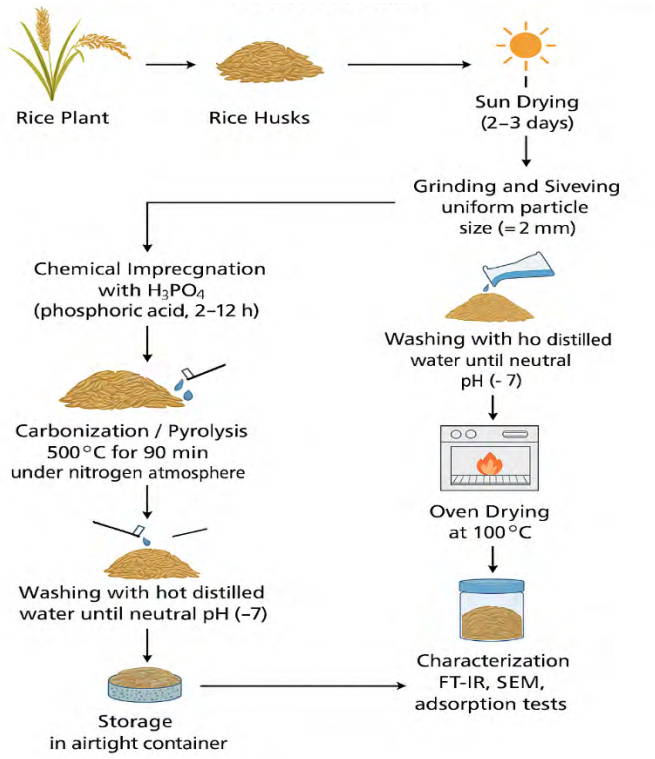

Figure 2. Preparation of Activated Carbon from Rice Husk

Adsorption Experiment

A standard solution of methyl violet (MV) dye with an initial concentration of 100 mg/L was prepared using distilled water. A series of solutions was prepared to obtain the required concentrations. In the adsorption experiments, 100 mL of an MV solution (50 mg/L) was used in a 100 mL conical flask. A weight of activated carbon was used as an adsorbent (0.0600 ± 0.0001 g). A shaker was used in a temperature-controlled water bath, and the mixture was shaken at 150 rpm for one hour to ensure that the adsorption equilibrium was reached – a standard study. To systematically evaluate the adsorption behaviour, the effect of several experimental variables was investigated: contact time, which was set within a range of 5 to 60 minutes; and the initial dye concentration, which ranged from 10 to 100 mg/L. The pH of the solution is controlled between 3 and 10 using 0.1 M sodium hydroxide or 0.1 M hydrochloric acid. Following each experiment, the residual MV dye concentration in the supernatant was determined using a UV–Vis spectrophotometer at the maximum absorption wavelength (λmax = 580 nm). The adsorption capacity and removal efficiency were subsequently calculated based on the difference between the initial and equilibrium concentrations of the dye (equations 1 and 2)[18].

$$E\ \% = \frac{C_o - C_e}{C_o} \times 100 \quad (1)$$

$$Qe\ = \frac{(C_o - C_e)V}{W} \quad (2)$$

Where C_o (mg/L) is the initial concentration of dye, and Ce (mg/L) is the concentration of dye at equilibrium.

3. Results and Discussion

Morphology Studies (FESEM)

Figure 3a of the field-emission scanning electron microscopy (FESEM) image of phosphoric acid-activated rice husk-derived activated carbon shows a heterogeneous and rough surface morphology. The image reveals a highly uneven surface with numerous holes and wrinkles, which are characteristic of successful chemical activation. The porous structure was formed through dehydration and oxidation during the activation of H_3POH, which promoted the formation of micro–mesopores through volatilisation and disruption of the lignocellulosic matrix [19,20]. The higher the activated carbon, the rougher and more porous its surface (characteristics related to a greater surface area and a higher density of embedded sites, both of which are important for achieving efficient adsorption) is. The uneven or coarse surface of this activated carbon indicates the suitability for applications such as dye removal from aqueous solutions (i.e., environmental remediation) [21,22].

The FESEM micrograph of activated carbon after adsorption of MV dye reveals significant changes in surface morphology compared to the pre-adsorption structure. The rough, porous surface appears smoother and partially covered, indicating that the dye molecules penetrate most of the active sites on the surface and fill most of the pores and surface cavities [23,24]. The appearance of deposits as clumps on the prepared surface usually indicates strong interactions between dye molecules and the active sites on the carbon surface, likely involving π–π stacking, electrostatic attraction, and hydrogen bonding. The reduced visibility of the microporosity confirms the success of the adsorption process and the efficiency of activated carbon in removing dye from aqueous solutions, as shown in Figure 3b [25].

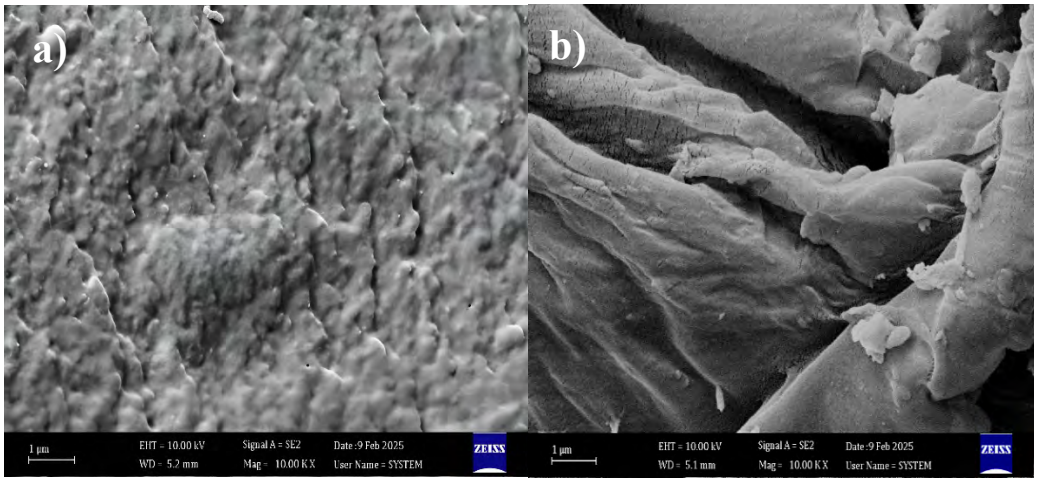

Figure 3. FESEM Image of a) AC-RH Surface b) AC-RH/MV Dye

Transmission Electron Microscopy (TEM)

Transmission electron microscopy (TEM) images show the nanostructure of rice husks from which phosphoric acid-activated carbon was prepared (Figure 4).

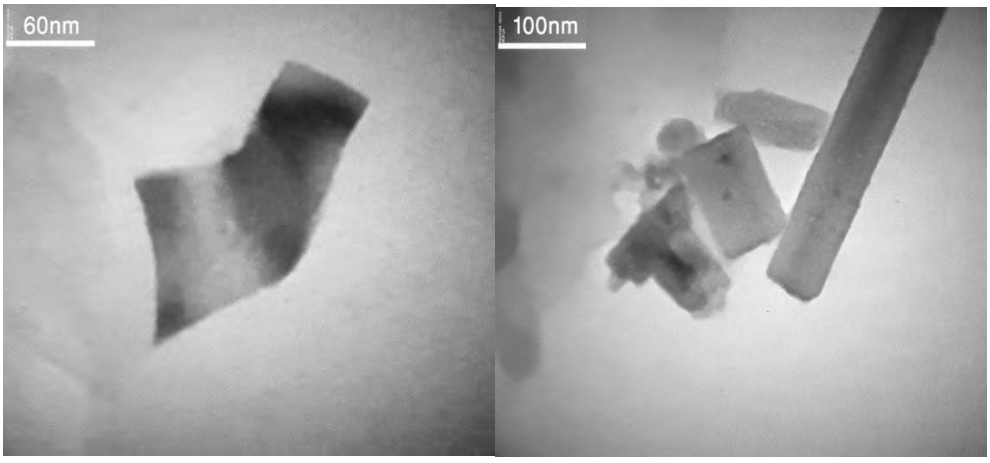

Figure 4. TEM Image of Activated Carbon from Rice Husk Surface

Two-dimensional (60 nm scale) images reveal thin, sheet-like carbon structures with irregular shapes, indicating partial crystallization and layered structure formation through acid activation. Further crystallization and more regular shapes are observed, confirming the successful activation process. The second image (100 nm scale) shows irregular and rod-like shapes. The variety of molecular shapes reflects the heterogeneous decomposition of rice husks during activation and carbonization. The combination of sheet-like shapes and aggregated nanostructures demonstrates that H_3PO_4 activation yields a porous, heterogeneous structure that is beneficial for adsorption applications [26,27].

Specific Surface Area

Using the adsorption/separation method with nitrogen, the specific surface area of acid-activated carbon (AC-RH) was determined, providing insight into its pore structure and surface reactivity. The Brunauer-Emmett-Teller (BET) method was employed. This technique evaluates gas adsorption onto a solid surface. The adsorption curve conformed to the IUPAC type IV adsorption curve, reflecting the presence of micro- and intermediate porosity bands. The appearance of H3 retardation rings confirmed the presence of cleavage-shaped pores and irregular pore shapes, characteristic features of layered carbon materials, demonstrating its efficiency as a porous adsorbent for gas-solid interaction studies. Therefore, the acid-activated carbon exhibited a specific surface area (BET) of 2.31 cm^3/g [28].

Effect of the Contact Time

In this study, the equilibrium time (5–60 minutes) for the adsorption efficiency of methyl violet (MV) dye was determined under constant experimental conditions: sample volume (100 mL), rice husk-enhanced activated carbon dosage (0.06), pH (5), and dye concentration (50 mg/L), as shown in Figure 5.

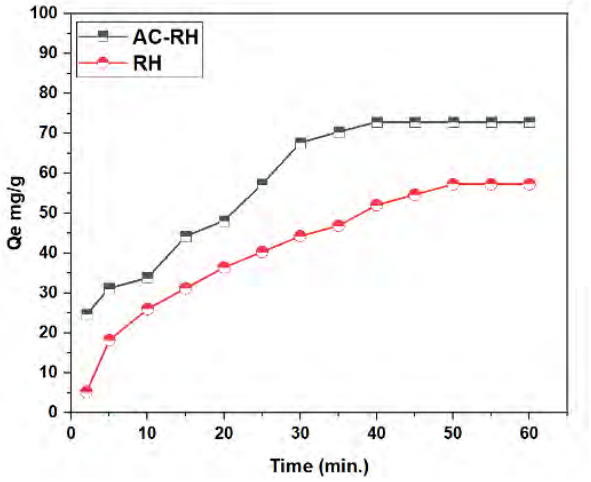

Figure 5. Effect of the Contact Time on AC-RH and RH on the Removal of MV Dye

The adsorption efficiency increased over time, reaching a removal rate of 87% for rice husk-enhanced activated carbon (AC-RH) and 68% for raw rice husk (RH). After this point, all sites reached complete saturation, resulting in a stable removal rate. This shows the saturation of the adsorption sites, indicating that no additional dye could be adsorbed. Notably, rice husk-derived activated carbon exhibited higher removal and adsorption efficiencies than raw rice husk. This improved performance is due to activated carbon having more active sites than unactivated carbon. This is a result of activation, which creates more surface sites and higher surface area, thereby enhancing interaction with MV molecules. On the contrary, functional sites are absent in raw rice husks; therefore, raw rice husks cannot effectively remove the dye. An optimal contact time of 60 minutes was chosen for further experiments based on the results shown in Figure 5.

Effect of AC-RC Mass

The influence of AC-RH mass on the adsorption efficiency of methyl violet (MV) dye was examined within the range of 0.01–0.09 g, while maintaining all other parameters constant. As shown in Figure 6, MV dye removal efficiency increased from 70% to 86% as the adsorbent mass was raised from 0.01 to 0.06 g [29,30].

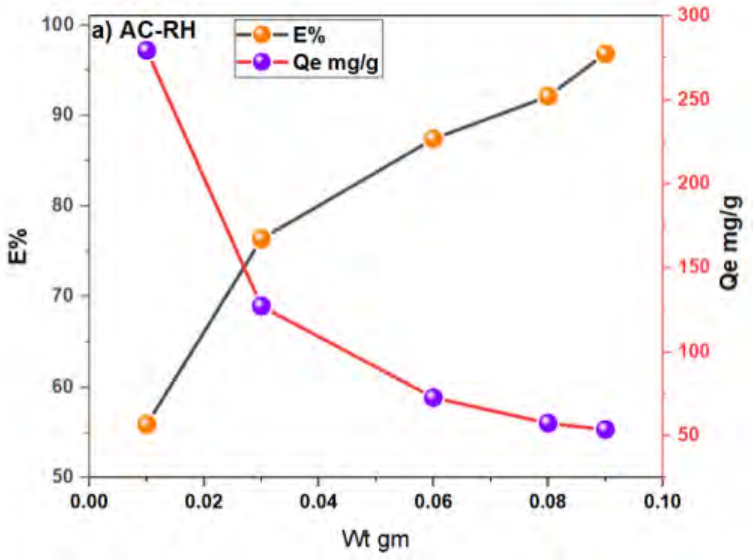

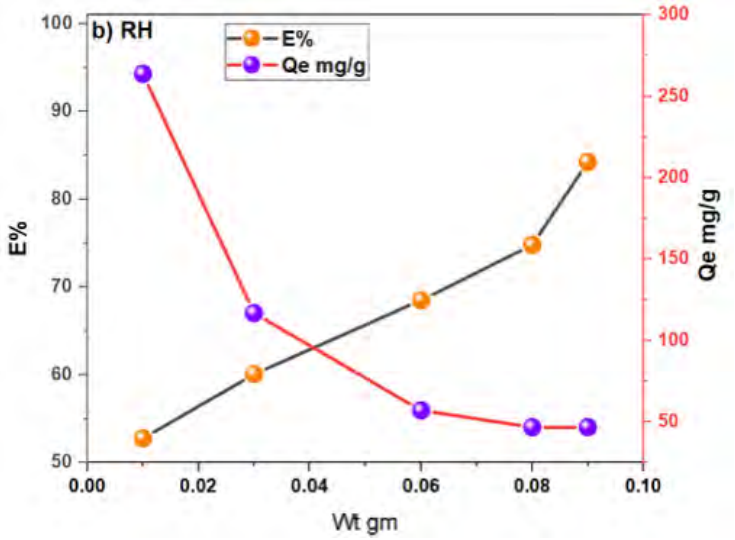

Figure 6. Effect of the Weight of a) AC-RH and b) RH on the Removal of MV Dye (initial dye concentration: 50 mg/L; contact time: 60 min; temperature: 25°C; agitation speed: 190 rpm)

The maximum efficiency was achieved at 0.06 g, which can be attributed to the greater availability of active binding sites as the adsorbent dosage increased. However, a further increase to 0.09 g resulted in a slight decline in extraction efficiency, likely due to particle aggregation at higher dosages that reduces the effective surface area. Therefore, an AC-RH mass of 0.06 g was selected as the optimum dosage for subsequent experiments [31-33].

Effect of Initial Concentration of MV Dye

The influence of the initial MV dye concentration on adsorption performance was systematically investigated at pH 8 over the range 10–100 mg/L.

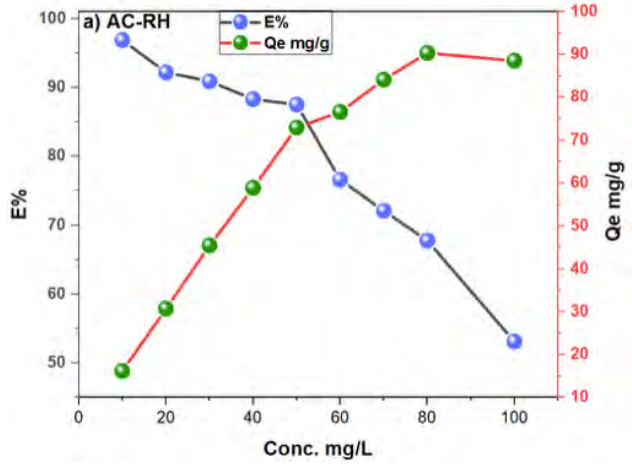

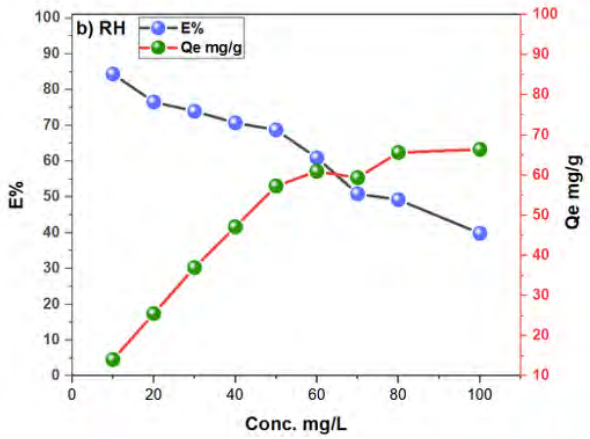

Figure 7. Effect of Initial Concentration of MV Dye on the a) AC-RH and b) RH (adsorbent dosage: 0.06 g; contact time: 60 min; temperature: 25°C; agitation speed: 190 rpm)

As illustrated in Figure 7, an increase in dye concentration resulted in an apparent rise in adsorption capacity (qe). This behaviour can be explained by the enhanced driving force for mass transfer at higher concentrations, which facilitates the diffusion of dye molecules from the solution to the surface of the adsorbent [3,34,35]. Thus, more dye molecules are adsorbed per unit mass of adsorbent as the concentration increases. As the dye concentration increases, the adsorption efficiency increases, while conversely, the removal percentage (%) decreases. This decrease in adsorption efficiency is usually attributed to saturation of the adsorbent surface with available adsorption sites, which cannot accommodate the excess number of dye ions at high concentrations. In other words, although each gram of adsorbent binds a greater quantity of dye at high concentrations, the removal percentage decreases because the number of dye molecules is much greater than the number of active sites. These results demonstrate that lower concentrations improve removal efficiency by increasing diffusion and intermolecular forces, but they also reduce it due to limited adsorption sites and surface-site saturation with dye [36,37].

Effect of pH of Solution

The effect of pH on the adsorption of methyl violet (MV) dye using rice husk activated carbon (AC-RH) and raw rice husk (RH) was investigated under optimal experimental conditions (initial dye concentration: 50 mg/L, activated carbon weight: 0.06 g, contact time: 60 minutes, stirring speed: 190 rpm, temperature: 25°C). The activated carbon demonstrated significantly higher efficiency than unactivated carbon, with average values of 95.63% for AC-RH and 78.11% for RH. The corresponding adsorption capacities were calculated to be 79.61 mg/g for AC-RH and 67.64 mg/g for RH, as shown in Figure 8. This indicates that the adsorption process relies primarily on pore filling rather than electrostatic interactions [16,38-40]

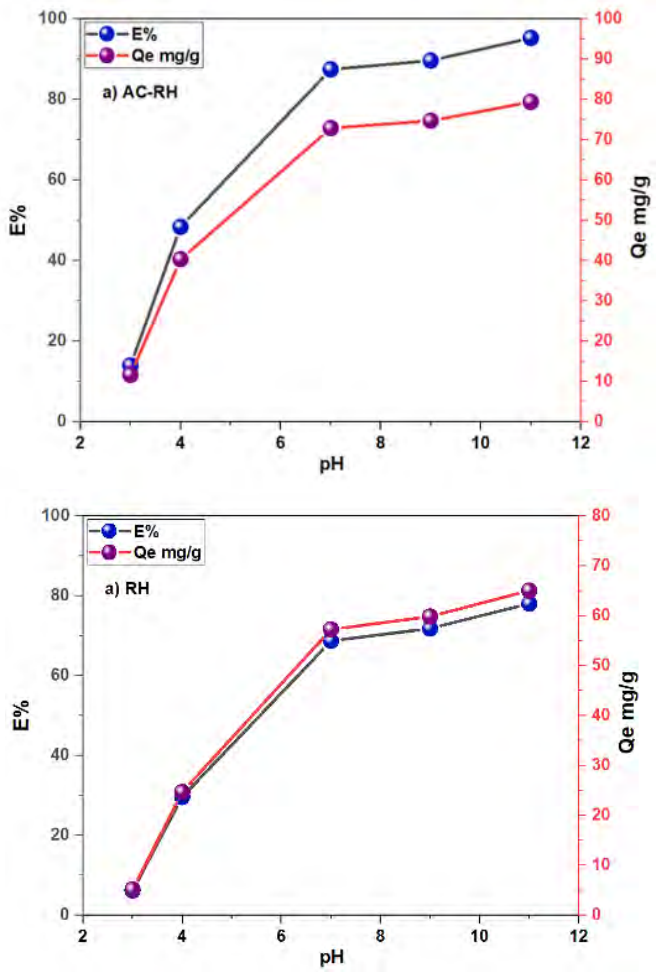

Figure 8. Effect of pH on the Removal of MV Dye (adsorbent dosage: 0.06 g; initial dye concentration: 50 mg/L; contact time: 60 min; temperature: 25°C; agitation speed: 190 rpm)

Adsorption Isotherm Curves

Adsorption isotherm models are used to correlate the amount of dye adsorbed at the solid/liquid interface with its solution concentration [41,42]. The Langmuir and the Freundlich models were used to describe the experimental data in this research. Langmuir theory assumes that adsorption occurs at a homogeneous surface, forming a saturated monolayer with no interactions among adsorbed molecules. Nevertheless, the Langmuir model did not fit the experimental data well ($R^2 = 0.8888$), as presented in Table 1. From the fitted Freundlich model, the maximum adsorption capacity was calculated to be 96.11 mg/g at 25°C. A good agreement is observed between this value and the previously reported one, indicating that the physisorption process occurs on a heterogeneous surface with a non-uniform distribution of active sites [43,44].

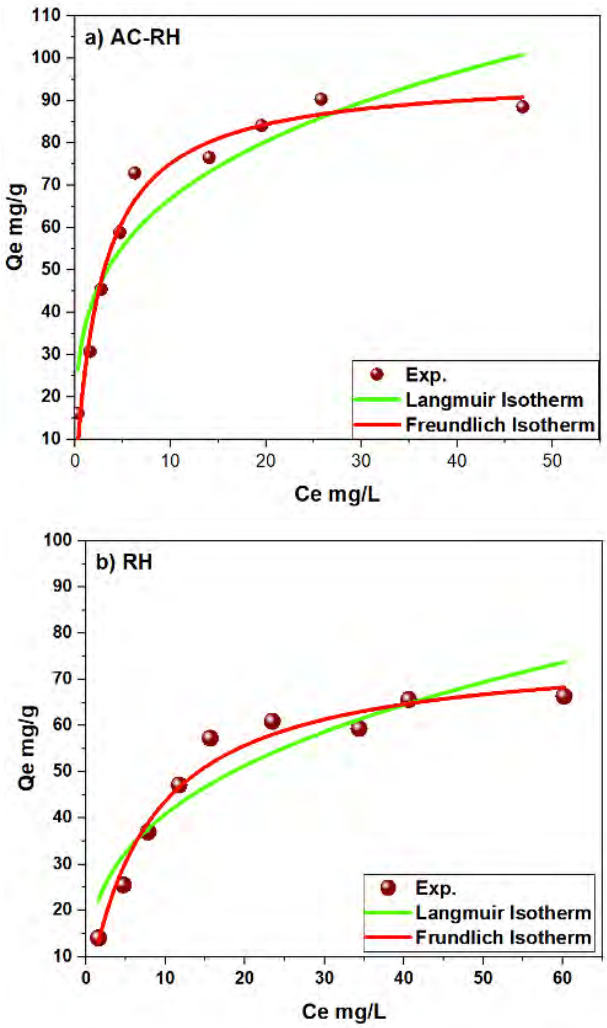

Figure 9. Isotherm Model on the Adsorption of Dye a) AC-RH b) RH

These results suggest that the Freundlich model provides a better fit for dye adsorption on H_3PO_4-modified activated carbon, as also reported elsewhere for similar adsorbents (Figure 9). Beyond statistical fitting, the better conformity of the adsorption data with the Freundlich isotherm indicates adsorption on a heterogeneous surface with multilayer formation. This behaviour is attributed to the presence of diverse functional groups and pore structures that enable multiple interactions such as electrostatic attraction, hydrogen bonding, and π–π interactions. In contrast, the Langmuir model assumes a homogeneous surface and monolayer adsorption, which may occur only at specific high-energy sites.

Table 1. Effect of Different Parameters of the Adsorption Isotherm

Isotherm	Parameter	MV dye temperature °C **25°C**
	AC-RH	
Freundlich	K_f	36.33±2.465
	1/n	0.211±0.011
	R^2	0.9788
Langmuir	$\mathbf{q_{max}}$ (mg/g)	96.11±2.22
	K_L(L/mg)	0.0355±0.002
	R^2	0.8888
	RH	
Freundlich	K_f	19.155±3.112
	1/n	0.344±0.054
	R^2	0.9456
Langmuir	$\mathbf{q_{max}}$ (mg/g)	76.22±1.55
	K_L(L/mg)	0.1±0.0015
	R^2	0.8977

Adsorption Desorption

Figure 10 illustrates the effect of regeneration cycles on the removal efficiency of methyl violet dye.

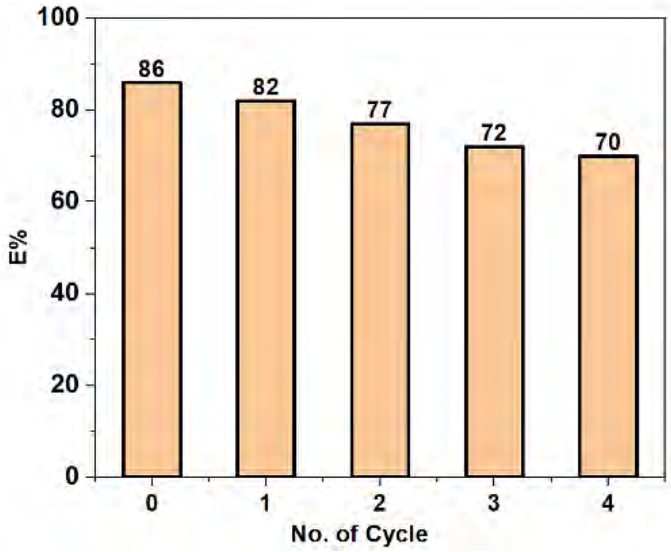

Figure 10. Effect of Regeneration of AC-RH on the Removal of MV Dye

The adsorption efficiency was initially high, reaching about 86% in the first cycle, and then gradually decreased with increasing reuse cycles to approximately 70% after the fourth cycle. This reduction can be attributed to the partial saturation of active adsorption sites, incomplete desorption of dye molecules during regeneration, and possible pore blockage or slight structural changes in the adsorbent. Nevertheless, the adsorbent maintained relatively good removal efficiency after multiple cycles, indicating acceptable stability and reusability for methyl violet removal from contaminated water [45].

4. Conclusion

This study investigated the preparation of high-surface-area, high-adsorption-efficiency activated carbon from rice husks (AC-RH) for the removal of methyl violet (MV) dye. The phosphoric acid-activated husks exhibited significantly higher adsorption efficiency compared to untreated rice husks, highlighting the role of chemical activation. Several adsorption factors were investigated, including dye concentration, activated carbon weight, and pH of solution. A maximum removal rate from an alkaline medium (pH 11) also indicated the electrostatic interaction mechanism in the adsorption process. At experimental conditions: 0.06 g/100 mL, pH 11, 25°C, the maximum adsorption performance for AC-RH was observed, with a removal rate of methyl violet (MV) as high as 87.89%, which is much higher than that of raw rice husks (68.13%). Adsorption isotherms were also analysed and were found to conform to the Freundlich adsorption model ($R^2 = 0.9788$), denoting heterogeneous multilayer adsorption on the adsorbent

surface. The best dye removal (97.66 mg/g) was achieved, significantly higher than that of untreated rice husks, confirming that chemical activation is an excellent treatment for improving surface properties and porosity. The adsorption efficiency was initially high, and then gradually decreased with increasing reuse cycles to approximately 70% after the fourth cycle. In conclusion, rice husk-derived activated carbon is a low-cost, eco-friendly, and efficient adsorbent for the removal of alkaline dyes from wastewater and can be employed as a better alternative for dye adsorption compared to conventional adsorbents.

5. References

1. Zhu H, Chen S, Luo Y. Adsorption mechanisms of hydrogels for heavy metal and organic dyes removal: A short review. *J. Agric. Food Res.*, 2023, 12, 100552. https://doi.org/10.1016/j.jafr.2023.100552
2. Bessaha F, Mahrez N, Marouf-Khelifa K, Çoruh A, Khelifa A. Removal of Congo red by thermally and chemically modified halloysite: Equilibrium, FTIR spectroscopy, and mechanism studies. *Int. J. Env. Sci. Technol.*, 2019, 16(8), 4253-4260. https://doi.org/10.1007/s13762-018-2041-z.
3. Chaudhary K, Sharma AK, Bharti P, Agrawal G. Reduced graphene oxide embedded carrageenan/acacia-based hydrogel nanocomposite for the efficient entrapment of safranine and methylene blue dyes. *J. Mol. Liq.*, 2025, 438, 128718.
4. Elelu SA, Adebayo GB, Abdus-Salam N, Iriowen EM. Preparation and characterization of adsorbents from physic nut plant (*Jatropha curcas* L). *Chemist*, 2018, 91(2), 42-49.
5. Kavitha G, Govindhan M, Premkumar S. Dye pollution and its implications for human health, aquatic ecosystems, and sustainable wastewater treatment: A comprehensive review. *J. Water Process Eng.*, 2025, 80, 109071. https://doi.org/109010.101016/j.jwpe.102025.109071
6. Khajavian M, Salehi E, Vatanpour V. Chitosan/polyvinyl alcohol thin membrane adsorbents modified with zeolitic imidazolate framework (ZIF-8) nanostructures: Batch adsorption and optimization. *Sep. Purif. Technol.*, 2020, 241, 116759.
7. Wang ZK, Li T-T, Peng HK, Ren H, Lin JH, Lou C-W. Natural-clay-reinforced hydrogel adsorbent: Rapid adsorption of heavy-metal ions and dyes from textile wastewater. *Water Env. Res.*, 2022, 94.
8. Thamer BM, Shaker AA, Abdul Hameed MM, Al-Enizi AM. Highly selective and reusable nanoadsorbent based on expansive clay-incorporated polymeric nanofibers for cationic dye adsorption in single and binary systems. *J. Water Process Eng.*, 2023, 54, 103918. https://doi.org/103910.101016/j.jwpe.102023.103918
9. Das T, Patel DK. Efficient removal of cationic dyes using lemon peel-chitosan hydrogel composite: RSM-CCD optimization and adsorption studies. *Int. J. Biol. Macromol.*, 2024, 275, 133561.
10. Aljeboree AM, Radi N, Ahmed Z, Alkaim AF. The use of sawdust as by

product adsorbent of organic pollutant from wastewater: Adsorption of Maxilon blue dye. *Int. J. Chem. Sci.*, 2014, 12(4), 1239-1252.
11. Alfatah T, Mistar EM, Supardan MD. Porous structure and adsorptive properties of activated carbon derived from *Bambusa vulgaris* striata by two-stage KOH/NaOH mixture activation for Hg^{2+} removal. *J. Water Process Eng.*, 2021, 43, 102294.
12. Ebrahimzadeh F, Akbari A. Investigation the adsorption mechanisms, chemical resistance and mechanical strength of the synthesized chitosan/activated carbon composite in methylene blue removal. *Sci. Rep.*, 2025, 15(1), 37820.
13. Hu W, Ren B, Lu D, Li B, Liu J, Liang W, Huang Y. A comprehensive evaluation of commercial activated carbon for key gasoline vapor removal based on the improved AHP method. *J. Env. Chem. Eng.*, 2024, 12(1), 111829.
14. Khan S, Ajmal S, Hussain T, Rahman MU. Clay-based materials for enhanced water treatment: Adsorption mechanisms, challenges, and future directions. *J. Umm Al-Qura Univ. Appl. Sci.*, 2025, 11(2), 219-234.
15. Li Y, Mou C, Xie Z, Zheng M. Carbon dots embedded hydrogel spheres for sensing and removing rifampicin. *Dyes Pigm.*, 2022, 198, 110023.
16. Brito LRD, Ganiyu SO, dos Santos EV, Oturan MA, Martínez-Huitle CA. Removal of antibiotic rifampicin from aqueous media by advanced electrochemical oxidation: Role of electrode materials, electrolytes and real water matrices. *Electrochim. Acta*, 2021, 396, 139254.
17. Wallenwein CM, Weigel V, Hofhaus G, Dhakal N, Schatton W, Gelperina S, Groeber-Becker FK, Dressman J, Wacker MG. Pharmaceutical development of nanostructured vesicular hydrogel formulations of rifampicin for wound healing. *Int. J. Mol. Sci.*, 2022, 23(24).
18. Zhou C, Wu Q, Lei T, Negulescu II. Adsorption kinetic and equilibrium studies for methylene blue dye by partially hydrolyzed polyacrylamide/cellulose nanocrystal nanocomposite hydrogels. *Chem. Eng. J.*, 2014, 251, 17-24.
19. Babakir BAM, Abd Ali LI, Ismail HK. Rapid removal of anionic organic dye from contaminated water using a poly(3-aminobenzoic acid/graphene oxide/cobalt ferrite) nanocomposite low-cost adsorbent via adsorption techniques. *Arabian J. Chem.*, 2022, 15(12), 104318.
20. Abbasi A, Ahmad I, Abd El-Gawad HH, Alshahrani WA, Alqarni ND, El-Bahy ZM, Ikram S. Appraisal of the adsorption potential of novel modified gellan gum nanocomposite for the confiscation of methylene blue and malachite green. *Int. J. Biol. Macromol.*, 2024, 259, 129221.
21. Dehvari M, Jamshidi B, Mansurovna BA, Babaei AA, Jorfi S. Enhancement the stability of the titanium/graphite photo-electrode in varying voltages for treatment of textile wastewater using reactive blue 19 as the model contaminant. *Sci. Rep.*, 2025, 15(1), 14446.
22. Doufene N, Benhalima T, Ferfera-Harrar H, Sadi A. Enhanced methylene blue sequestration using an eco-friendly carboxymethyl cellulose/xanthan gum-based Biocomposite combined with *Arundo donax* stem bio-waste. *Int. J. Biol. Macromol.*, 2025, 304, 141014. https://doi.org/141010.141016/j.ijbiomac.142025.141014

23. Dave PN, Kamaliya B, Macwan PM, Trivedi JH. Fabrication and characterization of a gum ghatti-cl-poly(N-isopropyl acrylamide-co-acrylic acid)/$CoFe_2O_4$ nanocomposite hydrogel for metformin hydrochloride drug removal from aqueous solution. *Curr. Res. Green Sustainable Chem.*, 2023, 6, 100349. https://doi.org/100310.101016/j.crgsc.102022.100349
24. de Farias ABV, da Costa TB, da Silva MGC, Vieira MGA. Development of novel composite adsorbents based on biopolymers/vermiculite using the ionic imprinting technique for cerium biosorption. *J. Env. Chem. Eng.*, 2022, 10(6), 108730.
25. Kareem A, Alrazak NA, Aljebori KH, Aljeboree AM, Algboory HL, Alkaim AF. Removal of methylene blue dye from aqueous solutions by using activated carbon/ureaformaldehyde composite resin as an adsorbent. *Int. J. Chem. Sci.*, 2016, 14(2), 635-648.
26. Mahdy AG, Moussa AAA, Mahmoud GE, El Refay HM. Chemical modification of rice husk surface with mixed iron–chromium oxide–hydroxide phases as an efficient adsorbent for removal of cationic dye as a pollutant. *Surf. Interfaces*, 2026, 87, 108971. https://doi.org/10.1016/j.surfin.2026.108971
27. Hadi ZA, Aljeboree AM, Alkaim AF. Adsorption of a cationic dye from aqueous solutions by using waste glass materials: Isotherm and thermodynamic studies. *Int. J. Chem. Sci.*, 2014, 12(4), 1273-1288.
28. Mosaa ZA, Bader AT, Aljeboree AM, Alkaim AF. Adsorption and removal of textile dye (methylene blue mb) from aqueous solution by activated carbon as a model (apricot stone source waste) of plant role in environmental enhancement. *Plant Arch.*, 2019, 19, 910-914.
29. Zhao Y, Chen Y, Zhao J, Tong Z, Jin S. Preparation of SA-g-(PAA-co-PDMC) polyampholytic superabsorbent polymer and its application to the anionic dye adsorption removal from effluents. *Sep. Purif. Technol.*, 2017, 188, 329-340. https://doi.org/310.1016/j.seppur.2017.1007.1044
30. Aljeboree AM. Adsorption and removal of pharmaceutical riboflavin (RF) by rice husks activated carbon. *Int. J. Pharm. Res.*, 2019, 11(2), 255-261.
31. Bessaha F, Marouf-Khelifa K, Batonneau-Gener I, Khelifa A. Characterization and application of heat-treated and acid-leached halloysites in the removal of malachite green: Adsorption, desorption, and regeneration studies. *Desalin. Water Treat.*, 2016, 57(31), 14609-14621. https://doi.org/14610.11080/19443994.19442015.11063090
32. Bhatt D, Gururani N, Srivastava A, Srivastava PC. Sorption studies of 4-NP onto goethite: Effects of contact time, pH, concentration, ionic strength and temperature. *Env. Earth Sci.*, 2021, 80(7), 273.
33. Zoya Z, Aisha A, Elham SA. Adsorption of methyl red on biogenic Ag@Fe nanocomposite adsorbent: Isotherms, kinetics and mechanisms. *J. Mol. Liq.*, 2019, 283, 287-298. https://doi.org/210.1016/j.molliq.2019.1003.1030
34. Chauhan K, Chauhan S, Kumar K, Kumari B, Gupta N, Chauhan GS. Dibutyltin dilaurate catalysed guar gum and toluene diisocyanate polyurethane foam for the removal of

malachite green from wastewater. *Polym. Int.*, 2025, 74(4), 307-323.
35. Chauhan S, Kumari B, Chauhan GS, Chauhan K, Ranote S, Kumar R, Kumar K. A highly efficient and green adsorbent for anionic dyes synthesized from whole pine needles modified with glycidyltrimethyl-ammonium chloride: Synthesis, kinetic, and thermodynamic investigation. *Biomass Convers. Biorefin.*, 2024, 14(24), 31413-31429.
36. Boudechiche N, Fares M, Ouyahia S, Yazid H, Trari M, Sadaoui Z. Comparative study on removal of two basic dyes in aqueous medium by adsorption using activated carbon from Ziziphus lotus stones. *Microchem. J.*, 2019, 146.
37. Bousemat H, Ziane-Hezil S, Bessaha F. Sustainable remediation of an anionic dye in aqueous solutions using modified aluminosilicate as a highly efficient and reusable adsorbent. *React. Kinet., Mech. Catal.*, 2025, 138(3), 1517-1534.
38. Cha B, Kim N, Yea Y, Jonghun H, Yoon Y, Kim S, Park CM. Comprehensive evaluation of antibiotic tetracycline and oxytetracycline removal by Fe-metal organic framework/biopolymer-clay hydrogel. *Ceram. Int.*, 2022, 49.
39. Chang M-Y, Juang R-S. Adsorption of tannic acid, humic acid, and dyes from water using the composite of chitosan and activated clay. *J. Colloid and Interface Sci.*, 2004, 278(1), 18-25. https://doi.org/10.1016/j.jcis.2004.1005.1029
40. Bukhari, A., Ijaz I, Zain H, Gilani E, Nazir A, Bukhari A, Raza S, Ansari J, Hussain S, Alarfaji SS, Saeed R, Naseer Y, Aftab R, Iram S. Removal of eosin dye from simulated media onto lemon peel-based low cost biosorbent. *Arabian J. Chem.*, 2022, 15(7), 103873. https://doi.org/103810.101016/j.arabjc.102022.103873
41. Chauhan S, Jamwal P, Chauhan GS, Kumar K, Kumari B, Ranote S. Tailoring of spherical nanocellulose via esterification with methionine followed by protonation to generate two different adsorbents for mercuric ions and Congo red. *Int. J. Biol. Macromol.*, 2024, 279, 135313.
42. Dai H, Huang Y, Huang H. Eco-friendly polyvinyl alcohol/carboxymethyl cellulose hydrogels reinforced with graphene oxide and bentonite for enhanced adsorption of methylene blue. *Carbohydr. Polym.*, 2018, 185, 1-11.
43. Cai Z, Zhou W, Chen W, Huang R, Zhang R, Sheng L, Shi M, Hu Y, Huang C, Chen Y. Preparation and properties of cationic starch-carrageenan-sodium alginate hydrogels with pH and temperature sensitivity. *Food Chem.*, 2024, 459, 140272. https://doi.org/140210.141016/j.foodchem.142024.140272
44. Cao L, Li N. Activated-carbon-filled agarose hydrogel as a natural medium for seed germination and seedling growth. *Int. J. Biol. Macromol.*, 2021, 177, 383-391.
45. Haghbin MR, Niknam Shahrak M, LotfiKatooli L, Mirzaei S. Potential of green-based microporous carbon for advanced water decontamination from azo dyes: Experiment and molecular dynamic simulation studies. *J. Env. Chem. Eng.*, 2024, 12(1), 111875.

The Chemist
Journal of the American Institute of Chemists

Adsorption of Brilliant Blue Dye by Synthesized g-C_3N_4: Characterization and Adsorption Parameters Insight

Manal Muhi Murad[1,2], Ayad F. Alkaim[2*]

[1]Department of Chemistry, Al-Qasim Green university, Iraq
[2]Department of Chemistry, College of Sciences for Girls, University of Babylon, Hilla, Iraq
**Corresponding author (E-mail: alkaimayad@gmail.com)*

Abstract: Graphitic carbon nitride (g-C_3N_4) has emerged as a promising metal-free nanomaterial for wastewater treatment due to its unique structural, thermal, and surface characteristics. In this study, g-C_3N_4 was successfully synthesized from melamine and thoroughly characterized using XRD, FESEM, FTIR, and EDX techniques to confirm its crystalline structure and morphology, identify the substance, and analyze its elemental composition and distribution. The synthesized material was evaluated as an efficient nanoadsorbent for the removal of Brilliant Blue dye from aqueous solutions. A comprehensive batch adsorption investigation was conducted to examine the effects of key operational parameters, including initial dye concentration, adsorbent dosage, and temperature. The results revealed that an increase in weight (0.025-0.1 g) increased the percentage of removal by 30-76% and decreased the adsorption capacity by 2.620-1.538 mg/g. When studying the effect of concentration, it was found that with an increase in concentration (1, 2, 3, 4, and 5) mg/L, the percentage of removal decreased by 40.00-13.14%, while the adsorption capacity increased by 0.8-1.3 mg/g. When studying the effect of temperature at different temperatures (40, 25, and 15)°C, it was found that the best removal was at a temperature of 40°C, where the percentage of removal decreased by 67-23.61% with an increase in concentration of 1-5 mg/L, while the adsorption capacity increased by 0.8-1.46 mg/g. This indicates that the reaction is endothermic, and, based on the R^2 value (0.9598), it follows the Freundlich model. The adsorption behavior indicated that both surface chemistry and environmental conditions play critical roles in controlling removal efficiency. Overall, this study highlights the potential of g-C_3N_4 as a high-performance nanoadsorbent for the removal of dyes from wastewater and provides valuable insights for future applications in environmental purification.

Key Words: g-C_3N_4, Brilliant Blue dye, adsorption, wastewater treatment, adsorption isotherm

1. Introduction

Chemical pollutants play a major role in the accumulation of toxins in aquatic ecosystems and bio-magnify up the food chain, ultimately affecting higher-level consumers [1]. A significant portion of the population relies on these water sources for drinking, sanitation, and recreational activities. Moreover, contaminated waterways can interfere with ecosystems, harm aquatic organisms, and diminish both environmental quality and the aesthetic value of urban areas [2,3]. The detection of chemical residues in wastewater is a growing global issue, primarily driven by human waste, inadequate disposal methods, and discharges from production facilities. These residues can often survive wastewater treatment procedures, resulting in the pollution of both surface and groundwater as well as soil, which presents serious threats to ecological systems and human health [4,5]. The presence of these chemical contaminants and dyes in water sources, even in low concentrations, poses a significant risk to human health and ecosystems. It may lead to severe mutagenic, genotoxic, and other ecotoxicological consequences for humans, animals, and plants [6,7].

Brilliant Blue (BB) is an anionic synthetic dye characterized by its vibrant, bright blue color. It is widely used across various industries, including food products, beverages, pharmaceuticals, and cosmetics. Also known as Brilliant Blue FCF, this dye features a triphenylmethane structure with the chemical composition: N-ethyl-N-(4-[(4-ethyl[(3-sulfophenyl)methyl]-amino]phenyl)(2 sulfophenyl)methylene]-2,5-cyclohexadien-1-ylidene)-3-sulfobenzene-methanaminium hydroxide inner salt, disodium salt, as shown in Figure 1(a) [8].

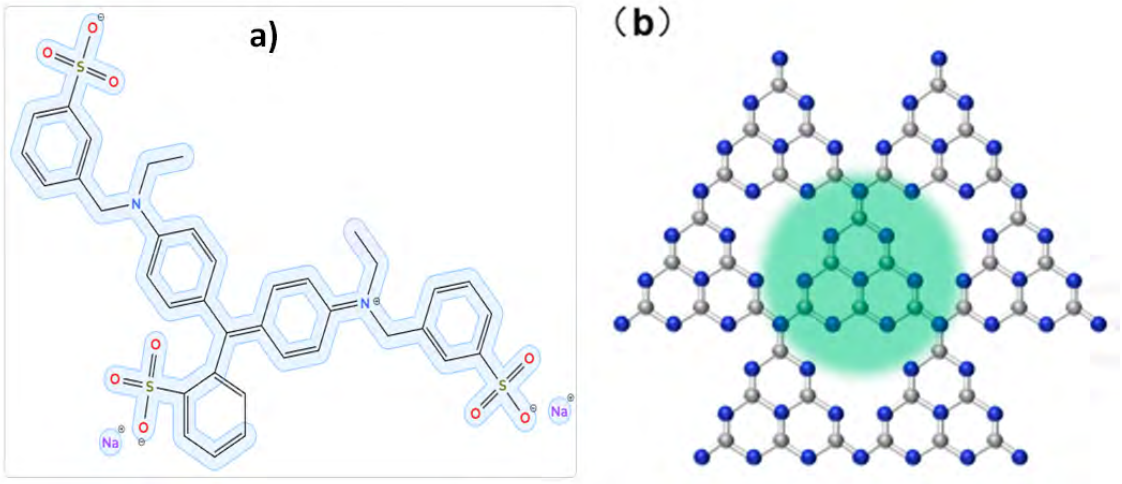

Fig 1. (a) Chemical Structure of Brilliant Blue (BB) Dye, (b) Chemical Structure of g-C_3N_4

Brilliant Blue, a widely used textile dye, persists as a non-degradable contaminant in aquatic environments. Its pronounced toxicity, vivid pigmentation, and resistance to standard treatment methods make it particularly hazardous to aquatic organisms,

presenting significant ecological risks. To address this challenge, nanotechnology—particularly the use of quantum dots (QDs)—has shown considerable promise as an innovative approach to environmental remediation [9,10]. To remove these organic dyes and eliminate their toxicity, several traditional treatment methods have been developed, including electrochemical, coagulation, ultrafiltration, photocatalysis, adsorption, and co-precipitation [11,12]. However, these techniques must be continually developed and refined to reduce operating costs [13,14]. Due to its cost-effectiveness, ease of operation, and high efficiency, the adsorption technique has become a widely adopted method for water purification [15,16]. Adsorption is a chemical and physical phenomenon that occurs as a result of forces present on the surface of a liquid or solid. Materials adhere to the surface due to these forces; as a result of a decrease in the system's free energy and entropy, adsorption occurs, a spontaneous process. Graphitic carbon nitride (g-C_3N_4), as shown in Figure 1(b), is a two-dimensional semiconductor polymer composed entirely of carbon and nitrogen, two of the most abundant elements on Earth, which together account for approximately 99% of the Earth's crust [17,18]. Graphitic carbon nitride (g-C_3N_4) exhibits exceptional physical and chemical properties, including robust chemical and thermal stability, cost-effectiveness, scalability, and environmental compatibility. These distinctive characteristics position g-C_3N_4 as a crucial material for addressing global environmental challenges through diverse applications, such as photocatalytic degradation of persistent dyes, pharmaceuticals, and pollutants; solar-driven hydrogen production; CO_2 reduction; nitrogen fixation; antimicrobial treatments; and advanced sensor technologies [19-21]. Nonetheless, pure g-C_3N_4 exhibits certain drawbacks, including limited visible-light response, a small surface area, and a low electron-hole separation rate. These negative aspects greatly diminish photocatalytic effectiveness [22,23].

The removal of dyes from aqueous solutions by adsorption is among the most effective techniques available. Consequently, adsorption methodologies facilitate the extraction of pigments from concentrated industrial effluents. Nevertheless, regenerating a significant proportion of adsorbents poses considerable challenges. Furthermore, the financial expenditure associated with adsorption processes utilizing such materials is substantial. In contemporary research, nanotechnology has emerged as one of the most noteworthy advancements for the effective removal of dyes from wastewater through adsorption. This technology demonstrates efficacy in treating water contaminated with trace amounts of organic and inorganic dyes and is more cost-effective than alternative methods. Recently, nanoparticles and nanocomposites have been identified as the most effective agents for both adsorption and photo-catalytic processes aimed at the complete removal of dyes from wastewater [24-27]. G-C_3N_4 is an organic semiconductor material with advantageous properties, including non-toxicity, reliability in terms of chemical resistance, and affordability [28].

In this study, a nanomaterial based on graphitic carbon nitride (g-C_3N_4) was synthesized from melamine, a precursor rich in carbon and nitrogen. The structural and morphological characteristics of the prepared nanomaterial were examined using XRD, SEM, FTIR, and EDX to elucidate its crystalline structure and surface morphology. The adsorption efficiency of g-C_3N_4 was subsequently evaluated for the removal of selected dye pollutants commonly found in wastewater, such as Brilliant Blue. By

measuring the absorbance of the treated sample and calculating the corresponding removal percentages, the overall performance of g-C_3N_4 as an effective adsorbent for eliminating dyes contaminants from polluted water was assessed.

2. Materials and Methods

Melamine: chemical formula ($C_3H_6N_6$) with molecular weight 126 g/mole and its purity 99.8%, production company (Zhejiang Polymer Chemical Co., Ltd.); Brilliant Blue dye: chemical formula ($C_{37}H_{34}N_2Na_2O_9S_3$) with molecular weight 792.85 g/mole and its purity 85%; ethanol: chemical formula (C_2H_5OH) with molecular weight 46.07 g/mole and its purity 70% production company (JOUDTOL); distilled water.

Preparation of g-C_3N_4

One method for producing g-C_3N_4 powder involved the direct thermal treatment of nitrogen-rich organic precursors, such as melamine. Melamine was heated to 500°C for 4 hours in a muffle furnace within a covered alumina crucible [29]. Then, the material was pulverized using a mortar and pestle. By applying this treatment, we have synthesized g-C_3N_4. Then, g-C_3N_4 was washed by ethanol to get rid of impurities. The purity of the synthesized g-C_3N_4 was confirmed through XRD, SEM, FTIR, and EDX measurements for use in this study as a nanosurface in the adsorption process.

Adsorption Study

A stock solution of Brilliant Blue dye was prepared at a concentration of 50 mg/L, and from this, different concentrations (1 , 2, 3, 4, and 5) mg/L were prepared in order to study the effect of concentration on the adsorption process of the BB dye. Then the effect of temperature for the same concentrations was also studied at (15, 20, and 40)°C, as well as the effect of surface mass (g-C_3N_4) for weights (0.025, 0.05, 0.075, 0.1) g at 25°C, after studying each effect, the prepared solutions were first and second separated using a centrifuge, and then the absorbance of the solutions was measured at the wavelength of the Brilliant Blue dye (560 nm). The removal percentage and adsorption capacity were calculated for equations 1 & 2:

$$R\% = \frac{C_o - C_e}{C_o} \times 100 \quad (1)$$

where C_o (mg/L) is the initial concentration of BB dye solution, C_e (mg/L) is the concentration of BB dye solution at equilibrium;

$$Q_e = \frac{(C_o - C_e)V}{W} \quad (2)$$

where Q_e is the adsorption capacity at equilibrium (mg/g), C_o is the initial concentration of solution (mg/L), C_e is the concentration of solution at equilibrium (mg/L), V is the volume of solution (L or ml) , and W is the mass of adsorbent (g).

3. Results and Discussion

FESEM/EDX

Scanning electron microscopy (SEM) was employed to examine the surface morphology and microstructural features of the synthesized g-C_3N_4. As shown in Figure 2(a) and (b), the material exhibits a well-defined rod-like nanostructure with relatively uniform geometry.

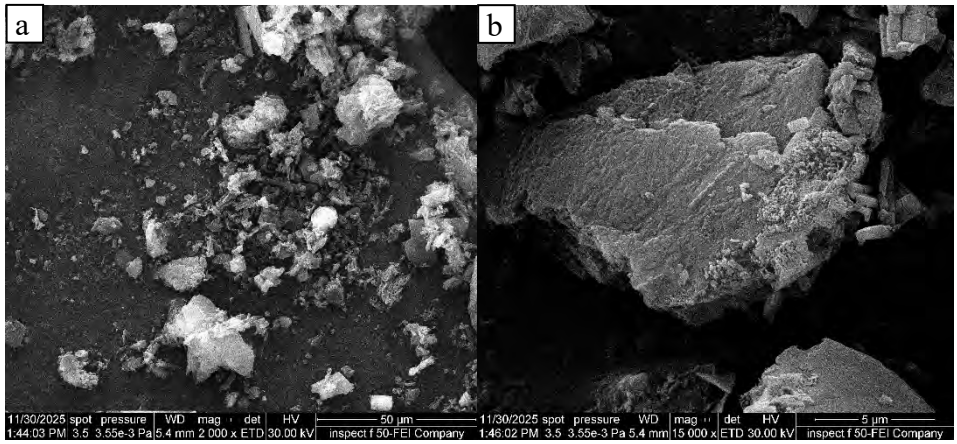

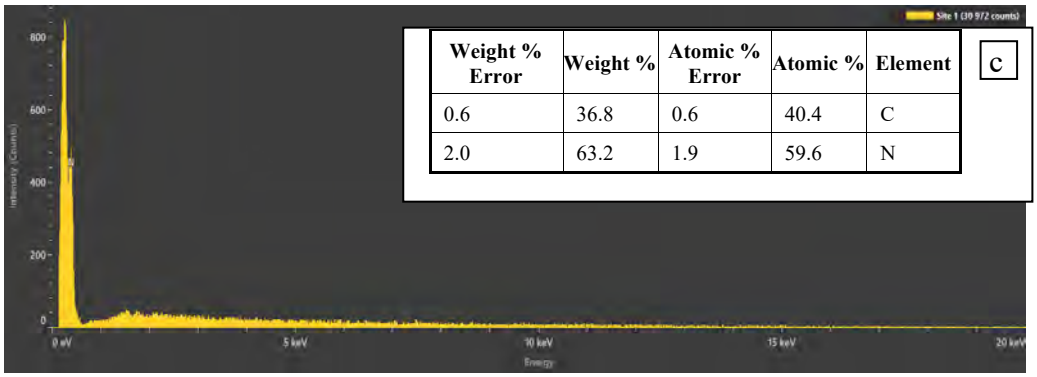

Weight % Error	Weight %	Atomic % Error	Atomic %	Element
0.6	36.8	0.6	40.4	C
2.0	63.2	1.9	59.6	N

c

Fig 2. (a-b) FESEM Image of g-C_3N_4 Nanoparticles, and (c) EDX of g-C_3N_4 Nanoparticles

The observed rods possess characteristic dimensions on the order of ~1.33 µm in length and ~50 µm in diameter, while the rod width is approximately 5 µm, indicating a highly anisotropic nanostructure. Notably, the surface of the g-C_3N_4 rods exhibits abundant nanoscale pores, cracks, and structural defects, contributing to a hierarchically porous architecture. These surface irregularities significantly increase the effective surface area and expose numerous accessible active sites [30,31]. The coexistence of mesopores and macropores, as evident in Figure 2(a) and (b), is particularly advantageous for adsorption-based wastewater treatment, as it minimizes mass-transfer resistance and facilitates rapid diffusion of organic pollutants and dye

molecules from the aqueous phase to the internal adsorption sites. Overall, the rod-like morphology, combined with the porous surface texture, enhances adsorption efficiency by promoting pollutant accessibility, accelerating transport kinetics, and improving the interaction between contaminants and the reactive surface of g-C_3N_4. This microstructural design is therefore highly favorable for applications in wastewater remediation and adsorption-driven purification processes [32,33]. EDX is a method for recognizing elements within a sample. Various shapes like squares, lines, and small areas (dots) can be analyzed using EDX. It serves as a vital research tool to enhance the efficiency of manufacturing processes. The EDX analysis (Figure 2c) confirmed that the produced g-C_3N_4 consists of Carbon (C) and Nitrogen (N) [34,35].

X-Ray Diffraction (XRD)

The crystalline structure of the synthesized g-C_3N_4 was investigated using X-ray diffracttion (XRD), and the resulting diffraction pattern is presented in Figure 3.

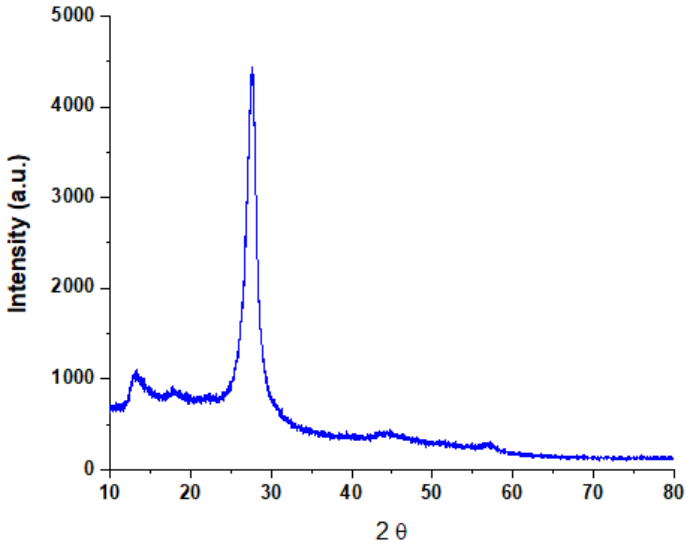

Fig 3. XRD of g-C_3N_4 Nanoparticles Surface

The diffractogram exhibits a dominant sharp diffraction peak centered at approximately $2\theta \approx 27.4°$, which is characteristic of the (002) crystallographic plane of graphitic carbon nitride. This peak corresponds to the interlayer stacking of conjugated aromatic layers, reflecting the periodic arrangement of tri-s-triazine (heptazine) units along the c-axis [36,37].

A weaker and broader diffraction feature observed in the low-angle region around $2\theta \approx 13.0°$ can be attributed to the (100) in-plane structural packing of the heptazine units. The broad nature of this peak indicates limited long-range order within the in-plane framework, which is typical of polymeric g-C_3N_4 materials synthesized via thermal polycondensation.

The pronounced intensity and sharpness of the (002) peak suggest a relatively high degree of interlayer ordering, while the overall peak broadening reflects the nano-scale dimensions and partial structural disorder of the material. The absence of

additional diffraction peaks confirms the phase purity of the synthesized g-C_3N_4, with no detectable crystalline impurities or secondary phases.

The reduced crystallinity combined with nanoscale structural disorder is advantageous for adsorption and photocatalytic applications, as it introduces defect sites and enhances surface reactivity. These structural features are consistent with the SEM observations and enhance mass transport and active-site availability during pollutant adsorption or catalytic processes [38,39].

Fourier Transform Infrared (FTIR)

Analyzing the FTIR spectra allows for a clear understanding of functional group linkages. Figure 4(a) shows the Fourier transform infrared (FTIR) spectra of g-C_3N_4, and Figure 4(b) also shows the Fourier transform infrared (FTIR) spectra of g-C_3N_4 after the adsorption of the Brilliant Blue dye.

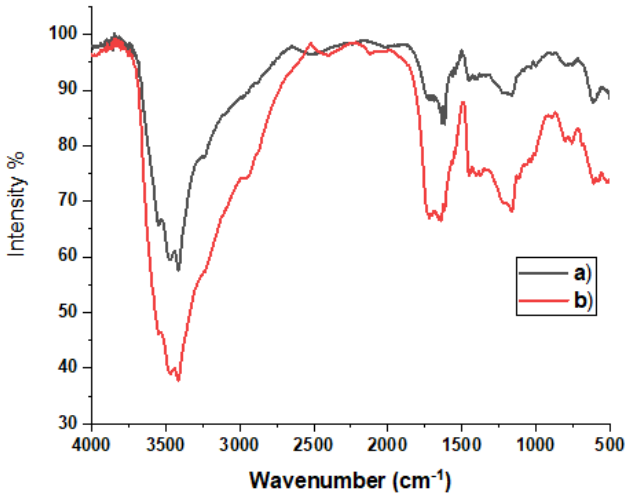

Fig 4. (a) FTIR for g-C3N4 Before Adsorption BB Dye, and (b) g-C3N4 After Adsorption BB Dye

Significant changes appeared in the Fourier transform infrared spectrum of the compound after the adsorption of Brilliant Blue dye. A slight shift in the N-H expansion band was observed, from 3090 cm^{-1} to 3080-3045 cm^{-1} [40,41]. This suggests possible interactions between the amine groups of the g-C_3N_4 surface and the sulfonate or aromatic groups of the dye molecules. Furthermore, more intense C=N, C-N bands were observed in the region between 1400-1600 cm^{-1}, possibly due to л - л stacking interactions between the aromatic rings of Brilliant Blue and the conjugated heptazine units of g-C_3N_4. Additional new peaks appeared at 1483, 1458, 1433, 1330, 1244, and 1209 cm^{-1} after adsorption. Overall, the appearance of new functional group vibrations, intensity changes, and spectral shifts indicates successful adsorption Brilliant Blue dye on the surface of g-C_3N_4 [42].

Adsorbent Dosage

One of the most important factors affecting the adsorption process is the weight of the adsorbent. Different amounts of g-C_3N_4 (0.025-0.1 g) on the adsorption of a dye (5 mg/L dye solution at pH 7), while keeping all other parameters constant, the solutions were shaken for 60 min at 25°C. Figure 5 shows that the amount of adsorbent material is directly related to the percentage removal, with higher pollutant uptake observed as the adsorbent dose increases.

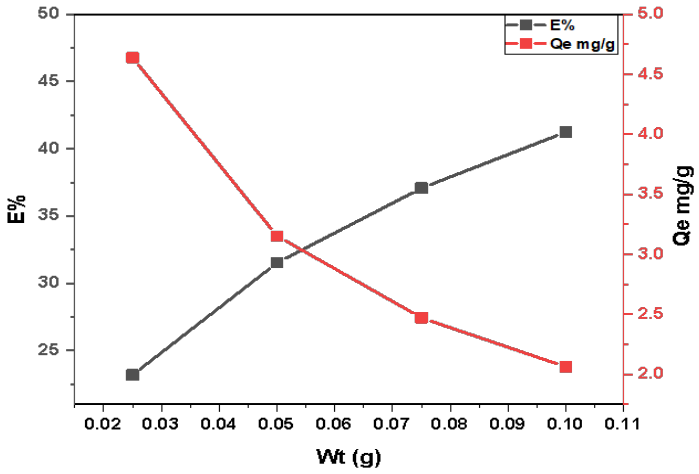

Fig 5. Effect of the Weight of g-C_3N_4 on the Removal of BB Dye

A higher adsorbent dose increases the number of active exchangeable sites on its surface, thereby facilitating ion capture. Furthermore, lower doses of adsorbents accelerate the adsorption rate due to the greater abundance of accessible active sites. Conversely, when a high adsorbent dose is used, dye ions may be unable to reach the adsorption sites until equilibrium is established. In general, increasing the adsorbent dose can reduce the total solute adsorption per unit mass of adsorbent due to interactions among the adsorbent's active sites.[1,38,43].

Effect of Concentration

Figure 6 shows solutions prepared at different concentrations (1-5) mg/L under the same conditions of weight (0.05 g) and temperature (25°C), where the adsorption capacity increases with increasing concentration and, therefore, the percentage of removal decreases with increasing concentration.

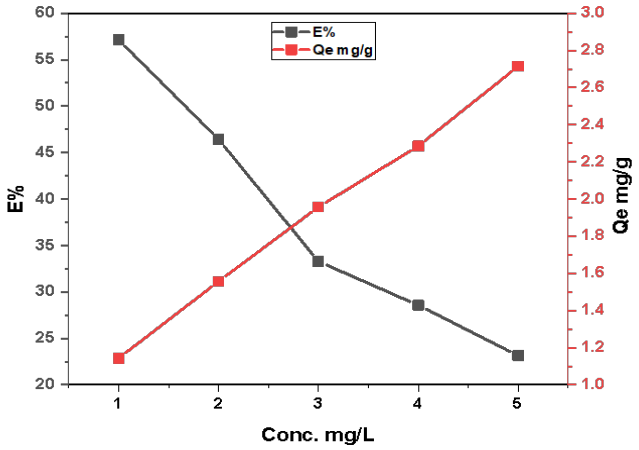

Fig 6. Effect of Concentration of BB Dye Solution on Adsorption Process

The dye molecules become more saturated with the adsorbent or surfaces, competing for the limited active sites, thus reducing the ability of the adsorbent or process to remove a greater percentage of the dye. The removal of dyes through sorption is closely related to their starting concentration [44,45]. This relationship is associated with the number of available active sites on the adsorbent and the concentration of dye molecules. In general, the initial dye concentration in water plays a crucial role as a driving force, facilitating mass transfer from the bulk solution to the adsorbent surface. Consequently, as the initial dye concentration increases, the driving forces also become stronger. Thus, in solutions with a high concentration of dye, the molecules encounter greater difficulty in locating binding sites on the adsorbent's surface [46,47].

Effect of Temperature

g-C_3N_4 was employed as a nanomaterial adsorbent for the treatment of contaminated dyes, specifically Brilliant Blue, under various temperature conditions (15, 25, and 40) °C and different concentrations of 1-5 mg/L of BB dye, as shown in Figure 7. The most effective adsorption was observed at 40°C.

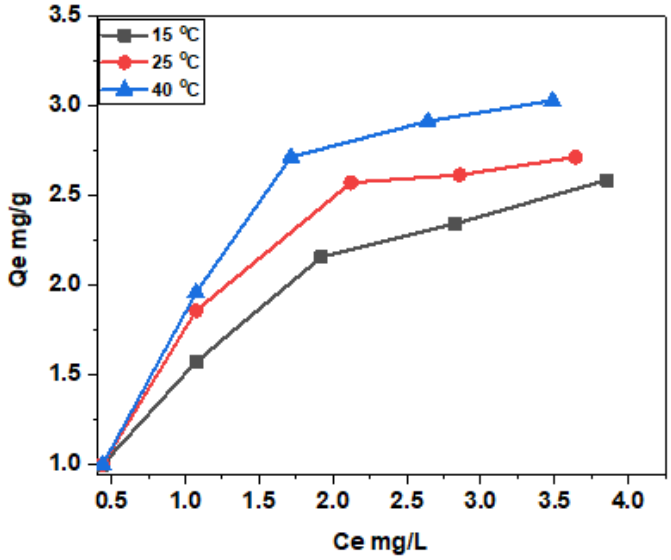

Fig 7. Temperature Effect on Adsorption of BB Dye

This is because raising the temperature provides the energy required for dye molecules to adhere to the g-C_3N_4 adsorbent surface. It is well known that physical adsorption is an endothermic process; as temperature rises, adsorption efficiency increases, leading to a higher removal percentage. Consequently, increasing the temperature increases the adsorption rate because the dye molecules have higher kinetic energy. This results in higher diffusion and adsorption rates, facilitating the establishment of equilibrium between the adsorbent, g-C_3N_4 , and the adsorbate, Brilliant Blue dye. Moreover, higher temperatures yielded optimal conditions for physical adsorption [48-50].

Thermodynamic Parameters

Thermodynamic analysis was performed to evaluate the feasibility and spontaneity of the sorption process. Key thermodynamic parameters, including the Gibbs free energy change (ΔG°), enthalpy change (ΔH°), and entropy change (ΔS°), were determined using the Van't Hoff approach [51]. The values of ΔH° and ΔS° were obtained from the slope and intercept of the linear plot of ln Kd versus 1/T (Figure 8), respectively, according to equation 3:

$$\ln K_d = \frac{\Delta S^\circ}{R} - \frac{\Delta H^\circ}{RT} \quad (3)$$

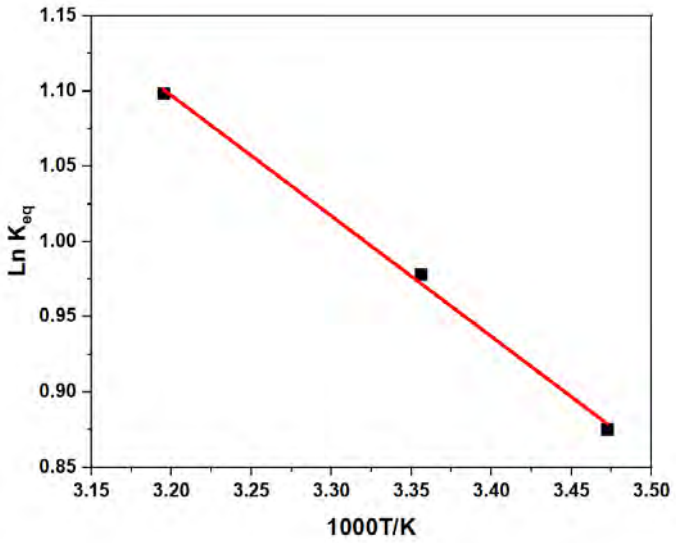

Fig 8. Van't Hoff's Plot on the Removal BB Dye onto g-C_3N_4 Nanoparticles

The thermodynamic parameters associated with adsorption from solutions offer significant insights into the nature and mechanism of the adsorption process. The standard Gibbs free energy change ΔG is computed as follows (equation 4):

$$\Delta G^\circ = - RT \ln K \quad (4)$$

A negative Gibbs free energy indicates the viability and spontaneity of the adsorption process [52].

The thermodynamic factors presented in Table 1 provide essential insight into the nature of BB dye adsorption onto g-C_3N_4. The positive ΔH values confirm that the adsorption process is endothermic, consistent with the observed decrease in Q_{max} as temperature increases. Moreover, the magnitude of ΔH 6.666 kJ mol^{-1}) is well below 40 kJ mol^{-1}, indicating that the adsorption is dominated by physisorption, where reversible intermolecular forces govern the interaction between the dye molecules and the adsorbent surface [53,54].

Table 1. Thermodynamic Factors for the Adsorption of BB onto g-C_3N_4 Nanoparticles

T/K	*ΔG°* *(kJ.mol^{-1})*	*ΔH°* *(kJ.mol^{-1})*	*ΔS°* *(J.K^{-1}.mol^{-1})*
288	-0.8674	6.666	30.435
298	-0.647		
313	-0.366		

From the values of Free Gibbs Energy (ΔG°) in Table 1 for all temperatures (15, 25, 40) °C are negative (-0.867, -0.647, and -0.366) kJ/mol. Respectively, this means the

adsorption process is spontaneous through this range of temperature [55].

A positive value of entropy ΔS° (30.435)kJ/K mol indicates increased randomness in (solid-liquid) adsorption systems due to structural changes in the surface of the adsorbent material during the process [49,56,57].

Adsorption isotherm

To assess the distribution of the adsorbate from the liquid phase to the solid phase until equilibrium is reached under controlled (constant) conditions, it is essential to utilize an instrument for studying adsorption isotherms [58,59]. In this research, the Langmuir and the Freundlich models were utilized to assess the adsorption properties. The Langmuir isotherm postulates that adsorption occurs in a monolayer on a surface with a limited number of uniform sites and that there is no interaction among the adsorbed molecules. It can be represented as (equation 5):

$$Q_e = \frac{q_m K_L C_e}{1+K_L C_e} \quad (5)$$

where q_e refers to the quantity of adsorbate that is adsorbed at equilibrium (mg /g), q_{max} signifies the maximum adsorption capacity achievable when monolayer coverage is complete (mg/g), C_e indicates the equilibrium concentration of the adsorbate present in solution (mg/L), and KL represents the Langmuir equilibrium constant, which is associated with the affinity for binding sites (L /mg) [3,60].

An empirical model that characterizes adsorption onto heterogeneous surfaces with a non-uniform distribution of adsorption heat is the Freundlich isotherm. Its equation is as follows (equation 6):

$$q_e = K_f C_e^{1/n} \quad (6)$$

The q_e is the amount of adsorbate adsorbed at equilibrium (mg/g), K_F is the Freundlich constant that indicates the adsorption capacity ($mg1^{-1}/n\ g^{-1}L1/n$), C_e is the equilibrium concentration of the adsorbate in solution (mg/L), and n is the heterogeneity factor (dimensionless), with values of $1 < n < 10$ indicating favorable adsorption [61,62].

The results in Table 2 indicate that the adsorption process occurred on a heterogeneous surface and may involve multilayer adsorption. The Freundlich model provides the best fit to the data ($R^2 = 0.9598$), indicating that the surface is heterogeneous and that adsorption occurs at sites with different energies. However, the Langmuir model also yielded good results ($R^2 = 0.9544$), as the difference between the two models is minimal.

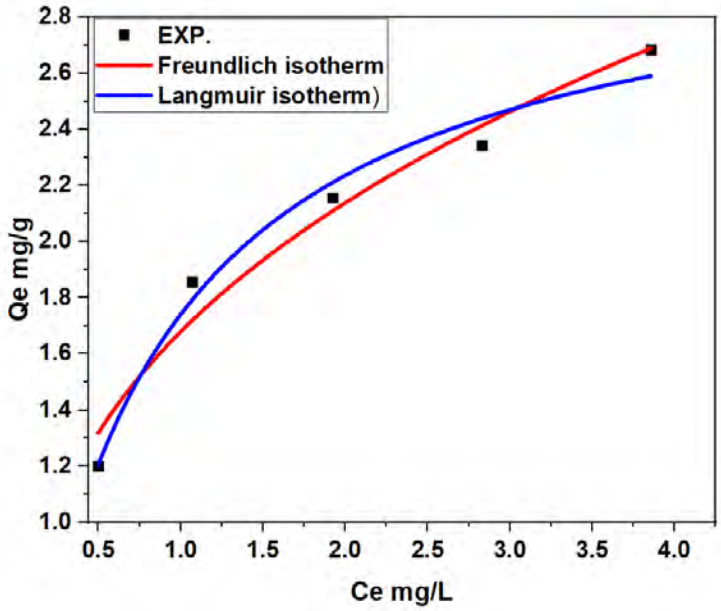

Fig 9. Adsorption Models Freundlich and Langmuir Isotherms

Figure 9 shows that the adsorption of Brilliant Blue dye best follows the Freundlich model. This indicates a heterogeneous distribution of adsorption sites on the adsorbent surface, as the increase in adsorption efficiency (Q_e) with increasing equilibrium concentration (C_e) reflects g-C_3N_4's efficiency in removing the dye at high concentrations [63,64].

Table 2. Adsorption Isotherm Models of the Freundlich and Langmuir

Nonlinear adsorption isotherm model		
Isotherm	**Parameter**	**Dye Temperature 25°C**
Freundlich	K_f	1.6.02 ± 0.044
	1/n	0.32 ± 0.022
	R^2	0.9598
Langmuir	q_m(mg/g)	2.88±0.023
	K_L(L/mg)	0.3111± 0.0113
	R^2	0.9544

4. Conclusion

The synthesized adsorbent exhibited an efficient adsorption performance toward the target pollutant, which can be attributed to its porous structure and the availability of

abundant active sites that facilitate mass transfer and surface interactions. Adsorption experiments demonstrated that initial concentration, temperature, and adsorbent dose significantly influence the adsorption behavior, confirming the dominant role of electrostatic interactions and mediated effects. Thermodynamic analysis revealed negative ΔG° values, indicating that the adsorption process is spontaneous, while the positive ΔH° value confirmed its endothermic nature. The positive ΔS° further suggested increased randomness at the solid–solution interface during adsorption. Overall, the results confirm that the adsorption process is feasible and energetically favorable. These findings highlight the potential of the prepared material as an effective adsorbent for wastewater treatment and provide a useful basis for future optimization and practical applications. Based on the R^2 value (0.9598), the data follows the Freundlich model. The adsorption behavior indicated that both surface chemistry and environmental conditions play critical roles in controlling removal efficiency.

5. References

1. Hameed BH, El-Khaiary MI. Sorption kinetics and isotherm studies of a cationic dye using agricultural waste: broad bean peels. *J. Hazard. Mater.*, 2008, 145. 639-648.
2. Huan S. Identifying complex relationship in sub-fields between digital economy and urban ag-glomeration water pollution in Yangtze River Economic Belt: Evidence from original large-scale social media text analysis. *Chaos, Solitons Fractals*, 2025, 200, 117016.
3. Habila MA, Alothman ZA, Ali R, Ghafar AA, Hassouna MSE-D. Removal of tartrazine dye onto mixed-waste activated carbon: Kinetic and thermodynamic studies. *Clean: Soil, Air, Water*, 2014, 42(12), 1824-1831.
4. Mohd Hanafiah Z, Wan Mohtar WHM, Abdul Maulud KN, Wan-Mohtar WAAQI, Ebrahim MN, Binti Abd Manan TS, Indarto A, Afan HA, Yaseen ZM. Global pharmaceutical pollution in waterways: Insights from sewage treatment point sources. *Emerging Contam.*, 2025, 11(4), 100585.
5. Haghbin MR, Niknam Shahrak M, LotfiKatooli L, Mirzaei S. Potential of green-based microporous carbon for advanced water decontamination from azo dyes: Experiment and molecular dynamic simulation studies. *J. Env. Chem. Eng.*, 2024, 12(1), 111875.
6. Meenu O, Samuel EJJ. Can manganese-based ternary photocatalysts provide effective solutions for pharmaceutical pollution in aquatic environments? A comprehensive review. *Inorg. Chem. Commun.*, 2026, 183, 115641.
7. Mosaa ZA, Bader AT, Aljeboree AM, Alkaim AF. Adsorption and removal of textile dye (methylene blue mb) from aqueous solution by activated carbon as a model (apricot stone source waste) of plant role in environmental enhancement. *Plant Arch.*, 2019, 19, 910-914.
8. Sreelekshmi RC, Govindasamy M, Saraswathyamma B. Synergistic RuS_2/CeS_2 nano-hybrid for electrochemical detection of Brilliant Blue dye. *J. Food Eng.*, 2026, 403, 112731.

9. Azzam MM, Labib AA, Handal HT, Mousa HA, Galal HR, Ibrahem IA, Fawzy MM, Ahmed MAM, Rwayhah YMN, Mohamed WAA. Study of photophysical properties on recycling for solar and photo degradation process of Brilliant Blue R dye and real industrial wastewater using Bentonite/TiO_2 QDs. *Mater. Sci. Eng.: B*, 2025, 314, 117991.
10. Zhou Z, Lin S, Yue T, Lee T-C. Adsorption of food dyes from aqueous solution by glutaraldehyde cross-linked magnetic chitosan nanoparticles. *J. Food Eng.*, 2014, 126, 133-141.
11. Jamalabad GS, Mohagheghi MMB. Effect of GO and rGO on the photocatalytic and adsorption properties of $SnFe_2O_4$ for crystal violet dye removal. *Eur. Phys. J. Plus*, 2025, 140(11).
12. Egerić M, Petrović D, Vujasin R, Wu YN, Li F, Janolin PE, Matović L, Devečerski A. Enhanced adsorption–photocatalytic degradation of the Congo red dye in the presence of the MOF/activated carbon composite catalysts. *Water (Switz.)*, 2025, 17(24).
13. Akhtar MN, Ghaffar J, Sheikh TA, Raza MA, Michalczyk M, Zierkiewicz W, Latif S, Alshammari AQ, Alshammari A, Imran M, Aldamen MA, Ahmed M. Experimental and theoretical insight into the adsorption mechanism of organic dye by a paddle wheel type Cu(II) complex. *J. Mol. Struct.*, 2026, 1351, 144240.
14. Hasan MM, Fatema Tuj Z. Valorized oxalic acid treated onion peel (*Allium cepa*) and jute stick (*Chorchorus olitorius*) wastes for dye removal from tannery effluents. *Desalin. Water Treat.*, 2024, 319, 100554.
15. Moatamed Sabzevar A, Ahmadpour A, Ghahramaninezhad M, Arami-Niya A. Tuning cross-linker type in the fabrication of beta-cyclodextrin/magnetic lignin adsorbents: Comparative study of cationic dye adsorption performance. *Env. Technol. Innovation*, 2025, 40, 104507.
16. Kareem A, Alrazak NA, Aljebori KH, Aljeboree AM, Algboory HL, Alkaim AF. Removal of methylene blue dye from aqueous solutions by using activated carbon/urea formaldehyde composite resin as an adsorbent. *Int. J. Chem. Sci.*, 2016, 14(2), 635-648.
17. Ravichandran B, Zhang W, Liu H, Khotseng L, Su H. Graphitic carbon nitride (g-C_3N_4) in fuel cells: A comprehensive review of synthesis, functionalization, and multifaceted electrocatalytic roles. *J. Alloys Compd.*, 2025, 1042, 183989.
18. Eti IA, Khatun M, Khatun MA, Rahman MO, Anis-Ul-Haque KM, Alam MJ. Removal of dye from wastewater using a novel composite film incorporating nanocellulose. *Adv. Polym. Technol.*, 2023, 2023(1), 4431941.
19. Bijari M, Shahbazi A. Flow-driven engineering of g-C_3N_4 nanosheet for additive-free, one-step, and sustainable synthesis of high-efficiency photocatalysts. *Mater. Today Commun.*, 2025, 114208.
20. Etemadi H, Afsharkia S, Zinatloo-Ajabshir S, Shokri E. Effect of alumina nanoparticles on the antifouling properties of polycarbonate-polyurethane blend ultrafiltration membrane for water treatment. *Polym. Eng. Sci.*, 2021, 61(9), 2364-2375.
21. Fatimah I, Fadillah G, Sahroni I, Kamari A, Sagadevan S, Doong R-A. Nanoflower-like composites of ZnO/SiO_2 synthesized using bamboo leaves ash as reusable photocatalyst. *Arabian J. Chem.*, 2021, 14(3), 102973.
22. Luo Y, Zhu Y, Han Y, Ye H, Liu R, Lan Y, Xue M, Xie X, Yu S, Zhang L.

g-C_3N_4-based photocatalysts for organic pollutant removal: A critical review. *Carbon Res.*, 2023, 2(1), 14.
23. Esmaeili H, Foroutan R. Adsorptive behavior of methylene blue onto sawdust of sour lemon, date palm, and eucalyptus as agricultural wastes. *J. Dispersion Sci. Technol.*, 2018, 40(7), 990-999. https://doi.org/910.1080/01932691.01932018.01489828
24. Modwi A, Elamin MR, Idriss H, Elamin NY, Adam FA, Albadri AE, Abdulkhair BY. Excellent adsorption of dyes via $MgTiO_3$@g-C_3N_4 nanohybrid: Construction, description and adsorption mechanism. *Inorganics*, 2022, 10(11), 210.
25. Aljeboree AM, Alkaim AF. Comparative removal of three textile dyes from aqueous solutions by adsorption: As a model (corn-cob source waste) of plants role in environmental enhancement. *Plant Arch.*, 2019, 19(1), 1613-1620.
26. Hayeeye F, Sattar M. Removal of crystal violet in aqueous solution by activated carbon from the pericarp of rubber fruit and bagasse: Kinetics, thermodynamics and adsorption studies. *Desalin. Water Treat.*, 2020, 202 420-434.
27. Elelu SA, Adebayo GB, Abdus-Salam N, Iriowen EM. Preparation and characterization of adsorbents from physic nut plant (*Jatropha curcas* L). *Chemist*, 2018, 91(2) 42-49.
28. Elamin MR, Ben Aissa MA, Al-Ayed AS, Modwi A. Adsorption performance of Congo red and malachite green in binary system using Co_3O_4 and Fe_2O_3 co-doped g-C_3N_4. *Inorg. Chem. Commun.*, 2026, 186, 116258.
29. Zhang H, Huang J, Zhong M, He F, Dong N, Su B, Lei Z. S-scheme g-C_3N_4/Bi_2MoO_6 heterojunction for enhanced adsorption and visible-light photocatalytic removal of antibiotics: Mechanistic insights and transformation pathways. *J. Photochem. Photobiol., A*, 2026, 476, 117098.
30. Zubair M, Manzar MS, Mu'azu ND, Anil I, Blaisi NI, Al-Harthi MA. Functionalized MgAl-layered hydroxide intercalated date-palm biochar for enhanced uptake of cationic dye: Kinetics, isotherm and thermodynamic studies. *Appl. Clay Sci.*, 2020, 190, 105587.
31. Zoya Z, Aisha A, Elham SA. Adsorption of methyl red on biogenic Ag@Fe nanocomposite adsorbent: Isotherms, kinetics and mechanisms. *J. Mol. Liq.*, 2019, 283, 287-298. https://doi.org/210.1016/j.molliq.2019.1003.1030
32. Garg R, Gupta R, Bansal A. Synthesis of g-C_3N_4/ZnO nanocomposite for photocatalytic degradation of a refractory organic endocrine disrupter. *Mater. Today: Proc.*, 2021, 44, 855-859.
33. Zinatloo-Ajabshir S, Mortazavi-Derazkola S, Salavati-Niasari M. Nd_2O_3-SiO_2 nanocomposites: A simple sonochemical preparation, characterization and photocatalytic activity. *Ultrason. Sonochem.*, 2018, 42, 171-182.
34. Chabib L, Miskam M, Kaus NHM, Shafie MH, Hamid M, Saragi IR, Isnaeni I, Amilia D, Dalimunthe IB, Wijoyo H. Optimization of g-C_3N_4 nanoparticles on structural, morphological, and optical properties as organic pollutants adsorbent in glycerin. *Case Stud. Chem. Env. Eng.*, 2025, 11, 101057.
35. Zinatloo-Ajabshir S, Ahmadi-Zeidabadi M, Amiri M, Sharifianjazi F. Innovative sono-synthesis of cerium dioxide nanomaterials using mentha extract

with efficient activity for cancer therapy application. *Results Eng.*, 2024, 23, 102720. https://doi.org/102710.101016/j.rineng.102024.102720
36. Zhokh A, Strizhak P. Crossover between Fickian and non-Fickian diffusion in a system with hierarchy. *Microporous Mesoporous Mater.*, 2019, 282, 22-28. https://doi.org/10.1016/j.micromeso.2019.1003.1016
37. Zheng X, Li X, Li J, Wang L, Jin W, Liu J, Pei Y, Tang K. Efficient removal of anionic dye (Congo red) by dialdehyde microfibrillated cellulose/chitosan composite film with significantly improved stability in dye solution. *Int. J. Biol. Macromol.*, 2018, 107, 283-289.
38. Sabah NA, Aljeboree A, Jasim KK. Eco-friendly and low-cost hydrogel nanocomposite to efficiently remove textile dye from aqueous solution: Thermodynamics and regeneration study. *J. Nanostruct.*, 2025, 15(1), 210-218.
39. Zhao Y, Zhou H, Song M, Xu Z, Sun Z, Xu Q, Chen Y, Liao X. Interface engineering of Ti-MOFs: Adsorption of anionic, cationic and neutral dyes in wastewater. *J. Mol. Struct.*, 2023, 1283, 135268.
40. Zhang L, Sellaoui L, Franco D, Dotto GL, Bajahzar A, Belmabrouk H, Bonilla-Petriciolet A, Oliveira MLS, Li Z. Adsorption of dyes Brilliant Blue, sunset yellow and tartrazine from aqueous solution on chitosan: Analytical interpretation via multilayer statistical physics model. *Chem. Eng. J.*, 2020, 382, 122952.
41. Zainul R, Basem A, Nemah AK, Kumar R, Kumar R, Sharma R, Aljeboree AM, Chahar M, Elmasry Y. BP-biphenylene monolayers: A promising anode material for high-performance magnesium-ion batteries. *Inorg. Chem. Commun.*, 2024, 168.
42. Li K, Chen M, Chen L, Zhao S, Xue W, Han Z, Han Y. Synthesis of g-C_3N_4 derived from different precursors for photodegradation of sulfamethazine under visible light. *Processes*, 2023, 11(2), 528.
43. Hameed BH. Equilibrium and kinetic studies of methyl violet sorption by agricultural waste. *J. Hazard. Mater.*, 2008, 154, 204-212.
44. Hadi ZA, Aljeboree AM, Alkaim AF. Adsorption of a cationic dye from aqueous solutions by using waste glass materials: Isotherm and thermodynamic studies. *Int. J. Chem. Sci.*, 2014, 12(4), 1273-1288.
45. Hameed Mahmood Z, Riadi Y, Hammoodi HA, Alkaim AF, Fakri Mustafa Y. Magnetic nanoparticles supported copper nanocomposite: A highly active nanocatalyst for synthesis of benzothiazoles and polyhydroquinolines. *Polycyclic Aromat. Compd.*, 2023, 43(4), 3687-3705.
46. Long R, Yu Z, Tan Q, Feng X, Zhu X, Li X, Wang P. Ti_3C_2 MXene/NH2-MIL-88B (Fe): Research on the adsorption kinetics and photocatalytic performance of an efficient integrated photocatalytic adsorbent. *Appl. Surf. Sci.*, 2021, 570, 151244.
47. Rahul null, Jindal R. Efficient removal of toxic dyes malachite green and fuchsin acid from aqueous solutions using Pullulan/CMC hydrogel. *Polymer*, 2024, 307, 127203. https://doi.org/127210.121016/j.polymer.122024.127203
48. Aljeboree AM, Abbas AS. Removal of pharmaceutical (paracetamol) by using CNT/ TiO_2 nanoparticles. *J. Global Pharma Technol.*, 2019, 11(1): 199-

205.
49. Sharma AK, Priya null, Kaith BS, Sharma N, Bhatia JK, Tanwar V, Panchal S, Bajaj S. Selective removal of cationic dyes using response surface methodology optimized gum acacia-sodium alginate blended superadsorbent. *Int. J. Biol. Macromol.*, 2019, 124, 331-345. https://doi.org/310.1016/j.ijbiomac.2018.1011.1213
50. Sharma AK, Dhiman A, Nayak AK, Mishra R, Agrawal G. Environmentally benign approach for the efficient sequestration of methylene blue and Coomassie Brilliant Blue using graphene oxide emended gelatin/ϛ-carrageenan hydrogels. *Int. J. Biol. Macromol.*, 2022, 219, 353-365. https://doi.org/310.1016/j.ijbiomac.2022.1007.1216
51. Serban GV, Iancu VI, Dinu C, Tenea A, Vasilache N, Cristea I, Niculescu M, Ionescu I, Chiriac FL. Removal efficiency and adsorption kinetics of methyl orange from wastewater by commercial activated carbon. *Sustainability*, 2023, 15, 12939. DOI: 10.3390/su151712939
52. Sahmoune MN. Evaluation of thermodynamic parameters for adsorption of heavy metals by green adsorbents. *Env. Chem. Lett.*, 2019, 17(2), 697-704.
53. Boparai HK, Joseph M, O'Carroll DM. Kinetics and thermodynamics of cadmium ion removal by adsorption onto nano zerovalent iron particles. *J. Hazard. Mater.*, 2011, 186(1), 458-465.
54. Bazargan-Lari R, Zafarani HR, Bahrololoom ME, Nemati A. Removal of Cu(II) ions from aqueous solutions by low-cost natural hydroxyapatite/chitosan composite: Equilibrium, kinetic and thermodynamic studies. *J. Taiwan Inst. Chem. Eng.*, 2014, 45(4) 1642-1648.
55. Girish CR. Determination of thermodynamic parameters in adsorption studies: A review. *Chem. Pap.*, 2025, 79(9), 5687-5706.
56. Xue J, Ji M, Lu Y, Pan D, Yang X, Yang X, Xu Z. The impact of chemical properties of the solid–liquid–adsorbate interfaces on the entropy–enthalpy compensation involved in adsorption. *Phys. Chem. Chem. Phys.*, 2024, 26(11), 8704-8715.
57. Shahcheragh SK, Bagheri Mohagheghi MM, Shirpay A. Effect of physical and chemical activation methods on the structure, optical absorbance, band gap and Urbach energy of porous activated carbon. *SN Appl. Sci.*, 2023, 5(12), 313.
58. Alibrahim KA. The adsorption behaviors of industrial dyes by natural mordenite: isotherm, kinetic, thermodynamic, and Box–Behnken design study. *Desalin. Water Treat.*, 2023, 298, 155-173.
59. Junejo R, Shams Jalbani N, Kaya S, Serdaroglu G, Şimşek S, Memon S. Experimental and DFT modeling studies for the adsorptive removal of reactive dyes from wastewater. *Sep. Sci. Technol.*, 2022, 57(3), 339-353.
60. Gutiérrez P, Aldas M, Gavilanes D, Cadena F, Valle V. Corn cob valorization: Synthesis of a polymer based on crystalline cellulose with poly(ethylene glycol) diacrylate and N-vinylcaprolactam. *Cleaner Eng. Technol.*, 2025, 27, 101019.
61. Guerra-Que Z, López-Margalli KS, Urrieta-Saltijeral JM, Silahua-Pavón AA, Martínez-García H, García-Alamilla P, Córdova-Pérez GE, Arévalo-Pérez JC, Torres-Torres JG. Activated carbon synthesised from lignocellulosic cocoa pod husk via alkaline and acid treatment for methylene blue adsorption:

Optimisation by response surface methodology, kinetics, and isotherm modelling. *RSC Adv.*, 2025, 15(55), 47231-47254.

62. Kumari B, Chauhan S, Chauhan GS, Kumar K, Jamwal P, Ranote S. A two-in-one thiosemicarbazide and whole pine needle-based adsorbent for rapid and efficient adsorption of methylene blue dye and mercuric ions. *Env. Sci. Pollut. Res.*, 2024, 31(14), 21591-21609. https://doi.org/21510.21007/s11356-21024-32446-21593
63. Shubha JP, Kavalli K, Adil SF, Assal ME, Hatshan MR, Dubasi N. Facile green synthesis of semiconductive ZnO nanoparticles for photocatalytic degradation of dyes from the textile industry: A kinetic approach. *J. King Saud Univ., Sci.*, 2022, 34(5), 102047.
64. Sharma S, Sharma G, Kumar A, AlGarni TS, Naushad M, Alothman ZA, Stadler FJ. Adsorption of cationic dyes onto carrageenan and itaconic acid-based superabsorbent hydrogel: Synthesis, characterization and isotherm analysis. *J. Hazard. Mater.*, 2021, 421, 126729. https://doi.org/126710.121016/j.jhazmat.122021.126729

The Chemist
Journal of the American Institute of Chemists

Synthesis, Evaluation of Antimicrobial Activity, and Docking Study of Schiff Base-Metronidazole Derivatives

Aya Yaseen Mahmood Alabdali[1*], Maha Salih Hussein[2]

[1]Department of Pharmacy, Faculty of Pharmacy, The University of Mashreq Baghdad 10023, Iraq
[2]Department of Chemistry, College of Education, University of Samarra Samarra 34010, Iraq
**Corresponding author (E-mail: ayaalabdali563@gmail.com, ayaalabdaly@hotmail.com)*

Abstract: In recent years, bacterial infections have increased due to resistance and rising air pollution. Since metronidazole is a key drug for treating many diseases, our research focused on the synthesis and modification of novel Schiff base derivatives of metronidazole. The research involved esterifying the hydroxyl group and reducing the nitro group to prepare a Schiff base from the corresponding ester and a chlorometronidazole derivative. Their structures were characterized using IR, ^{1}H, and ^{13}C NMR spectroscopy. Its antibacterial activity against *Pseudomonas aeruginosa* and *Staphylococcus aureus* was then investigated. Derivatives 3 showed the highest inhibition, with diameters of 21 and 25 mm, respectively. Furthermore, molecular docking predicted the strength and type of binding to the protein with (PDB ID: 3U1Y) against *Pseudomonas aeruginosa* and the protein with (PDB ID:5CDQ) against *Staphylococcus aureus*. Schiff base derivatives 3 showed the highest binding at -7.36, -9.15 kcal/mol, respectively. These results indicate that these new compounds are promising antibacterial agents for the future.

Key Words: Metronidazole, Schiff bases, *Pseudomonas aeruginosa*, *Staphylococcus aureus,* docking

1. Introduction

Among the most significant global concerns are microbial infections, which pose a major threat to public health and contribute significantly to increased mortality world-wide. Although many fungi, viruses, and parasites play a role in infections, bacteria are the most common cause of infectious disorders. Given that multidrug resistance is a major obstacle to combating infectious bacterial diseases, there is an urgent need to

develop new drug compounds to control microbial infections [1].

Metronidazole is a broad-spectrum antimicrobial used clinically to treat many diseases, including infectious ones [2-3]. Its long-term use is often accompanied by numerous side effects [4-6], so much research focuses on its derivatives with novel structures and potential medical and pharmaceutical applications [7-9].

Schiff bases are an emerging class of organic compounds formed by condensation reactions between aromatic amines and carbonyl compounds (aldehydes and ketones). Schiff base chemistry, or imine chemistry, has recently gained significant traction in modern research, primarily due to the presence of the azomethine bond in their structure, which imparts high chemical stability and physicochemical properties that make them promising candidates for numerous biological and pharmaceutical applications [10-12]. Several studies have indicated that metronidazole Schiff base compounds possess distinctive and significant antimicrobial properties [13-16].

In light of previous observations, and as an extension of research and reports on Schiff-metronidazole bases, the main objective of this study was to develop the efficacy of metronidazole by combining it with a Schiff base to improve its pharmacological and biological efficacy, through modification of the nitro group and the hydroxyl group, as its combination is expected to lead to improved antibacterial activity against *Pseudomonas aeruginosa*; *Staphylococcus aureus*, in addition to improving its safety and efficacy as a novel antimicrobial agent. Finally, the results were strengthened by conducting a molecular simulation study of the new Schiff bases to validate the target compounds' activity.

2. Materials and Methods

Chemicals and Instruments

All chemicals and solvents were supplied by Aldrich. An SMP40 automated instrument was used to measure the melting point, and the results were uncorrected. Infrared spectra were recorded using an FT-IR-8400S spectrometer at the College of Education, Samarra University. Proton and carbon nuclear magnetic resonance spectra were recorded using a Varian spectrometer, 400 MHz, at Gaziantep University, Turkey, using d6-dimethyl sulfoxide (DMSO-d6) as the solvent. Thin-layer chromatography (TLC) was used to track reactions and determine product purity. Fluka (USA) used 0.2 mm fluorescently activated silica gel G, and measurements were performed using various solvents. UV-Vis fluorescence at 254 nm was also used.

2-(2-methyl-5-nitro-1H-imidazol-1-yl) ethyl benzoate (Met.b)

Metronidazole benzoat**e** was prepared using the method mentioned in the previous literary method [17] in a hood. Metronidazole (8.5 g, 0.05 mol) was carefully dissolved in 35 ml of pyridine, and a solution of benzoyl chloride (5.8 ml, 0.05 mmol) in 15 ml of pyridine was added dropwise. The mixture was stirred at 25°C

for half an hour, then at room temperature overnight. The precipitate was filtered and washed with water. The compound was re-crystallized in ethanol. Pale Yellow powder, Yield: 77%; m. p. 101-102. IR spectrum, (KBr, ύ=cm^{-1}), C-H arom.: 3062, C-H aliph.: 2960, C=O: 1718, NO_2 group: 1523,1361. ^{1}H NMR (400 MHz, DMSO-d_6) δ 8.04 (s, 1H, imidazole), 7.85 (d, J = 7.2 Hz, 2H), 7.65 (t, J = 7.4 Hz, 1H), 7.51 (t, J = 7.7 Hz, 2H), 4.75 (t, J = 5.4 Hz, 2H, C$\underline{H}_2$-O), 4.65 (t, J = 9.9 Hz, 2H, C$\underline{H}_2$-N), 2.47 (s, 3H, C$\underline{H}_3$). ^{13}C NMR (101 MHz, DMSO) δ 165.27 ($\underline{C}$=O), 151.39 ($\underline{C}$-NO_2), 138.55, 133.51, 133.12, 129.02, 128.96, 128.76, 62.87(CH_2-O), 44.69 (CH_2-N), 13.88 ($\underline{C}H_3$). Anal. Calcd. For $C_{13}H_{13}N_3O_4$ (275.26): C, 56.72; H, 4.76; N, 15.27; O; 23.25, Found C, 56.80; H, 4.79; N, 15.32; O; 23.29. LCMS: (ESI$^-$-MS, m/z) Calcd. for $C_{13}H_{13}N_3O_4$ $(M-H)^-$: 275.26, Found: 274.31.

1-(2-chloroethyl)-2-methyl-5-nitro-1H-imidazole (Met.Cl)

Metronidazole-chloride was prepared using the method mentioned in the previous literature [18,19] with some modifications. Metronidazole (5.2 g, 0.030 mol) was dissolved in $SOCl_2$ (3 ml, 0.04 mol) with 10 ml of chloroform, then the mixture was refluxed for 4 hours, and then cooled. The mixture was stirred at high speed in a cold bath at 10°C for 2 hours. A yellow precipitate was formed. The precipitate was washed with a small amount of cold ethanol to remove residual solvent and $SOCl_2$.

Dark Yellow powder, Yield: 88%; m. p. 79-80. IR spectrum, (KBr, ύ=cm^{-1}), C-H arom.: 3037, C-H aliph.: 2970, NO_2 group: 1541,1369, C-Cl: 736. ^{1}H NMR (400 MHz, DMSO) δ 8.16 (s, 1H), 4.67 (t, J = 6.0 Hz, 2H), 4.01 (t, J = 5.9 Hz, 2H), 2.53 (s, 3H). ^{13}C NMR (101 MHz, DMSO) δ 151.90 ($\underline{C}$-NO_2), 138.38, 132.88, 50.65, 44.81, 14.17($\underline{C}H_3$). Anal. Calcd. For $C_6H_8ClN_3O_2$ (189.60): C, 38.01; H, 4.25; Cl, 18.70; N, 22.16; O; 16.88 Found C, 38.08; H, 4.29; Cl, 18.79; N, 22.19; O; 16.94. LCMS: (ESI$^-$-MS, m/z) Calcd. for $C_6H_8ClN_3O_2$ $(M-H)^-$: 189.60, Found: 188.73.

General method of reducing the nitro group of metronidazole benzoate (Met.b) and metronidazole chloride (Met.Cl)

Met.b or Met.Cl (0.004 mol) was dissolved in 25 ml of ethanol, to which (2.0 g, 0.012 mol) of $Na_2S_2O_4$ solution was added. The mixture was heated and stirred for 3 hours at 40°C, then 6 ml of dilute hydrochloric acid (2N) was added and stirred for 3 hours. The mixture was cooled to room temperature, and the solution was neutralized with 25% sodium hydroxide. The product was extracted with (10 ml) dichloromethane three times, the organic layer was washed with water and dried with sodium sulfate, and the solvent was evaporated with a rotary evaporator to obtain a powder precipitate.

2-(5-amino-2-methyl-1H-imidazol-1-yl) ethyl benzoate 1

Yellow powder, Yield: 77%; m. p. 101-102. IR spectrum, (KBr, ύ=cm^{-1}), N-H_2: 4452,3363, C-H arom.: 3026, C-H aliph.: 2981, C=O: 1714.^{1}H NMR (400 MHz, DMSO) δ 7.94 (d, *J* = 8.0 Hz, 2H), 7.83 (s, 1H, imidazole), 7.63 (t, *J* = 7.8 Hz, 1H), 7.55 (s, 2H, NH_2), 7.49 (t, *J* = 7.9 Hz, 2H), 4.75 (t, *J* = 5.4 Hz, 2H, CH_2-O), 4.65 (t, *J* = 9.9 Hz, 2H, C$\underline{H}_2$-N), 2.46 (s, 3H, C$\underline{H}_3$). ^{13}C NMR (101 MHz, DMSO) δ 167.99 (C=O), 153.67 (C-NH_2), 146.93, 135.93, 129.14, 127.65, 127.19, 124.76, 124.56, 121.25, 62.02(CH_2-O), 46.42 (CH_2-N), 16.50 (CH_3). Anal. Calcd. For $C_{13}H_{15}N_3O_2$ (245.28): C, 63.66; H, 6.16; N, 17.13; O; 13.05, Found C, 63.70; H, 6.19; N, 17.19; O; 13.07. LCMS: (ESI$^-$-MS, m/z) Calcd. for $C_{13}H_{15}N_3O_2(M-H)^-$: 245.28, Found: 244.32.

1-(2-chloroethyl)-2-methyl-1H-imidazol-5-amine 2

Dark Yellow powder, Yield: 88%; m. p. 79-80. IR spectrum, (KBr, ύ=cm^{-1}), N-H_2: 4433,3400, C-H arom.: 3020, C-H aliph.: 2866, C-Cl: 773. ^{1}H NMR (400 MHz, DMSO) δ 7.06 (s, 1H, imidazole), 4.74 (s, 2H, NH_2), 4.67 (t, *J* = 5.9 Hz, 2H), 4.01 (t, *J* = 5.9 Hz, 2H), 2.53 (s, 3H). ^{13}C NMR (101 MHz, DMSO) δ 149.17 (C-NH_2), 142.50, 115.99, 52.87, 48.26, 14.19(CH_3). Anal. Calcd. For $C_6H_{10}ClN_3$ (159.62): C, 45.15; H, 6.32; Cl, 22.21; N, 26.33, Found C, 45.18; H, 6.34; Cl, 22.25; N, 26.39. LCMS: (ESI$^-$-MS, m/z) Calcd. for $C_6H_{10}ClN_3$ $(M-H)^-$: 159.62, Found: 158.69.

General method for the synthesis of Schiff base compounds 3-6

Dissolve (0.002 mol) of reduced compounds 1,2 in 25 ml of ethanol and add a (0.002 mol) solution of (p-nitro or p-chloro)-benzaldehyde with 3-4 drops of glacial acetic acid in 10 ml of ethanol. Heat the mixture in a reflux for 5-8 hours. The completion of the reaction was confirmed by TLC. The resulting mixture was left in a refrigerator, a precipitate formed, filtered, dried, and recrystallized in ethanol. The physical characteristics of Schiff bases-metronidazole 3-6 are itemized in Table 1.

Table 1. The Physical Characteristics of Schiff Bases-Metronidazole 3-6

Compound No.	Chemical Structure	Mol. Wt. g/mol	Color	m.p°C	Yield
3	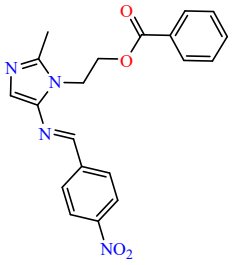	378.39	Yellow	148-150	77%
4	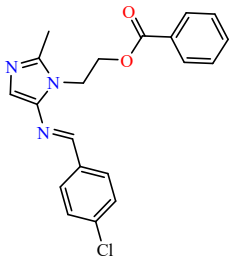	367.83	Yellow	129-130	74%
5	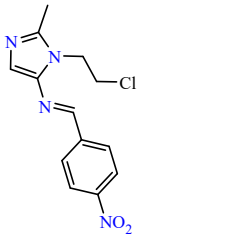	292.72	Yellow	133-134	72%
6	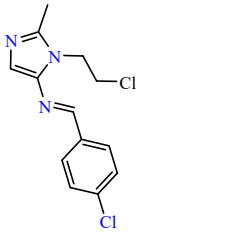	282.17	Yellow	123-125	70%

(E)-2-(2-methyl-5-((4-nitrobenzylidene) amino)-1H-imidazol-1-yl) ethyl benzoate—3

Pale Yellow powder, Yield: 77%; m. p. 148-150. IR spectrum, (KBr, ύ=cm^{-1}), C-H arom.: 3058, C-H aliph.: 2993, C=O: 1726, NO_2 group: 1541,1375. ^{1}H NMR (400 MHz, DMSO-d6) δ 9.09 (s, 1H,CH=N), 8.41 (d, J = 8.6 Hz, 2H), 8.16 (d, *J* = 8.6 Hz, 2H), 8.01 (d, *J* = 7.2 Hz, 1H), 7.76 (s, 1H), 7.66 (t, J = 7.6 Hz, 2H), 7.51 (t, *J* = 6.6 Hz ,2H), 4.61 (t, *J* = 19.3 Hz, 2H,O-CH_2), 4.39 (t, *J* = 10.6 Hz, 2H,N-CH_2), 2.47 (s, 3H).^{13}C NMR (101 MHz, DMSO) δ 168.81(C=O), 159.51(C-NO_2), 147.13, 146.62, 145.60, 145.48, 131.55, 131.09, 128.96, 128.80, 127.97, 127.82, 127.51, 127.40, 125.93, 124.10, 63.89, 46.42, 15.42. Anal. Calcd. For $C_{20}H_{18}N_4O_4$ (378.39): C, 63.49; H, 4.80; N, 14.81; O, 16.91, Found C, 63.51; H, 4.84; N, 14.85; O, 16.95. LCMS: (ESI$^-$-MS, m/z) Calcd. for $C_{20}H_{18}N_4O_4$ $(M-H)^-$: 378.39, Found: 377.41.

(E)-2-(5-((4-chlorobenzylidene) amino)-2-methyl-1H-imidazol-1-yl) ethyl benzoate—4

Pale Yellow powder, Yield: 74%; m. p. 129-130. IR spectrum, (KBr, ύ=cm^{-1}), C-H arom.: 3039, C-H aliph.: 2993, C=O: 1706, C-Cl: 773. ^{1}H NMR (400 MHz, DMSO) δ 8.90 (s, 1H,C<u>H</u>=N), 8.01 (d, *J* = 7.4 Hz, 2H), 7.86 (s, 1H), 7.74 (q, *J* = 7.9 Hz, 2H), 7.64 – 7.50 (m, 3H), 7.50 – 7.41 (m, 2H), 7.23 (s, 1H), 4.60 – 4.43 (m, 2H, CH_2-O), 4.35 (d, *J* = 18.6 Hz, 2H, C<u>H</u>$_2$-N), 2.42 (s, 3H,CH_3). ^{13}C NMR (101 MHz, DMSO) δ 165.61(<u>C</u>=O), 158.80, 148.44, 146.42, 145.84, 138.41, 132.97, 132.97, 130.82, 130.57, 129.62, 129.45, 128.86, 126.36, 125.22, 58.48, 47.80, 15.47 (<u>C</u>H_3). Anal. Calcd. For $C_{20}H_{18}ClN_3O_2$ (367.83): C, 65.31; H, 4.93; Cl, 9.64; N, 11.42; O, 8.70, Found C, 65.34; H, 4.96; Cl, 9.69; N, 11.45; O, 8.74. LCMS: (ESI$^-$-MS, m/z) Calcd. for $C_{20}H_{18}N_4O_4$ (M-H)$^-$: 367.83, Found: 366.77.

(E)-N-(1-(2-chloroethyl)-2-methyl-1H-imidazol-5-yl)-1-(4-nitrophenyl) methanimine—5

Dark Yellow powder, Yield: 72%; m. p. 133-134. IR spectrum, (KBr, ύ=cm^{-1}), C-H arom.: 3026, C-H aliph.: 2974, NO_2 group: 1533,1375, C-Cl: 778. ^{1}H NMR (400 MHz, DMSO) δ 9.09 (s, 1H, CH=N), 8.42 (d, *J* = 8.7 Hz, 2H), 8.17 (d, *J* = 8.7 Hz, 2H), 7.10 (s, 1H), 4.41 (t, *J* = 7.2 Hz, 2H), 3.43 (t, *J* = 7.0 Hz, 2H), 2.51 (s, 3H). ^{13}C NMR (101 MHz, DMSO) δ 159.60 (<u>C</u>H=N), 151.58(<u>C</u>-NO_2), 149.26, 141.21, 136.54, 127.54, 127.35, 125.69, 125.50, 122.56, 50.82, 44.11, 13.16(<u>C</u>H_3). Anal. Calcd. For $C_{13}H_{13}ClN_4O_2$ (292.72): C, 53.34; H, 4.48; Cl, 12.11; N, 19.14; O, 10.93, Found C, 53.39; H, 4.50; Cl, 12.19; N, 19.18; O, 10.99. LCMS: (ESI$^-$-MS, m/z) Calcd. for $C_{13}H_{13}ClN_4O_2$ (M-H)$^-$: 292.72, Found: 291.67.

(E)-N-(1-(2-chloroethyl)-2-methyl-1H-imidazol-5-yl)-1-(4-chlorophenyl) methanimine—6

Dark Yellow powder, Yield: 70%; m. p. 123-125. IR spectrum, (KBr, ύ=cm^{-1}), C-H arom.: 3062, C-H aliph.: 2974, C-Cl: 810. ^{1}H NMR (500 MHz, DMSO-d_6) δ 8.90 (s, 1H, CH=N), 7.72 – 7.68 (m, 4H), 6.94 (s, 1H, imidazole), 4.38 (t, *J* = 1.0 Hz, 2H), 4.01(t, *J* = 1.0 Hz, 2H), 2.47 (s, 3H). ^{13}C NMR (101 MHz, DMSO) δ 157.83(<u>C</u>H=N), 146.60, 140.16, 133.53, 131.32, 128.89, 128.69, 123.19, 47.29, 44.49, 15.19(<u>C</u>H_3). Anal. Calcd. For $C_{13}H_{13}Cl_2N_3$ (282.17): C, 55.34; H, 4.64; Cl, 25.13; N, 14.89, Found C, 55.39; H, 4.68; Cl, 25.16; N, 14.91. LCMS: (ESI$^-$-MS, m/z) Calcd. for $C_{13}H_{13}Cl_2N_3$ (M-H)$^-$: 282.17, Found: 281.23. the selected spectra for ^{1}H NMR and ^{13}C NMR of compound in current study (Met.b; and Met.Cl compounds are shown in Figures 1 and 2, respectively).

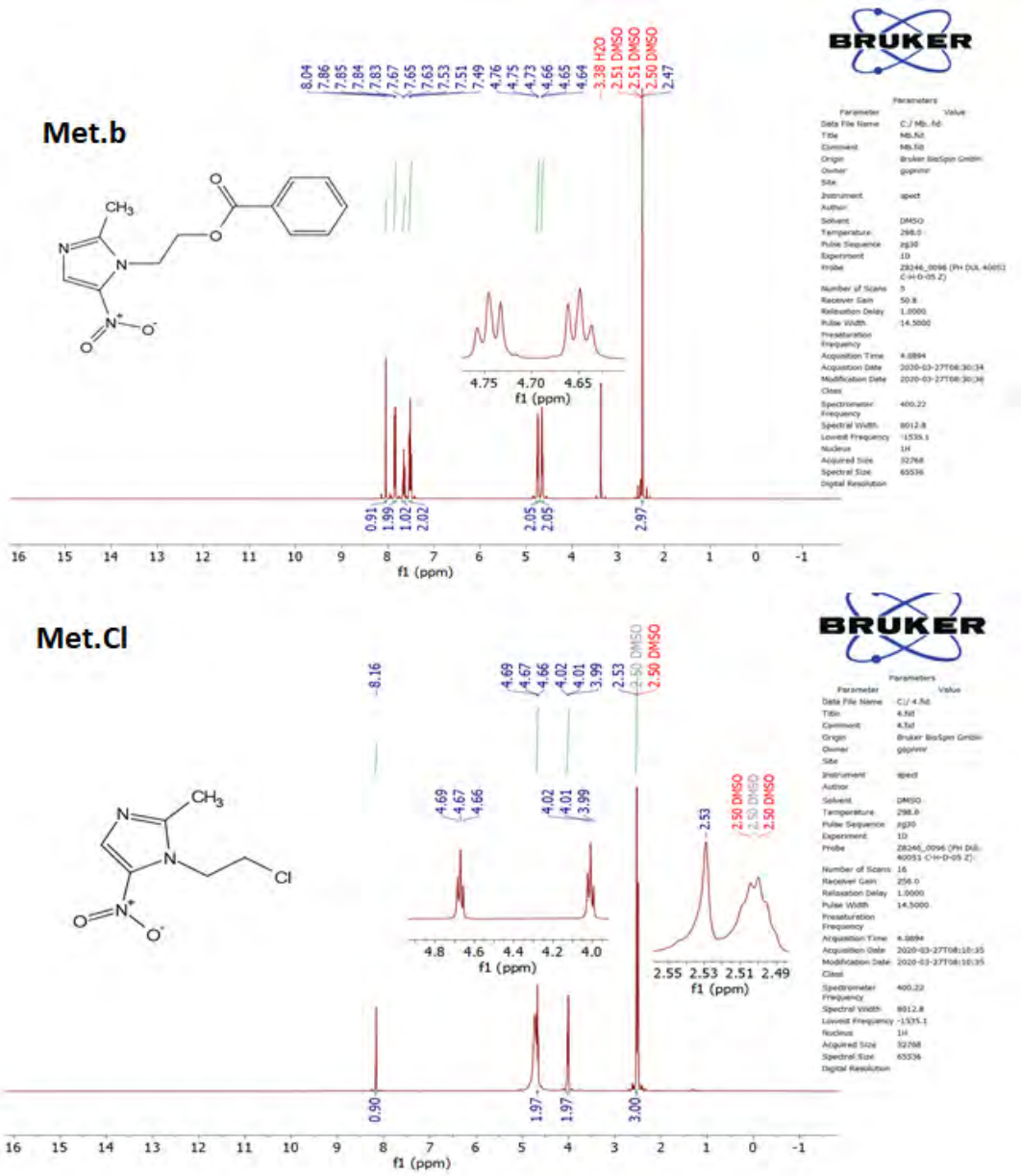

Figure 1. ^{1}HNMR Spectra for Met.b: 2-(2-methyl-5-nitro-1H-imidazol-1-yl) ethyl benzoate; **Met.Cl**: 1-(2-chloroethyl)-2-methyl-5-nitro-1H-imidazole

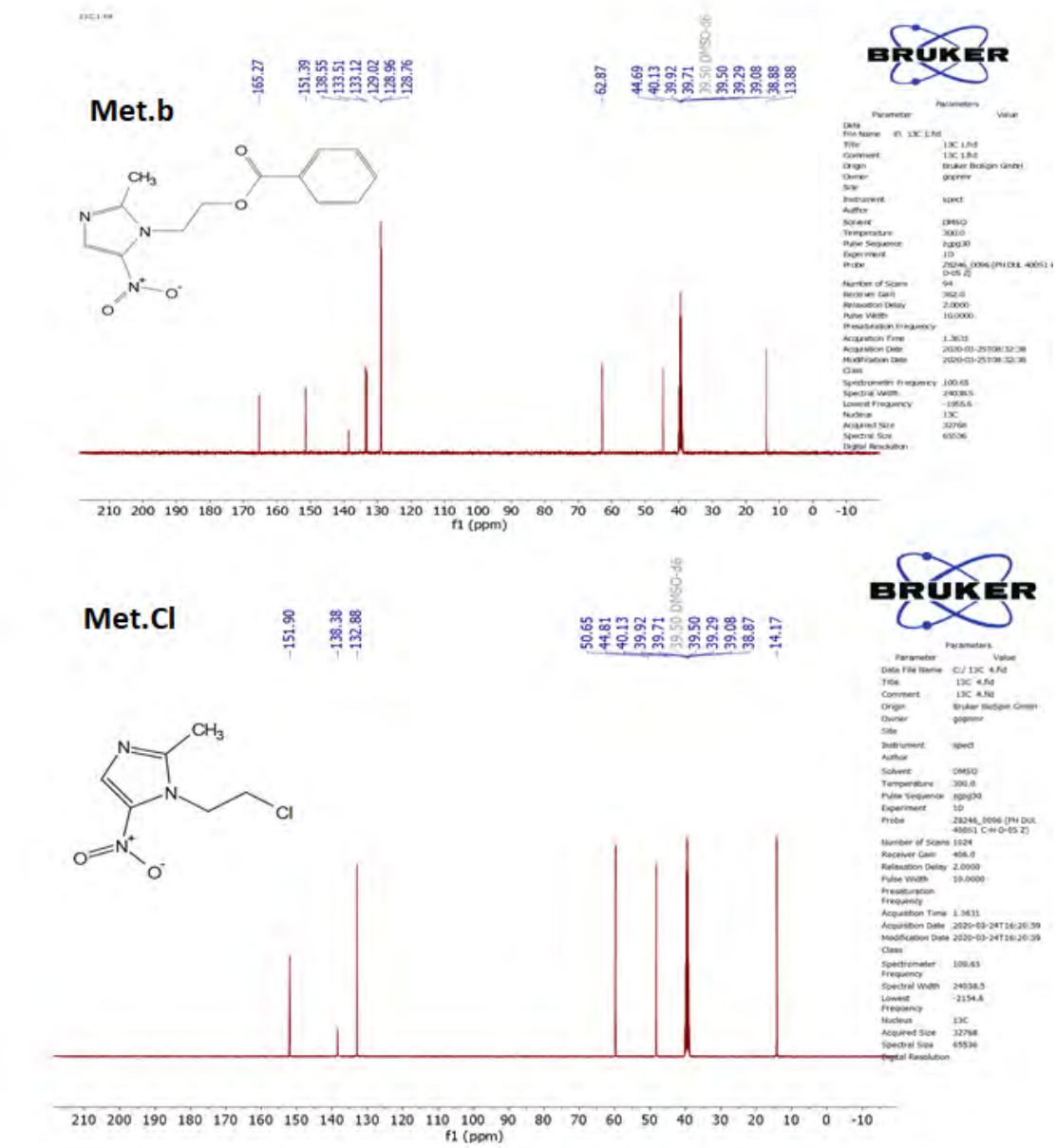

Figure 2. ^{13}CNMR Spectra for Met.b: 2-(2-methyl-5-nitro-1H-imidazol-1-yl) ethyl benzoate; **Met.Cl**: 1-(2-chloroethyl)-2-methyl-5-nitro-1H-imidazole

Biological Evaluation

The antibacterial activity was carried out in the laboratories of the Department of Biology/College of Education/University of Samarra. *Pseudomonas aeruginosa*, a gram-negative bacterium, and *Staphylococcus aureus*, a gram-positive bacterium, were isolated from patients at Samarra General Hospital and diagnosed using Vitck 2. The agar diffusion method was used by Wells etching on Muller-Hinton Agar medium. Cork borers were drilled with equal dimensions to prevent overlapping of inhibition diameters and with a diameter of 6 mm, to contain 0.5 ml of compound solutions for each hole after spreading 1.0 ml of bacterial suspension on the medium to

test the sensitivity of bacteria to the prepared compounds at concentrations of 25, 50, and 100 mg/ml using DMSO as a solvent. Then, the plates were incubated at 37°C for 24 hours, and the results were read by measuring the diameter of the inhibition zone [20,21]. The images of the bacterial plates are shown in Figures 3 and 4.

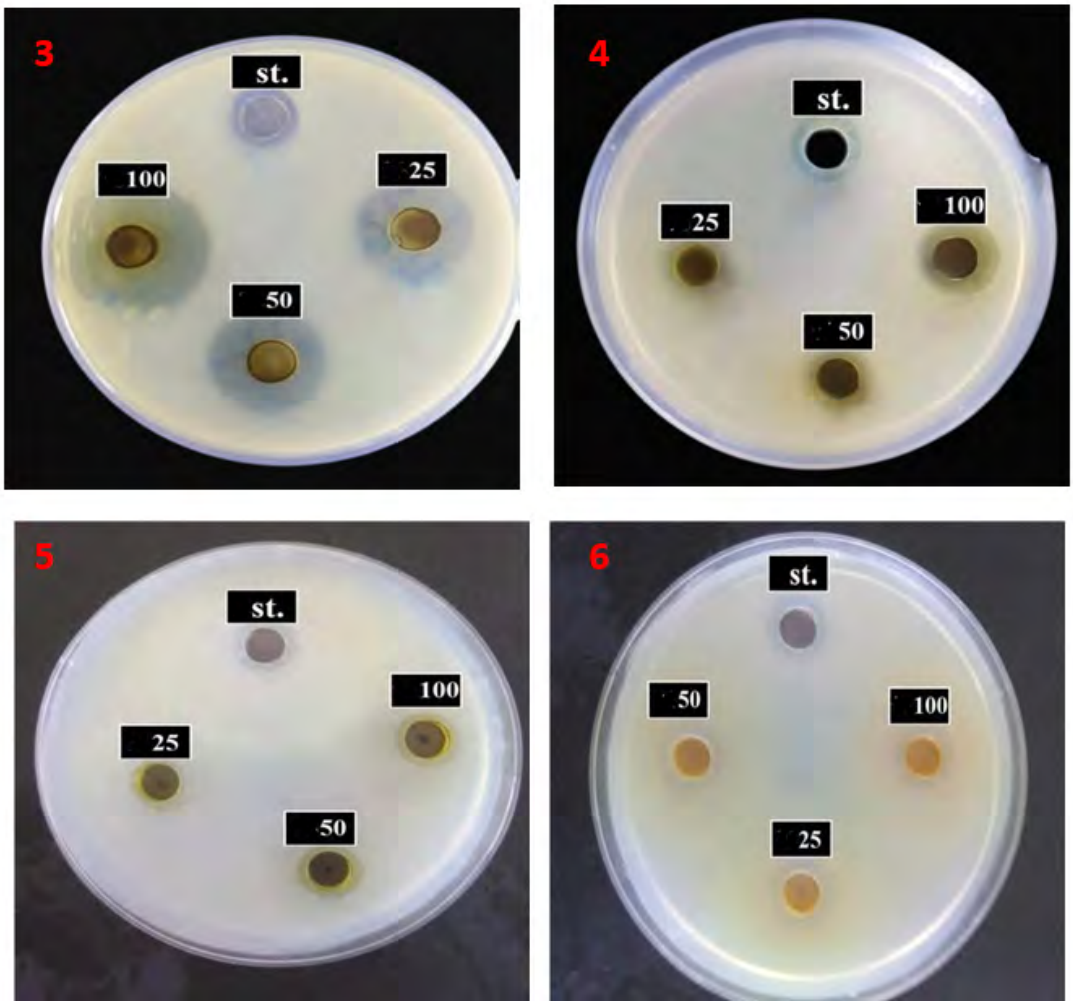

Figure 3. Inhibitory Activity of the Prepared Compounds against *Pseudomonas aeruginosa* (**3**: (E)-2-(2-methyl-5-((4-nitrobenzylidene) amino)-1H-imidazol-1-yl) ethyl benzoate; **4**: (E)-2-(5-((4-chlorobenzylidene) amino)-2-methyl-1H-imidazol-1-yl) ethyl benzoate; **5**: (E)-N-(1-(2-chloroethyl)-2-methyl-1H-imidazol-5-yl)-1-(4-nitrophenyl) methanimine; **6**: (E)-N-(1-(2-chloroethyl)-2-methyl-1H-imidazol-5-yl)-1-(4-chlorophenyl) methanimine)

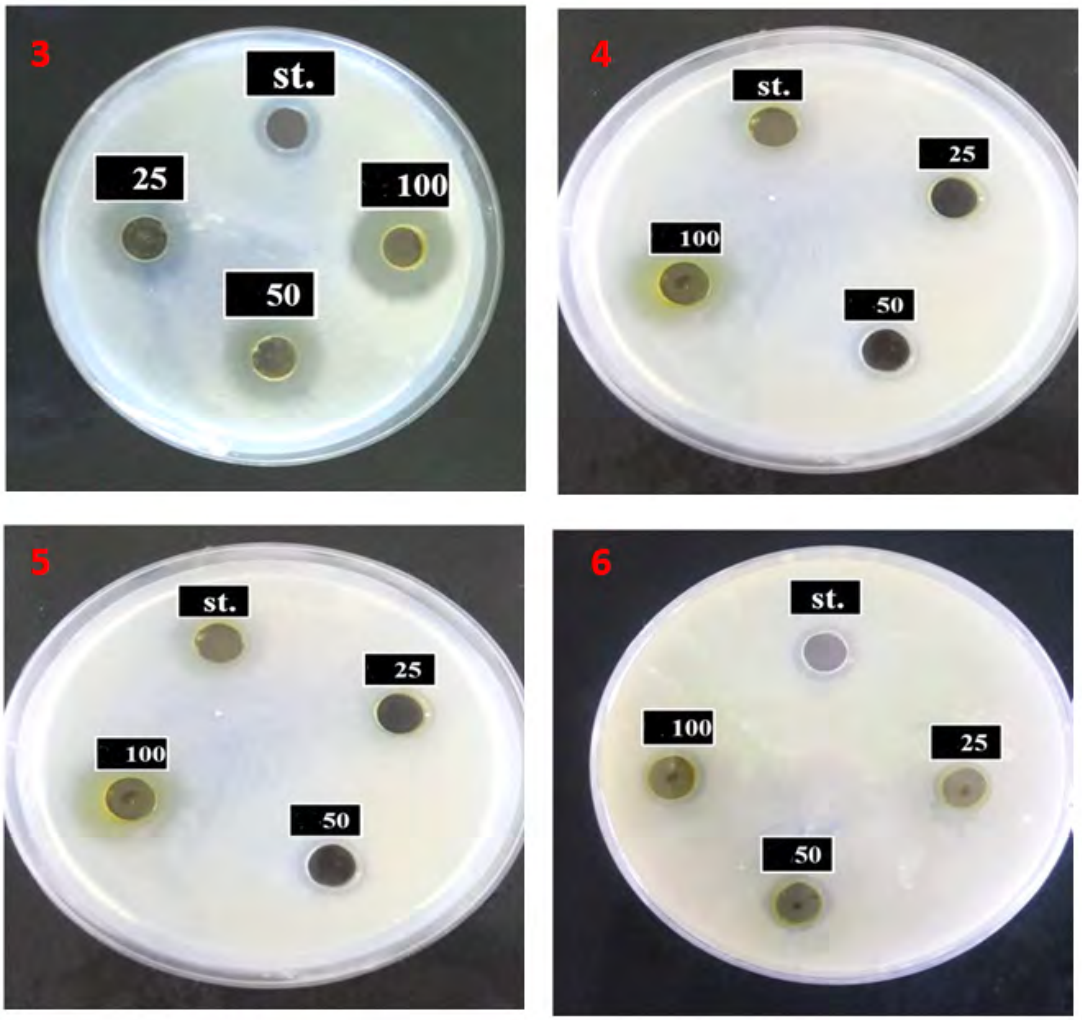

Figure 4. Inhibitory Activity of the Prepared Compounds Against *Staphylococcus aureus* (**3***:* (E)-2-(2-methyl-5-((4-nitrobenzylidene) amino)-1H-imidazol-1-yl) ethyl benzoate; **4**: (E)-2-(5-((4-chlorobenzylidene) amino)-2-methyl-1H-imidazol-1-yl) ethyl benzoate; **5**: (E)-N-(1-(2-chloroethyl)-2-methyl-1H-imidazol-5-yl)-1-(4-nitrophenyl) methanimine; **6**: (E)-N-(1-(2-chloroethyl)-2-methyl-1H-imidazol-5-yl)-1-(4-chlorophenyl) methanimine)

In silico Studies

Ligand preparation

The series of synthesis metronidazole derivatives. The ligands were first sketched using ChemDraw 2020. Their two-dimensional structures were then converted into three-dimensional structures using Chem3D. This allowed molecular viewing and structural manipulation. The 3-D structures were kept in the mol2 file format and then were converted to .pdb format with Open Babel. This was done to ensure that the structures can be used by AutoDock.

In turn, prior to docking, all hydrogen atoms were introduced into the structures with the

help of the "Add Hydrogens" option in AutoDock Tools (ADT). In this way, proper valence and adequate protonation levels were achieved. Next, each compound was protonated via the "Protonate 3D" tool in Discovery Studio 4.5. In this way, the ionization levels were adjusted according to the physiological conditions, namely, pH 7.4. Moreover, this step made sure that the molecules had realistic charge values. Thus, the structures were once again saved in the .pdb format. Then, the ligands were processed with AutoDock Tools, MGLTools, v1.5.7. In this step, Gasteiger partial charges were assigned to all atoms.

Moreover, non-polar hydrogens were combined to make the calculations of the molecule more convenient. The definition of flexible and rotatable bonds with ADT helped the docking software to study many different configurations of the ligand while docking. The last thing to do was to save the structure of the ligands in the .pdbqt format, which is needed for docking in AutoDock Vina [22].

Receptor preparation

We retrieved the crystal structures of target proteins from RCSB-PDB. Specifically, we selected bacterial *Pseudomonas aeruginosa* with target LpxC enzyme (PDB ID: 3U1Y) and bacterial gram-positive *Staphylococcus aureus* complex structure of Moxifloxacin with *S. aureus* DNA gyrase and DNA (PDB ID;5CDQ) as receptors models for docking experiments. We chose these structures for their high-resolution data and co-crystallized ligands, which allow us to determine active sites with greater precision.

The downloaded PDB file was prepared for docking using Discovery Studio Visualizer 4.5 software by deleting any molecule of water, ion, or any other heteroatom that does not bind to the protein. The cocrystalized ligands (native cocrystals of 3U1Y, and cocrystals (Moxifloxacin) of 5CDQ) were kept temporarily to identify the active site, but later on deleted before performing docking studies.

Further modification was done on receptors through AutoDock Tools (ADT) and MGLTools Version 1.5.7. Polar hydrogens were introduced to properly simulate hydrogen bonding. On the other hand, nonpolar hydrogens were combined to decrease the number of atoms used in computations. Kollman united atom charges were introduced in all protein atoms. These charges are needed in docking because they allow for electrostatic calculations. Active sites were identified based on the crystal structure of coexisting ligands.

All the receptors were saved in .pdbqt format, which is mandatory while carrying out docking in AutoDock Vina. This technique improved the models of receptors for LpxC enzyme (PDB ID: 3U1Y), and bacteria gram-positive (PDB ID: 5CDQ) [23].

Docking Method

Molecular docking studies were carried out using AutoDock Vina, which was installed on a computer running the Windows 10 operating system, comprising 32 cores. This

analysis was aimed at predicting the most favorable binding mode as well as binding energy for the ligand-target interaction, especially focusing on grid box parameters. The parameters were defined using AutoDock Tools (ADT). When setting the grid box location, the crystallographic binding site of the ligands was taken into account. Since proper conformational sampling was to be ensured, the size of the grid box was marginally adjusted. This allowed the flexible monomeric units of synthesized ligands and their free side chains sufficient rotational and translational freedom during the docking process [24].

The coordinates of the binding site for the gram-positive target protein (PDB ID: 5CDQ) were taken from the X-ray crystal structure. Here, the grid box with dimensions of 64 × 64 × 64 grid points at an interval of 0.375 Å with coordinates x = 41.504, y = -52.516, and z = 65.034 was generated, thus leading to 274,625 grid points per grid map.

For LpxC (PDB ID: 3U1Y), the docking grid box was generated around the co-crystallized ligand binding site. The grid dimensions were 60 × 54 × 70 points with a grid spacing of 0.375 Å and center coordinates of x = 16.508, y = 2.197, and z = 24.593. Docking calculations were then performed using AutoDock Vina, and ten binding poses were generated for each ligand. The best binding pose of all generated binding poses was selected based on its highest binding affinity value (kcal/mol). Default values for scoring and optimization were maintained.

The analysis and depiction of the ligand-receptor binding interactions, which include hydrogen bonding, hydrophobic interactions, and pi-pi stacking, were performed using AutoDock Tools and Discovery Studio 4.5 [25].

Visualization and interpretation of docking results

Among the AutoDock Vina output, the conformations of the ligands with the lowest binding energies (kcal/mol) were selected. In order to study and visualize the specific binding interactions of the ligands with the receptors at their respective binding sites, Discovery Studio Visualizer (DSV; 64-bit Windows 10) was used.

DSV analysis yielded various types of molecular interactions, for example hydrogen bond formation, hydrophobic effect, and metal binding, among others. Through this analysis, an understanding was gained about the nature of the ligand-receptor binding and the critical residues involved in such interactions. Interaction diagrams were derived from the 2D DSVs and 3D binding visualizations. They were originally simple images but were subsequently saved in .tif format.

Validation of results

The validity of the docking technique was evaluated by carrying out redocking experiments utilizing the ligands found in the crystal structure of the target proteins.

In the case of gram-positive target (5CDQ), the co-crystallized ligand, namely, Moxifloxacin was stripped off, and it was then docked again back into the protein's active site using the exact docking procedure that was applied on the metronidazole derivatives. DSV analysis was employed to precisely determine the ligand-receptor interaction sites, in addition to identifying all other types of interactions that may take place between the molecules, such as hydrogen bonding and hydrophobic interaction. The docking of metronidazole derivatives was validated by comparing their predicted binding mode with that of the reference ligand.

The docked complex formed by the gram-negative drug target-inhibitor (PDB ID: 3U1Y) was first removed from its bacterial LpxC protein target, after which it was subsequently re-docked back into its active site region in order to reproduce the binding mode observed experimentally. DSV technique was utilized in mapping the interaction of the inhibitor molecule with the active site residues. These data served as controls for the validation of the docking process.

This docking method employed in this experiment to the two sets of target proteins provided a good benchmark for the targets. In this way, an accurate prediction of the binding activity of the ligand under consideration was assured. This helped to ensure the accuracy of the docking results of the synthesized ligands [26,27].

3. Results and Discussion

Chemistry

The Schiff-metronidazole target bases were prepared by modifying the nitro and hydroxyl groups in metronidazole by converting it to the corresponding ester and chloro derivative, then reducing the nitro group using $Na_2S_2O_4$ as a mild reducing agent, as following the previous method research [22], to prepare an amine group to enter the Schiff reaction with a 4-nitro or 4-chlorobenzaldehyde, where the condensation reaction took place in an acidic medium of acetic acid and by refluxed to obtain Schiff bases 3-6, as shown in Scheme 1.

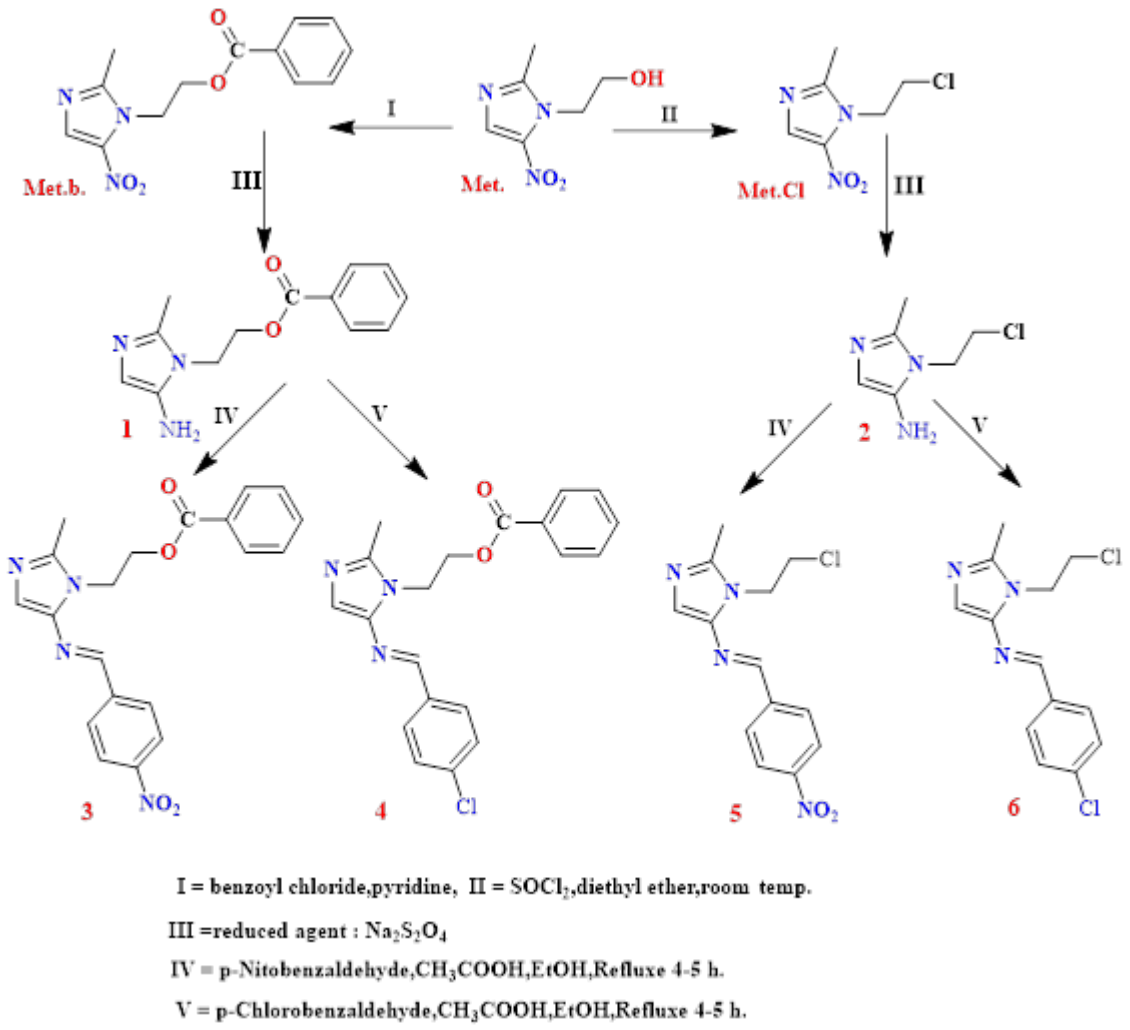

Scheme 1. Synthesis of the Schiff Bases-Metronidazole Target Compounds 3-6

This reaction is carried out via the common mechanism for preparing Schiff bases, where first, the nucleophilic addition reaction of the amine to the carbonyl group of the aldehyde takes place after protonation with the acid as a catalyst for the carbonyl to increase its electrophilicity, and second, the elimination step by removing the water molecule and removing the acid proton to obtain the target Schiff bases 3-6, as shown in Scheme 2.

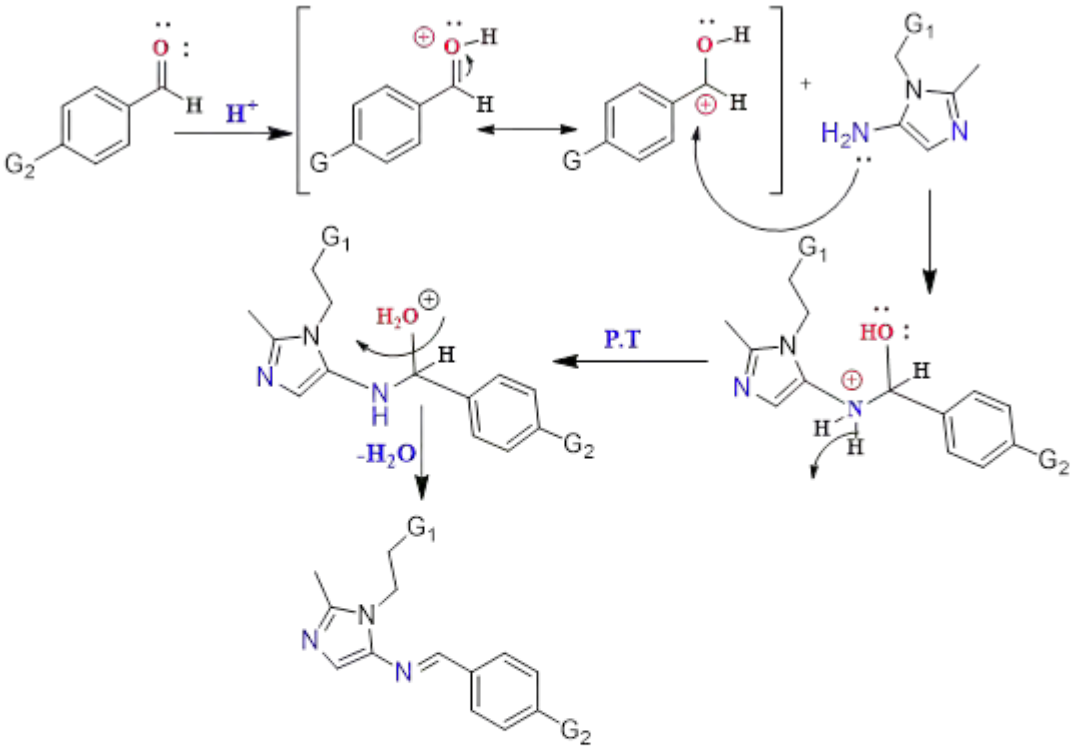

Metronidazole-Schiff bases 3-6

Comp. No.	3	4	5	6
G1	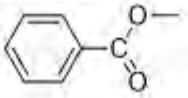	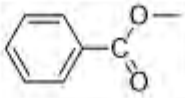	-Cl	-Cl
G2	$-NO_2$	-Cl	$-NO_2$	-Cl

Scheme 2. Mechanism Synthesis of the Schiff-Metronidazole 3-6

FTIR spectroscopy was used to characterize the precursor 1,2 the reduced Metronidazole. The spectra showed: disappearance of the bands of the $-NO_2$ group at about (1541-1361) cm^{-1}, two absorption bands appeared due to the asymmetric and symmetric stretching of $-NH_2$ at about 3452-3363 cm^{-1}, and this confirms reduction of the Nitro group. Also, the ^{1}H & ^{13}C-NMR spectra confirmed the appearance of a proton signal for the amine group NH_2 at 7.55,4.74 ppm and a signal at 153.67,149.17 ppm for the carbon attached to it (Figure 5).

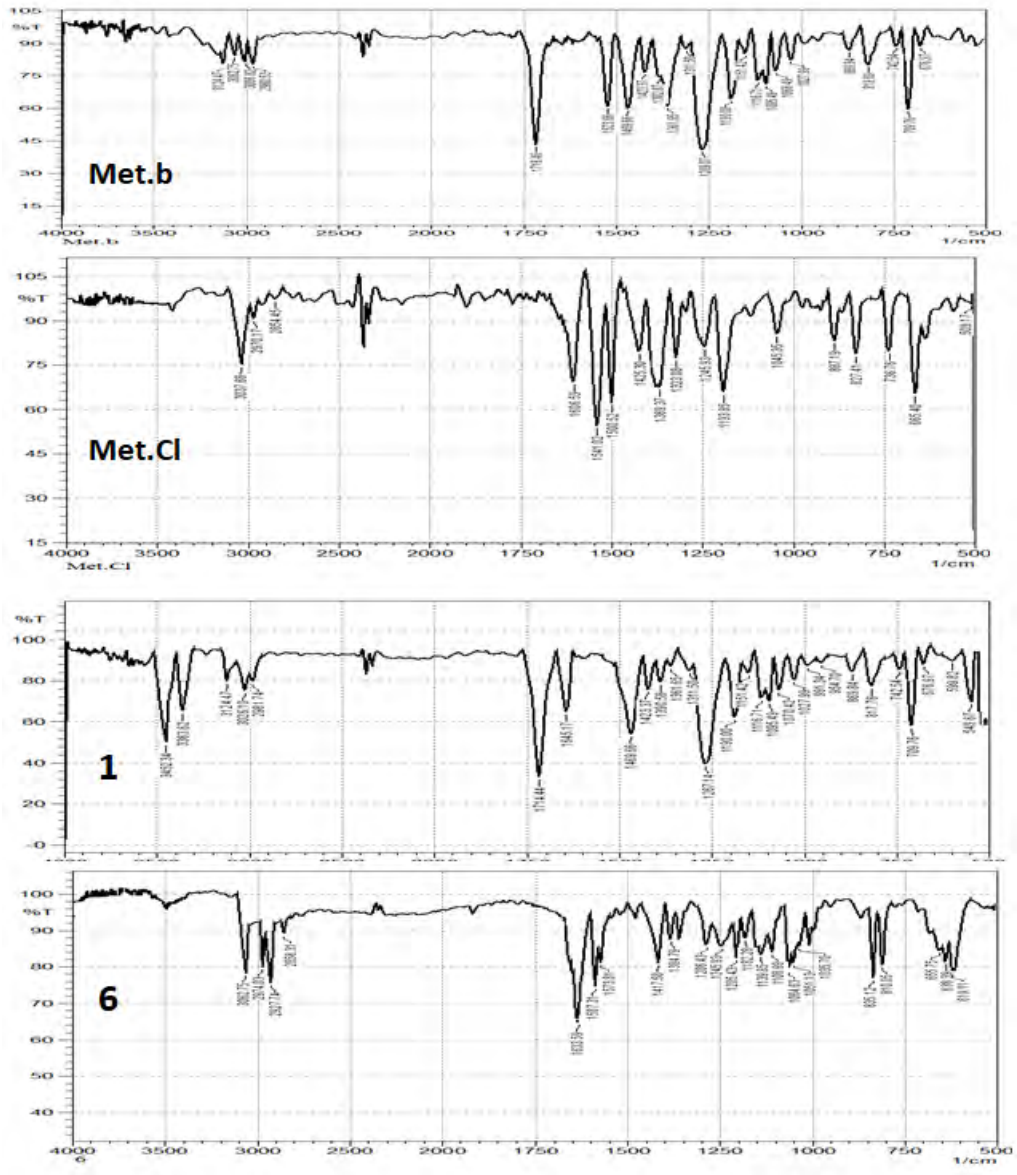

Figure 5. FT-IR Spectra for Met.b: 2-(2-methyl-5-nitro-1H-imidazol-1-yl) ethyl benzoate; **Met.Cl**: 1-(2-chloroethyl)-2-methyl-5-nitro-1H-imidazole; **1**: 2-(5-amino-2-methyl-1H-imidazol-1-yl) ethyl benzoate; **6**) (E)-N-(1-(2-chloroethyl)-2-methyl-1H-imidazol-5-yl)-1-(4-chlorophenyl) methanimine

The structures of Schiff bases-metronidazole derivatives were identified and confirmed by FTIR spectroscopy. The spectra showed the disappearance of the two amine stretch bands and the appearance of a medium-intensity stretch band of the azomethine bond, which overlaps with the aromatic C=C stretch bands of the compounds at 1500-1600 cm^{-1}. As for the ^{1}H & ^{13}C-NMR spectra, the azomethine proton signal appeared at 8.90, 9.09 ppm, in addition to the appearance of the methyl signal at 2.42-2.51 ppm, the triple signals duo to -CH_2-CH_2- at about 3.43-4.61 ppm, and the aromatic protons appeared in the range of 6.94-8.42 ppm, while the carbonyl carbon of the corresponding 3,4 ester derivative appeared at 168.81, 165.61 ppm.

Biological Activity

To explore the antibacterial activity of the newly synthesized homologues, Schiff bases 3-6 were tested against *Pseudomonas aeruginosa*, a gram-negative bacterium, and *Staphylococcus aureus*, a gram-positive bacterium. These bacteria were carefully selected because they cause common and serious human diseases, exhibit resistance to many known antibiotics, are easy to culture, and exhibit antibacterial properties.

Hybrid metronidazole Schiff bases 3-6 were selected to test their antibacterial activity against *Pseudomonas aeruginosa* and *Staphylococcus aureus*. The tested compounds showed good activity against both bacterial species compared to metronidazole and metronidazole benzoate, as measured by zones of inhibition. Derivatives 3 and 4 showed the best inhibition against *Pseudomonas aeruginosa* at 100 mg/ml (21 and 20 mm), respectively, outperforming metronidazole (15 mm). Furthermore, compounds 3, 4, and 5 showed good activity against *Staphylococcus aureus*: (25, 23, and 22 mm), respectively, at 100 mg/ml compared to the reference antibiotic, metronidazole. Conversely, it was found that compound 3 achieved the highest inhibition even at a concentration of 25 mg/ml. This relates to the structure-activity relationship, as compound 3 contains a nitro group at the para position in the phenyl ring, which enhances the electronic properties for binding to the bacterial protein.

Figures 6 and 7 and the attached images of the plates illustrate the bacterial activity of both types.

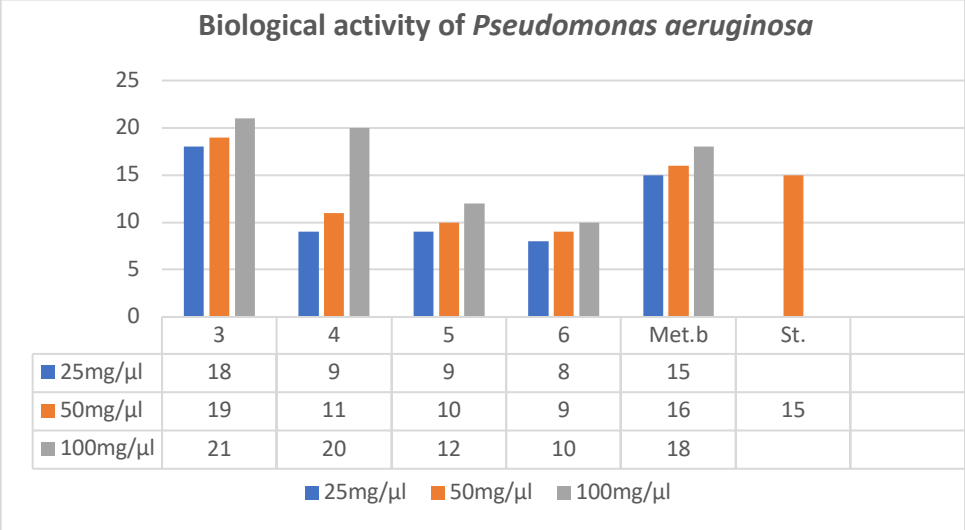

Figure 6. Inhibitory Activity of the Prepared Compounds Against *Pseudomonas aeruginosa*

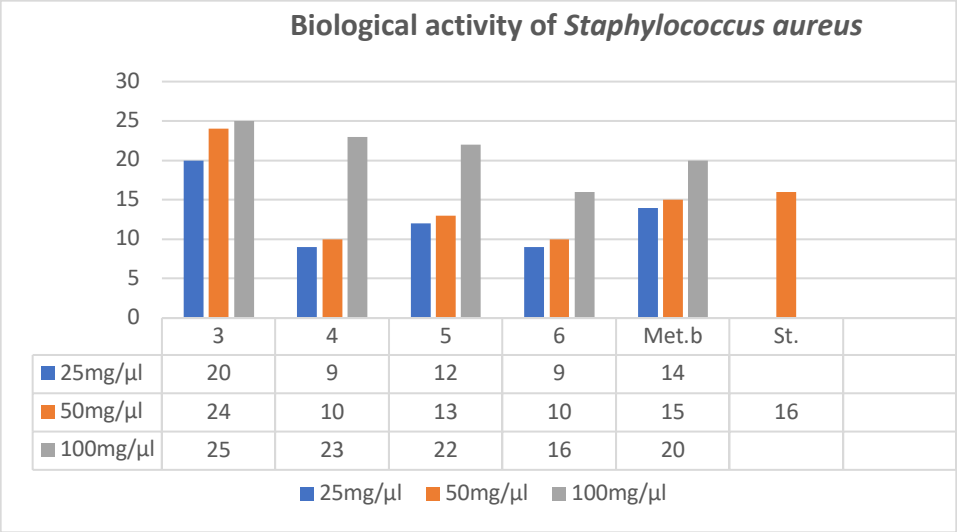

Figure 7. Inhibitory Activity of the Prepared Compounds Against *Staphylococcus aureus*

Molecular Docking

Molecular docking studies of synthesized metronidazole derivatives compounds against various bacterial targets indicated promising interactions, as indicated by the docking scores, are shown in Table 2.

Table 2. The Physical Characteristics of Schiff Bases-Metronidazole 3-6

Name	2D Structure	Dock score interaction energy for bacteria (gram-positive) kcal/mol pdb code 5CDQ	Dock score interaction energy for bacteria (gram-negative) kcal/mol pdb code 3U1Y
Positive control (co-crystal ligand Moxifloxacin) (pdb:5CDQ)	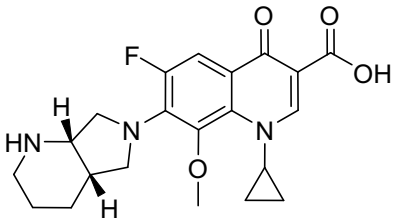	-10.58	/
Positive control (co-crystal ligand (pdb:3U1Y)	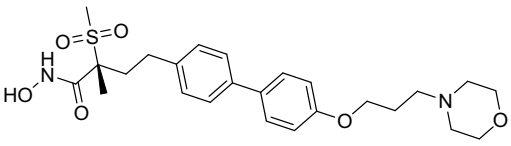	/	-7.48

3	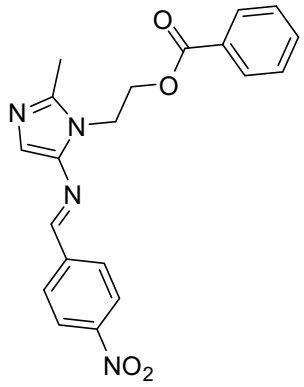	-9.15	-7.36
4	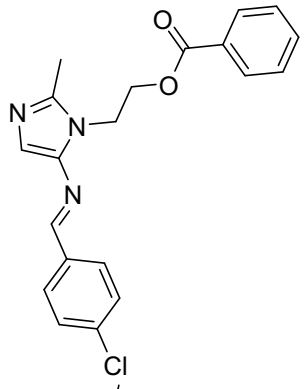	-8.13	-7.36
5	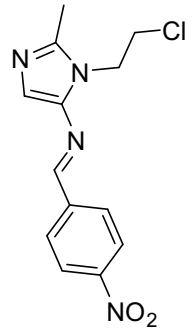	-7.93	-6.25
6	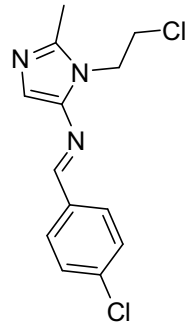	-6.97	-5.58
Met.	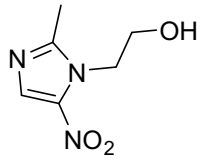	-6.15	-5.01

Met.Cl	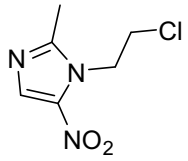	-5.81	-4.86
Met.b	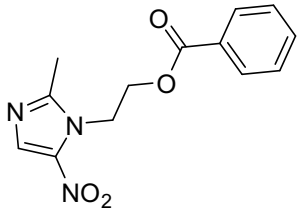	-7.09	-6.67

For compound 3, the gram-positive bacterial target with a PDB ID of 5CDQ yielded a docking score of -9.15 kcal/mol, indicating strong interactions. Attractive charge, p-anion bonds were observed with amino acids ARG A:122, PTR A:123, and GLU D:477, along with extended bonding with nucleotide DT E:8. Hydrophobic interactions (p-p stacked, p-Alkyl) with nucleotides, including DG E:2009, DA F:2013, and DC F:2012, help stabilize the complex and increase its affinity for the active site, as shown in Figure 8.

A

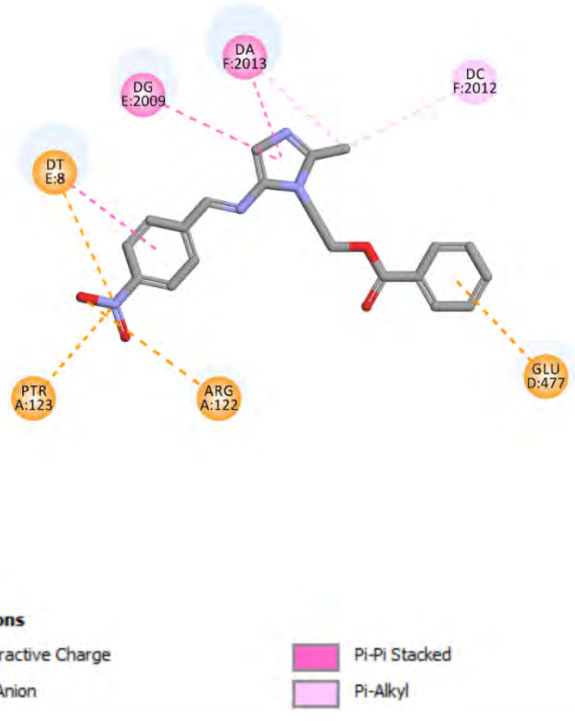

B

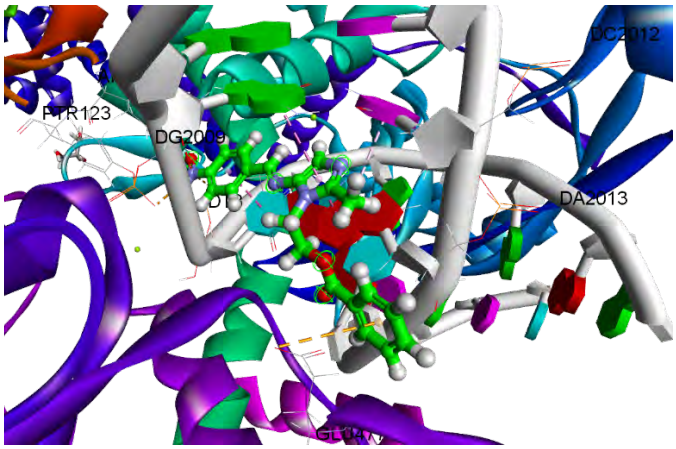

Figure 8. (A) 2D Interactions of Compound 3 Inside 5CDQ Target, (B) 3D Interactions of Compound 3 Inside 5CDQ Target

For the gram-negative bacterial target (PDB ID: 3U1Y), compound 3 showed a favorable docking score of -7.36 kcal/mol, indicating good binding affinity toward the active site. Structural analysis revealed that the benzene–nitro moiety formed conventional hydrogen bonds with THR B:190 and PHE B:191**.** Additionally, the ligand exhibited π–cation**,** π–anion, and electrostatic attractive interactions with ASP B:241, which collectively enhanced binding stability. Hydrogen bonding occurred between carbonyl group of ester bridge with LYS B:142. A metal-acceptor and attractive charge interaction with the catalytic Zn^{2+} ion further stabilized the binding, further π- π stacked with PHE B:160 and additional hydrophobic interactions with amino acids, including THR B:60, THR B:61, ILE B:158, LYS B:261, HIS B:264 and ALA B:265, help stabilize the complex and increase its affinity for the active site, as shown in Figure 9.

A

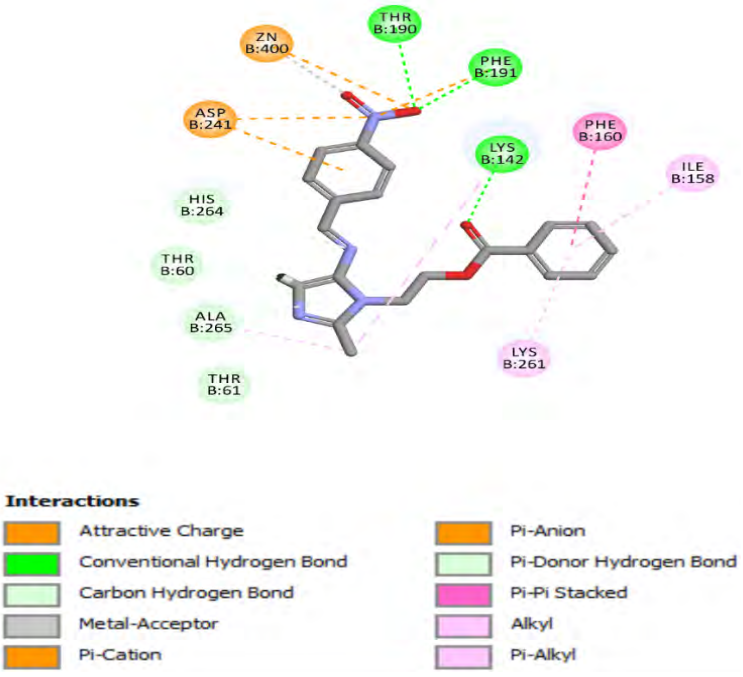

B

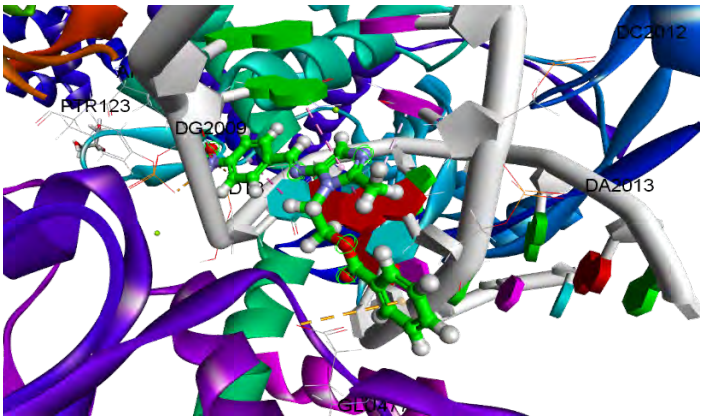

Figure 9. (A) 2D Interactions of Compound 3 Inside 3U1Y Target, (B) 3D Interactions of Compound 3 Inside 3U1Y Target

In the pose for compound 4, the gram-positive bacterial target showed a docking score of -8.13 kcal/mol against PDB ID 5CDQ, with important interactions involving hydrogen bonding with DA F:2013, as well as three π-cation bonds with nucleotides DT E:8, DG E:2009, DC F:2012. Also, it showed π-anion interaction with the amino acid GLU D:477. Furthermore, the complex is stabilized by hydrophobic interactions with DT E:8, DG E:2009, and DA F:2013, as illustrated in Figure 10.

A

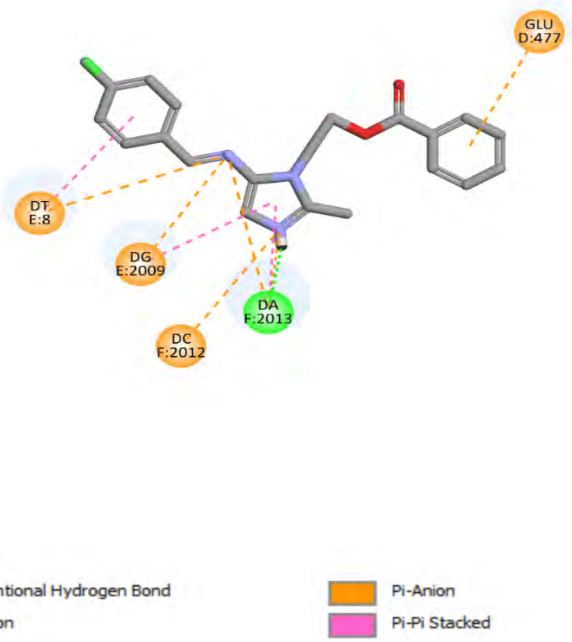

B

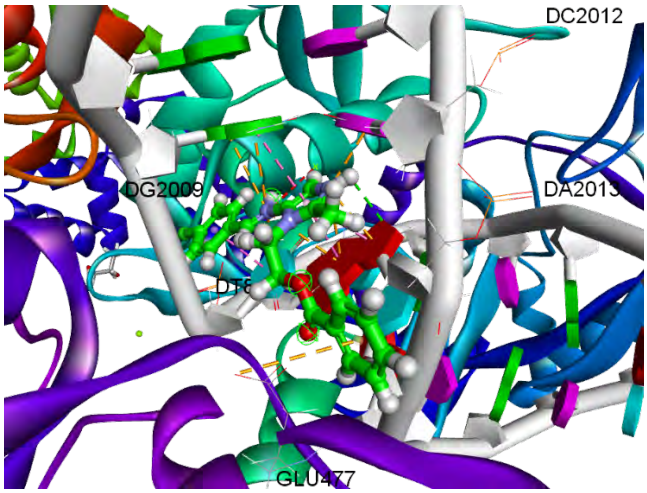

Figure 10. (A) 2D Interactions of Compound 4 Inside 5CDQ Target, (B) 3D Interactions of Compound 4 Inside 5CDQ Target

For the gram-positive bacterial target (PDB ID: 3U1Y), although no direct coordination with the Zn^{2+} ion was detected, compound 4 demonstrated multiple stabilizing non-covalent interactions within the active site. The carbonyl and ester oxygen atoms formed hydrogen bonds with LYS B:142 and LYS B:238**,** respectively. The ionized pyrazole NH group established hydrogen bonding interactions with THR B:6 and THR B:61, while the imine nitrogen atom exhibited an attractive electrostatic interaction with ASP B:241. Additionally, the benzene ring participated in a π–anion interaction with ASP B:241, whereas π–π stacking interactions were observed between the aromatic rings of compound 4 and PHE B:160 and PHE B:191, contributing to the stabilization of the ligand–protein complex. Furthermore, hydrophobic interactions with amino acids, including ILE B:158, HIS B:237, LYS B:261, and ALA B:265, help stabilize the complex and increase its affinity for the active site, as shown in Figure 11.

A

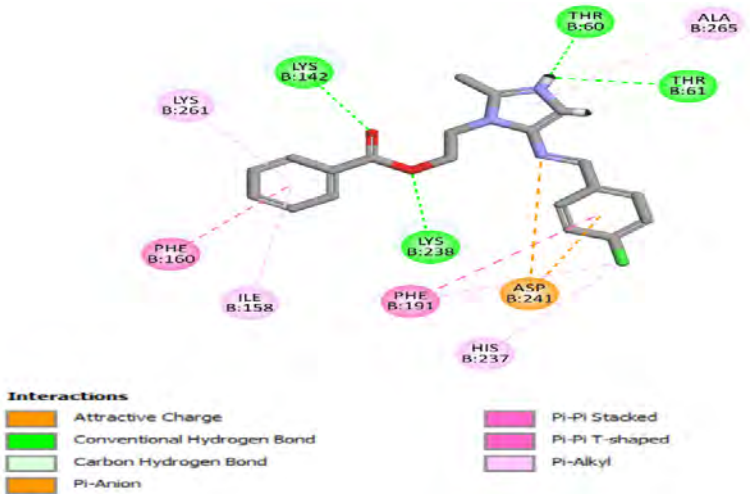

B

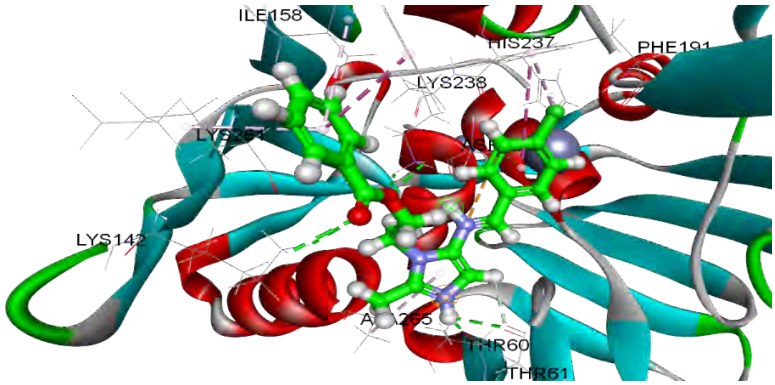

Figure 11. (A) 2D Interactions of Compound 4 Inside 3U1Y Target, (B) 3D Interactions of Compound 4 Inside 3U1Y Target

5. Conclusion

This research was designed to develop new antibacterial agents via Schiff bases from metronidazole, which showed a significantly more inhibitory effect than metronidazole against *Staphylococcus aureus* and *Pseudomonas aeruginosa*. Compound 3 gave the highest inhibition of both types of bacteria at a diameter of 21,25 mm, respectively, at a concentration of 100 mg/ml. Also, in the docked study, the compound 3 has the best binding site from metronidazole derivatives for both protein targets, where for bacteria *Staphylococcus aureus* (gram-positive), pdb code 5CDQ, and for bacteria *Pseudomonas aeruginosa* (gram-negative), pdb code 3U1Y.This is attributed to the presence of electron pairs of the nitrogen atom in azomethine, as well as the presence of the electron-withdrawing nitro group in the para position, which gives the compound high electronic properties due to resonance and conjugation, thus enhancing the binding to bacterial proteins. These conclusions afford an insight into the expansion and optimization of more effective antibacterial Schiff bases.

5. Disclosure of Interest

The authors declare that they have no known competing financial interests or personal relationships that could have appeared to influence the work reported in this paper.

6. Funding

The authors report that there is no funding associated with the work featured in this article.

7. References

1. Dini I. Mechanisms of bacterial resistance and innovative strategies to overcome antimicrobial resistance. *Antibiotics*, 2026, 15(3), 319. https://doi.org/10.3390/antibiotics15030319
2. Löfmark S, Edlund C, Nord CE. Metronidazole is still the drug of choice for treatment of anaerobic infections. *Clin. Infect. Dis.*, 2010, 50(Supplement_1), S16–S23.
3. Aachari A, Khamar M, Cherkaoui E, Bechar S. Synthesis, structural characterization, and antimicrobial evaluation of dimethyl methylene phosphate: An innovative phosphorylated compound with broad-spectrum potential. *Chemist*, 2025, 96(1).
4. Shahzad I, Alasmari MS, Zamir A, Rasool MF, Alqahtani F. Clinical pharmacokinetics of metronidazole: A systematic review and meta-analysis. *Antimicrob. Agents Chemother.*, 2025, 69(9), e01904-01924.
5. Ayinde O, Ross JD. The frequency and duration of side-effects associated with the use of oral metronidazole: A prospective study of VITA trial participants. *Int. J. STD AIDS*, 2023, 34(12), 897-902.
6. Ahmadi H, Heydari M, Abdouss M, Jamalpoor Z, Fathi-Karkan S, Rahdar A, Pandey S. Metronidazole delivery strategies: Optimizing cancer therapy through novel approaches for enhanced delivery, cytotoxicity, and side effect reduction. *Eur. J. Med. Chem. Rep.*, 2024, 12, 100202.
7. Khabnadideh S, Rezaei Z, Khalafi Nezhad A, Motazedian MH, Eskandari M. Synthesis of metronidazole derivatives as antigiardiasis agents. *Daru, J. Pharm. Sci.*, 2007, 15(1), 17-20.
8. Dhahir, AA, Hussein MS, Mohammed MO. Synthesis and antibacterial evaluation of new derivatives of metronidazole. *Int. J. Pharm. Res.*, 2020, 12, 1210-1220.
9. Mohammad HJ, Hussein MS. Synthesis of new scaffolds thiazolidine-4-one ring and characterization from derivatives of 1, 3-benzodioxole Schiff bases and its activity on antioxidant, molecular docking with PDE3A. *AIP Conf. Proc.*, 2024, 3219(1), 050003.
10. Wang SF, Yin Y, Qiao F, Wu X, Sha S, Zhang L, Zhu HL. Synthesis, molecular docking and biological evaluation of metronidazole derivatives containing piperazine skeleton as potential antibacterial agents. *Bioorg. Med. Chem.*, 2014, 22(8), 2409-2415.
11. Chen N, Yang L, Ding N, Li G, Cai J, An X, Wang, Z, Qin J, Niu Y. Recurrent neural network (RNN) model accelerates the development of antibacterial metronidazole derivatives. *RSC Adv.*, 2022, 12(35), 22893-22901.
12. Hassan KH, Al-Hussaniy HA, Ibraim Oraibi A, Bashar Al-Qazzan M, Zainee HY, Al-Jashamy K, Imad Hussein M. Thermodynamic and kinetic assessment of cobalt II adsorption using green synthesized NiO/γ-Al_2O_3 nanoparticles. *Salud, Ci. Tecnol. - Ser. Conf.*, 2025.
13. Noory MS, Hussein MS. Synthesis and characterization of 2-pyrone compounds derived from coumalic acid and evaluation of the antimicrobial activity of some of them. *AIP Conf. Proc.*, 2023, 2834(1), 030025.

14. Humeedi MD, Hussein MS. Synthesis new derivatives of quinoline and study the biological activity for some of them. *AIP Conf. Proc.*, 2022, 2450(1), 020019.
15. Kassan NE, Saadeh HA, Talib WH, Mahasneh AM, Kaur H, Goyal K, Sehgal R, Mubarak MS. Synthesis and biological activity of novel Schiff bases derived from metronidazole. *Med. Chem. Res.*, 2014, 23(11), 4872-4882.
16. Al-Zuhairi MI, Shakya AK, Numan NA, Al-Tameemi SJ, Al-Qazzan MB. Evaluating the activity of *Momordica charantia* (bitter gourd) fruit and *Curcuma longa* (turmeric) rhizome extract as anti-hyperlipidemic agents in experimental animals. *Int. J. Drug Delivery Technol.*, 2025, 15(3), 1101-1108.
17. Johansen M, Larsen C. A comparison of the chemical stability and the enzymatic hydrolysis of a series of aliphatic and aromatic ester derivatives of metronidazole. *Int. J. Pharm.*, 1985, 26(3), 227-241.
18. Li HQ, Xiao ZP, Fang RQ, Zhu HL. The syntheses and crystal structures of metronidazole-derived compounds. *J. Chem. Crystallogr.*, 2008, 38(6), 461-466.
19. Pi WX, Yang YM, Li HQ, Zhu HL. Chlorometronidazole. *Struct. Rep.*, 2005, 61(9), o2880-o2881.
20. Mokhtar Z, Eissa ME, Al-Qazzan MB, Kasabri V, Al-Akeedi M, Awad SH, Yousef TA, Al-Karmalawy AA. Synthesis, characterization, molecular modelling, and antimicrobial evaluation of novel drug–polymer composites grafted with polyvinylpyrrolidone. *J. Mol. Struct.*, 2026, 145842.
21. Hossain TJ. Methods for screening and evaluation of antimicrobial activity: A review of protocols, advantages, and limitations. *Eur. J. Microbiol. Immunol.*, 2024, 14(2), 97-115.
22. Al-Akeedi M, Najdawi M, Al-Balas Q, Al-Qazzan MB, Telfah ST. Novel anthraquinone amide derivatives as potential glyoxalase-I inhibitors. *J. Med. Life*, 2024, 17(1), 87-98
23. Al-Qazzan M, Al-Balas Q, Alnajjar B, Al-Akeedi M. Discovery of hydroxytriazole as a potential glyoxalase-I inhibitor utilizing computer-aided drug design techniques. *Sci. Rep.*, 2026.
24. Mokhtar Z, Ali AJ, Awad SH, Bashar M, Al-Qazzan MA. Preparation of new Schiff base derivatives from chitosan grafted with polyvinylpyrrolidone and study of their antimicrobial activity. *Trop. J. Pharm. Res.*, 2025, 24(7), 935-948.
25. Al-Qazzan M, Al-Balas Q, Alnajjar B, Kasabri V, Al-Hiari Y, Zayed A, AlKhateeb R, Al-Akeedi M. Cytotoxic, anti-inflammatory, antioxidant, and anti-glyoxalase-I evaluation of chelating substances: *In silico* and *in vitro* study. *PLoS One*, 2025, 20(10), e0333405.
26. Alzghoul M, Al-Hiari Y, Kasabri V, Hamdan I, Arabiyat S, Al-Balas Q, AlQazzan MB, AlSaad D, Telfah A. Unique bidentate chelators of functionalized heterocyclic fluoroquinolones with dual anti-inflammatory and selective cytotoxic effects via a C7-C8 ethylene diamine bridge. *Curr. Med. Chem*., 2026.
27. Busari HK, Azeez LA, Aremu HK, Ayinla SO, Jinadu LA, Obaleye JA. Zinc and copper complexes of 4-methylbenzoic acid and 2-methylimidazole: Synthesis, character-ization, antimicrobial and molecular docking studies. *Chemist*, 2023, 94(2).

The Chemist
Journal of the American Institute of Chemists

Selective Nitric Acid Oxidation of Methylanthracenes Derived from Pyrolysis Tar: Mechanism and Structure-Reactivity Relationships

Nuraliev Shukhrat Bakhtiyorovich[1], Nuraliev Samatjon Rakhmonkulovich[2], Berdiyarov Uktam Mengturaevich[3], Nurmanov Suvankul Erkhanovich[4], Khamidov Anvar Mamadalievich[5*]

[1]Associate Professor, Namangan Branch of Kimyo International University in Tashkent, Namangan, Republic of Uzbekistan
[2]Associate Professor, Head of the Department of Chemistry, Navoi State University, Navoi, Republic of Uzbekistan
[3]Associate Professor, Termez State University of Engineering and Agrotechnology, Surkhandarya, Republic of Uzbekistan
[4]Professor, National University of Uzbekistan named after Mirzo Ulugbek, Tashkent, Republic of Uzbekistan
[5]Associate Professor, Turin Polytechnic University in Tashkent, Republic of Uzbekistan
**Corresponding author (E-mail: anvar.khamidov@polito.uz)*
https://orcid.org/0009-0004-8411-3498

Abstract: This study investigates the selective nitric acid oxidation of methylated anthracenes (2-methylanthracene and 9-methylanthracene) isolated from pyrolysis tar, focusing on reaction mechanisms and structure-reactivity relationships. Tar fractions in the 290–360°C boiling range were separated by fractional distillation, yielding anthracene derivatives with defined compositions. Target compounds were purified through solvent extraction and recrystallization techniques, followed by structural confirmation using FT-IR, ^{1}H and ^{13}C NMR spectroscopy, and GC-MS analysis. The isolated 2-methylanthracene and 9-methylanthracene were subsequently subjected to nitric acid oxidation in acetic acid medium under controlled temperatures (100–130°C). The oxidation pathway proceeds via radical intermediates, initiated by $NO_2^{\bullet}$ and $NO_3^{\bullet}$ species generated from nitric acid decomposition, leading to stepwise transformation of the methyl substituent into corresponding carboxylic acid functionalities. Experimental results demonstrate that reaction temperature and time significantly influence product yield, with optimal conditions observed at 120°C and 1.5 h, achieving maximum yields of 72.1% for 9-anthracenecarboxylic acid and 70.5% for the 2-isomer. At higher temperatures, competing side reactions, including over-oxidation and partial ring degradation, reduce selectivity. Spectroscopic data confirms successful conversion of methylanthracenes into anthracene carboxylic acids, consistent with proposed mechanistic pathways. The findings provide insight into the reactivity of methyl-

substituted polycyclic aromatic hydrocarbons and highlight an efficient approach for valorization of coal tar-derived feedstocks into high-value aromatic carboxylic acids.

Key Words: Pyrolysis tar, methylanthracenes, polycyclic aromatic hydrocarbons (PAHs), anthracene derivatives, structure-reactivity relationship, coal tar valorization

1. Introduction

Anthracene is a polycyclic aromatic hydrocarbon (PAH) composed of three linearly fused benzene rings and has long attracted considerable attention from chemists and materials scientists due to its unique structural and electronic properties [1]. Owing to its extended π-conjugated system, anthracene and its derivatives exhibit remarkable photochemical and photophysical characteristics, including strong fluorescence, charge transport behavior, and the ability to form supramolecular gel-like assemblies [2]. These properties make anthracene-based compounds highly attractive as functional organic materials.

Anthracene derivatives are widely investigated as important organic building blocks because of their favorable photophysical and electrochemical properties, ease of structural modification, and early demonstrated electroluminescent behavior [3,4]. As a result, they have found promising applications in organic light-emitting diodes (OLEDs), organic field-effect transistors (OFETs), optical and electronic switches, scintillation detectors for high-energy photons and particles, and functional materials incorporated into mesophases, polymers, films, and crystalline systems [5,6]. Furthermore, increasing global interest in hydrogen-based energy technologies has stimulated new investigations into the potential use of anthracene derivatives in magnesium hydride systems [7]. Meng *et al.* also reported anthracene-oligomer-based semiconductors with high field-effect mobility and excellent operational stability, further demonstrating the technological importance of anthracene-containing materials [8].

In addition to their technological relevance, anthracene derivatives have attracted significant interest because of their pronounced biological activity, particularly their interactions with tumor cell lines. Their planar conjugated structure facilitates effective interaction with DNA base pairs, which is closely related to their biological effects and potential pharmaceutical applications [9]. The structural versatility of the anthracene framework also enables the synthesis of numerous functional derivatives with tunable physicochemical and biological properties.

More broadly, polycyclic aromatic hydrocarbons (PAHs) constitute an important class of compounds in modern materials science and organic electronics [10]. PAHs are considered promising precursors for the bottom-up synthesis of structurally defined nanocarbon materials and graphene-like architectures [11-13]. Their unique optical and electronic properties additionally provide significant opportunities for biological and optoelectronic applications [14]. However, despite their technological value, many PAHs are recognized as hazardous environmental pollutants generated by anthropogenic activities, and their carcinogenic nature has motivated extensive research into PAH

removal and transformation technologies [15].

Coal tar is a complex by-product formed during the high-temperature carbonization and gasification of coal for the production of coke and gaseous fuels [16,17]. It is generally obtained as a dark brown or black viscous liquid or semi-solid material with a characteristic odor, formed together with aqueous ammoniacal liquor during cooling of volatile products generated in coal processing [16]. With the increasing development of coal gasification technologies as alternative energy sources, the generation of coal-derived by-products such as coal tar, sulfur compounds, ammonium sulfate, and crude benzol has become an important environmental concern [17].

Coal tar is an exceptionally complex mixture containing hundreds of organic compounds, many of which possess significant industrial value [18]. Its composition includes aromatic hydrocarbons such as benzene, toluene, xylene, naphthalene, anthracene, and related polycyclic aromatic hydrocarbons (PAHs), as well as phenolic and nitrogen-containing heterocyclic compounds [18,19]. These substances are widely used as raw materials and intermediates in the production of synthetic fibers, engineering plastics, dyes, pharmaceuticals, preservatives, perfumes, pesticides, resins, and other industrial chemicals [19]. Because of this chemical diversity, coal tar is considered an important feedstock for the recovery of high-value aromatic compounds.

Despite its industrial significance, coal tar and coal tar residues (CTR) are recognized as hazardous environmental pollutants due to their high content of toxic and carcinogenic PAHs [20,21]. The migration and distribution of coal tar contaminants in water systems are influenced by interfacial molecular diffusion and the high viscosity of the tar phase, which significantly affects mass-transfer processes [19-21]. Consequently, considerable attention has been devoted to the development of efficient technologies for PAH removal, separation, and valorization.

Recent studies have demonstrated the potential of microwave-assisted extraction for reducing priority PAH content in coal tar residues [22]. In addition, increasing interest has been directed toward the selective isolation of valuable compounds from coal tar for the preparation of advanced carbon materials and functional resins [23]. Various carbonaceous adsorbents, including chars produced from biomass pyrolysis and activated using CO_2 or steam, have also been investigated for tar removal from syngas streams [24,25]. The physicochemical properties and applicability of such chars strongly depend on their mineral composition and heavy metal content [26].

In this work, methylanthracenes were isolated from coal tar-derived fractions and structurally characterized using FT-IR, NMR, and GC-MS techniques. Their selective nitric acid oxidation to anthracenecarboxylic acids were investigated with emphasis on reaction mechanism and the influence of temperature and time on product yield and selectivity.

2. Materials and Methods

All chemicals and reagents used in this study were of analytical grade purity (hydrochloric acid, methanol, isopropyl alcohol, and toluene).

Method for the Isolation of 2-Methylanthracene

For the purpose of isolating anthracene and its derivatives required for this scientific research, a tar-derived sample in the boiling range of 290-360°C was separated under atmospheric pressure into two fractions based on boiling point: 290-330°C and 335-360°C.

From the 330-360°C fraction, 700 mL was collected and transferred into a 1000 mL flask together with 3-4 g of boiling chips, followed by distillation setup. The temperature was gradually increased at a rate of 10-15°C per minute. The obtained samples were further identified as anthracene, 2-methylanthracene, and 9-methylanthracene crystals based on their solubility in solvents and melting point characteristics. It was determined that the fraction consisted of approximately 38-40% phenanthrene, 15-18% anthracene, 2-3.5% 2-methylanthracene, 3-4% 9-methylanthracene, and 28-30% phenanthrene derivatives and other compounds (Table 1).

Table 1. Compounds Obtained from the Tar Product (Temperature Range: 330-360°C)

№	Compound name	Melting point (°C)	Boiling point (°C)	Component fraction (%)
1	Phenanthrene	99-101	335-345	38-40
2	Anthracene	215-218	335-345	15-18
3	2-Methylanthracene	204-205	345-360	2-3
4	9-Methylanthracene	77-99	345-360	3-4
5	Unidentified product		345-360	28-30

The IR spectra of the compounds were recorded using FT-IR 2000 System (PerkinElmer) and Bruker Invenio S-2021 spectrometers in the range of 4000-400 cm^{-1}.

^{1}H NMR spectra were recorded on a Unity+600 (Varian) spectrometer operating at 600 MHz using CD_3OD, $CDCl_3$, DMSO-d6, and pyridine-d5 as solvents. Tetramethylsilane (TMS) was used as an internal standard for ^{1}H NMR measurements. In ^{13}C NMR spectra, the chemical shift of the solvent was used as the reference standard.

Initially, it was established that 2-methylanthracene is readily soluble in ethanol; therefore, technical ethanol was used as the solvent. The raw material was first heated

with technical ethanol to 40°C. After dissolution, the mixture was filtered, allowing separation from anthracene and phenanthrene derivatives. The obtained filtrate was then cooled to room temperature. The filtered mass was treated with 10% sulfuric acid to adjust the pH to 2-3 and filtered again, followed by neutralization with 10% sodium hydroxide solution to pH 7-8 and subsequent filtration.

The resulting 2-methylanthracene crystals were further purified by recrystallization from ethanol and by distillation to remove residual solvent. The product was dried at room temperature for 3 hours. The mass of the obtained 2-methylanthracene crystals was 19 g, corresponding to 2.7% of the total fraction.

The obtained 2-methylanthracene was identified as a light-yellow compound with a melting point of 203-204°C and a boiling point of 357°C.

Method for the Isolation of 9-Methylanthracene

After the separation of 2-methylanthracene from the "tar product", the remaining fraction was used for the isolation of 9-methylanthracene. First, the mixture was heated to 65-70°C. According to the literature data, the melting points of related compounds are as follows: 2-methylphenanthrene (57°C), 3-methylphenanthrene (63°C), 4-methylphenanthrene (53.5°C), while 9-methylanthracene has a melting point of 77-79°C. Since the melting points of the above phenanthrene derivatives are lower than that of 9-methylanthracene, this difference was used for separation. The mixture was therefore filtered at 70°C to isolate 9-methylanthracene.

For purification, 9-methylanthracene was recrystallized from toluene. The compound was then isolated from toluene by evaporation. The obtained 9-methylanthracene crystals were dried in open air for 3 hours. The mass of the obtained 9-methylanthracene crystals, determined using an analytical balance, accounted for 3.56% of the total fraction (23.1 g).

3. Results and Discussion

IR spectroscopic analysis (Figure 1) showed a characteristic absorption band at 3049.70 cm^{-1} corresponding to aromatic C-H stretching vibrations, confirming the presence of an aromatic ring.

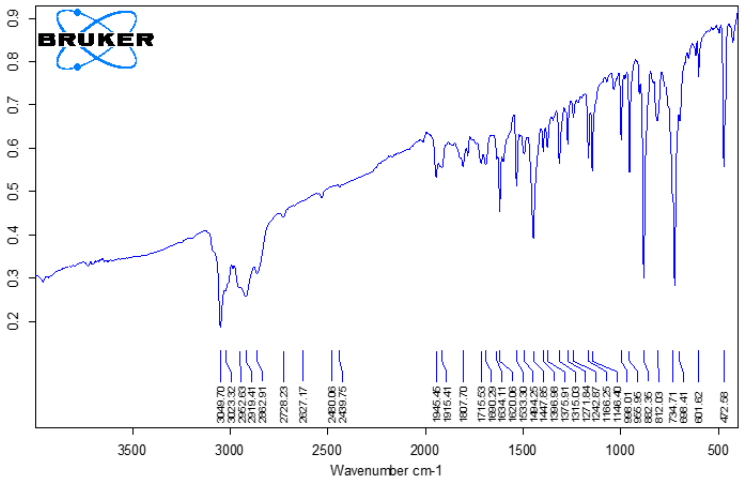

Figure 1. IR Spectrum of 9-Methylanthracene

The absorption bands at 2919.41-2862.91 cm^{-1} are attributed to C-H stretching vibrations of the CH_3 group, indicating the presence of a methyl substituent in the molecule. The bands observed at 1620.06-1447.85 cm^{-1} correspond to C=C stretching vibrations of the aromatic ring system.

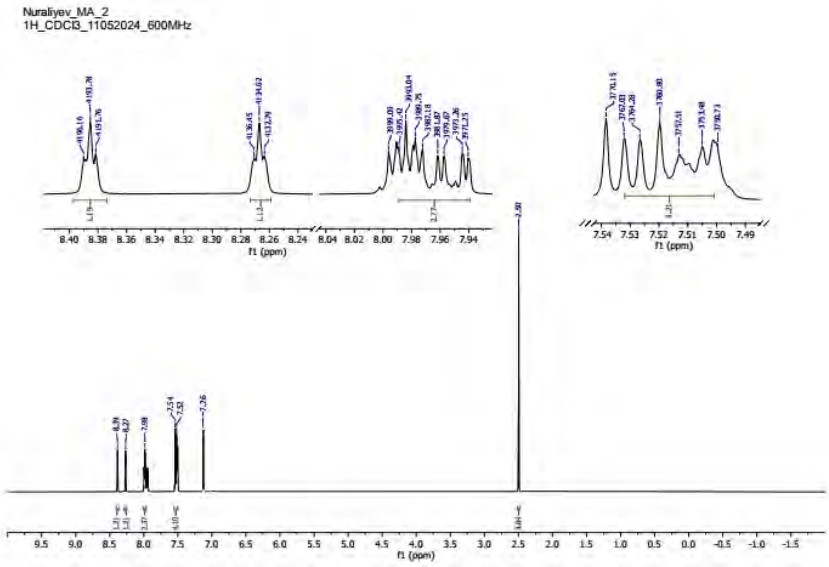

Figure 2. ^{1}H NMR Spectrum of 2-Methylanthracene

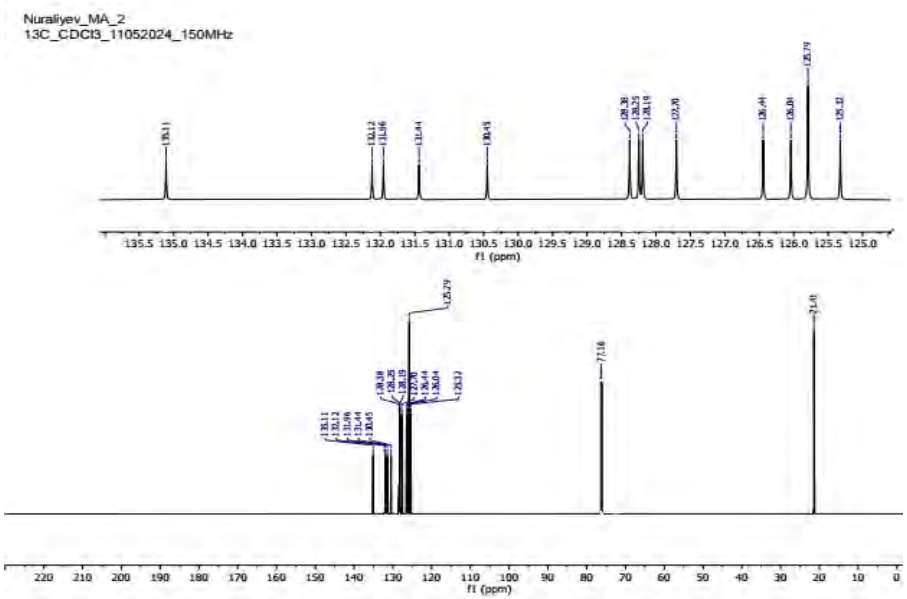

Figure 3. ^{13}C NMR Spectrum of 2-Methylanthracene

^{1}H and ^{13}C NMR spectra were recorded (Figures 2 and 3). The ^{1}H NMR spectrum (600 MHz, $CDCl_3$) showed signals at δ 8.39 (t, J = 2.11 Hz, 1H), 8.27 (t, J = 1.99 Hz, ^{1}H), 7.98 (ddd, J = 5.82, 3.42, 2.50 Hz, 2H), 7.95 (dt, J = 8.60, 2.10 Hz, 1H), 7.55-7.49 (m, 4H), and 2.50 (s, 3H). These signals are characteristic of aromatic protons of the anthracene framework, while the singlet at δ 2.50 (3H) corresponds to the methyl group.

GC-MS analysis showed a molecular ion peak at m/z: theoretical = 192.00, observed $[M]^+$ = 192.00, which is in full agreement with the molecular formula of 2-methylanthracene ($C_{15}H_{12}$).

The ^{13}C NMR spectrum (150 MHz, $CDCl_3$) exhibited signals at δ 135.11, 132.12, 131.96, 131.44, 130.45, 128.38, 128.25, 128.19, 127.70, 126.44, 126.04, 125.79, 125.32, and 21.41 ppm, corresponding to aromatic carbon atoms and the methyl carbon, respectively.

The obtained crystals of 9-methylanthracene were yellow in color, and the melting point was found to be 76-78°C. The structure was confirmed by ^{1}H NMR spectroscopy (Figure 4).

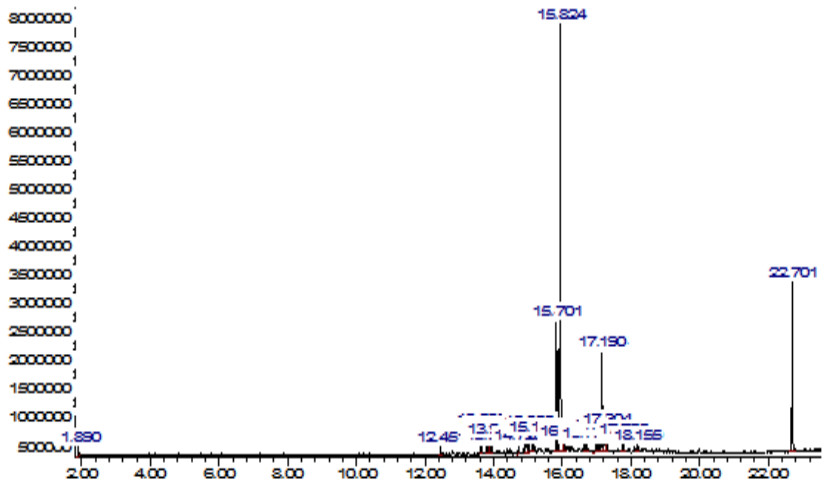

Figure 4. Chromatographic Parameters of the Initial Fraction Sample

The results of the mass spectral analysis showed that the obtained fraction contains several compounds valuable for industrial applications.

^{1}H NMR (600 MHz, $CDCl_3$) δ 8.34 (t, J = 2.19 Hz, ^{1}H), 7.98-7.91 (m, 4H), 7.54-7.47 (m, 4H), 3.09 (s, 3H). ^{13}C NMR (150 MHz, $CDCl_3$) δ 131.46, 130.54, 129.74, 129.15, 125.47, 125.38, 125.22, 124.99, 15.63. m/z (GC-MS): theoretical = 192.00, observed = $[M]^+$ 192.00 (Figures 5).

Figure 5. Chromatographic-Mass Spectrum of 9-Methylanthracene

The chemical shift values in the ^{1}H NMR spectrum (ppm) depend on the electron density around the protons. As electron density decreases, deshielding increases and the chemical shift value shifts to higher ppm. Protons in aromatic rings typically appear in the range of 7-9 ppm. This is associated with the deshielding effect caused by the circulating π-electron cloud of the aromatic system.

Multiplet signals arise due to spin–spin coupling between neighboring protons. The coupling constant (J) reflects the strength of interaction between adjacent protons. Due to the symmetry of the anthracene molecule, equivalent protons give rise to identical signals in the spectrum.

^{1}H NMR Spectrum of 9-Methylanthracene

Aromatic protons usually appear as multiplets because protons in aromatic rings are coupled with each other through multiple neighboring interactions. Since these protons are located close to each other within the aromatic system, their signals become complex and often appear as overlapping multiplet patterns.

The 9-methylanthracene molecule contains a total of 12 hydrogen atoms: 9 hydrogen atoms are located on the aromatic rings, while 3 hydrogen atoms belong to the methyl (-CH_3) group. In the anthracene framework, the aromatic protons exhibit signals corresponding to their different chemical environments, but due to strong spin-spin coupling, they generally appear as multiplets.

As shown in Figure 6, several signals are observed in the range of 7.50-8.34 ppm, which correspond to aromatic protons. These signals are characteristic of the anthracene aromatic system.

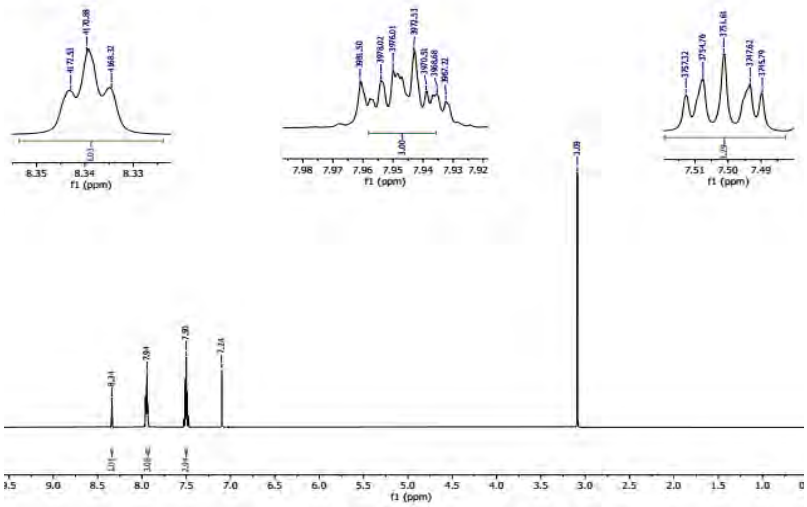

Figure 6. ^{1}H NMR Spectrum of 9-Methylanthracene

The methyl group protons typically resonate in the 3-4 ppm region. In this spectrum, a singlet signal observed at around 3.09 ppm corresponds to the protons of the methyl group. This singlet appearance is due to the absence of coupling with neighboring protons.

The solvent signal ($CDCl_3$) appears at 7.24 ppm, which is typical for deuterated chloroform commonly used as an NMR solvent.

The synthesis reactions of the corresponding acids from 2- and 9-methylanthracene were investigated in this work. Initially, 9-methylanthracene was dissolved in acetic acid and subjected to oxidation using nitric acid, leading to the formation of the corresponding carboxylic acid.

The reaction equation and mechanism for the oxidation of 9-methylanthracene using nitric acid are presented below (equation 1):

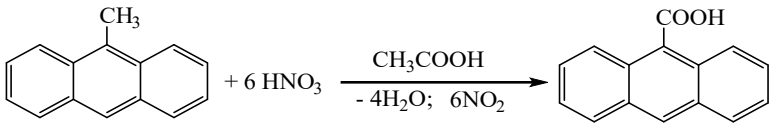

(1)

Nitric acid initially oxidizes the methyl group (-CH_3) at the 9-position of 9-methylanthracene to a hydroxymethyl group (-CH_2OH). Due to the stability of the anthracene ring system, the methyl substituent at the 9-position is relatively reactive and therefore susceptible to oxidation.

Nitric acid (HNO_3) decomposes to generate reactive nitrogen oxide species (e.g., NO_2, NO_3) that act as radical oxidizing agents (equation 2) [24].

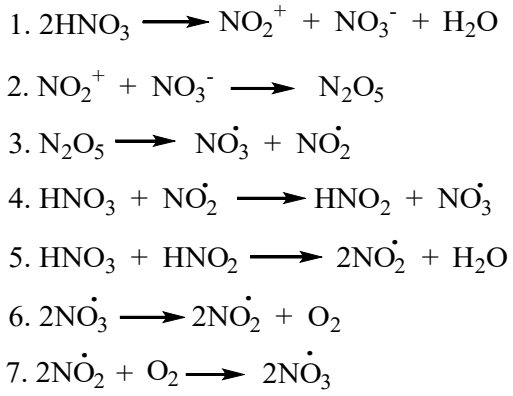

(2)

The $NO_2^{\bullet}$ radical formed during the decomposition of nitric acid can react with atmospheric oxygen to generate the $NO_3^{\bullet}$ radical (as shown in reaction **7**). The resulting $NO_3^{\bullet}$ radical initiates the oxidation process by abstracting hydrogen atoms from the methyl group of 9-methylanthracene, thereby promoting successive oxidation steps and overall reaction progression.

In the initial stage, the $NO_2^{\bullet}$ radical, due to its relatively high stability and reactivity, interacts with molecular oxygen to form $NO_3^{\bullet}$. The formed $NO_3^{\bullet}$ species then abstracts a hydrogen atom from the methyl group of 9-methylanthracene (equation 3), leading to the formation of a methyl anthracenyl radical.

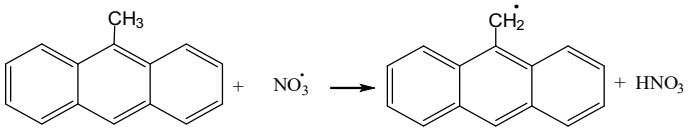

(3)

In the second step, after the formation of the 9-methylanthracene radical ($RCH_2^{\bullet}$), it reacts with molecular oxygen (O_2) present in the reaction medium (equation 4), leading to the formation of an intermediate peroxide radical ($C_{14}H_9$-$CH_2OO^{\bullet}$).

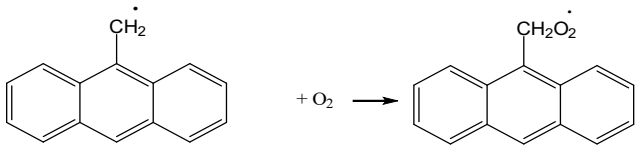

(4)

Here, R represents 9-methylanthracene.

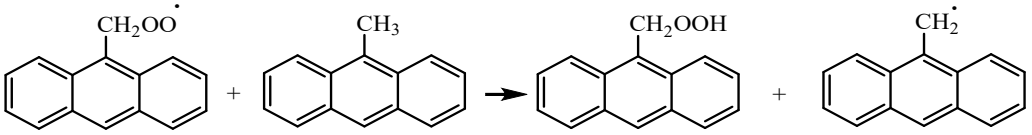

(5)

In the subsequent step, the peroxide radical reacts with methyl anthracene (equation 5), resulting in the formation of a hydroperoxide ($C_{14}H_9$-CH_2OOH) and regeneration of the methyl anthracenyl radical. The newly formed methyl anthracenyl radical then re-enters the reaction cycle by reacting again with molecular oxygen in the second step, thereby propagating the oxidation process.

In this step, the hydroperoxide ($C_{14}H_9$-CH_2OOH) first reacts with the $NO_3^{\bullet}$ radical (equation 6) to form a peroxide radical ($C_{14}H_9$-$CH_2OO^{\bullet}$).

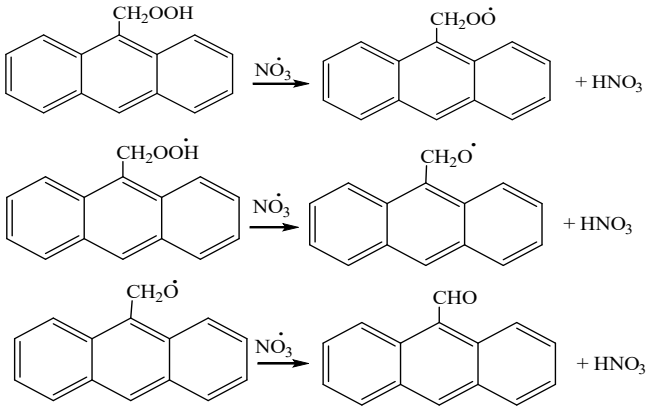

(6)

In the subsequent stage, this intermediate undergoes further transformation leading to the formation of a carbonyl group ($C_{14}H_9$-CHO), which represents an oxidized aldehyde intermediate in the reaction pathway.

The final stage of the reaction involves the oxidation of the carbonyl group (-CHO) to a carboxyl group (-COOH). In this step, the $NO_3^{\bullet}$ radical acts as an oxidizing agent and converts the carbonyl intermediate into the corresponding carboxylic acid, completing the overall oxidation process (equation 7).

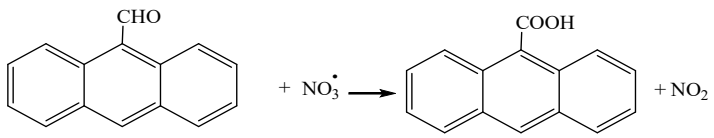

(7)

The IR spectrum (Figure 7) of the synthesized 9-anthracenecarboxylic acid shows characteristic absorption bands confirming its structure.

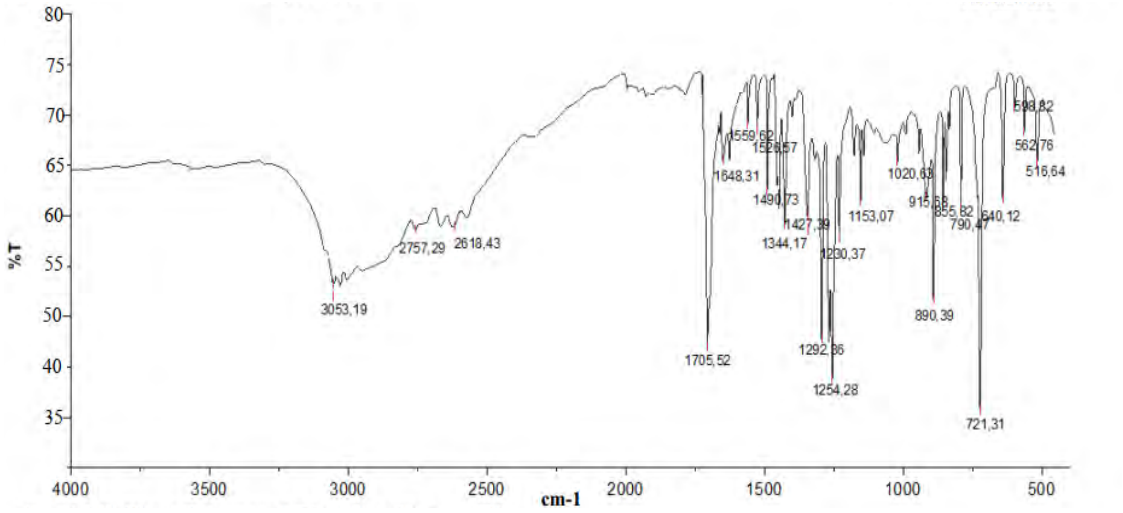

Figure 7. IR Spectrum of 9-Anthracenecarboxylic Acid

The band observed at 3053.19 cm^{-1} corresponds to asymmetric stretching vibrations of aromatic C-H bonds in the ring system. A broad absorption in the range of 2618.43-2757.29 cm^{-1} is attributed to the O-H stretching vibration of the carboxylic acid group.

The strong absorption band at 1705.52 cm^{-1} is characteristic of the C=O stretching vibration of the carbonyl group. Absorption bands in the region of 1559.57-1526.15 cm^{-1} are assigned to C=C stretching vibrations of the aromatic ring. In addition, the bands observed at 1292.86-1254.28 cm^{-1} correspond to C-O stretching vibrations, typical for carboxylic acid derivatives.

The chemical shift values in the ^{1}H NMR spectrum (ppm) depend on the electron density of protons. A decrease in electron density leads to increased deshielding, resulting in higher chemical shift values. Protons in aromatic rings typically appear in the range of 7-9 ppm, which is associated with the deshielding effect of the aromatic π-electron cloud (Figure 8).

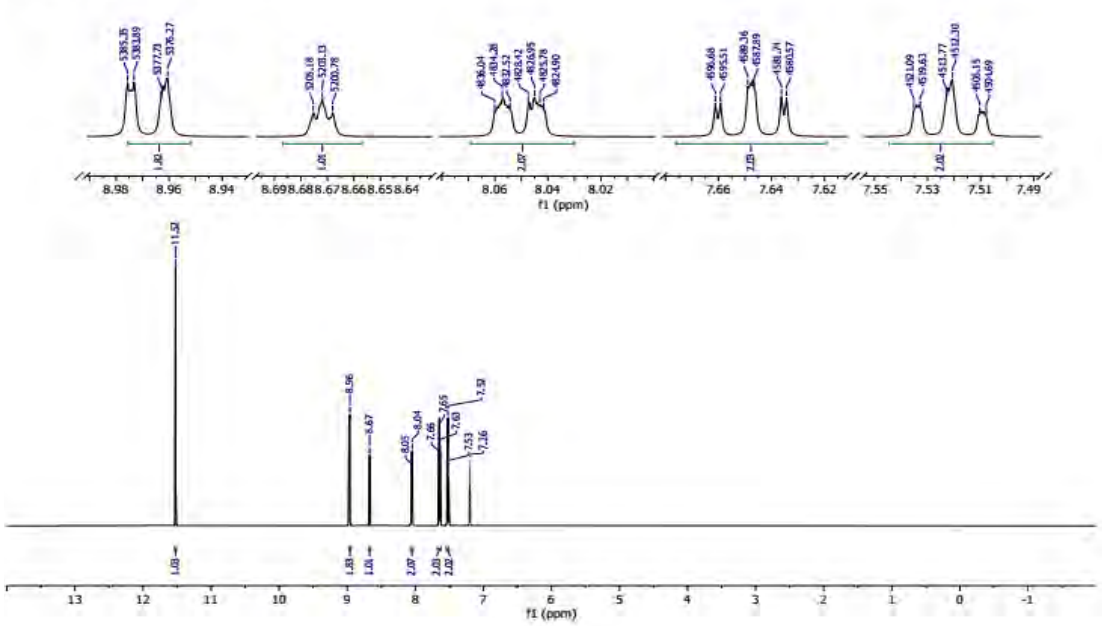

Figure 8. ^{1}H NMR Spectrum of 9-Anthracenecarboxylic Acid

Multiplet signals arise due to spin–spin coupling between neighboring protons. The coupling constant (J) reflects the strength of interaction between adjacent protons. Owing to the symmetry of the anthracene molecule, equivalent protons produce identical signals.

Aromatic protons generally appear as multiplets because they are strongly coupled with each other within the aromatic system. Since these protons are located in close proximity, their signals overlap, resulting in complex multiplet patterns.

The 9-anthracenecarboxylic acid molecule contains 9 aromatic protons distributed over three fused aromatic rings, as well as one carboxylic acid proton (-COOH). The aromatic proton signals are observed in the range of 7.52-8.96 ppm, corresponding to the aromatic system.

The carboxylic acid proton typically appears in the 10-13 ppm region as a singlet, since it does not couple with neighboring protons. In the recorded spectrum, a signal at 11.52 ppm corresponds to the -COOH proton. The solvent signal ($CDCl_3$) is observed at 7.260 ppm, which is characteristic for deuterated chloroform used in NMR spectroscopy.

In the ^{13}C NMR spectrum, the compound contains 15 carbon atoms. Carboxyl carbon signals are generally observed in the range of 170-185 ppm, while aromatic carbons appear in the 110-160 ppm region.

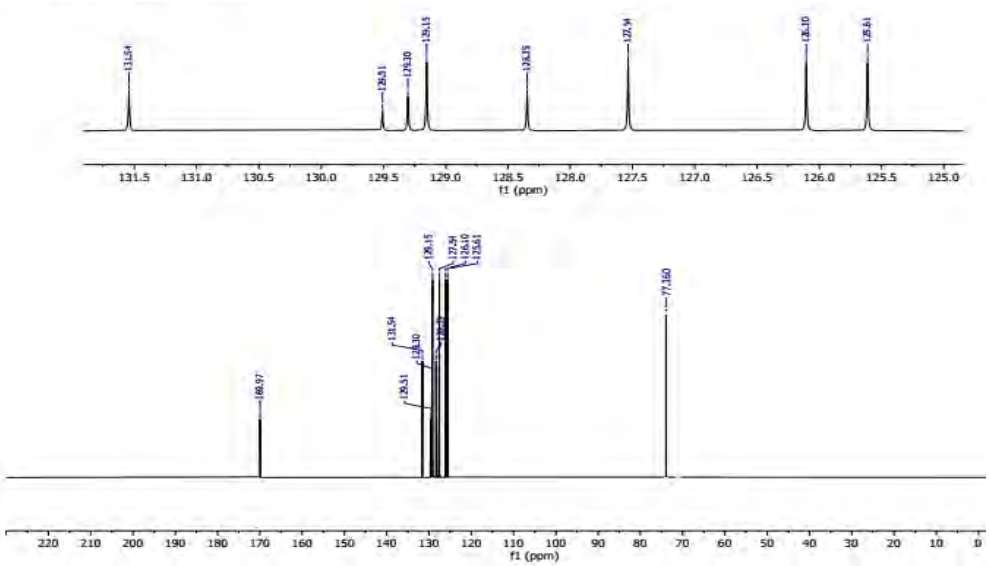

Figure 9. ^{13}C NMR Spectrum of 9-Anthracenecarboxylic Acid

In the spectrum shown in Figure 9, the signal at 170.097 ppm corresponds to the carbonyl (C=O) carbon atom. Signals in the range of 125.61-131.54 ppm are attributed to aromatic carbon atoms. The solvent signal ($CDCl_3$) appears at 77.160 ppm.

Based on the above spectral data, it can be concluded that the obtained spectra are consistent with the structure of 9-anthracenecarboxylic acid. The synthesis of 2- and 9-anthracenecarboxylic acids was carried out at 100-130°C with a reaction time of 1-1.5 hours. During the synthesis process, the effects of reaction time, temperature, and solvent nature on the product yield were investigated.

To study the influence of temperature on the product yield, a series of experiments were performed. 2- and 9-methylanthracene were used as starting materials, nitric acid as the oxidizing agent, and acetic acid as the solvent. The results of the experiments are presented in Table 2.

Table 2. Effect of Temperature and Reaction Time on the Yield of 9-Anthracenecarboxylic Acid Synthesis

Temperature,°C	Reaction time, h	Product yield, %	
		9-AKK	2-AKK
100	0.5	26.3	19.2
	1.0	30.5	26.4
	1.5	38.1	32.6
	2.0	40.4	37.5
110	0.5	32.6	25.7
	1.0	38.2	31.3
	1,5	42.4	37.1
	2.0	51.9	43.4
120	0.5	49.0	45.3
	1.0	63.9	57.9
	1.5	**72.1**	**70.5**
	2.0	70.3	69.2
130	0.5	51.3	48.8
	1.0	59.1	46.4
	1.5	63.2	41.2
	2.0	60.8	39.7

Based on the analysis of the results, it was observed that increasing the temperature from 100 to 130°C leads to an increase in the yield of both 2- and 9-anthracenecarboxylic acids. At 100°C with a reaction time of 1.5 hours, the yield of 9-anthracenecarboxylic acid was 38.1%, while the yield of 2-anthracenecarboxylic acid was 32.6%. At 120°C, the yields increased to 72.1% and 70.5%, respectively. This behavior can be explained by the acceleration of nitric acid decomposition at elevated temperatures, resulting in an increased concentration of reactive species that facilitate the oxidation of 2- and 9-methylanthracene.

However, when the temperature was raised to 130°C and above, side reactions began to occur, including further oxidative transformations and partial degradation of the aromatic ring system, which negatively affected the product yield.

In addition, it should be noted that the formation mechanisms and identification of by-products were not investigated in this study. The decrease in product yield at higher nitric acid concentrations is mainly attributed to the formation of nitro derivatives of 2- and 9-methylanthracene as well as partial ring cleavage reactions. Conversely, reducing the nitric acid concentration results in insufficient generation of reactive species ($NO_2^{\bullet}$, $NO_3^{\bullet}$), which are necessary for the oxidation process, as reported in the literature.

4. Conclusion

This work demonstrates an efficient strategy for the separation and valorization of polycyclic aromatic hydrocarbons (PAHs) from coal tar-derived fractions, highlighting their potential as a valuable chemical feedstock. Two key intermediates, 2-methylanthracene and 9-methylanthracene, were successfully isolated from high-boiling coal tar fractions and comprehensively characterized using FT-IR, ^{1}H and ^{13}C NMR, and GC-MS techniques, confirming their structural purity and identity. Subsequent selective oxidation using nitric acid in acetic acid medium enabled their transformation into corresponding anthracene carboxylic acids under controlled conditions.

The oxidation process was found to proceed via a radical pathway involving $NO_2^{\bullet}$ and $NO_3^{\bullet}$ species, with reaction efficiency strongly dependent on temperature and reaction time. Optimal conversion was achieved at 120°C and 1.5 h, providing the highest product yields, while higher temperatures promoted undesirable side reactions and reduced selectivity. These findings clearly demonstrate a direct correlation between molecular structure, reaction conditions, and oxidation behavior of methyl-substituted anthracenes.

Overall, the study provides new insights into the structure–reactivity relationships of PAHs under oxidative conditions and offers a practical approach for converting coal tar-derived aromatic hydrocarbons into high-value functionalized carboxylic acids. This contributes to both the sustainable utilization of coal tar resources and the development of advanced aromatic building blocks for material and chemical applications.

5. Acknowledgments

The authors express their gratitude to the Faculty of Chemistry, National University of Uzbekistan named after Mirzo Ulugbek, for their support in the conduct of this work.

6. Funding Sources

This research did not receive any specific grant from funding agencies in the public, commercial, or not-for-profit sectors.

7. References

1. Seadajk FF, Jain V, Ballal S, Singh A, Devi A, Sharma GC, Joshi KK, Kazemi M, Javahershenas R. Research on transition metals for the multicomponent synthesis of benzo-fused γ-lactams. *RSC Adv.*, 2025.
2. Baviera GS, Donate PM. Recent advances in the syntheses of anthracene derivatives. *Beilstein Org. Chem.*, 2021, 17, 2028-2050.
3. Huang J., Su J.-H., Tian H. The development of anthracene derivatives for organic light-emitting diodes. *J. Mater. Chem.,* 2012, 22, 10977.
4. Biswas S, Manikandan R, Shauloff N, Bhaumik SK, Jelinek R. High-performance functionalized anthracene organic supercapacitors. *RSC Appl. Interfaces*, 2024, 1, 920-927.
5. Costa RF, Oliveira MS, Aguiar ASN, Custodio JMF, Di Mascio P, Sabino JR, Verde GV, Souza JCP, Santin LG, Camargo AJ, Barbosa IC, Oliveira SS, Napolitano HB. Synthesis and structural studies of two new anthracene derivatives. *Crystals*, 2021, 11(8), 934.
6. Leo K. A new bright future for organic light-emitting transistors. *Innovation.*, 2025, 6(11).
7. Franck HG, Stadelhofer JW in Industrielle Aromatenchemie: Rohstoffe, Springer Verlag, 1988.
8. Park J-H, Chung DS, Park J-W, Ahn T, Kong H, Jung YK, Lee J, Yi MH, Park CE, Kwon S-K, Shim H-K. Soluble and easily crystallized anthracene derivatives: Precursors of solution-processable semiconducting molecules. *Org. Lett.*, 2007, 9(13).
9. Somashekar MN, Chetana PR. Review on anthracene and its derivatives: Applications. *Res. Rev.: J. Chem.*, 2016, 5(2), 45-52.
10. Chen CS, Rao PSC, Lee LS. Evaluation of extraction and detection methods for determining polynuclear aromatic hydrocarbons from coal tar contaminated soils. *Chemosphere*, 1996, 32(6), 1123-1132
11. Li H, Lu D, Qian B-Y, Lin J, Zhang H-J. Direct synthesis of K-region functionalized polycyclic aromatic hydrocarbons via twofold intramolecular C–H/C–H arylation. *Org. Lett.*, 2024, 26(51), 11140-11144.
12. Mougnol JBB, Waanders F, Fosso-Kankeu E, Al Alili AR. Leaching of polycyclic aromatic hydrocarbons from the coal tar in sewage wastewater, acidic and alkaline mine drainage. *Int. J. Environ. Res. Public Health*, 2022, 19(8), 4791.
13. Yang X, Rominger F, Mastalerz M. Contorted polycyclic aromatic hydrocarbons with two embedded azulene units. *Angew. Chem.*, 2019, 131, 17741-17746.
14. Erchinger JE, Okumura T, Nakata K, Shimizu D, Daniliuc CG, Amaike K, Glorius F, Itami K, Ito H. Functionalization and solubilization of polycyclic aromatic compounds by sulfoniumization, *Chem. Sci.*, 2025, 16(19), 8262-8267.
15. Robles-Mora G, Barrera J, Valdez L, García Díaz C. Polycyclic aromatic hydrocarbon sorption by functionalized humic acids immobilized in micro- and nano-zeolites. *Sustainability*, 2021, 13, 10391.
16. Sonia M-E, Zoraida G in Woodhead Publishing Series in Electronic and Optical Materials, 2023, ch. 2, pp 23-54.

17. Ratnaningsih W, Sukandar DW, Thesis, Bandung, 2021.
18. Fardhyanti DS, Damayanti A. Analysis of bio-oil produced by pyrolysis of coconut shell. *Int. J. Chem., Mater. Biomol. Sci.*, 2017, 11(9), 651-654.
19. Lv Q, Ma Y, Yao Q, Sun M. A review on the extraction of phenols from coal tar: Composition distribution and analysis, methods and mechanism, process and industrialization prospect. *Energy Fuels*, 2025, 39(3), 1479-1506.
20. Cheng J, Zhou F, Si T, Zhou J, Cen K. Mechanical strength and combustion properties of biomass pellets prepared with coal tar residue as a binder. *Fuel Process. Technol.*, 2018, 179, 229-237.
21. Gao L, Dong F-Q, Dai Q-W, Zhong G-Q, Halik U, Lee D-J. Coal tar residues based activated carbon: Preparation and characterization. *J. Taiwan Inst. Chem. Eng.*, 2016, 63, 166-169.
22. Li W, Wang Y, Zhu F, Li X, Zhou Q, Liu G, Peng Z, Qi T, Shen L. Evaluating the effects of formation and stabilization of opal/sand aggregates with organic matter amendments. *Environ. Manage.*, 2023, 337.
23. Rui H, Xiangzhou Y, Lunjing Y, Lina H, Weiren B, Liping C, Jian L, Jiancheng W, Yong SO. Carbon precursors in coal tar: Extraction and preparation of carbon materials. *Sci. Total Environ.*, 2021, 788, 147697.
24. Villot A, Pena J, Gerente C. Recovery of pyrolysis char from residual biomass in accordance with the principles of the circular economy. *Fuel*, 2023, 331, 125837.
25. Ravenni G, Sárossy Z, Ahrenfeldt J, Henriksen UB. Activity of chars and activated carbons for removal and decomposition of tar model compounds – A review. *Renewable Sustainable Energy Rev.*, 2018, 94, 1044-1056.
26. Hervy M, Berhanu S, Weiss-Hortala E, Chesnaud A, Gérente C, Villot A, Pham Minh D, Thorel A, Le Coq L, Nzihou A. Multi-scale characterisation of chars mineral species for tar cracking. *Fuel*, 2017, 189, 88-97.

The Chemist
Journal of the American Institute of Chemists

Fatty Acids Profiling and Skincare Formulation from *Ricinus communis* (Castor) Seed Oil

Olubunmi Atolani[a], Maryam Omowumi Bakare[a], Taiwo Janet Ogundoro[a]*, Ezekiel Adebiyi[a]

[a]*Department of Chemistry, University of Ilorin, Nigeria*
**Corresponding author (E-mail: ogundorotaiwo@gmail.com)*

Abstract: Castor oil, a valuable vegetable oil extracted from the seeds of the castor bean (*Ricinus communis*), has attracted significant attention due to its wide-ranging benefits. It serves numerous industrial and medicinal purposes. In this study, the total composition of fatty acid and biological analysis of castor seed oil obtained using water and hexane as extractants was determined. The oils were transesterified via methanolysis to obtain fatty acid methyl esters, subjected to Gas Chromatography-Mass Spectroscopy (GC-MS) analysis, and analysed for its *in vitro* anti-inflammatory potential. Eleven fatty acids were identified in the water-extracted oil: ricinoleic acid (83.51%), linoleic acid (7.13%), elaidic acid (4.62%), palmitic acid (2.23%), stearic acid (1.51%), linolenic acid (0.64%), oleic acid (0.90%), cis-11-eicosenoic acid (0.70%), palmitoleic acid (0.63%), ricinic acid (0.28), and lauric acid (0.09%). The hexane-extracted oil afforded 9 fatty acids which include: ricinoleic acid (72.43%), linoleic acid (8.76%), ricinic acid (8.40%), elaidic acid (6.17%), palmitic acid (3.65%), stearic acid (1.69%), oleic acid (1.38%), linolenic acid (0.67%), lauric acid (0.21%) and myristic acid (0.09%). The ricinoleic acid was found to be the major fatty acid in both oils. *In vitro* assessment of the ability of the oil to inhibit albumin denaturation, a dose-dependent activity which was comparable to the reference drug, indomethacin, was demonstrated. The high concentration of ricinoleic acid present in the oil is considered the primary contributor to its observed anti-inflammatory properties.

Key Words: Fatty acid, castor seeds, anti-inflammatory, cosmetic formulation, FAME, GC-MS

1. Introduction

Natural plant oils have gained increasing attention in modern skincare due to their rich lipid content and ability to enhance skin hydration, barrier function, and overall health [1]. Lipids serve a central role in skincare due to their ability to enhance skin hydration, support barrier integrity, and deliver bioactive compounds beneficial to skin health [2]. The effectiveness of any plant oil in cosmetic applications is largely determined by its fatty acid composition, as fatty acids influence the emolliency, absorption rate, stability, oxidative resistance, and compatibility of oil for different skin types [3]. Fatty acid profiling serves as a scientific tool for assessing the quality, stability, and suitability of oils used in skincare formulations [4].

Ricinus communis (castor) seed oil, the major source of the triglyceride, triricinolein (Figure 1), is a widely used natural lipid having been recognized in traditional medicine, pharmaceuticals, and cosmetic applications.

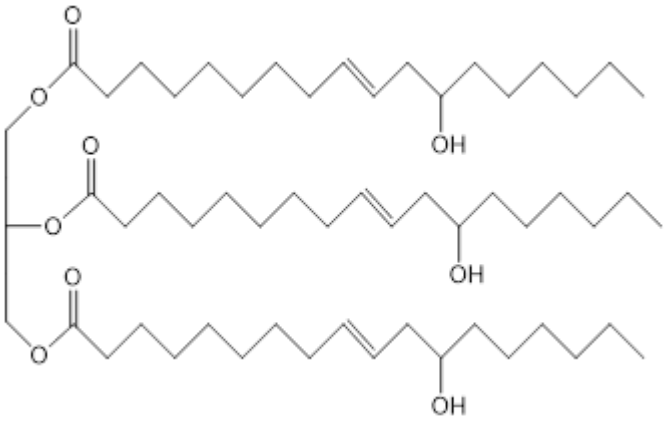

Figure 1. Structure of Castor Oil (Triglyceride: Triricinolein)

Extracted from the seeds of the castor plant, it is known for its high viscosity, glossy texture, and beneficial skin properties [5]. Castor oil is particularly unique because it contains an exceptionally high proportion of ricinoleic acid, a hydroxylated fatty acid responsible for its strong moisturizing, anti-inflammatory, and antimicrobial effects [6]. These characteristics make it a promising ingredient for developing skincare formulations targeted at improving skin hydration, soothing irritation, and enhancing skin barrier integrity. Castor bean oil, among all vegetable oils, is distinctive because of its high level of ricinoleic acid (over 85%), which is a fatty acid consisting of 18 carbons, a double bond between C9 and C10, and a hydroxyl group attached to C12 [7]. Despite its extensive use, scientific evaluation of its fatty acid composition remains important to ensure consistency, detect adulteration, and optimize its application in evidence-based skincare products [8]. Hydrogenated castor oil and castor acids with melting points higher than the non-hydrogenated material are used in cosmetics [7]. The hydrogenated form is solid and has no harmful effect on the skin, so it is used as

emulsifying agent in skin creams [9]. Castor oil is used as an emulsifier and non-ionic solubilizer which is produced by mixing ethylene oxide and castor oil [10]. Pomace is castor residue. It has a high amount of nitrogen and is used as animal feed and as organic fertilizer without any reported major harmful effects [11]. The leaves are used as food for silkworms and the stalks are used for fuel purpose in India [12].

Fatty acid profiling of *Ricinus communis* seed oil is essential for understanding its functional attributes and optimizing its use in formulation science [13]. It is performed using gas chromatography, provides detailed information on the lipid makeup of castor oil by identifying the types and proportions of fatty acids present. This analysis is vital because variations in fatty acid composition can arise due to differences in seed quality, geographic origin, and extraction methods [14]. Although castor oil has been widely utilized for various purposes, there is still limited research linking its lipid profile directly to the formulation performance of specific skincare products. This calls for a need to further investigate how *Ricinus communis* (Castor) seed oil composition influences formulation stability, absorption, and functional benefits when applied to the skin.

2. Experimental

Chemicals and Materials

The solvents and reagents used were analytical grade and were obtained from Sigma-Aldrich Chemical Limited and British Drugs House Chemical Ltd (BDH). These include methanol, ethanol, water, n-hexane, diethylether, hydrochloric acid, potassium hydroxide solution, phenolphthalein indicator, glycerine and tocopherols. Other materials such as virgin coconut oil, shea butter, honey, emulsifier, and beeswax were obtained locally in high quality. Castor seeds (*Ricinus communis*) were obtained from a farm in Ilorin South Local Government Area, Ilorin, Kwara State, Nigeria (Figure 2).

a

b

c

d

Figure 2. a – Fresh Castor Fruit; b - Dried Castor Fruit; c - Castor Seeds; d - Extracted Castor Oil

The plant sample was identified as *Ricinus communis* and documented in the herbarium at the Department of Plant Biology, University of Ilorin, Ilorin Nigeria. The seeds were obtained by removing the castor shaft and the castor coat, then air-dried for 24 hours and pulverized using electric blender. For the water extraction, the sample was roasted

at moderate temperature for moisture reduction, easier pulverization and improved oil yield before it was pulverized.

Solvent Extraction of Castor Seed Oil

The pulverized castor seed was extracted cold with n-hexane for 5 days. The extract was then concentrated using rotary evaporator. The oil obtained was kept in a cool place for further analysis.

Aqueous Extraction of Castor Seed Oil

Water was added to the roasted pulverized castor seeds and was mixed thoroughly to disperse the paste until a runny consistency was obtained, after which it was heated for 50 minutes to loosen the oil from the thick paste. The paste was then strained to remove the castor seed residue, and the runny paste was then poured into a container with a fitted lid. It was placed in a freezer for 48 hours to allow the oil to separate out. The oil was collected over the aqueous paste and kept in a cool place for further work.

Transesterification

Castor seed oil (1 g) obtained via solvent extraction was treated with 100 mL of 0.1 M methanolic potassium hydroxide, which was then poured into a round bottom flask and refluxed for 30 minutes to hydrolyze and convert the lipid into methyl esters. The methyl ester formed was extracted with n-hexane and diethylether and washed with water in a separating funnel. It was allowed to settle down to form two distinct layers. The upper layer (Organic layer) was distilled, and the resulting oil was recovered. The process was repeated for the water extracted oil.

Determination of the Physicochemical Properties of *Ricinus communis* (Castor Seed) Oil

Both extracted oils were subjected to physicochemical evaluations following standard procedure [13].

Acid Value Test

The acid value of the oil samples was determined by titration method. Castor seed oil (0.5 g) was dissolved in 50 mL solvent of equal volume of diethylether and ethanol.

The solution was titrated with standardized 0.1 M potassium hydroxide solution using phenolphthalein indicator. The acid value was calculated using the formula (equation 1):

$$\text{Acid value} = \frac{56.1 \times M \times V}{W} \quad (1)$$

where:
M= molarity of standard potassium hydroxide KOH
V= volume (mL) of standardized 0.1M potassium hydroxide consumed by sample
W= weight (g) of Castor sample.

Saponification Test

Castor seed oil (0.5 g) was weighed into a conical flask and 25 mL of methanolic potassium hydroxide was added. The solution was connected to a reflux condenser and boiled gently on a steam bath for 30 minutes. The hot solution was titrated against 0.5 M hydrochloric acid using phenolphthalein indicator to the end point when the pick colour disappeared. The saponification value was calculated using the formula (equation 2):

$$SV = \frac{56.1 \times M \times (V_B - V_T)}{W} \quad (2)$$

where:
SV= Saponification value
VB = volume (mL) of 0.5 M hydrochloric acid required to titrate blank
VT = volume (ml) of 0.5 M hydrochloric acid required to titrate sample
M = molarity of hydrochloric acid solution
W = Weight (g) of samples in used.

Formulation of Skin Care Cream

The recipes for the preparation of the organic cream contain components which included natural bee wax, emulsifier, honey, shea butter, virgin coconut oil, tocopherols and glycerine. First, the bee wax, emulsifier, honey, shea butter, virgin coconut oil, tocopherols, and glycerine was melted inside a beaker on a hotplate, which was followed by the addition of the hexane-extracted castor seed oil. The hexane-extracted castor seed oil was selected as a result of the presence of higher amounts of ricinoleic acid. The procedure was repeated using different amounts of castor seed (*Ricinus communis*) oil. The mixtures were poured into different containers for cooling, solidification and storage.

The recipe (Table 1), indicated above, presents seven samples to systematically investigate the influence of castor oil concentration on the overall performance of a semi-solid topical formulation. In all samples, the quantities of wax, emulsifier,

honey, shea butter, virgin coconut oil, tocopherols, and glycerine were kept constant, while the amount of castor oil was progressively increased from 0.5 g (Sample A) to 10.0 g (Sample G). This controlled approach allows for a clear evaluation of the specific contribution of castor oil to the physicochemical and functional characteristics of the formulation.

Table 1. Formulation (Recipe) of Skin Care Cream from Castor Seed Oil

Formulations	Wax (g)	Emulsifier (g)	Honey (g)	Shea butter (g)	Virgin Coconut Oil (g)	Tocopherols (g)	Glycerine (g)	Castor oils (g)
Sample A	0.5	1.0	0.2	0.5	0.5	0.1	1.0	0.5
Sample B	0.5	1.0	0.2	0.5	0.5	0.1	1.0	1.0
Sample C	0.5	1.0	0.2	0.5	0.5	0.1	1.0	1.5
Sample D	0.5	1.0	0.2	0.5	0.5	0.1	1.0	2.0
Sample E	0.5	1.0	0.2	0.5	0.5	0.1	1.0	3.0
Sample F	0.5	1.0	0.2	0.5	0.5	0.1	1.0	5.0
Sample G	0.5	1.0	0.2	0.5	0.5	0.1	1.0	10.0

Wax (0.5 g) was included to impart structural rigidity and enhance the consistency of the formulation, while the emulsifier (1.0 g) ensured the formation and stability of the oil–water interface. Honey (0.2 g) and glycerine (1.0 g) served as humectants, promoting moisture retention and contributing to the hydrating properties of the formulation. Shea butter (0.5 g) and virgin coconut oil (0.5 g) acted as emollients, improving skin conditioning and barrier function. Tocopherols (0.1 g) were incorporated as antioxidants to enhance oxidative stability and protect the lipid components from degradation.

Castor oil was selected as the variable component due to its high viscosity, ricinoleic acid content, and well-documented emollient and occlusive properties. The gradual increase in castor oil concentration across Samples A–G was expected to significantly influence the rheological behaviour, spreadability, and sensory attributes of the formulations. At lower concentrations (Samples A–C), the formulations are anticipated to exhibit lower viscosity, improved spreadability, and a lighter skin feel. Intermediate concentrations (Samples D–E) are likely to provide a balance between emolliency and acceptable sensory properties. In contrast, higher castor oil levels (Samples F–G) are expected to produce thicker, more occlusive formulations, which may enhance moisturization but could negatively impact spreadability and user acceptability.

Furthermore, increasing the oil phase without a corresponding increase in emulsifier concentration may affect emulsion stability, particularly in formulations with high castor oil content. This variation is critical for determining the maximum castor oil concentration that can be incorporated without compromising formulation stability. The formulation design enables a systematic assessment of the role of castor oil in modulating the physical, functional, and aesthetic properties of the topical system, thereby

facilitating the identification of an optimal composition for the intended application.

Gas Chromatography Mass Spectroscopy Analysis

The FAME obtained was subjected to Gas Chromatography-Mass Spectroscopy System with a GC, (Shimadu GC-2010) and S model (Shimadu MS-QP 2010). Fatty acid standards were first injected, and the calibration was kept for further analysis. Carrier gas (He) was used. Temperature was first maintained isothermally and then programmed to rise from 60 to 280°C. The flowrate was adjusted to 0.8 mL/min. The mass range of the mass spectrometer operates at 70eV ionisation energy and FAMES was identified by comparing the retention time with those of the authentic standard and further confirmed by comparing the mass fragmentation pattern with those of NIST library.

Anti-inflammatory Evaluation: Albumin Denaturing Inhibition Assay

The extracted castor seed oil was subjected to biological analysis (protein albumin denaturation). The reaction mixture (5 mL) of each of the formulations comprised of 0.2 mL of eggs albumin, 2.8 mL of phosphate buffered saline (PBS, pH 6.4) and 2 mL of varying concentration of extracts. A similar volume of double distilled water served as a control. Then, the mixture was incubated at 37°C in an incubator for about 15 mins and then heated at 70°C for 5 mins. After cooling, their absorbance was measured at 660 nm by using a pure blank. Diclofenac sodium (standard drug) was used as a reference drug and treated as such for the determination of absorbance. The percentage inhibition of protein denaturation was calculated by the formula (equation 3):

$$\% \text{ Inhibition} = \frac{\text{Absorbance of control- Absorbance of Sample}}{\text{Absorbance of Control}} \times 100 \quad (3)$$

Indomethacin was used as standard drug.

3. Results and Discussion

Result of Physicochemical Properties of *Ricinus communis* Seed Oil

The physicochemical parameters of the water and hexane-extracted oils are as presented in Table 2.

Table 2. Physicochemical Parameters of the Extracted *Ricinus communis* Seed Oils

Parameters extracted	Aqueous-extracted Castor oil	Hexane-extracted Castor oil
Colour	Brown colour	Pale yellow
% Oil yield	14.8	4.99
% of Transesterified oil	12	37
Saponification Value (mg KOH/g)	167	168.5
Acid value (mg KOH/g)	3.93	2.81

The physicochemical properties of castor oil vary significantly based on the extraction method employed. The comparison between virgin extracted and solvent extracted samples highlights differences in colour, yield, transesterification efficiency, and chemical indices. Water-extracted castor oil exhibits a brown coloration, while solvent extracted oil is pale yellow. The darker colour of the water-extracted oil may be attributed to the presence of natural pigments, residual seed coat materials, or higher levels of impurities retained during mechanical extraction. Solvent extraction produces lighter-coloured oils due to more efficient removal of pigments and impurities. Water-extracted extraction produced a higher yield (14.8%) compared to solvent extraction (4.99%). This suggests that adopted water extraction method is more effective in recovering oil from castor seeds under the conditions used. The lower yield from solvent extraction may be attributed to incomplete penetration of the solvent or losses during recovery. However, the solvent extracted oil showed a higher transesterification percentage (37%) compared to water-extracted oil (12%). This indicates that solvent-extracted oil is more amenable to conversion into biodiesel or other esters, possibly due to lower impurity levels and better accessibility of triglycerides to catalysts.

Both oils exhibit similar saponification values (167 mg KOH/g for water-extracted vs. 168.5 mg KOH/g hexane-extracted). This suggests that the average molecular weight of fatty acids in both oils is comparable, and the extraction method does not significantly alter the fundamental triglyceride composition. Virgin oil has a higher acid value (3.93 mg KOH/g) compared to solvent oil (2.81 mg KOH/g). A higher acid value indicates greater free fatty acid content, which may result from hydrolysis during mechanical extraction or storage. The hexane extraction appears to produce oil with lower free fatty acid content, which is advantageous for industrial applications such as biodiesel production, where high acid values can interfere with transesterification.

Gas Chromatography Mass Spectroscopy Analysis for Fatty Acid

The two transesterified castor oils were subjected to GC-MS analysis. The fatty acid profile of each of the extracted oil are shown in Table 3.

Table 3. Fatty Acid Profile of Water- and Hexane-Extracted Castor Seed Oil

S/N	Fatty Acid	RT (mins)	%Composition Water-Extracted Oil	%Composition Hexane-Extracted Oil
1	Lauric acid	12.76	0.09	0.21
2	Palmitic acid	18.32	2.23	3.68
3	Myristic acid	15.68	-	0.09
4	Linoleic acid	20.34	7.13	10.02
5	Linolenic acid	20.39	0.64	-
6	Elaidic acid	20.45	4.62	6.17
7	Oleic acid	20.52	0.90	1.38
8	Stearic acid	20.82	1.51	1.60
9	Ricinoleic acid	22.90	83.51	72.43
10	Cis-11-Eicosenoic acid	23.18	0.70	-
11	Ricinic acid	23.72	0.28	8.40
12	Palmitoleic acid	25.28	0.71	-

The fatty acids profile obtained from the GC-MS fragments reveals a distinctive composition dominated by ricinoleic acid (83.51%). This exceptionally high proportion is characteristic of castor oil and confirms the identity of the sample. Ricinoleic acid (commercial source of a hydroxylated fatty acid) is well-documented for its diverse pharmacological and industrial applications, including anti-inflammatory, antimicrobial, and laxative properties, as well as its role in the production of bio-based polymers, lubricants, and biodiesel. Its predominance in the sample emphasis the unique chemical nature of castor oil compared to other vegetable oils. Linoleic acid (7.13%) and elaidic acid (4.62%) represent the next most abundant fatty acids. Linoleic acid is an essential polyunsaturated fatty acid which contributes nutritional value and plays a role in maintaining membrane fluidity and cellular signalling. Elaidic acid, which is a trans isomer of oleic acid, is less common in natural oils but its presence here may reflect specific metabolic or processing pathways. Together, these fatty acids add functional diversity to the oil.

Palmitic acid (2.23%), stearic acid (1.51%), and oleic acid (0.90%) are minor components that contribute to the saturated and monounsaturated fractions of the oil. Although present in small amounts, these fatty acids influence the physicochemical properties of the oil, including oxidative stability and melting behaviour. Trace amount of lauric, linolenic, cis-11-eicosenoic, ricinic, and palmitoleic acids (<1%) further highlight the chemical complexity of the sample. The overall

profile demonstrates that castor oil is highly specialized, with ricinoleic acid as its defining component. Unlike common edible oils such as soybean or sunflower oil, which are rich in linoleic or oleic acids, castor oil's composition makes it more suitable for pharmaceutical and industrial applications than for widespread dietary use. The role of seed and seed oil in food and as dietary supplement cannot be overemphasized [15-17].

The presence of essential fatty acids, albeit in smaller proportions, suggests some nutritional relevance, but the oil's primary value lies in its bioactive and functional properties.

The fatty acids profile (Table 3) obtained from the GC-MS fragments of solvent-extracted castor seed oil revealed ricinoleic acid as the major constituent with amount, 72.43%. Ricinoleic acid (a hydroxylated C18 fatty acid) is unique among vegetable oils and is primarily responsible for the oil's distinctive physicochemical and biological properties. Its abundance explains the wide industrial and pharmaceutical applications of castor oil, including its use in lubricants, coatings, cosmetics, and as a bio-based feedstock. Medicinally, ricinoleic acid is associated with anti-inflammatory, anti-microbial, and laxative activities, making it the defining constituent of castor oil.

Secondary components include linoleic acid (10.02%) and ricinic acid (8.4%), both present in appreciable amounts. Linoleic acid contributes nutritional value and plays a role in maintaining membrane fluidity and cellular signaling. Ricinic acid adds chemical diversity, which may influence the oil's functional properties. Elaidic acid (6.17%) also appears in notable proportion, reflecting unsaturation and potential structural isomerization during extraction or processing. Minor fatty acids such as palmitic (3.65%), stearic (1.6%), and oleic (1.38%) acids contribute to the saturated and monounsaturated fractions of the oil. Despite the lower component, they still enhance oxidative stability and influence melting behaviour. Trace levels of lauric (0.21%) and myristic acid (0.09%) further highlight the chemical complexity and significance of the oil. However, their biological contributions are likely limited. This composition distinguishes castor oil from other vegetable oils, reinforcing its specialized role in medicine, cosmetics, and industry rather than as a conventional dietary fat.

Anti-inflammatory Evaluation

Albumin denaturation is a widely accepted *in vitro* model for evaluating anti-inflammatory potential, as protein denaturation is a key event in inflammatory processes. Figure 3 illustrates the percentage inhibition of albumin denaturation by *Ricinus communis* (castor seed) oil and its formulated cream compared to the standard anti-inflammatory drug, indomethacin.

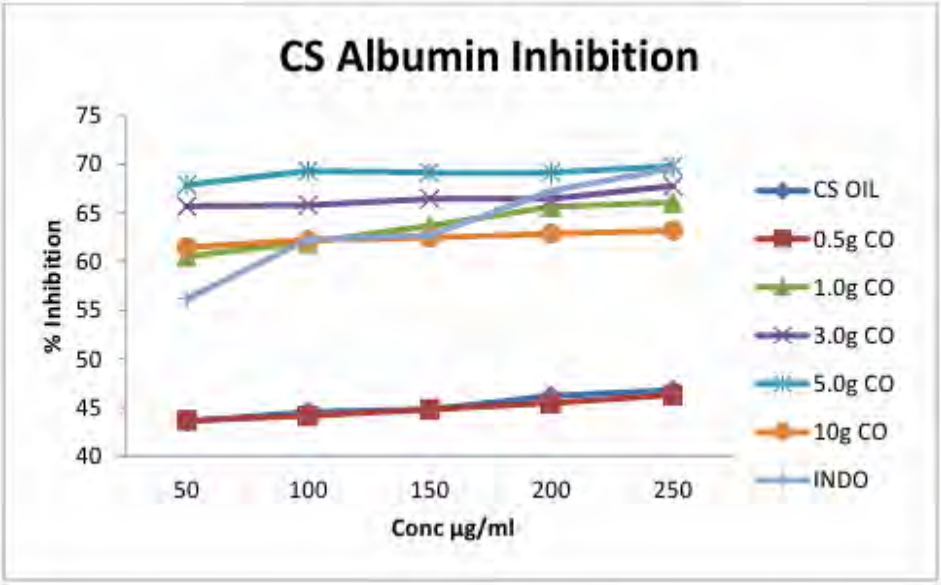

Figure 3. Inhibition (%) of Albumin Denaturation by Castor Seed Oil and the Formulated Products

The result revealed that 10 g castor oil showed inhibition levels comparable to indomethacin, suggesting that castor oil at high concentrations possesses significant anti-inflammatory potential. This highlights the possibility of castor oils serving as alternatives to conventional synthetic drugs. Samples with castor oil concentrations 3.0 and 5.0 g castor exhibited a noticeable inhibition, reinforcing the dose-dependent trend. However, lower concentrations at 0.5 g and 1.0 g were largely ineffective. This suggested that therapeutic efficacy of castor oil may only be achieved at higher doses.

The results indicate that both the crude castor oil and the formulated cream exhibit substantial inhibitory effects on albumin denaturation, suggesting strong anti-inflammatory properties. The inhibition percentages were comparable to, and in some cases approached, those of indomethacin, highlighting the therapeutic relevance of castor oil-based formulations. The high activity can be attributed to the presence of ricinoleic acid, the major fatty acid identified in the GC-MS analysis, which is known for its anti-inflammatory and analgesic properties.

The dose-response relationship observed is consistent with pharmacological principles, where increased concentrations enhance biological activity until a plateau is reached. While high-dose castor oil shows promise and potential safety. A clear dose-dependent trend is observed across most samples, with inhibition increasing with increasing concentration. This aligns with pharmacological principles and underscores the importance of optimizing dosage for therapeutic applications. The findings suggest that the oil is a promising candidate for natural anti-inflammatory cosmetic formulations.

4. Conclusion

The study successfully characterized the chemical constituents of *Ricinus communis* oil and demonstrated its potential for cosmetic and therapeutic applications. Through transesterification, the oil was converted into fatty acid methyl esters (FAME) and formulated into a cosmetic cream. GC-MS analysis revealed 11 distinct compounds in both water- and hexane-extracted oils, with ricinoleic acid identified as the predominant component. Notably, both the raw oil and the formulated cream exhibited significant anti-inflammatory activity, comparable to the standard drug indomethacin. These findings highlight *Ricinus communis* oil as a promising natural resource for developing anti-inflammatory cosmetic formulations and suggest its potential role in pharmaceutical and cosmeceutical industries.

5. References

1. Wang Y, Jinjin D, Wang Y, Guanai M, Zhang X. Advances in plant essential oils and drug delivery systems for skincare. *Front. Pharmacol.*, 2025, 16, 1578280. https://doi.org/10.3389/fphar.2025.1578280
2. Siqueira RAGB, Hradkova I, Leite-Silva VR, Andréo-Filho N, Lopes PS. Skin lipids and their influence on skin microbiome and skin care. *ACS Omega*, 2025, 10(27), 28534-28546. DOI: http://pubs.acs.org/journal/acsodf
3. Abdalla S, Aroua MK, Gew LT. A comprehensive review of plant-based cosmetic oils (virgin coconut oil, olive oil, argan oil, and jojoba oil): Chemical and biological properties and their cosmeceutical applications. *ACS Omega*, 2024, 9(44), 44019-44032. https://doi.org/10.1021/acsomega.4c04277
4. Ojha PK, Poudel DK, Rokaya A, Maharjan S, Timsina S, Poudel A, Satyal R, Satyal P, Setzer WN. Chemical compositions and essential fatty acid analysis of selected vegetable oils and fats. *Compounds*, 2024, 4(1), 37-70. https://doi.org/10.3390/compounds4010003
5. Avramovic JM, Marjanović Jeromela AM, Krstić MS, Kiprovski BM, Veličković AV, Rajković DD, Veljković VB. Castor oil extraction: methods and impacts. *Sep. Purif. Rev.*, 2025, 54(1), 60-82. https://doi.org/10.1080/15422119.2024.2361674
6. Talwan P, Gautam D, Kumar R, Sharma S, Dhiman S, Gill R, Thakur A, Sharma D, Sharma S, Kumar A. A review of the chemical composition, modification, and biomedical appli-cation of *Ricinus communis*. *Indian J. Nat. Prod. Resour.*, 2024, 15(1), 21-42. https://doi:10.56042/ijnpr.v15i1.155
7. Dhanuskar S, Naik SN, Pant KK. Castor oil-based derivatives as a raw material for the chemical industry. In: Catalysis for Clean Energy and Environmental Sustainability: Biomass Conversion and Green Chemistry, Springer International Publishing, Cham, 2021, vol 1, pp 209-235. https://doi:10.1007/978-3-030-65017-9_8
8. Azeem M, Mahmood S, Shaheen A, Tariq A, Khan I, Arshad M. Analytical

methods in cosmetics. In: Sustainable Cosmeceuticals: Integrating Natural and Biotechnological Innova-tions, Springer Nature Switzerland, Cham, 2025, pp 291-331. https://doi.org/10.1007/978-3-031-86087-4_12

9. Mawazi SM, Ann J, Othman N, Khan J, Alolayan SO, Al Thagfan SS, Kaleemullah M. A review of moisturizers: History, preparation, characterization and applications. *Cosmetics*, 2022, 9(3), 61. https://doi.org/10.3390/cosmetics9030061

10. Desai S, Chakraborty M, Jana AK, Kohli HP. Viscosity reduction and stability study of Indian heavy crude oil/water emulsion using hydrogenated castor oil ethoxylate with 40 moles of ethylene oxide as surfactant. *Results Surf. Interfaces*, 2025, 19, 100504. https://doi.org/10.1016/j.rsurfi.2025.100504

11. Malenica D, Kass M, Bhat R. Sustainable management and valorization of agri-food industrial wastes and by-products as animal feed: For ruminants, non-ruminants and as poultry feed. *Sustainability*, 2022, 15(1), 117. https://doi.org/10.3390/su15010117

12. Kumara RR. Breeding in host plants of Eri silkworm for rearing suitability. *Mysore J. Agric. Sci.*, 2023, 57(3), 24-43.

13. Adama KK, Anani OA. Experimental and theoretical assessment of phenomena linked with separation and purification of biodiesel from *Ricinus communis* seed oil. *Heliyon*, 2023, 9(6). https://doi.org/10.1016/j.heliyon.2023.e16536

14. Hossain A, Pal A, Salem S. Development of method and analysis protocol for fatty acids derivatives of castor oil by using gas chromatography-mass spectrometry. *Biocatal. Agric. Biotechnol.*, 2024, 61, 103408. https://doi.org/10.1016/j.bcab.2024.103408

15. Atolani O, Areh ET, Oguntoye OS, Zubair MF, Fabiyi OA, Oyegoke RA, Tarigha DE, Adamu N, Adeyemi OS, Kambizi L, Olatunji GA. Chemical composition, antioxidant, anti-lipo-oxygenase, antimicrobial, anti-parasite and cytotoxic activities of *Polyalthia longifolia* seed oil. *Med. Chem. Res.*, 2019, 28(4), 515-527. https://doi.org/10.1007/s00044-019-02301-z

16. Adeyemi KD, Ogundele VO, Atolani O. Dietary supplementation of *Allium cepa* skin alters intramuscular fat, muscle cholesterol, and fatty acids in rabbits. *J. Sci. Food Agric.*, 2022, 102(9), 3683-3692. https://doi.org/10.1002/jsfa.11715

17. Adeyemi KD, Abdulrahman A, Ibrahim SO, Zubair MF, Atolani O, Badmos AA. Dietary supplementation of *Tetracarpidium conophorum* (African walnut) seed enhances muscle n-3 fatty acids in broiler chickens. *Eur. J. Lipid Sci. Technol.*, 2020, 122, 1900418. https://doi.org/10.1002/ejlt.201900418

The Chemist
Journal of the American Institute of Chemists

Study the Mechanical and Thermal Properties of Unsaturated Polyester Reinforced with Different Proportions of Novolac

Zahra Marwan Mohamad Abdalla[1], Ebtehag Z. Sulyman[2]

College of Education for Women, Department of Chemistry, University of Mosul, Iraq
(E-mail: zahraa.24gep46@student.uomosul.edu.iq; ebthalim@uomosul.edu.iq)

Abstract: In this study, unsaturated polyester (UPE) was reinforced with novolac resin in various quantities (0.5%–5.0%) and the mechanical and thermal characteristics of the composites were examined. Novolac was prepared by condensation of phenol and formaldehyde in the presence of an acid and ground to a uniform powder and extruded in the form of test pieces in combination with UPE. The mechanical properties of the composites were tested, and the composites were characterized by FTIR, TGA, DSC and SEM techniques. It is observed from the results that mechanical properties are at their highest at 1% novolac ratio with its optimum values of modulus (~830 MPa), compressive strength (~120 MPa), hardness (~86 Shore-D) and impact resistance (~1.7 kJ/m²). The appropriate ratio was determined to be 2.5% for maximizing thermal stability and stiffness at high temperature (up to 50°C, doubling the modulus to ~1900 MPa), which was confirmed by analytical methods such as FTIR (confirmation of chemical crosslinking), SEM (observation of surface texture and particle dispersion), and TGA/DSC (measurement of glass transition temperature, Tg). Finally, the addition of 1 to 2.5% novolac resin improves the mechanical and thermal properties of UPE composites, making them suitable for various industrial applications.

Key Words: Thermal stability, thermal properties of unsaturated polyester, novolac, reinforced of polymers

1. Introduction

Composite materials are sophisticated engineering systems composed of two or more materials with different chemical and physical properties, mechanically bonded without fusion to produce a single material with enhanced functionality compared to the original materials used in its manufacture [1,2]. A composite material typically consists of two main components: a substrate, which is the bonding material that holds the other materials together and protects them from various external factors, and reinforce-

ment, which is embedded in the substrate in the form of fibers, molecules, or sheets to bear the main mechanical loads [3]. Recent research efforts focus on developing sustainable composite materials based on natural fibers and biodegradable materials, as well as improving manufacturing methods to make them more economical [4-6]. Polyesters, in general, are synthetic polymers with a multi-purpose basic structure and consist of ester groups in the main chains of macromolecules. Polyesters are characterized by high tensile strength, exceptional stiffness, and resistance to abrasion and creep under static loads [7,8]. These materials also exhibit moderate elasticity, with elongation at break ranging from 15% to 30%, depending on the polyester type and the heat treatment used [9-11]. Therefore, they are suitable for use in various fields, such as textiles [12,13], packaging [14] and engineering applications [15]. Regarding thermal properties, unsaturated polyesters exhibit different thermal characteristics due to the formation of cross-links during heat treatment (Figure 1) [16].

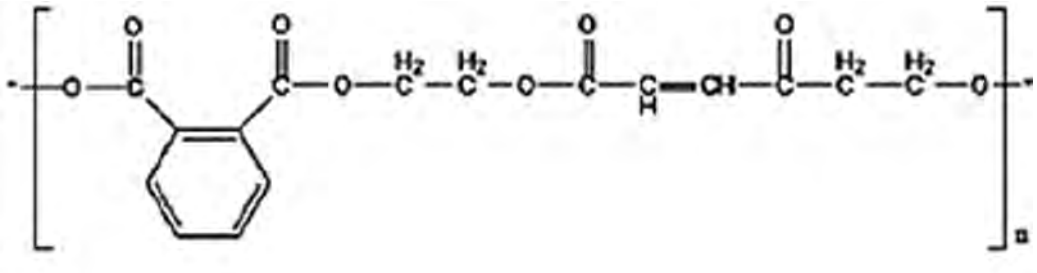

Figure 1. The Structure of Unsaturated Polyesters Resin [17]

Novolac resins are an important class of thermoplastic phenol-formaldehyde polymers, prepared via an acid-catalyzed condensation reaction between phenols and formaldehyde in a molar ratio of less than one [17]. The term "novolac" is derived from Latin and Swedish origins meaning "new varnish," reflecting its historical use as an alternative to natural varnishes such as cobalt resin [18]. These resins are characterized by a linear or partially branched structure, with methylene bridges ($-CH_2-$) forming between aromatic rings at ortho and para positions. The degree of branching depends on the reaction conditions and the ratio of monomers (Figure 2) [19].

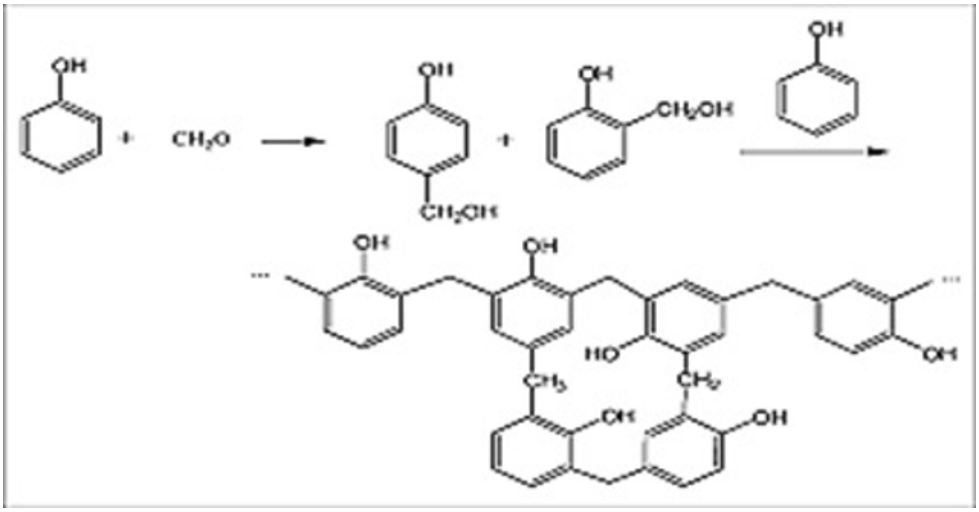

Figure 2. Structure of Novolac Resin [20]

Structurally, the polymer chain in novolac resins terminates upon complete formaldehyde consumption, resulting in a thermoplastic material incapable of self-crosslinking without the addition of an external crosslinking agent [21]. Novolac resins possess unique physical and chemical properties that make them suitable for precision engineering applications. These properties include an amorphous solid state at room temperature, a ductility range of 65–105°C, and solubility in polar organic solvents such as alcohols and acetone [21].

2. Experimental

Materials

Base material

The base material was unsaturated polyester resin from the Turkish company (AKPA KIMYA). It is a transparent, viscous liquid at room temperature and is a type of thermosetting polymer widely used in industrial applications.

The reinforcing materials

The reinforcement material is a formaldehyde resin (novolac). Phenol-formaldehyde polymer is prepared in an acidic medium with an excess of phenol, requiring a hardening agent such as hexamine to complete the polymerization and hardening process.

In a glass flask, the following quantities of reagents were added: 2 g of phenol, 2.5 mL of formaldehyde, 1 mL of hydrochloric acid,

and 5 mL of glacial acetic acid. The flask was covered to prevent the evaporation of volatile substances, and the solution was then heated gradually with continuous stirring for five minutes until the reaction was complete and a pink, solidified polymer was obtained (Figure 3).

Figure 3. The Prepared Novolac

The resulting precipitate was then washed several times with distilled water to remove impurities and unreacted reagents and allowed to dry completely at room temperature. After complete drying, the polymer was ground using a grinder and mortar and then sieved through a standard sieve with 75 µm openings to obtain a pure powder with uniform particle size [23], as shown in the Figure 4.

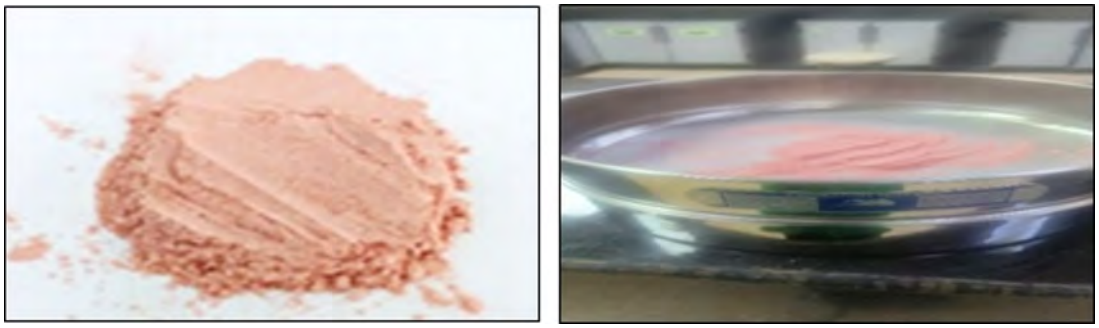

Figure 4. Ground and Sieved Novolac

Sample preparation

After preparing the Novolac, it was mixed with polyester in specific weight percentages (0.5%, 1.0%, 1.5%, 2.0%, 2.5%, 3.0%, 3.5%, 4.0%, 4.5%, 5.0%). Samples for mechanical property testing were then prepared by manual molding according to the requirements of each type of test [24], as shown in the Figure 5.

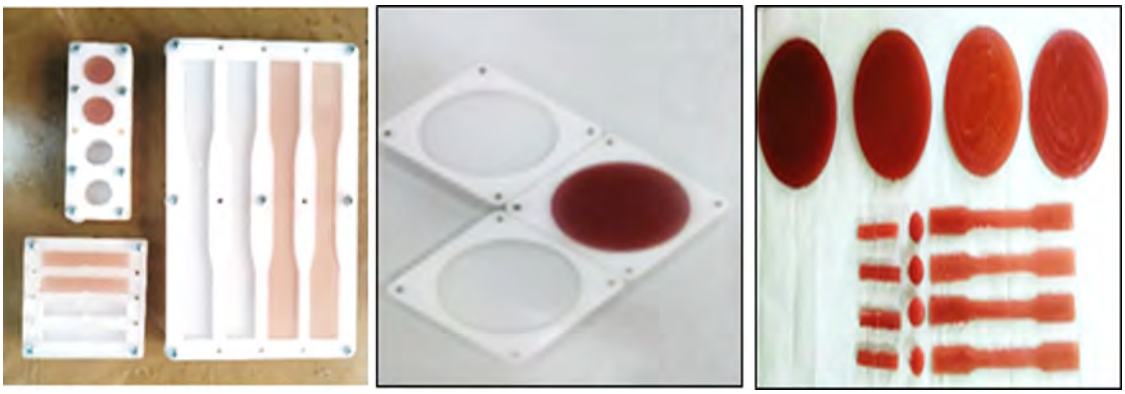

Figure 5. Casting Molds and Resulting Samples for Mechanical Properties Tests

3. Results and Discussion

The modulus of elasticity of unsaturated polyester resin (UPE) reinforced with varying proportions of novolac resin was measured. The results showed a significant increase in stiffness with the addition of novolac, peaking at 1% and 2.5% (approximately 830 MPa), respectively. However, slight fluctuations were then recorded, with a sharp decrease observed once the novolac content exceeded 3.5%. This indicates that the reinforcer ratio is optimal, and that excessive reinforcement may lead to phase separation or the formation of agglomerates, potentially weakening the polymer network [25].

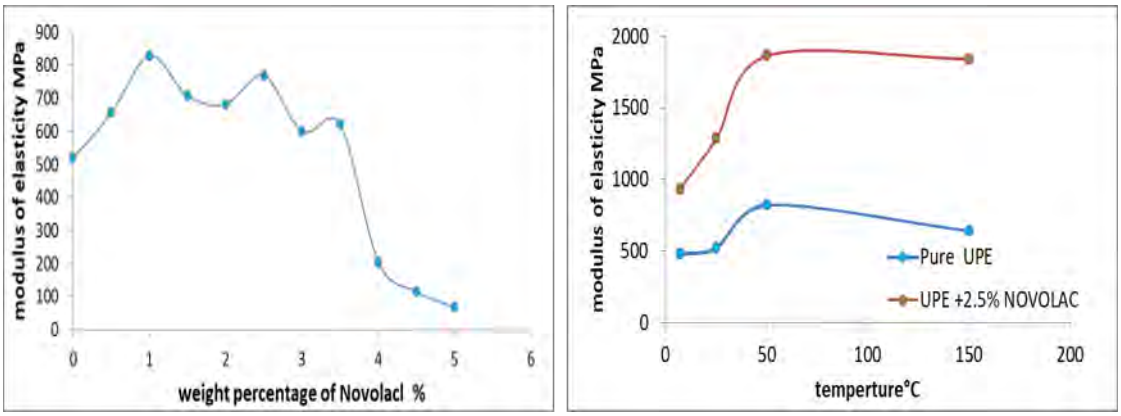

Figure 6. Modulus of Elasticity of Unsaturated Polyester Resin (UPE) (a) reinforced with varying percentages of novolac resin; **(b)** pure polyester and the polyester reinforced with 2.5% novolac under the influence of temperatures

The modulus of elasticity of pure polyester was also compared with polyester reinforced with 2.5% novolac under the influence of different temperatures (Figure 6), and it was found that the reinforced polyester had a significant advantage as the modulus of

elasticity doubled to about 1900 MPa at 50°C and remained stable at 150°C, while the unreinforced polyester showed less stability and lower values, confirming the role of novolac material in increasing crosslinking density and enhancing the thermal and mechanical stability of the composite material [26].

The compressive strength of unsaturated polyester resin (UPE) that had been reinforced with different percentages of novolac resin was determined. The samples recorded a considerable improvement, which reached their maximum of 1% (around 120 MPa) then gradually reduced with the percentage reaching 5%. This implies that the best reinforcement percentage will be 1% since further reinforcement may result in agglomeration or phase separation, which will make the structure weak.

In the comparison of the thermal behavior of pure polyester to the sample that was reinforced with 2.5 percent novolac, pure polyester demonstrated the reduction in strength with increasing temperature whereas the reinforced sample demonstrated a peak in strength at low temperature (25°C), then decreased its strength very fast, making it to be lower than the pure polyester at high temperatures (150°C), as shown in Figure 7 [20].

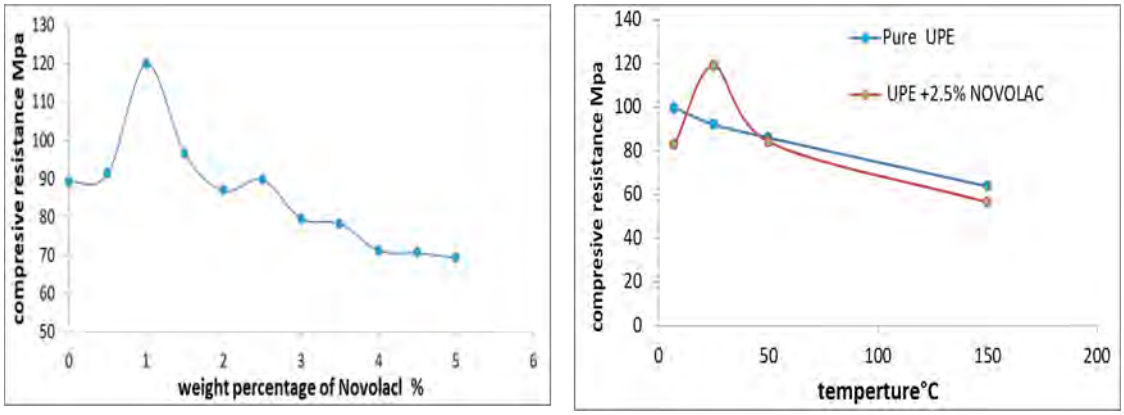

Figure 7. Compressive Strength of Unsaturated Polyester Resin (UPE) (a) reinforced with varying percentages of novolac resin; **(b)** pure polyester and the polyester reinforced with 2.5% novolac under the influence of temperatures

The Shore-D hardness properties of unsaturated polyester resin (UPE) reinforced with varying percentages of novolac resin were investigated. The hardness value gradually increased, reaching a maximum at 1% (approximately 86 Shore-D), indicating increased crosslinking at this percentage. The hardness then decreased with increasing novolac content, reaching its lowest value at 5%. This decrease is attributed to phase segregation or heterogeneity of the polymer mixture [27].

The hardness was also compared as a function of temperature for pure polyester and the sample reinforced with 2.5% novolac. The reinforced sample exhibited better hardness readings across the temperature range, demonstrating the effect of novolac on enhancing the material's thermal stability and resistance to rapid

softening. The hardness peaked at approximately 93 Shore-D at 50°C and continued to decrease with increasing temperature [28], reaching its lowest value below 150°C, as shown in Figure 8.

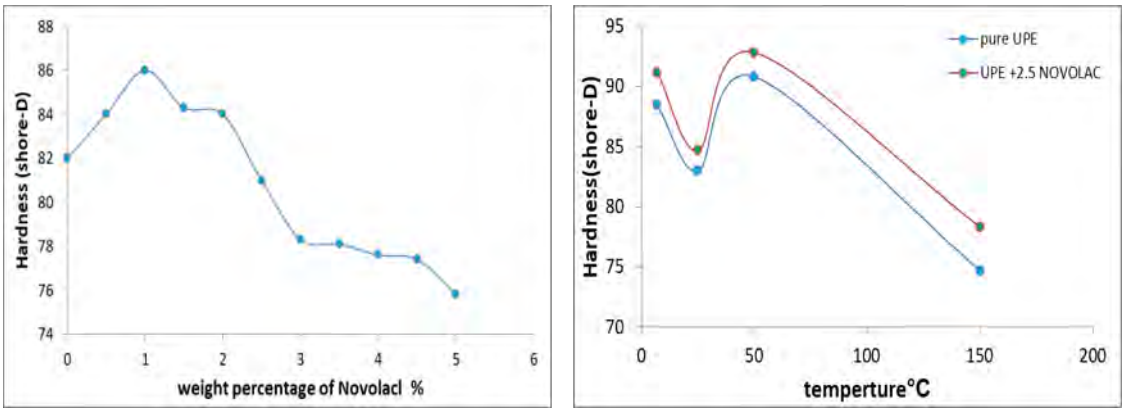

Figure 8. Shore-D Hardness of Unsaturated Polyester Resin (UPE) (a) reinforced with varying percentages of novolac resin; **(b)** pure polyester and the polyester reinforced with 2.5% novolac under the influence of temperatures

The impact resistance of pure unsaturated polyester (UPE) resin reinforced with varying percentages of novolac resin was studied. We observed an improvement in impact resistance, reaching a peak at 1% (approximately 1.7 kJ/m²), indicating that this percentage enhances the material's energy absorption capacity. However, increasing the novolac percentage beyond this point resulted in an overall decrease in resistance, with a sharp drop at higher percentages (4–5%). This is typically attributed to increased polymer network fragility or heterogeneity in the mixture.

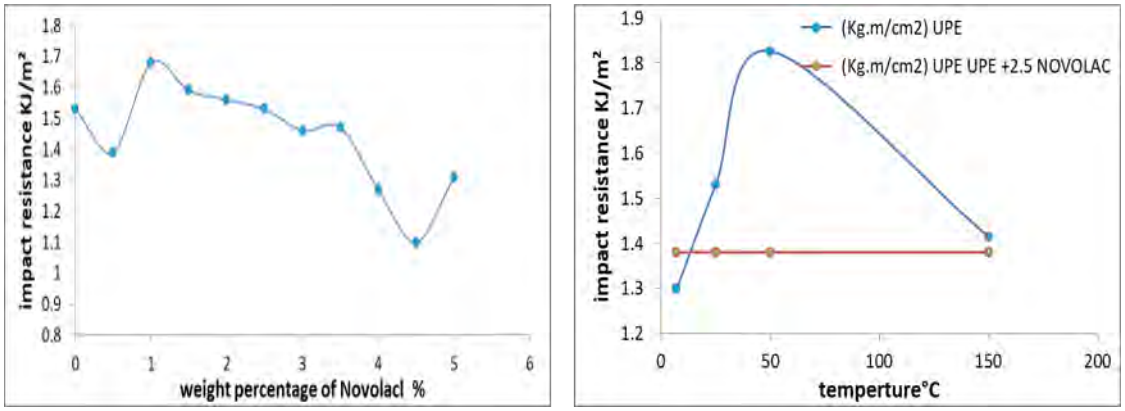

Figure 9. Shore-D Hardness of Unsaturated Polyester Resin (UPE) (a) reinforced with varying percentages of novolac resin; **(b)** pure polyester and the polyester reinforced with 2.5% novolac under the influence of temperatures

Regarding the thermal behavior of impact resistance between pure polyester and the sample reinforced with 2.5% novolac (Figure 9): pure polyester showed high sensitivity to temperature, rising sharply to a peak at 50°C before decreasing again, while the reinforced sample showed remarkable stability and consistency in shock resistance values across the thermal range (from 0 to 150°C) without being greatly affected by the rise in temperature, although its values were lower than the peak achieved by pure polyester at 50°C.

The chemical structures of the neat (unreinforced) unsaturated polyester and the sample containing 2.5% novolac were compared by Fourier Transform Infrared (FTIR) spectroscopy (Figure 10). Direct comparison shows that the incorporation of novolac leads to significant changes in the structure, as evidenced by the appearance of a number of new distinct peaks in the reinforced sample that are absent or very weak in the neat UPE spectrum.

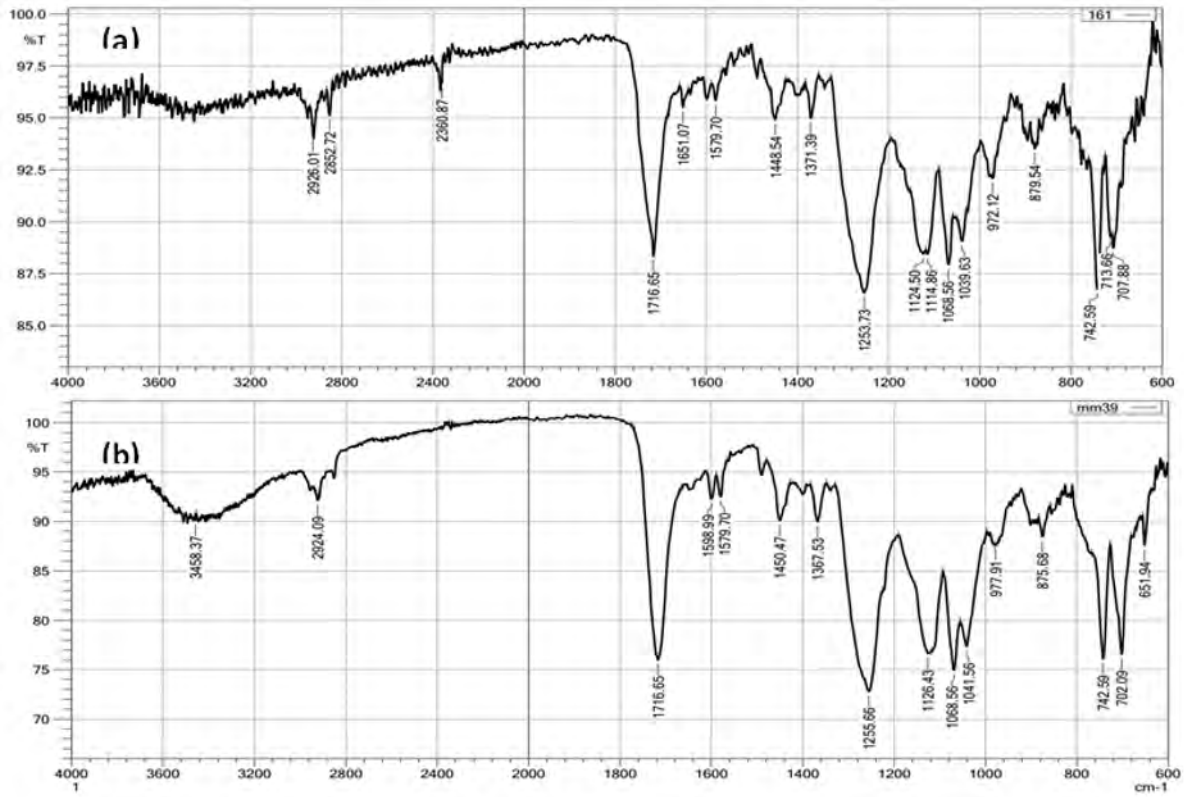

Figure 10. FTIR Spectrum of (a) Pure Unsaturated Polyester and (b) Unsaturated Polyester Containing 2.5% Novolac

Especially, new peaks at 1651.07 cm^{-1} and 1579.70 cm^{-1} are present in the aromatic region in the reinforced sample, which are attributed to C=C aromatic bond stretching. The formation of these new peaks confirms that highly aromatic novolac rings are successfully incorporated into the polyester matrix. Moreover, new absorption bands are observed in the lower wavenumber region at 1124–1039 cm^{-1} that are not present in the

neat resin. The appearance of these new peaks is ascribed to the formation of chemical crosslinking between the polyester and novolac networks.

Also, a strong peak at 3458.37 cm^{-1} due to O-H bond stretching of phenolic hydroxyl groups of the novolac is clearly observed in the reinforced sample but less intense in the pure polyester. Both the spectra show high peaks at 1716.65 cm^{-1} (C=O bond stretching) and 1255.66 cm^{-1} (C-O bond stretching). However, the reinforced sample shows noticeable variation in the intensity and shape of these peaks as compared to the neat sample which further indicates changes and increased density in the polymer network.

The thermogravimetric analysis (TGA) curve of a 1% novolac-reinforced sample during heat treatment at different temperatures shows that the sample starts with a slight weight loss at 72.9°C, which is due to the evaporation of moisture and residual solvents. This gradual weight loss continues up to 107.3°C, where the initial thermal decomposition of the short polymer chains and less stable components takes place. The weight loss of the curve starts to be significant at 232.3°C, which corresponds to the beginning of the main stage of the thermal decomposition of the unsaturated polyester network where hydrogen bonds and weaker crosslinks between the ester and the polymer chains are starting to break. The rate of weight loss is still high up to 339.5°C. Essentially, the major degradation of the organic polymer backbone is complete. The residual mass at 346.47°C is indicative of the char or inorganic matter content of the sample, which is negligible (~0.000 mg), suggesting the high purity and near complete thermal volatilization of the organic components in the reinforced polymer (Figure 11).

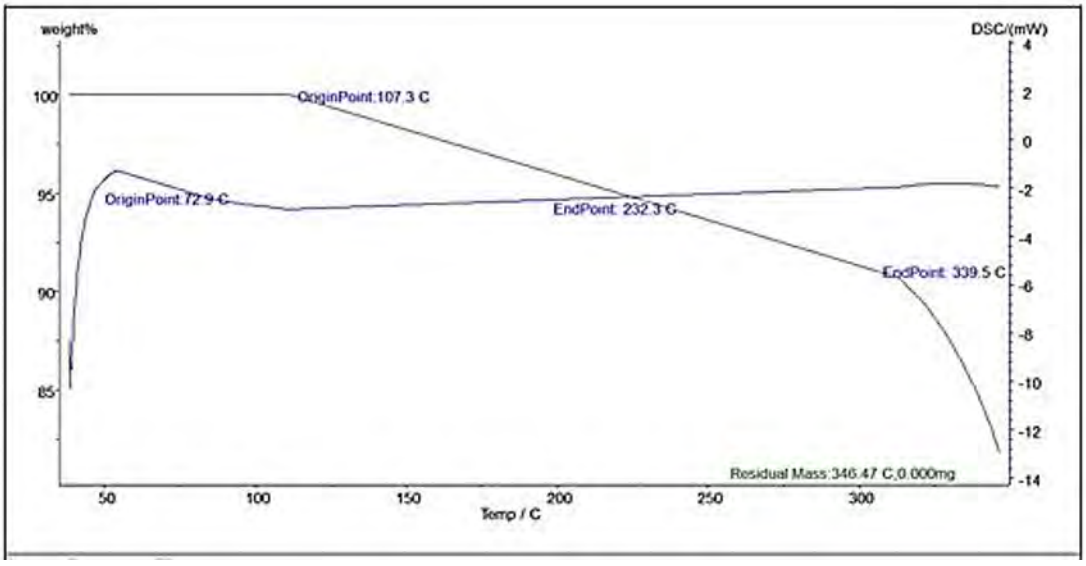

Figure 11. Thermogravimetric Analysis (TGA) and Differential Thermal Scanning Curve DSC

The variations of heat flux with temperature are shown in the Differential Scanning Calorimetry (DSC) curves. The direct comparison of the neat (unreinforced) unsatur-

ated polyester with the novolac-reinforced sample clearly shows a significant thermal enhancement. The (Tg) of the novolac-reinforced sample shifts significantly to 72.9°C with base line. This comparative increase in the glass transition temperature confirms the role of the novolac addition to increase the stiffness and crosslinking densities in the polymer network. The higher degree of cross linking restricts the movement of the polymer chains and therefore, more thermal energy is required to change from glassy state to rubbery state. One can observe a relative stability of the curve in the interval between 107.3°C and 232.3°C where the material is in a stable glassy state. The curve begins to decline slowly at approximately 232.3°C, indicating the beginning of the endothermic decomposition processes, decreasing to 339.5°C where the primary thermal degradation takes place [29] (Figure 11).

The morphology of the pure unsaturated polyester and the novolac-reinforced sample is clearly different, as seen in Figure 12, which were obtained by scanning electron microscopy (SEM).

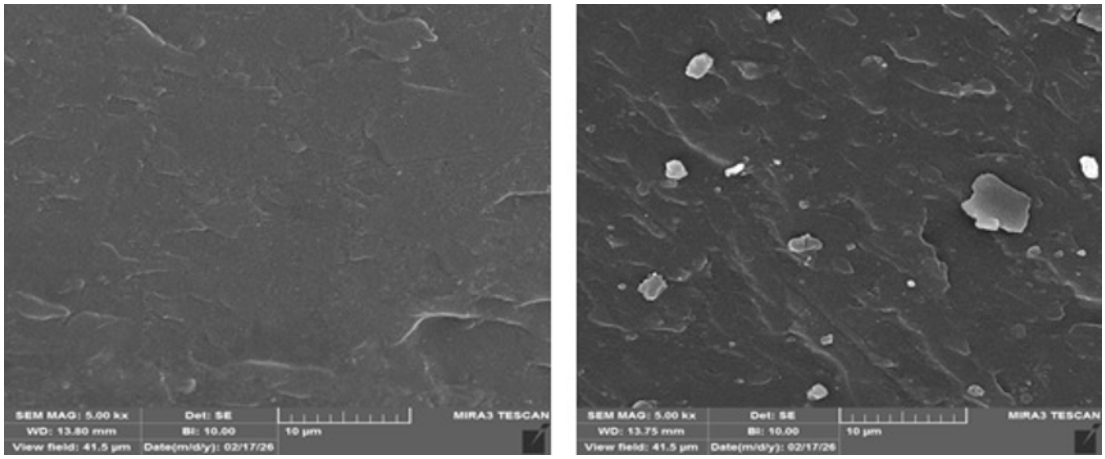

Figure 12. Scanning Electron Microscopy (SEM) of (a) Pure Unsaturated polyester and (b) Unsaturated Polyester Containing 2.5% Novolac

The surface of the pure material is relatively smooth and homogenous, which suggests a single-phase polymer structure without separate phases. The novolac-reinforced sample is, however, found to have a distinctively heterogeneous morphology. The novolac particles are seen as bright white phases, and their size and shape range from small spheres to irregular masses, all dispersed throughout the polyester matrix. The novolac particles are clearly visible in the image, and the matrix is the UPE. The novolac particles are clearly visible in the image, while the matrix is the UPE. In addition, the surface of the reinforced sample is more rugged than the pure sample. Although this phase-separated morphology and the resulting mechanical interlocking and stress transfer are advantageous at optimal concentrations (e.g., 2.5%), the inherent heterogeneity typically found in the SEM micrographs demonstrates that at higher concentration (e.g., >3.5%), these separated phases have a tendency to agglomerate, creating stress concentration points and compromising the strength of the polymer network [30].

4. Conclusion

The present work successfully proved that the novolac resin incorporation into the unsaturated polyester (UPE) significantly improved the mechanical and thermal properties, while the optimal performance is highly dependent on the novolac concentration. The most significant results demonstrate that the 1% novolac composition exhibits the best ambient mechanical performance with maximum values of approximately 830 MPa for modulus of elasticity, 120 MPa for compression strength, 86 Shore-D for hardness and 1.7 kJ/m2 for impact resistance. The optimum value was determined to be 2.5% novolac ratio for higher thermal stability requirements. At this level, the composite modulus of elasticity was doubled to around 1900 MPa at 50°C and showed a very high stability up to 150°C. The composite also exhibited an exceptional high temperature hardness with a maximum of 93 Shore-D at 50°C. The higher glass transition temperature (Tg) is attributed to the enhanced crosslinking density and the formation of new chemical bonds between the phenolic hydroxyl groups of novolac and the ester groups of the polyester, which is responsible for the superior performances confirmed by analytical techniques like FTIR, TGA, DSC and SEM. The material had a melting point of 72.9°C and showed a delayed thermal decomposition. However, it was conclusively found that the novolac content beyond 3.5% leads to phase separation and particle agglomeration which disrupts the stress transfer and degrades the mechanical properties. In summary, these novolac-reinforced UPE composites, especially at the optimal ratios of 1% to 2.5%, are highly suitable for demanding industrial applications that require high mechanical strength and thermal stability, such as mold making, automotive parts, and electrical insulators.

5. References

1. Bhong M, Khan TK, Devade K, Krishna BV, Sura S, Eftikhaar HK, Thethi HP, Gupta N. Review of composite materials and applications. *Mater. Today: Proc.*, 2023.
2. Sai MKS. Review of composite materials and applications. *Int. J. Latest Trends Eng. Technol.*, 2016, 6(3), 129-135.
3. Chauhan AK, Singh A, Kumar D, Mishra K. Properties of composite materials. In: Composite Materials, CRC Press, 2021, pp 61-78.
4. Egbo MK. A fundamental review on composite materials and some of their applications in biomedical engineering. *J. King Saud Univ., Eng. Sci.*, 2021, 33(8), 557-568.
5. Narayana KJ, Burela RG. A review of recent research on multifunctional composite materials and structures with their applications. *Mater. Today: Proc.*, 2018, 5(2), 5580-5590.
6. Sharma AK, Bhandari R, Sharma C, Dhakad SK, Pinca-Bretotean C. Polymer matrix composites: A state of art review. *Mater. Today: Proc.*, 2022, 57, 2330-2333.
7. Darie-Niță RN, Râpă M, Frąckowiak S. Special features of polyester-based materials for medical applications. *Polymers*, 2022, 14(5), 951.
8. Masuelli MA. Introduction of fibre-reinforced polymers—polymers and

composites: concepts, properties and processes. In: Fiber Reinforced Polymers: The Technology Applied for Concrete Repair, IntechOpen, 2013.
9. Isa MT, Ahmed AS, Aderemi BO, Taib RM, Mohammed-Dabo IA. Effect of fiber type and combinations on the mechanical, physical and thermal stability properties of polyester hybrid composites. *Composites, Part B*, 2013, 52, 217-223.
10. Ezeh EM. Advances in the development of polyester resin composites: A review. *World J. Eng.*, 2026, 23(1), 97-117.
11. Kumar S, Prasad L, Patel VK, Kumar V, Kumar A, Yadav A, Winczek, J. Physical and mechanical properties of natural leaf fiber-reinforced epoxy polyester composites. *Polymers*, 2021, 13(9), 1369.
12. Hansen S, Atwood KB. Polyester fibers. In: Kirk-Othmer Encyclopedia of Chemical Technology, Wiley, 2005. https://doi.org/10.1002/0471238961.1615122508011419.a01.pub2
13. Wang S, Salmon S. Progress toward circularity of polyester and cotton textiles. *Sustainable Chem.*, 2022, 3(3), 376-403.
14. Massa DJ. Polyester materials and properties. *Polyester Films*, 2023, 19-46.
15. Mangaraj S, Yadav A, Bal LM, Dash SK, Mahanti NK. Application of biodegradable polymers in food packaging industry: A comprehensive review. *J. Packag. Technol. Res.*, 2019, 3(1), 77-96.
16. Ezeh EM. Advances in the development of polyester resin composites: A review. *World J. Eng.*, 2026, 23(1), 97-117.
17. Islam MN, Ar-Rashid H, Islam F, Karmaker N, Koly FA, Mahmud J, Keya KN, Khan RA. Fabrication and characterization of E-glass fiber reinforced unsaturated polyester resin based composite materials. *Nano Hybrids Compos.*, 2019, 24, 1-7.
18. Șucu T, Shaver MP. Inherently degradable cross-linked polyesters and polycarbonates: resins to be cheerful. *Polym. Chem.*, 2020, 11(40), 6397-6412.
19. Laoubi K, Hamadi Z, Benyahia AA, Serier A, Azari Z. Thermal behavior of E-glass fiber-reinforced unsaturated polyester composites. *Composites, Part B*, 2014, 56, 520-526.
20. Kodrić M, Đorđević D, Tarbuk A, Islam S, Čorak I, Đorđević S, Motaleb KA. Chemical modification of polyester knitted fabric with ultrasound to improve hydrophilicity and wettability. *Fibers Polym.*, 2025, 26(7), 2937-2945.
21. Ketema A, Worku A. Review on intermolecular forces between dyes used for polyester dyeing and polyester fiber. *J. Chem.*, 2020, 2020(1), 6628404.
22. Saeed JKM, Sulyman EZ, Al-Ahmady KK. Improving mechanical and thermal properties of unsaturated polyurea by adding copper(ιι)oxide nanoparticles. *Ochrona przed Korozją*, 2025, (68)7, 206-214.
23. Sulyman EZ, Abed AG, Younis AQ. Gravimetric and differential thermal analysis and activation energy studies of unsaturated polyester using date seeds powder and walnut shells. *Int. J. Res. Pharm. Sci.*, 2019, 10(4), 3811-3821.
24. Sulyman EZ, Sulyman NZ. Preparation of polymeric composites from polypropylene and palm fronds and the study of some of their physical properties. *Baghdad Sci. J.*, 2020, 17(3), 0772-0772.
25. Doyle L, Weidlich I. Moisture uptake

and effects of hygrothermal exposure on closed-cell semicrystalline polyethylene terephthalate foam. *Polym. Degrad. Stab.*, 2022, 202, 110009.
26. Sulyman EZ, Hamid AS, Thaer AH. Preparation of polymeric aggregate of unsaturated poly ester with sawdust and studying its physical and mechanical properties. *Int. J. Res. Pharm. Sci.*, 2019, 10(3), 2280-2289
27. Kumar A, Patil PB, Pinjari DV. Eco-friendly adhesives for wood panels: Advances in lignin, tannin, protein, and rubber-based solutions. *J. Adhes. Sci. Technol.*, 2025, 39(17), 2628-2669.
28. Doyle L, Weidlich I. Moisture uptake and effects of hygrothermal exposure on closed-cell semicrystalline polyethylene terephthalate foam. *Polym. Degrad. Stab.*, 2022, 202, 110009.
29. Tian Q, Krakovský I, Yan G, Bai L, Liu J, Sun G, Rosta L, Chen B, Almásy L. Microstructure changes in polyester polyurethane upon thermal and humid aging. *Polymers*, 2016, 8(5), 197.
30. Hemadi EK, Al-Ahmady KK, Sulyman EZ. Improving mechanical and thermal properties of unsaturated polyester resin by adding automotive glass waste. *Ochrona przed Korozją*, 2024, (10), 294-305.

The Chemist
Journal of the American Institute of Chemists

Study of the Mechanical and Thermal Properties of Unsaturated Polyester Reinforced with Different Proportions of Aluminum Foil Waste

Noor Sadeeq Yahya, Ebtehag Zaki Sulyman

Department of Chemistry, College of Education for Women, University of Mosul, Mosul, Iraq (E-mail: noor.24gep50@student.uomosul.edu.iq; ebthalim@uomosul.edu.iq)

Abstract: The aim of the study is to examine the impact of the aluminum foil flakes waste as the filler to strengthen the composite in terms of mechanical and thermal characteristics of unsaturated polyester resin (UPR) composite. The material that was used as the matrix material was unsaturated polyester resin (Camehvar Resins, CE-80, Turkey) with the density of about 1.2 g/cm^3, cured by using methyl ethyl ketone peroxide (MEKP) at a ratio of 0.6 g/100 g resin. Foams made of aluminum were added in different concentrations (04.5 wt.%), to research its effect on compressive strength, impact resistance, Shore-D hardness, modulus of elasticity and thermal conductivity at temperatures of 7°C to 150°C. It was shown that the addition of aluminum flake waste greatly increased the composite properties, and optimal reinforcement percentage was found to be 2.5%. Since compressive strength, impact resistance and Shore-D hardness, modulus of elasticity, and hardness were measured at this concentration, the compressive strength was up to 126.4 MPa, impact resistance was up to 1.69 kJ/m^2, Shore-D hardness was up to 93.5 and the modulus of elasticity was up to 1669 MPa. There was also significant improvement in thermal conductivity to 3.7×10^{-4} W/m at 150°C in the reinforced composite than 2.95×10^{-4} W/m in pure UPR. On top of the 2.5% optimum, the property degradation was evident as a result of particle agglomeration and bad interfacial bonding. The use of such methods as FTIR, SEM, EDX, TGA and DSC allowed us to determine that reinforcement was done by physical interactions but did not change the chemical structure of the polymer, and the use of particles of aluminum enhanced thermal stability and served as impediments to the movement of polymer chains.

Key Words: Unsaturated polyester resin, composite materials , reinforcement materials of polymers, mechanical properties of Unsaturated polyester resin , thermal conductivity of polymers

1. Introduction

The composite materials, based on unsaturated polyester resin (UPR), have been widely used because of the good combination of mechanical performance, ease of processing and cost-effectiveness. The UPR has a satisfactory mechanical strength and a good chemical resistance, making it an ideal matrix for reinforced composite systems [1,2]. It has been demonstrated that mechanical properties like tensile strength, compressive resistance and hardness can be significantly improved when metallic fillers, particularly aluminum particles or flakes, are added to polymeric matrices. Aluminum fillers are very rigid and thermally stable, which allows better transfer of load between the reinforcement and the matrix [3,4]. Aluminum reinforcement effectiveness is strongly influenced by particle size, shape and quality of dispersion in the polymer matrix [5,6]. Aluminum particles restrict the movement of polymer chains, thus increasing the stiffness of the polymer chains. This improved the material's ability to withstand deformation stress. Furthermore, the enhanced interfacial bonding between the aluminum fillers and polyester matrix prevents crack propagation, thereby increasing the fracture resistance [7-9]. However, excessive use of filler contents can lead to agglomeration of particles which can create stress concentration zones that affect negatively the mechanical performance of the composite [10-12].

To evaluate such mechanical improvements in a comprehensive manner, it is necessary to define clearly certain parameters. Hardness, usually defined as the resistance of a material to localized plastic deformation (especially indentation or scratching of the surface), is an important measure of the durability of a composite surface. Shore hardness is highly relevant for polymeric composites where a durometer measures the depth of an indentation under a given load, thus providing a quick, non-destructive and standardized measurement of surface stiffness that is particularly sensitive to the addition of stiff metallic fillers such as aluminum . Moreover, the Young's modulus is employed to measure the composite overall stiffness, and it is also defined as the specific modulus, defined as the ratio of tensile stress to tensile strain in the linear elastic deformation region. The direct incorporation of aluminum flakes influences the Young's modulus by limiting the mobility of the polymer chains and consequently, enhancing the resistance of the material to elastic deformation under applied forces.

In addition to the mechanical improvements, the thermal behavior of UPR composites is also highly affected by the aluminum reinforcement . In the composite structure, aluminum particles act as heat-dissipating elements, which slows down the thermal degradation and improves the overall thermal stability. The temperature window relevant for the aluminum powder spans from the processing and curing temperatures (approx. 25°C to 120°C) to the thermal degradation testing thresholds (up to 600°C or 800°C). The entire range is thermally stable with the aluminum powder without phase change because of its melting point of about 660°C. In contrast, the thermal degradation of unsaturated polyester matrix is generally observed in the temperature range 200°C to 450°C. Previous thermogravimetric analysis (TGA) results indicated that the aluminum-filled polyester composites exhibited higher decomposition onset temperatures than the neat polyester resin [13-16]. The optimal filler concen-

tration that provides the mechanical improvements without losing the structural homogeneity is a key factor to determine the overall performance of these composites [17–19]. It has been indicated that the moderate aluminum loading yields the best mechanical and thermal properties, while the excessive loading may result in the loss of the composite integrity due to the poor dispersion of the fillers [20-23].

The present work investigates the effect of waste aluminum foil flake powder on mechanical and thermal properties of unsaturated polyester composites. To assess these properties, several composite samples were prepared with different concentrations of the aluminum waste powder, and a series of mechanical and thermal tests were carried out. The main objective of this study is to find the optimum filler loading that improves the performance as well as support sustainable recycling of aluminum waste. The results of this study will contribute to the development of high performance, cost effective and environment friendly composite materials.

2. Matrix Material

The Base Material and Hardener

Unsaturated polyester resin (UPR) was chosen as the base material in this study due to its suitable viscosity, high compatibility with reinforcing fillers, and ability to harden at room temperature without requiring high temperatures. Thanks to these properties, unsaturated polyester resin can be used in the production of polymer-based composite materials.

The unsaturated polyester resin used in this study was low viscosity, with an approx.-imate density of 1.2 g/cm³. This resin was manufactured by Kamivar Resins (CE-80, Turkey). Methyl ethyl ketone peroxide (MEKP), a transparent hardener, was used as a liquid resin hardener at a rate of 0.6 g/100 g of resin. The hardening process began after approximately thirty minutes at room temperature, where the resin gradually transformed into a gel-like substance. It was then poured into molds to fully harden.

Reinforcement Material

Aluminum foil waste was ground using an industrial mill. It was then sieved using a 200-mesh sieve with a size of 75 microns to obtain a perfectly pure and fine powder, as shown in Figure 1.

Figure 1. Powder of Aluminum Foil Flask Waste

Preparation Method

Several molds were designed and manufactured with dimensions and shapes suitable for the requirements of the equipment used to study mechanical properties such as tension, impact, compression, etc. The mold walls were coated with petroleum jelly to allow for the removal of samples from the molds after hardening without damage. The molds were fixed horizontally on a glass base covered with greaseproof paper to prevent the samples from sticking to the base and to obtain dimensionally symmetrical samples.

A quantity of unsaturated polyester was weighed for all the molds, and a hardener was added at a rate of 2%. The mixture was stirred slowly for 2-3 minutes, then the polymer was poured into the molds and left to harden for 24 hours at room temperature. The process was repeated for each percentage of aluminum powder added. To study the effect of heat treatment on the prepared samples, the samples were subjected to different temperatures (150, 50, 25, and 7°C) for 24 hours (Figure 2).

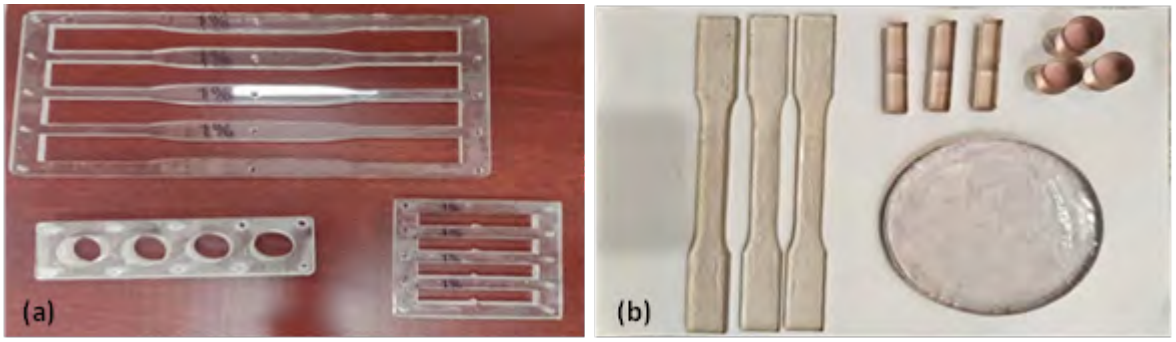

Figure 2. (a) The Casting Molds; (b) The Samples After Removal from the Molds

3. Results and Discussion

The graph shows how the content of aluminum foil flake waste powder on the compressive strength of unsaturated polyester is influenced (Table 1 and Figure 3). The compressive strength attains great heights of about 92 MPa, then reaches a peak of about 127 MPa at 2.5% aluminum power.

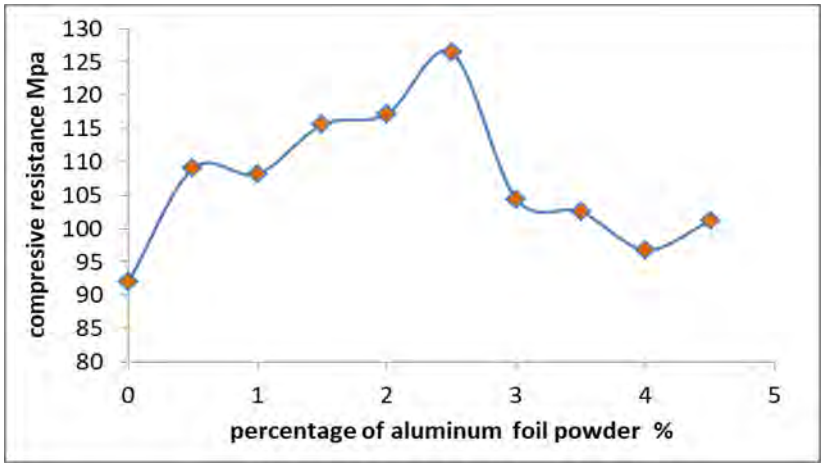

Figure 3. Compressive Strength of Unsaturated Polyester (UPR) Before Reinforcement (pure sample) and After Reinforcement by Aluminum Foil Flakes Waste, at 25°C

The strength then decreases gradually with an increase in the powder content. This is explained by the fact that incorporation of fine particles of aluminum increases the capability of the material to resist stresses caused by even distribution of the metal particles in polymer and also, due to the development of effective chemical and physical bonds. But after the optimum percent (2.5), the particles are agglutinated and agglomerated, breaking the internal composition of the composite material and hence, compromising its compressive strength [24].

Table 1. Compressive Strength of Unsaturated Polyester (UPR) Before (pure sample) and After Reinforcement by Aluminum Foil Flakes Waste, at 25°C

Percentage of reinforcement materials (%)	Compressive resistance (MPa) (UPE + Aluminum foil flakes waste)
0	92
0.5	109
1	108.2
1.5	115.6
2	117.2
2.5	126.4
3	104.4
3.5	102.5
4	96.8
4.5	101.2

The graph is a comparison between the compressive strength of pure unsaturated polyester (UPE) and the composite material that is reinforced with 2.5% aluminum foil flakes waste in a vast temperature span (Table 2 and Figure 4). The curves clearly show that the mechanical properties of both materials are negatively affected by increasing temperature, with compressive strength gradually decreasing as the temperature rises.

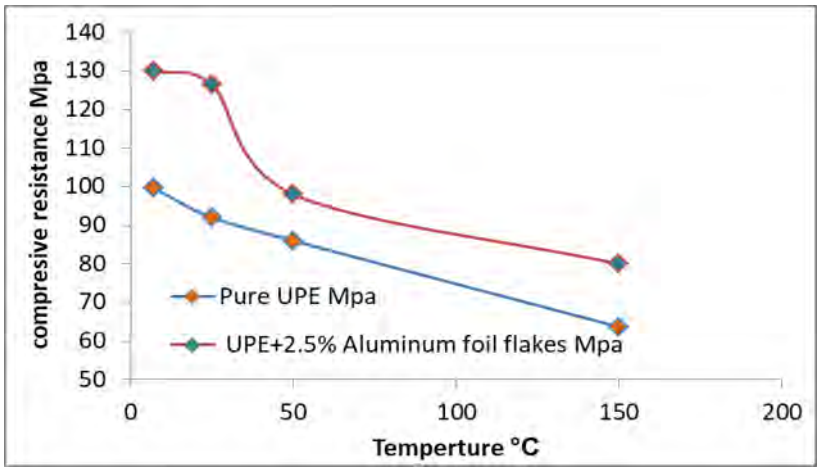

Figure 4. Compressive Strength of Unsaturated Polyester Before and After Reinforcement at Different Temperatures

However, the composite sample exhibits significantly higher performance and efficiency than the pure sample at all measured temperatures. The composite also

displays a high compressive strength of approximately 130 MPa at lower temperatures, compared to 100 MPa for the pure sample. At temperatures up to 150°C, the reinforced sample exhibits a higher value (approximately 80 MPa) than the pure sample, whose strength drops to approx.-imately 64 MPa. This superior mechanical performance of the composite material at high temperatures is attributed to the effectiveness of the aluminum foil as a more thermally stable reinforcing material than the polymer matrix. This foil withstands some of the pressures that have been introduced and prevents the movement of polymer chains in the form of a chain of material due to thermal energy, thus slowing down the softening process of the material, increasing the structural integrity of the material up to high thermal and mechanical loading [25].

Table 2. Compressive Strength of Unsaturated Polyester Before and After Reinforcement at Different Temperatures

Temperature (°C)	Compressive strength (MPa)	
	Pure UPE	UPE+2.5% Aluminum foil flakes waste
7	99.7	130
25	92	126.4
50	86	98
150	63.7	80

The graph illustrates the relationship between the percentage of aluminum foil powder added to unsaturated polyester and the impact resistance of the devices, measured in kJ/m² (Table 3 and Figure 5). The impact resistance value starts at approx.-imately 1.5 kJ/m² for the pure material (without the addition), then gradually increases with increasing powder content, reaching a peak of approximately 1.69 kJ/m² at a 2.5% aluminum powder concentration.

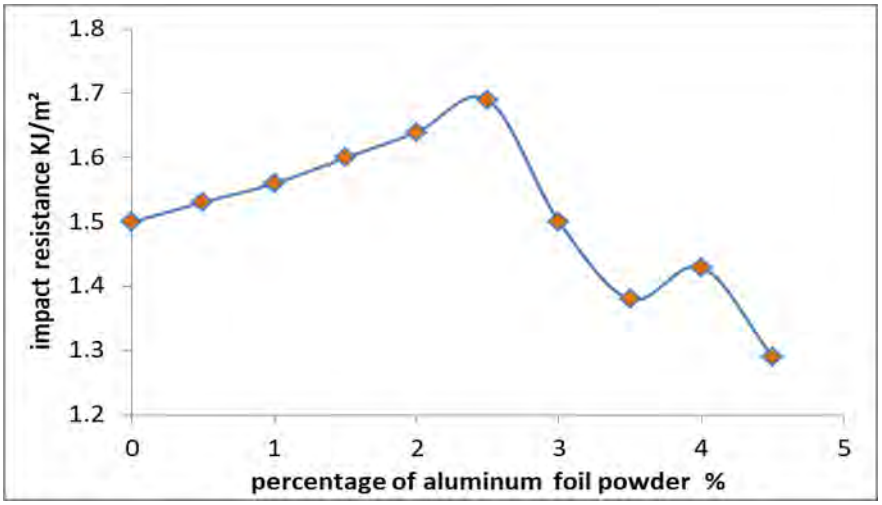

Figure 5. Impact Resistance of Unsaturated Polyester (UPR) Before (pure sample) and After Reinforcement by Different Weights of Aluminum Foil Flakes Waste, at 25°C

Beyond this optimum percentage, the value drops significantly to approximately 1.29 kJ/m² at a 4.5% concentration. This rise in the impact resistance up to 2.5% is due to the fact that the fine aluminum particles are capable of absorbing impact energy and spreading the stress uniformly throughout the polymer structure. This avoids the formation of cracks and increases the life of the composite material. These particles also serve as mechanical barriers and prevent crack growth and enhance the energy storage capacity and resistance to damage of the material. The downward arrow at the higher percentage is because of the greater concentration that results in the concentration of particles, formation of clusters that are crack initiation centers, loss of impact resistance, and reduction in overall structural performance of the material [26].

Table 3. Impact Resistance of Unsaturated Polyester (UPR) Before (pure sample) and After Reinforcement by Aluminum Foil Flakes Waste, at 25°C

Percentage of reinforcement materials (%)	Impact resistance (kJ/m²) (UPE + Aluminum foil flakes waste)
0	1.5
0.5	1.531
1	1.56
1.5	1.6
2	1.64
2.5	1.69
3	1.5
3.5	1.38
4	1.43
4.5	1.29

The comparative graph illustrates the impact resistance behavior of pure unsaturated polyester (Pure UPE) and a composite material reinforced with 2.5% aluminum foil flakes waste over a wide temperature range, from room temperature to 150°C (Table 4 and Figure 6).

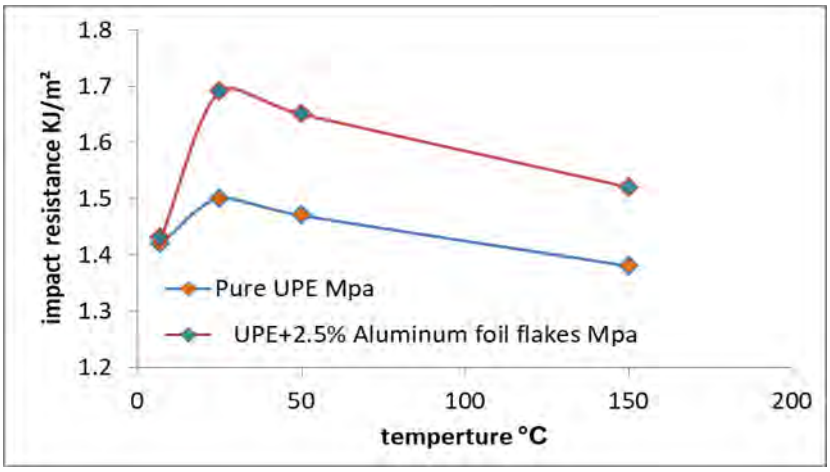

Figure 6. Impact Resistance of Unsaturated Polyester Before and After Reinforcement at Different Temperatures

The curves show that both materials also have an initial rise in impact resistance at lower temperatures and the composite material has its peak operational efficiency at about 1.7 kJ /m 2, while the pure material reaches approximately 1.5 kJ/m². However, the composite material consistently outperforms the pure material at all temperature points. When impact resistance reaches its peak, the impact resistance of both materials begins to gradually decrease with increasing temperature. The impact resistance of the composite material drops to approximately 1.52 kJ/m², while that of the pure material drops to approximately 1.38 kJ/m² at 150°C. This is because the high mechanical properties of the composite material result from the placement of the aluminum foil flakes waste, which enhances the material's ability to absorb and dissipate impact energy and prevents the propagation of micro-cracks in the polymer matrix. Furthermore, the heat softens the polymer matrix after reaching peak resistance, reducing the efficiency of the bonds and consequently decreasing the material's durability and ability to withstand impact loads [27].

Table 4. Impact Resistance of Unsaturated Polyester Before and After Reinforcement at Different Temperatures

Temperature (°C)	Impact resistance (kJ/m²)	
	Pure UPE	UPE+2.5% Aluminum foil flakes waste
7	1.42	1.43
25	1.5	1.69
50	1.47	1.65
150	1.38	1.52

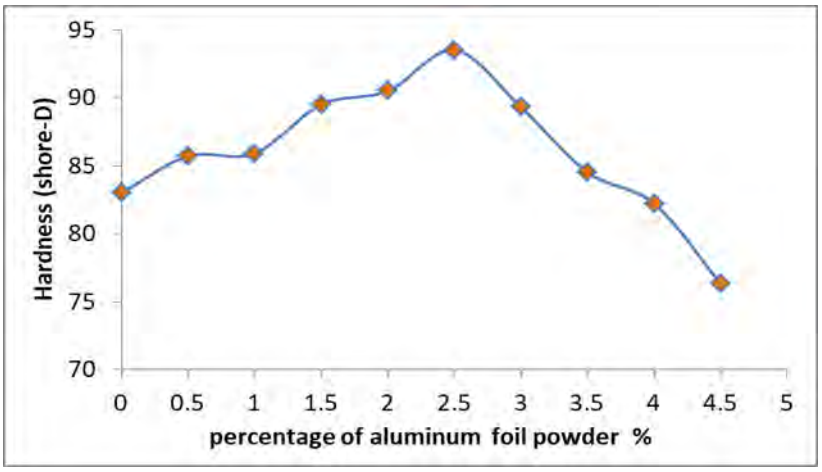

Figure 7. Hardness (Shore-D) of Unsaturated Polyester (UPR) Before Reinforcement (pure sample) and After Reinforcement by Aluminum Foil Flakes Waste, at 25°C

The graph illustrates the relationship between the percentage of aluminum foil flakes waste powder added to the unsaturated polymer and the Shore-D hardness value (Table 5 and Figure 7). The hardness value of the pure material (without the additive) starts at approximately 83, then gradually and steadily increases with increasing powder content, reaching a peak of around 93.5 at a 2.5% addition rate. Another important observation is that beyond this optimum percentage, there is a sharp and sudden drop in the hardness value to approximately 76 at a 4.5% addition rate. This is attributed to a 2.5% improvement in hardness due to the stiffness of the aluminum particles relative to the polymer matrix. The particles restrict the movement of the polymer chains, thus improving the surface's resistance to scratching and deformation. The sharp drop beyond the optimum percentage can be attributed to the effect of particle aggregation, where the material becomes homogeneous and the interfacial bond between the filler and the matrix weakens, creating weak areas and resulting in reduced hardness [28]

Table 5. Hardness (Shore-D) of Unsaturated Polyester (UPR) Before (pure sample) and After Reinforcement by Aluminum Foil Flakes Waste, at 25°C

Percentage of reinforcement (% materials)	Hardness (Shore-D) UPE+ Aluminum foil flakes waste
0	83
0.5	85.7
1	85.9
1.5	89.5
2	90.5
2.5	93.5
3	89.3
3.5	84.5
4	82.2
4.5	76.3

The behavior of two materials (pure unsaturated polyester (UPE) and a com-posite material containing 2.5% alum-inum foil flakes waste, in terms of material stiffness (measured in Shore-D), over a temperature range from room temperature to 150°C (Table 6 and Figure 8), is plotted in a comparative graph.

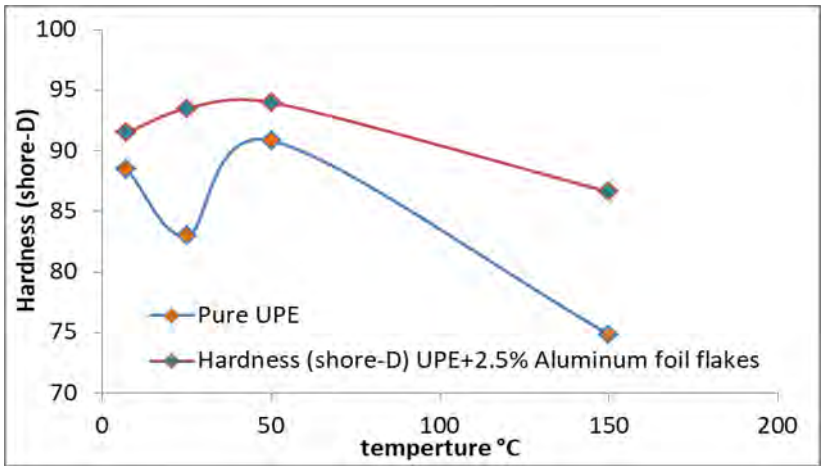

Figure 8. Hardness (Shore-D) of Unsaturated Polyester Before and After Reinforcement at Different Temperatures

The curves clearly show that the composite material significantly outperforms the pure material in maintaining its stiffness when exposed to heat. Although the pure sample exhibits changes in values at low temperatures (a decrease followed by an increase up to 50°C), a sharp and sudden drop in stiffness is observed after exceeding 50°C, reaching a minimum value of approximately 75 Shore-D at 150°C. The composite sample, on the other hand, is remarkably stable, reaching a maximum value of approximately 94 Shore-D at 50°C, followed by a gradual and moderate decrease to stabilize at approximately 86–87 Shore-D at 150°C. This is because the presence of solid aluminum foil flakes waste acts as a physical barrier, limiting the movement of the polymer chains. In this case, the thermal energy that would normally increase the movement of the polymer chains is limited, thus slowing down the thermal softening process. In contrast, high temperatures in the pure material temporarily separate the polymer chains and promote their movement, causing the polymer to rapidly lose its hardness and scratch resistance at temperatures above 150°C [29].

Table 6. Hardness (Shore-D) of Unsaturated Polyester (UPR) Before (pure sample) and After Reinforcement by Aluminum Foil Flakes Waste, at 25°C

Temperature (°C)	Hardness (Shore-D)	
	Pure UPE	UPE+2.5% Aluminum foil flakes waste
7	88.5	91.5
25	83	93.5
50	90.83	94
150	74.83	86.6

This graph illustrates the relationship between the added reinforcement percentage and the modulus of elasticity, measured in megapascals (MPa) (Table 7 and Figure 9).

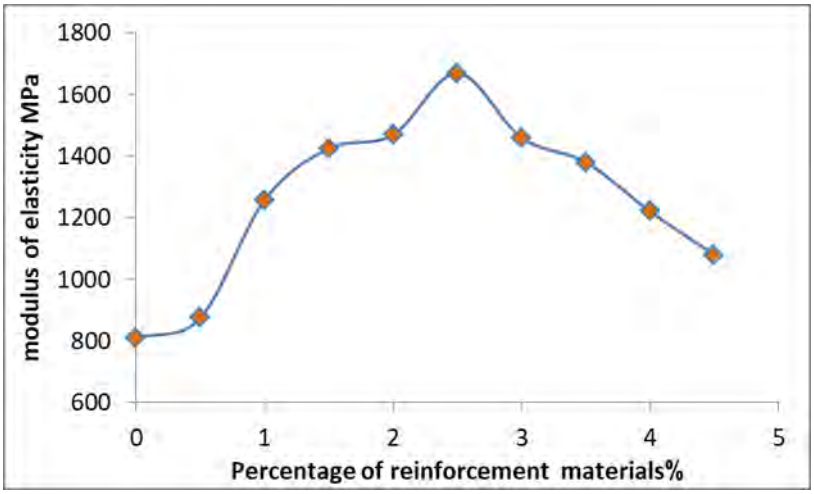

Figure 9. Modulus of Elasticity of Unsaturated Polyester (UPR) Before (pure sample) and After Reinforcement by Aluminum Foil Flakes Waste, at 25°C

The modulus of elasticity starts at approximately 800 MPa for the pure material (without reinforcement), then gradually increases, and then significantly, with increasing reinforcement percentage, reaching a maximum value of approximately 1700 MPa at a reinforcement percentage of about 2.5%. The modulus of elasticity then gradually decreases after this optimum percentage, reaching approximately 1100 MPa at a reinforcement percentage of 4.5%. The significant increase in the modulus of elasticity up to 2.5% is attributed to the high stiffness of the reinforcement material (aluminum foil flakes waste) compared to the polymer matrix, which enhances the material's resistance to elastic deformation under stress. These solid particles contribute to increasing the rigidity of the composite material, as it can withstand a large proportion of the load placed upon it, and reduce the maximum deformation of the

polymer matrix. This decrease from the optimal ratio is attributed to the increased concentration, which leads to the clumping of particles and the lack of good homogeneous distribution, resulting in weak areas in the internal structure, in addition to a decrease in the efficiency of stress transfer between the filler and the matrix, and thus the overall modulus of elasticity [30].

Table 7. Modulus of Elasticity of Unsaturated Polyester (UPR) Before (pure sample) and After Reinforcement by Aluminum Foil Flakes Waste, at 25°C

Percentage of reinforcement (% materials)	Modulus of elasticity (MPa) UPE + Aluminum foil flakes waste
0	810
0.5	875
1	1258
1.5	1425
2	1469
2.5	1669
3	1459
3.5	1380
4	1220
4.5	1080

The following comparative graph illustrates the modulus of elasticity (stiffness) behavior of pure unsaturated polyester (Pure UPE) and a composite material reinforced with 2.5% aluminum foil flakes waste at temperatures ranging from room temperature to 150°C (Table 8 and Figure 10).

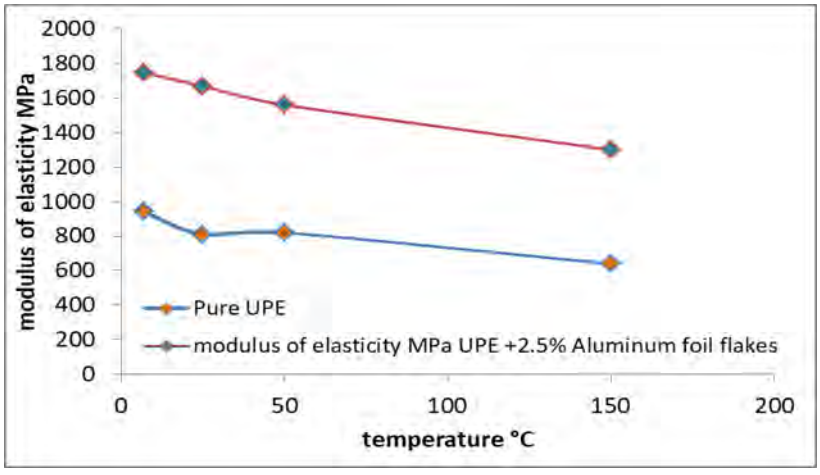

Figure 10. Modulus of Elasticity of Unsaturated Polyester Before and After Reinforcement at Different Temperatures

The curves clearly demonstrate the significant mechanical advantage of the composite material compared to the pure material at all tested temperatures. The modulus of elasticity of the composite starts at a high value of approximately 1750 MPa, nearly double that of the pure material, which starts at around 950 MPa. The values of both samples gradually decrease with increasing temperature, reaching approx.-imately 1300 MPa for the composite and around 650 MPa for the pure material at 150°C. This marked superiority in the modulus of elasticity of the composite is attributed to the rigidity of the aluminum foil flakes waste, which significantly enhances the material's strength, thus improving its resistance to elastic deformation under loads. The foil also restricts the movement of the polymer chains, even at high temperatures. This gradual decrease in values with increasing temperature can be explained by the fact that time and temperature cause the polymer matrix to soften thermally, as the polymer chains gain additional kinetic energy, thus reducing the overall stiffness of the material. However, the addition of metal fillers reduces this decrease and preserves the properties of the composite material [31].

Table 8. Modulus of Elasticity of Unsaturated Polyester Before and After Reinforcement at Different Temperatures

Temperature (°C)	Modulus of elasticity (MPa)	
	Pure UPE	UPE +2.5% Aluminum foil flakes waste
7	940	1745
25	810	1669
50	820	1560
150	640	1300

This graph compares the thermal conductivity, in watts/m² × 10^{-4}, of pure unsaturated polyester (UPE) and a composite material made of pure unsaturated polyester reinforced with aluminum foil powder (UPE + aluminum foil powder) over a temperature range from room temperature to 150 °C (Table 9 and Figure 11). The curves clearly show that the composite material has significantly higher thermal conductivity values than the pure material at all tested temperatures.

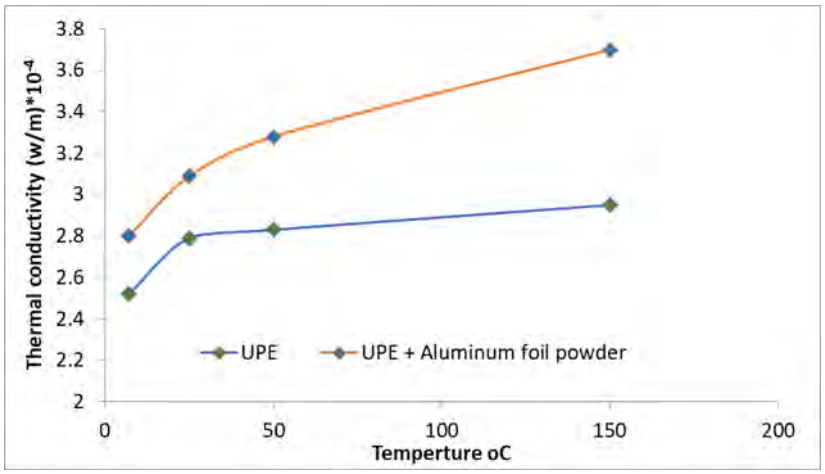

Figure 11. Thermal Conductivity of Unsaturated Polyester Before and After Reinforcement at Different Temperatures

At room temperature, the thermal conductivity of the reinforced composite is approximately 2.8 × 10^{-4} W/m², compared to 2.5 × 10^{-4} W/m² for the pure material. This variation rises up to 150 o C where the thermal conductivity of the composite material has attained about 3.7 x 10^{-4} W/m, in contrast to 2.95 x 10^{-4} W/m in the pure material. This massive enhancement in the thermal conductivity of the composite can be explained by the fact that the aluminum foil flakes waste is metallic in nature and has a far greater thermal conductivity compared to the polymer matrix which is an insulator. This foil serves as a heat conductor in the material and makes the thermal energy flow through the polymer material easier. Moreover, the thermal conductivity was higher with high temperature simply because the thermal activity of the molecules is also higher, thereby improving the transfer of energy. The composite material has enhanced thermal performance thus being applicable in applications that need effective heat dissipation [32].

Table 9. Thermal Conductivity of Unsaturated Polyester Before and After Reinforcement at Different Temperatures

Temperature (°C)	Thermal conductivity (w/m)*10^{-4}	
	UPE	UPE + Aluminum foil flask waste
7	2.52	2.8
25	2.79	3.09
50	2.83	3.28
150	2.95	3.7

The Fourier transform infrared (FTIR) spectrum reveals characteristic absorption peaks for the chemical structure of pure unsaturated polyester and the sample reinforced with 2.5% aluminum foil flakes waste powder (Figure 12). The peaks at 2926–2958 cm^{-1} represent the tensile vibrations of the CH bonds, while a high peak at 1716–1732 cm^{-1} is found in the carbonyl (C=O) group of the ester group.

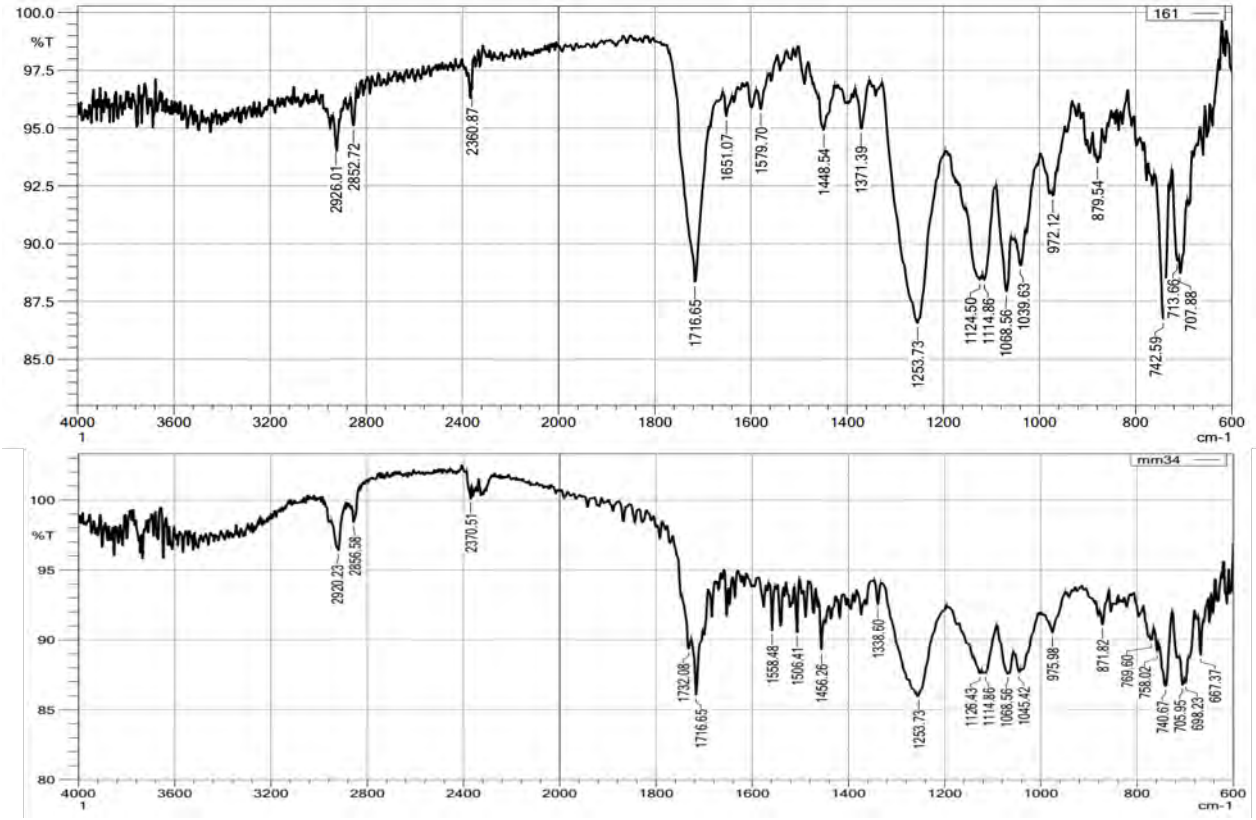

Figure 12. Fourier Transform Infrared (FTIR) Spectrum of (a) Pure Unsaturated Polyester and (b) Sample Reinforced with 2.5% Aluminum Foil Flakes Waste Powder

Other peaks are found at 1253 cm^{-1} for the C–O bond, at 1448–1456 cm^{-1} for the bending vibrations of the C–H bonds, in the region of 1068–1124 cm^{-1} for the C–O–C bonds, and finally, the spectrum at 707–879 cm^{-1} is attributed to the aromatic rings. Comparing the two spectra, it is clear that the main absorption peaks are exactly the same in both the pure sample and the composite material, and no new peaks were observed, indicating that the addition of aluminum foil flakes waste powder did not change the chemical composition of the polymer, and that the reaction was carried out through physical interactions between the filler and the polymer matrix without changing the structural integrity of the material [33].

The distribution of aluminum particles in the polymer structure was investigated using scanning electron microscopy (SEM) images of an unsaturated polyester structure reinforced with aluminum foil flakes waste powder (Figure 13). The images show the size of the aluminum particles distributed across the entire surface of the material.

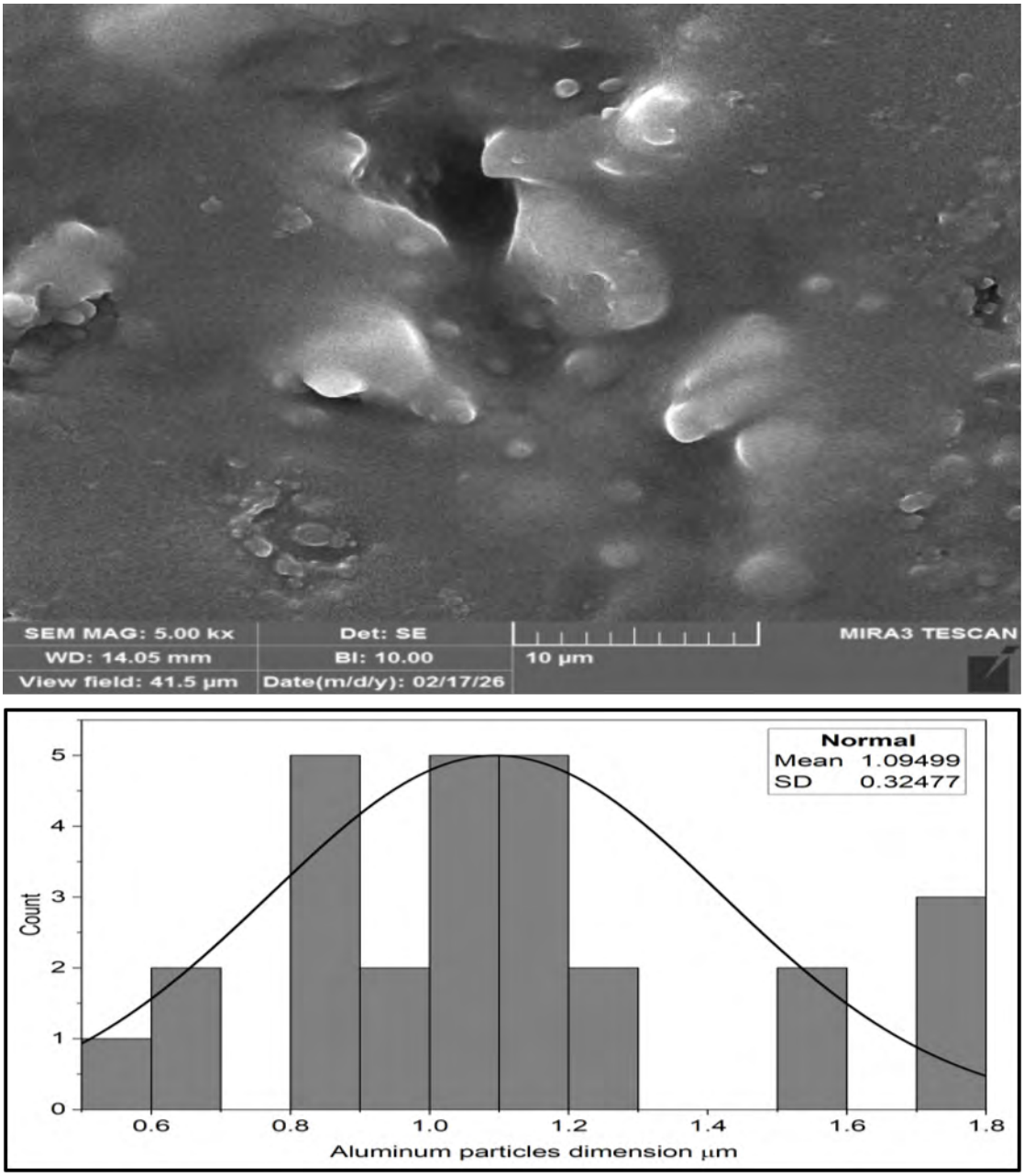

Figure 13. Scanning Electron Microscopy (SEM) Images of an Unsaturated Polyester Structure Reinforced with Aluminum Foil Flakes Waste Powder

The particle size distribution was statistically analyzed to predict the lateral distribution, with an average particle size of 1.09 µm and a standard deviation of 0.32, falling within the range of approximately 0.6 µm to 1.8 µm. It is also indicated in the images that there are changes in the distribution of the particles, hence the agglomeration in some regions, which can influence the mechanical properties of the composite material. Moreover, the contact between the polymer matrix and the particles of aluminum can be observed, which is essential to transfer stress and

increases mechanical properties. The observation that the particles were partially homogeneous will enhance the level of reinforcement and the overall mechanical performance of the composite material [34].

Energy-Dispersive X-ray spectroscopy (EDX) analysis of unsaturated polyester reinforced with 2.5% aluminum foil flakes waste powder can be used to determine the elemental composition of the composite material (Figure 14).

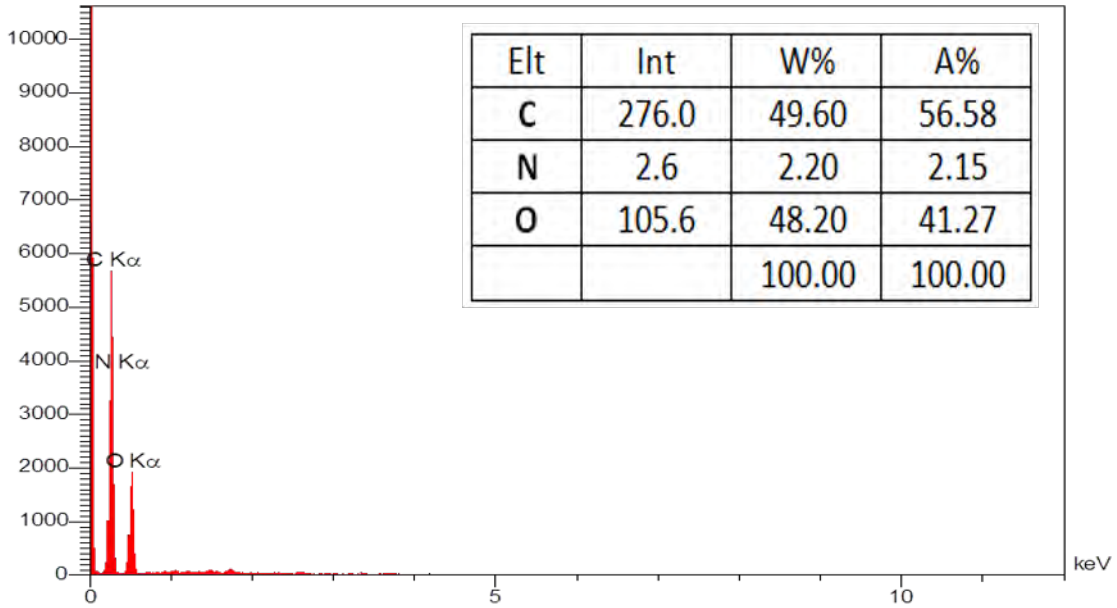

Elt	Int	W%	A%
C	276.0	49.60	56.58
N	2.6	2.20	2.15
O	105.6	48.20	41.27
		100.00	100.00

Figure 14. Energy-Dispersive X-ray Spectroscopy (EDX) of Unsaturated Polyester Reinforced with 2.5% Aluminum Powder

The results show three main components: carbon (C) at 49.60% wt. and 56.58% atomic mass, oxygen (O) at 48.20% wt. and 41.27% atomic mass, and nitrogen (N) at 2.20% wt. and 2.15% atomic mass. The high percentages of carbon and oxygen indicate that the unsaturated polyester is a chemical compound composed of hydrocarbon chains and oxygen-containing ester groups. Trace amounts of nitrogen may be present, which could be explained by impurities or additives introduced during the manufacturing process. It should also be noted that the low aluminum content at the time of analysis may be due to the low percentage of aluminum added (2.5%), which may be below the detection threshold of the instrument used [35].

The thermogravimetric analysis (TGA) curve shows the thermal properties of unsaturated polyester reinforced with 2.5% aluminum foil flakes waste powder over a temperature range up to 350°C (Figure 15). The curve exhibits remarkable thermal stability up to the starting point at 156.0°C, where the composite begins to experience gradual weight loss.

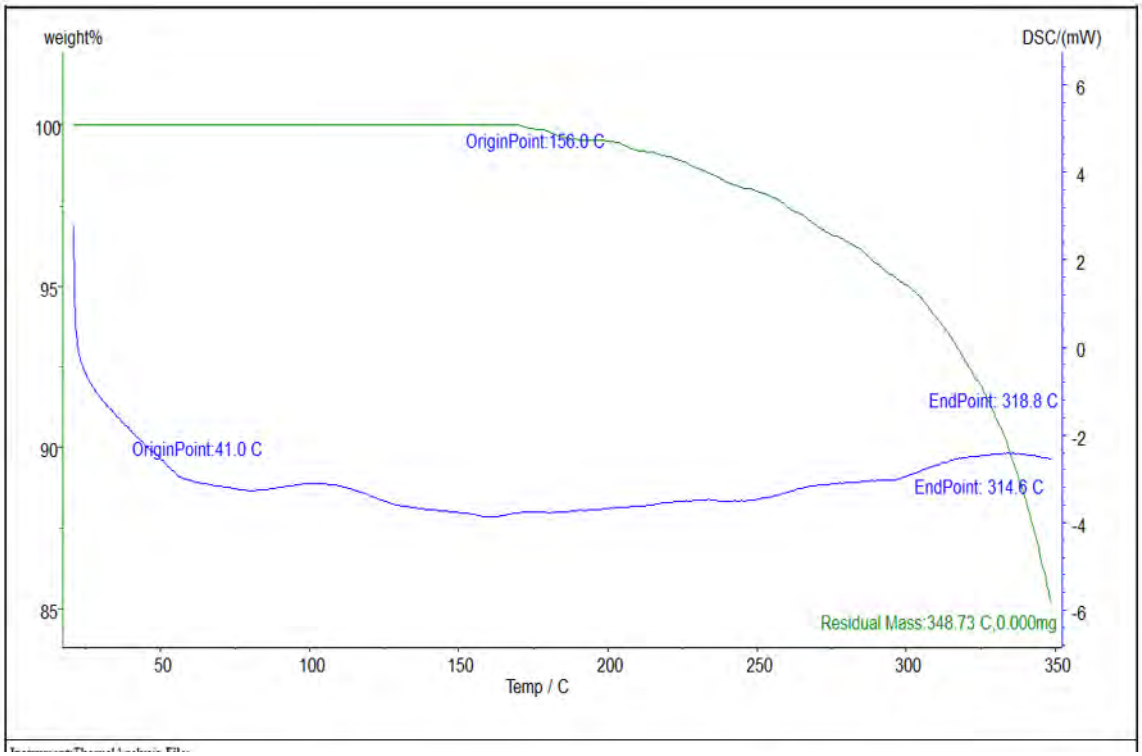

Figure 15. Thermogravimetric Analysis (TGA) and Differential Thermal Scanning (DSC) Curves of Unsaturated Polyester Reinforced with 2.5% Aluminum Foil Flakes Waste Powder

The thermal decomposition process can be divided into three main stages: the first stage (41–156.5°C), characterized by slight weight loss due to moisture evaporation and solvent residue; the second stage (156–318.8°C), the main thermal decomposition stage, where significant weight loss occurs due to the dissociation of polymer chains and the destruction of ester groups; and the final stage, completed at the endpoint (318.8°C). The results show that the final residue mass was 0.000 mg at 348.73°C, indicating complete decomposition of the organic material. This is because the presence of aluminum molecules in the composite material gives it relative thermal stability. These molecules serve as a thermal barrier and slow down the transfer of heat and restrict the movement of the polymer chains. This, respectively, postpones the breakdown of thermal degradation and increases the thermal resistance of the composite material. The differential thermal scanning (DSC) curve demonstrates the change in the heat flux (DSC/mW) of the composite material as a function of the temperature, which implies the physical and thermal transformations that take place in the composite material. The point where the curve starts is 41.0°C, the glass transition temperature (Tg) of the composite material, the point at which the material changes into a not-so-solid, more flexible and elastic one. Heat flux changes were recorded at approximately 314.8°C (the endpoint) between the main thermal and chemical decomposition reactions of the polymer. The overall shape of the curve indicates relative thermal stability within the intermediate temperature range (50–150°C), after which the heat flux gradually decreases as the temperature approaches the decomposition

region. The presence of aluminum molecules in the polymer structure influences the heat flux behavior. It impedes the movement of polymer chains and alters the degree of glass transition, but it improves the thermal and mechanical properties of the composite material when exposed to different operating conditions [36].

4. Conclusion

The current paper indicates that waste in the form of aluminum foil flakes reinforcing filler is a highly appropriate material in improving the mechanical and thermal characteristics of unsaturated polyester resin (UPR) composites, with the best concentration of reinforcement being 2.5 wt.%. Compressive strength (increasing by a factor of 2.2), impact resistance (1.5 to 1.69 kJ/m^2), Shore-D hardness (83 to 93.5), and modulus of elasticity (810 to 1669 MPa) at 25°C and increased thermal conductivity values (3.7 x 10^3 W/m at 150°C versus 2.95 x 10^3 W/m, unreinforced matrix) were significantly improved at this. The enhancements in high temperature (7°C-150°C) can be explained by the high rigidity and thermal stability of aluminum flakes which serve as an effective coating with regard to inhibiting the mobility of polymer chains and slowing down the process of thermal softening. The techniques of characterization, such as FTIR, SEM, EDX, TGA, and DSC, proved the fact that the reinforcement took place mainly because of physical interactions without changing the chemical structure of the polyester matrix, and agglomeration of the particles above the optimal loading percentage led to a decrease in the properties due to the lack of strong bonds between the particles and concentration sites.

5. Acknowledgment

I extend my sincere thanks to the University of Mosul and the College of Education for Women for their support in completing the research.

6 References

1. Ezeh EM. Advances in the development of polyester resin composites: A review. *World J. Eng.*, 2026, 23(1), 97-117.
2. Thomas S, Malhotra SK in Unsaturated Polyester Resins: Fundamentals, Characterization, and Applications, Elsevier, 2014.
3. Callister WD, Rethwisch DG in Materials Science and Engineering: An Introduction, 10th ed., Wiley, 2020.
4. Valizade N, Farhat Z. A review on abrasive wear of aluminum composites: mechanisms and influencing factors. *J. Compos. Sci.*, 2024, 8(4), 149.

5. Mahfoudh K, Sulyman EZ. Improving the mechanical and thermal properties of unsaturated polyester resin by adding aluminum oxide Al_2O_3. *Funct. Mater.*, 2026, 33(1), 83-91.
6. Mohammed Saeed JK, Sulyman EZ, Al-Ahmady KK. Improving mechanical and thermal properties of unsaturated polyurea by adding copper(II) oxide nanoparticles. *Ochrona przed Korozją*, 2025, (7), 206-214.
7. Gibson RF in Principles of Composite Material Mechanics, 4th ed., CRC Press, 2016.
8. Wypych G. The effect of fillers on the mechanical properties of filled materials. In: Handbook of Fillers, 4th ed., ChemTec Publishing, 2016, pp 467-531.
9. Singhal V, Shelly D, Saxena A, Gupta R, Verma VK, Jain A. Study of the influence of nanoparticle reinforcement on the mechanical and tribological performance of aluminum matrix composites—A review. *Lubricants*, 2025, 13(2), 93.
10. Hemadi EK, Al-Ahmady KK, Sulyman EZ. Improving mechanical and thermal properties of unsaturated polyester resin by adding automotive glass waste. *Ochrona przed Korozją*, 2024, (10), 294-305.
11. Mazumdar SK in Composites Manufacturing: Materials, Product, and Process Engineering, CRC Press, 2002.
12. Kuan HTN, Tan MY, Shen Y, Yahya MY. Mechanical properties of particulate organic natural filler-reinforced polymer composite: A review. *Compos. Adv. Mater.*, 2021, 30, 26349833211007502.
13. Spinelli MC, Batista SS, Santos PA, Santos KMG, Neto CR, Silva EP, Caires LS, Lima RM, Santos AM, Tavares SMO, Moreira RAS, Faria DRM, Amado JAD, Marques JES, Souza LG. Mechanical and thermal characterization of sustainable polyester composites reinforced with Mill Scale. *NDT*, 2026, 4(1), 4.
14. Goyal RK, Negi YS, Tiwari AN. High performance polymer composites on PEEK reinforced with aluminum oxide. *J. Appl. Polym. Sci.*, 2006, 100(6), 4623-4631.
15. Ibraheem EK, Bdaiwi W. Enhancing mechanical and thermal properties of unsaturated polyester composites through Sidr leaves' particle reinforcement. *Rev. Compos. Mater. Av.*, 2024, 34(3), 269.
16. Chawla KK in Composite Materials: Science and Engineering, 3rd ed., Springer, 2013.
17. Abbas MA, Al-Turaihi AS. A review of particulate fillers in unsaturated polyester composites: Property enhancement and applications. *Iraqi J. Mech. Mater. Eng.*, 2025, 24(3), 32-56.
18. Al-Mufti SM, Almontasser A, Rizvi SJ. Unsaturated polyester resin filled with cementitious materials: A comprehensive study of filler loading impact on mechanical properties, microstructure, and water absorption. *ACS Omega*, 2023, 8(23), 20389-20403.
19. Sawpan MA, doctoral dissertation, "Mechanical Performance of Industrial Hemp Fibre Reinforced Polylactide and Unsaturated Polyester Composites", The University of Waikato, 2010.
20. Mallick PK in Fiber-Reinforced Composites: Materials, Manufacturing, and Design, 3rd ed., CRC Press, 2007.
21. Sadeghi B, Cavaliere P, Sadeghian B. Enhancing strength and toughness of aluminum laminated composites through hybrid reinforcement using dispersion engineering. *J. Compos. Sci.*, 2023, 7(8), 332.
22. Wu X, Zhang W. A review on aluminum matrix composites' charac-

teristics and applications for automotive sector. *Heliyon*, 2024, 10(20).
23. Mishra B, Varshney S, Gupta MK. Effect of fillers on the performance of fibre reinforced polymer hybrid composites: a comprehensive review. *Polym.-Plast. Technol. Mater.*, 2025, 64(14), 2179-2213.
24. Mohan KS, Awad NM, Hussein WA, Farhan AJ. Influence of aluminum fine powder content on the some mechanical properties of epoxy and polyester composites. *IOP Conf. Ser.: Mater. Sci. Eng.*, 2020, 757(1), 012005. https://doi.org/10.1088/1757-899X/757/1/012005
25. Rahman MA, Khan MM, Ahmed S. Thermal-mechanical performance of polymer composites reinforced with waste aluminum fillers. *Polym. Test.*, 2022, 108, 107118. https://doi.org/10.1016/j.polymertesting 2022.107118
26. Zhang L, Wang Y, Liu H. Impact behavior of particulate-filled polyester composites: Role of filler dispersion and interfacial bonding. *Composites, Part B*, 2020, 183, 107115. https://doi.org/10.1016/j. compositesb.2019.107115
27. Gupta RK, Singh P, Kumar A. Temperature-dependent impact response of metal-filled polymer composites for structural applications. *J. Appl. Polym. Sci.*, 2023, 140(8), e53421. https://doi.org/10.1002/app.53421
28. El-Shekeil YA, Albores V. Hardness enhancement in polymer composites through optimal metallic filler loading. *Mater. Des.*, 2021, 201, 109120. https://doi.org/10.1016/j.matdes.2021.109120
29. Ibrahim ME, Osman AF. Thermal stability of surface hardness in aluminum-reinforced polyester composites. *J. Therm. Anal. Calorim.*, 2022, 147(4), 2145-2156. https://doi.org/10.1007/s10973-021-11234-8
30. Chen X, Li J, Zhou T. Stiffness optimization of polymer composites using waste aluminum fillers: Experimental and theoretical analysis. *Compos. Struct.*, 2021, 261, 113125. https://doi.org/10.1016/j.compstruct.2020.113125
31. Mohammed AS, Ali KH. Elevated temperature performance of elastic modulus in particulate-reinforced thermoset composites. *Polym. Degrad. Stab.*, 2023, 208, 110122. https://doi.org/10.1016/j.polymdegradstab.2023.110122
32. Kumar S, Patel R, Singh V. Thermal conductivity enhancement in polymer matrices using metallic waste fillers: Mechanisms and applications. *Int. J. Heat Mass Transfer*, 2022, 184, 122134. https://doi.org/10.1016/j.ijheatmasstransfer.2021.122134
33. Abdullah MZ, Rahman NA. FTIR characterization of filler-matrix interactions in aluminum-reinforced polyester composites. *Spectrochim. Acta, Part A*, 2021, 248, 119128. https://doi.org/10.1016/j.saa.2020.119128
34. Hassan MK, Ali SM. Microstructural analysis of particle dispersion and interfacial adhesion in metal-filled polymer composites via SEM. *Microsc. Res. Tech.*, 2022, 85(3), 891-903. https://doi.org/10.1002/jemt.23945
35. Lee JH, Kim SY, Park DH. Elemental composition analysis of polymer composites using EDX spectroscopy: Methodology and interpretation. *J. Mater. Anal.*, 2021, 36(2), 145-157. https://doi.org/10.1016/j jmatana.2021.02.003
3 Ahmed F, Mahmoud R. Thermal

6. degradation kinetics and glass transition behavior of aluminum-filled polyester composites: A TGA/DSC study. *Thermochim. Acta*, 2023, 719, 179-191. https://doi.org/10.1016/j.tca.2023.179191

The AIC Code of Ethics

Approved by the AIC Board of Directors, April 29, 1983

The profession of chemistry is increasingly important to the progress and the welfare of the community. The Chemist is frequently responsible for decisions affecting the lives and fortunes of others. To protect the public and maintain the honor of the profession, the American Institute of Chemists has established the following rules of conduct. It is the Duty of the Chemist:

1. To uphold the law; not to engage in illegal work nor cooperate with anyone so engaged;

2. To avoid associating or being identified with any enterprise of questionable character;

3. To be diligent in exposing and opposing such errors and frauds as the Chemist's special knowledge brings to light;

4. To sustain the institute and burdens of the community as a responsible citizen;

5. To work and act in a strict spirit of fairness to employers, clients, contractors, employees, and in a spirit of personal helpfulness and fraternity toward other members of the chemical profession;

6. To use only honorable means of competition for professional employment; to advertise only in a dignified and factual manner; to refrain from unfairly injuring, directly or indirectly, the professional reputation, prospects, or business of a fellow Chemist, or attempting to supplant a fellow chemist already selected for employment; to perform services for a client only at rates that fairly reflect costs of equipment, supplies, and overhead expenses as well as fair personal compensation;

7. To accept employment from more than one employer or client only when there is no conflict of interest; to accept commission or compensation in any form from more than one interested party only with the full knowledge and consent of all parties concerned;

8. To perform all professional work in a manner that merits full confidence and trust; to be conservative in estimates, reports, and testimony, especially if these are related to the promotion of a business enterprise or the protection of the public interest, and to state explicitly any known bias embodied therein; to advise client or employer of the probability of success before undertaking a project;

9. To review the professional work of other chemists, when requested, fairly and in confidence, whether they are:
    a. subordinates or employees
    b. authors of proposals for grants or contracts
    c. authors of technical papers, patents, or other publications
    d. involved in litigation;

10. To advance the profession by exchanging general information and experience with fellow Chemists and by contributing to the work of technical societies and to the technical press when such contribution does

not conflict with the interests of a client or employer; to announce inventions and scientific advances first in this way rather than through the public press; to ensure that credit for technical work is given to its actual authors;

11. To work for any client or employer under a clear agreement, preferable in writing, as to the ownership of data, plans, improvements, inventions, designs, or other intellectual property developed or discovered while so employed, understanding that in the absence of a written agreement:
    a. results based on information from the client or employer, not obtainable elsewhere, are the property of the client or employer
    b. results based on knowledge or information belonging to the Chemist, or publicly available, are the property of the Chemist, the client or employer being entitled to their use only in the case or project for which the Chemist was retained
    c. all work and results outside of the field for which the Chemist was retained or employed, and not using time or facilities belonging to a client or employer, are the property of the Chemist;

12. Special data or information provided by a client or employer, or created by the Chemist and belonging to the client or employer, must be treated as confidential, used only in general as a part of the Chemist's professional experience, and published only after release by the client or employer;

13. To report any infractions of these principles of professional conduct to the authorities responsible for enforcement of applicable laws or regulations, or to the Ethics Committee of The American Institute of Chemists, as appropriate.

The Chemist
Journal of the American Institute of Chemists

Manuscript Style Guide

The Chemist is the official online refereed journal of The American Institute of Chemists (AIC). We accept submissions from all fields of chemistry defined broadly (e.g., scientific, educational, socio-political). *The Chemist* will not consider any paper or part of a paper that has been published or is under consideration for publication anywhere else. The editorial office of *The Chemist* is located at: The American Institute of Chemists, Inc. 315 Chestnut Street Philadelphia, PA 19106-2702, Email: aicoffice@theaic.org.

Categories of Submissions

RESEARCH PAPERS

Research Papers (up to ~5000 words) that are original will only be accepted. Research Papers are peer-reviewed and include an abstract, an introduction, up to 5 figures or tables, sections with brief subheadings and a maximum of approximately 30 references.

REPORTS

Reports (up to ~3000 words) present new research results of broad interest to the chemistry community. Reports are peer- reviewed and include an abstract, an introductory paragraph, up to 3 figures or tables, and a maximum of approximately 15 references.

BRIEF REPORTS

Brief Reports (up to ~1500 words) are short papers that are peer-reviewed and present novel techniques or results of interest to the chemistry community.

REVIEW ARTICLES

Review Articles (up to ~6000 words) describe new or existing areas of interest to the chemistry community. Review Articles are peer-reviewed and include an abstract, an introduction that outlines the main point, brief subheadings for each section and up to 80 references.

LETTERS

Letters (up to ~500 words) discuss material published in The Chemist in the last 8 months or issues of general interest to the chemistry community.

BOOK REVIEWS

Book Reviews (up to ~ 500 words) will be accepted.

Manuscript Preparation

RESEARCH PAPERS, REPORTS, BRIEF REPORTS & REVIEW ARTICLES

- **The first page** should contain the title, authors and their respective institutions/affiliations and the corresponding author. The general area of chemistry the article represents should also be indicated, i.e. General Chemistry, Organic Chemistry, Physical Chemistry, Chemical Education, etc.

- **Titles** should be 55 characters or less for Research Papers, Reports, and Brief Reports. Review articles should have a title of up to 80 characters.

- **Abstracts** explain to the reader why the research was conducted and why it is important to the field. The abstract should be 100-150 words and convey the main point of the paper along with an outline of the results and conclusions.

- **Text** should start with a brief introduction highlighting the paper's significance and should be understood to readers of all chemistry disciplines. All symbols, abbreviations, and acronyms should be defined the first time they are used. All tables and figures should be cited in numerical order.

- **Units** must be used appropriately. Internationally accepted units of measurement should be used in conjunction with their numerical values. Abbreviate the units as shown: cal, kcal, µg, mg, g (or gm), %, ^{o}C, nm, µm (not m), mm, cm, cm^{3}, m, in. (or write out inch), h (or hr), min, s (or sec), ml [write out liter(s)], kg. Wherever commonly used units are used their conversion factors must be shown at their first occurrence. Greek symbols are permitted as long as they show clearly in the soft copy.

- **References and notes** should be numbered in the order in which they are cited, starting with the text and then through the table and figure legends. Each reference should have a unique number and any references to unpublished data should be given a number in the text and referred to in the references. References should follow the standards presented in the AIC Reference Style Guidelines below.

REFERENCE STYLE GUIDELINES

References should be cited as numbers within square brackets [] at the appropriate place in the text. The reference numbers should be cited in the correct order throughout the text (including those in tables and figure captions, numbered according to where the table or figure is designated to appear). The references themselves are listed in numerical order at the end of the final printed text along with any Notes. Journal abbreviations should be consistent with those presented in Chemical Abstracts Service Source Index (CASSI) (http://www.cas.org) guide available at most academic libraries.

- **Names** and initials of all authors should always be given in the reference and must not be replaced by the phrase *et al*. This does not preclude one from referring to them by the first author, et al in the text.

- **Tables** should be in numerical order as they appear in the text and they should not duplicate the text. Tables should be completely understandable without reading the text. Every table should have a title. Table titles should be placed above the respective tables.

  Table 1. Bond Lengths (Å) of 2-aminophenol

- **Figure legends** should be in numerical order as they appear in the text. Legends should be limited to 250 words.

  Figure 1. PVC Melt Flow Characterized by Analytical Structural Method

- **Letters and Book Reviews** should be clearly indicated as such when being submitted. They are not peer-reviewed and are published as submitted. Legends should be placed after/under the respective figures.

- **Journals -** The general format for citations should be in the order: **author(s), journal, year, volume, page**. Page number ranges are preferred over single values, but either format is acceptable. Where page numbers are not yet known, articles may be cited by DOI (Digital Object Identifier). For example:

  Booth DE, Isenhour TL. *The Chemist*, 2000, 77(6), 7-14.

- **Books -** For example:

  Turner GK in *Chemiluminescence: Applications*, ed. Knox Van Dyke, CRC Press, Boca Raton, 1985, vol 1, ch. 3, pp 43-78.

- **Patents** should be indicated in the following form:

  McCapra F, Tutt D, Topping RM, UK Patent Number 1 461 877, 1973.

- **Reports and bulletins, etc. -** For example:

  Smith AB, Jones CD, *Environmental Impact Report for the US*, final report to the National Science Foundation on Grant AAA-999999, Any University, Philadelphia, PA, 2006.

- **Material presented at meetings -** For example:

  Smith AB. Presented at the Pittsburgh Conference, Atlantic City, NJ, March 1983, paper 101.

- **Theses -** For example:

  Jones AB, Ph.D. Thesis, Columbia University, 2004.

- For material presented at a meeting, congress or before a Society, etc., but not published, the following form should be used:

  Jones AB, presented in part at the 20th American Institute of Chemists National Meeting, Philadelphia, PA, June, 2004.

- For material accepted for publication, but not yet published, the following form should be used:

  Smith AB. *Anal. Chem*., in press

- For material submitted for publication but not yet accepted the following form should be used:

  Jones AB, *Anal. Chem*. submitted for publication.

- For personal communications the following should be used:

  Smith AB, personal communication.

- If material is to be published but has not yet been submitted the following form should be used:

  Smith AB, unpublished work.

Reference to unpublished work should not be made without the permission of those by whom the work was performed.

Manuscript Selection

The submission and review process is completely electronic. Submitted papers are assigned by the Editors, when appropriate, to at least two external reviewers anonymously. Reviewers will have approximately 10 days to submit their comments. In selected situations the review process can be expedited. Selected papers will be edited for clarity, accuracy, or to shorten, if necessary. The Editor-in-Chief will have final say over the acceptance of submissions. Most papers are published in the next issue after acceptance. Proofs will be sent to the corresponding author for review and approval. Authors will be charged for excessive alterations at the discretion of the Editor-in-Chief.

Conditions of Acceptance

When a paper is accepted by *The Chemist* for publication, it is understood that:

- Any reasonable request for materials to verify the conclusions or experiments will be honored.

- Authors retain copyright but agree to allow *The Chemist* to exclusive license to publish the submission in print or online.
- Authors agree to disclose all affiliations, funding sources, and financial or management relationships that could be perceived as potential conflicts of interest or biases.
- The submission will remain a privileged document and will not be released to the public or press before publication.
- The authors certify that all information described in their submission is original research reported for the first time within the submission and that the data and conclusions reported are correct and ethically obtained.
- The Chemist, the referees, and the AIC bear no responsibility for accuracy or validity of the submission.

Authorship

By submitting a manuscript, the corresponding author accepts the responsibility that all authors have agreed to be listed and have seen and approved of all aspects of the manuscript including its submission to *The Chemist*.

Submissions

Authors are required to submit their manuscripts, book reviews and letters electronically. They can be submitted via email at aicoffice@theaic.org with "Submission for consideration in *The Chemist*" in the subject line. All submissions should be in Microsoft® Word format.

Copyright Assignment & Warranty Form for The Chemist

It is the policy of *The Chemist* to require all contributors to transfer the copyright for their contributions (hereafter referred to as the manuscript) to The American Institute of Chemists, Inc. (hereafter referred to as The AIC) the official publisher of *The Chemist*. By signing this agreement you assign to The AIC to consider publishing your manuscript the exclusive, royalty-free, irrevocable copyright in any medium internationally for the full term of the copyright. This agreement shall permit The AIC to publish, distribute, create derivative works, and otherwise use any materials accepted for publication in *The Chemist* internationally. A copy of the Copyright and Warranty Form for *The Chemist* will be sent to the author(s) whose manuscript is accepted for publication. The AIC will not publish any accepted manuscript in *The* Chemist without its author(s) fully complying with this requirement.

For further information or if you can any questions please contact the Publisher of *The Chemist* at (215) 873-8224 or via email at publications@theaic.org.

Website: http://www.theaic.org/ Email: aicoffice@theaic.org Phone: 215-873-8224

Announcements

INVITATION TO AUTHORS

Authors are invited to submit manuscripts for ***The Chemist,*** the official online refereed journal of The American Institute of Chemists (AIC). We accept submissions from all fields of chemistry defined broadly (e.g., scientific, educational, socio-political). *The Chemist* will not consider any paper or part of a paper that has been published or is under consideration for publication anywhere else.

Research Papers (up to ~5000 words) that are original will only be accepted. Research Papers are peer-reviewed and include an abstract, an introduction, up to 5 figures or tables, sections with brief subheadings and a maximum of approximately 30 references.

Reports (up to ~3000 words) present new research results of broad interest to the chemistry community. Reports are peer- reviewed and include an abstract, an introductory paragraph, up to 3 figures or tables, and a maximum of approximately 15 references.

Brief Reports (up to ~1500 words) are short papers that are peer-reviewed and present novel techniques or results of interest to the chemistry community.

Where to Send Manuscripts?

Please submit your manuscripts by email (aicoffice@theaic.org) to the attention of:

The Editor-in-Chief, The Chemist
The American Institute of Chemists, Inc.
315 Chestnut Street,
Philadelphia, PA 19106-2702
Email: aicoffice@theaic.org

Review Articles (up to ~6000 words) describe new or existing areas of interest to the chemistry community. Review Articles are peer-reviewed and include an abstract, an introduction that outlines the main point, brief subheadings for each section and up to 80 references.

Letters (up to ~500 words) discuss material published in *The Chemist* in the last 8 months or issues of general interest to the chemistry community.

Book Reviews (up to ~ 500 words) will be accepted.